DISCLAIMER

This report was prepared as an account of work sponsored by an agency of the United States Government. Neither the United States Government nor any agency thereof, nor any of their employees, makes any warranty, express or implied, or assumes any legal liability or responsibility for the accuracy, completeness, or usefulness of any information, apparatus, product, or process disclosed, or represents that its use would not infringe privately owned rights. Reference herein to any specific commercial product, process, or service by trade name, trademark, manufacturer, or otherwise does not necessarily constitute or imply its endorsement, recommendation, or favoring by the United States Government or any agency thereof. The views and opinions of authors expressed herein do not necessarily state or reflect those of the United States Government or any agency thereof. Reference herein to any social initiative (including but not limited to Diversity, Equity, and Inclusion (DEI); Community Benefits Plans (CBP); Justice 40; etc.) is made by the Author independent of any current requirement by the United States Government and does not constitute or imply endorsement, recommendation, or support by the United States Government or any agency thereof.

WHOLESCALE FINAL TECHNICAL REPORT: SAN EMIDIO 2020 — 2024

KURT L. FEIGL, SABRINA L. BRADSHAW, AND THE WHOLESCALE TEAM

Federal Agency and Organization:	DOE EERE – Geothermal Technologies Program
Recipient Organization:	University of Wisconsin System
DUNS Number:	161202122
Recipient Address:	Research and Sponsored Programs 21 N. Park Street, Suite 6401; Madison, WI 53715-1218
Award Number:	DE-EE0009032
Project Title:	WHOLESCALE – Water & Hole Observations Leverage Effective Stress Calculations And Lessen Expenses
Project Period[1,2]:	July 31st 2020 through October 31st 2024
Principal Investigator:	Kurt Feigl, Professor, feigl@wisc.edu, (608) 262 0176
Report Submitted by:	Kurt Feigl, Professor, feigl@wisc.edu, (608) 262 0176
Date of Report Submission:	June 18th, 2025

Project Partners:

University of Wisconsin-Madison (UW) Department of Geoscience	http://geoscience.wisc.edu
Lawrence Livermore National Laboratory (LLNL)	https://www.llnl.gov
Ormat Technologies, Inc.	http://www.ormat.com
University of Nevada-Reno (UNR)	http://geodesy.unr.edu
National Renewable Energy Laboratory (NREL)	https://www.nrel.gov

Signature: *Kurt L Feigl* Date 2025/06/18

*The Prime Recipient certifies that the information provided in this report is accurate and complete as of the date shown.

Acknowledgment: "This material is based upon work supported by the Department of Energy's Office of Energy Efficiency and Renewable Energy (EERE) under the Geothermal Technologies Office under Award Number DE-EE0009032."

[1] The award document was signed on September 9th, 2020.
[2] Modification 004 extended the project period through October 31st 2024.

Table of Contents

SECTION I. EXECUTIVE SUMMARY

The WHOLESCALE acronym stands for Water & Hole Observations Leverage Effective Stress Calculations and Lessen Expenses. The goal of the WHOLESCALE project is to simulate the spatial distribution and temporal evolution of stress in the geothermal system at San Emidio in Nevada, United States. To reach this goal, the WHOLESCALE team has developed a methodology to incorporate and interpret data from four methods of measurement into a multi-physics model that couples thermal, hydrological, and mechanical (T-H-M) processes. The WHOLESCALE team has applied this methodology at the San Emidio geothermal field, located ~100 km north of Reno, Nevada in the northwestern Basin and Range province.

The WHOLESCALE team includes 30 individuals working at two universities, two national laboratories, and one industry partner. Two master-degree students and five post-doctoral researchers have gained professional experience and earned partial financial support via the WHOLESCALE project.

The WHOLESCALE team has taken advantage of the perturbations created by changes in pumping operations during planned shutdowns in 2016, 2021, and 2022 to infer temporal changes in the state of stress in the geothermal system at San Emidio, Nevada, U.S.

The WHOLESCALE results support the working hypothesis that increasing pore-fluid pressure reduces the effective normal stress acting across fault zones. During normal operations, pumping in deep production wells decreases fluid pressures and thus increases the effective normal stresses on faults, reducing microseismicity. During planned shutdowns, the cessation of production increases pore-fluid pressure and reduces effective normal stress.

The WHOLESCALE products generated during the 4-year period between 2020 and 2024 include: three articles published in the open-access, peer-reviewed scientific literature, two master's theses, 20 presentations or papers at scientific conferences, and 17 data sets available on public repositories.

The WHOLESCALE project has been completed in two phases that included three performance periods separated by two Go/No-go Stage Gate Reviews. Tasks were classified by data type (i.e., Geologic Structure, Borehole, Geodesy, Hydrology, Seismology, and Modeling).

The first phase of the project started July 31, 2020 and included ongoing project coordination (Task 1), a project kickoff (Task 2), analysis of existing data (Task 3), development of the initial stress model & deployment design (Task 4), and Go/No-go Decision Point #1 (Task 5). Phase II began with implementing the 2022 deployment (Task 6), followed by Go/No-go Decision Point #2 (Task 7) The remainder of Phase II consisted of analyzing data collected during deployment (Task 8), calibration of the stress model on all observations (Task 9), and the Final Review (August 23, 2024) & Reporting (Task 10).

SECTION II. INTRODUCTION

The WHOLESCALE team includes personnel from two universities (UW &UNR, two national laboratories (LLNL and NREL), and one industry partner (Ormat) (Table 1). We count as members of the WHOLESCALE team those individuals who have performed at least two of the CRediT[3] roles.

Table 1. List of individuals who contributed to the WHOLESCALE project.

Name	Title	Conceptualization	Data curation	Formal Analysis	Funding acquisition	Investigation	Methodology	Project administration	Resources	Software	Supervision	Validation	Visualization	Writing – original draft	Writing – review &	ORCID	Org.	State
Kurt Feigl	PI	1	1	1	1	1	1	1	1	1	1	1	1	1	1	https://orcid.org/0000-0002-2059-6708	UW	WI
Hiroki Sone	Co-PI	1			1	1					1			1	1	https://orcid.org/0000-0001-5525-1294	UW	WI
Jesse Hampton	Co-PI	1			1	1					1			1	1	https://orcid.org/0000-0001-8568-3100	UW	WI
Michael Cardiff	Co-PI	1			1	1					1			1	1	https://orcid.org/0000-0002-6720-6084	UW	WI
Cliff Thurber	Faculty	1		1	1	1					1			1	1	https://orcid.org/0000-0002-4940-4618	UW	WI
Herb Wang	Faculty	1			1	1					1			1	1	https://orcid.org/0000-0002-1631-4608	UW	WI
Corné Kreemer	Faculty		1		1	1					1			1	1	https://orcid.org/0000-0001-6882-9809	UNR	NV
Chris Sherman	Staff Scientist	1			1	1					1			1	1	https://orcid.org/0000-0003-3550-0657	LLNL	CA
Ian Warren	Staff Scientist (a)				1	1					1			1	1	https://orcid.org/0000-0002-5870-8891	NREL	CO
Sabrina Bradshaw	Asst Project Manager		1			1		1						1	1	https://orcid.org/0000-0002-3846-4893	UW	WI
Sui "Jay" Tung	Associate Scientist (b)			1		1				1		1		1	1	https://orcid.org/0000-0002-4708-2133	UW	WI
Hao Guo	Postdoctoral, Scientist		1	1			1			1				1	1	https://orcid.org/0000-0001-8287-3689	UW	WI
Ben Heath	Postdoctoral (c)			1			1			1						https://orcid.org/0000-0002-9460-3042	UW	WI
Erin Cunningham	Postdoctoral (d)			1			1			1						https://orcid.org/0000-0002-9680-6812	UW	WI
Xi Luo	Postdoctoral (e)			1			1			1						https://orcid.org/0009-0004-6401-9971	UW	WI
Matteo Cusini	Postdoctoral									1			1			https://orcid.org/0000-0002-6024-861X	LLNL	CA
Oddy Mudatsir	Graduate Student			1									1			https://orcid.org/0009-0005-8958-3381	UW	WI
Zirou Jin	Graduate Student					1										https://orcid.org/0000-0001-7056-8281	UW	WI
Collin Roland	Graduate Student (f)		1				1			1						https://orcid.org/0000-0003-1004-0746	UW	WI
Ben Jahnke	Graduate Student (g)		1											1	1	https://orcid.org/0000-0002-1837-7522	UW	WI
Samantha Kleich	Graduate Student (h)			1		1								1	1	https://orcid.org/0000-0002-5999-0710	UW	WI
Anya Wolterman	Research Specialist (i)		1			1				1						https://orcid.org/0000-0003-4250-578X	UW	WI
Sam Batzli	Staff Scientist		1													https://orcid.org/0000-0002-9597-5614	UW	WI
Neal Lord	Technician		1			1										https://orcid.org/0000-0003-1457-0381	UW	WI
Peter Sobol	Technician		1			1										https://orcid.org/0009-0003-2083-6323	UW	WI
John Murphy	Resource Manager					1			1							https://orcid.org/0000-0003-4911-0027	Ormat	NV
John Akerley	Resource Manager	1			1				1							https://orcid.org/0000-0001-7055-3450	Ormat	NV
Matthew Folsom	Project Geophysicist (j)			1										1	1	https://orcid.org/0000-0002-9079-6684	Ormat	NV
Courtney Brailo	Project Geologist				1	1										https://orcid.org/0009-0000-6156-7762	Ormat	NV
Gabrielle Ramirez	Project Geologist				1	1										http://orcid.org/0009-0007-7271-9208	Ormat	NV

(a) now Principal Geoscientist at Zanskar Geothermal & Minerals, ID
(b) now Assistant Professor at Texas Tech University, TX
(c) now Duty Scientist at National Tsunami Warning Center, AK
(d) now Geophysicist at now at Oak Ridge National Laboratory, TN
(e) now pursuing Master's Degree in Data Science
(f) now Hydrologist at U.S. Geologic Survey
(g) now Associate Geologist at Cella Mineral Storage, NY
(h) now Geotech Staff now at Shannon & Wilson, OR
(i) now pursuing Master's Degree Civil & Environmental Engineering
(j) now Senior Project Geoscientist at Geologica

University of Wisconsin-Madison (UW) http://geoscience.wisc.edu/
University of Nevada-Reno (UNR) http://geodesy.unr.edu/
Lawrence Livermore National Laboratory (LLNL) https://www.llnl.gov/
National Renewable Energy Laboratory (NREL) https://www.nrel.gov/
Ormat Technologies, Inc. (Ormat) http://www.ormat.com/

[3] Contributor Roles Taxonomy (CRediT) https://credit.niso.org/

Definitions

The following table lists acronyms and defines terms used in this report.

Table 2. Acronyms & Glossary

3DFFS	3-dimensional far-field sonic log
AF	Antithetic Fault
ASF	Alaska Satellite Facility https://asf.alaska.edu/
BBF	Basin Bounding Fault
Brady	Brady Hot Springs, Nevada (field site for POROTOMO)
CRediT	Contributor Roles Taxonomy (CRediT) https://credit.niso.org/
DAS	Distributed Acoustic Sensing
DMP	Data Management Plan
DOE	Department of Energy
DITF	drilling-induced tensile fracture
EERE	Office of energy efficiency and renewable energy
EPIC	EarthScope Primary Instrument Center https://epic.earthscope.org/ (formerly the IRIS PASSCAL Instrument Center)
ESA	European Space Agency
FF	Fan Fault
FOA	Funding Opportunity Announcement
FTR	Final Technical Report
Gannt chart	Bar chart showing a project schedule originally designed by Henry Gantt
GEOS	Open-source modeling software https://www.geos.dev/
GPS	Global Positioning System
InSAR	Interferometric Synthetic Aperture Radar
MSE	Microseismic Events
NF	Nightingale Fault
NWF	NW-striking Fault.
OSTI	Office of Scientific and Technical Information at U.S. Department of Energy
PERT	Program Evaluation Review Technique
PF	Piedmont Fault
POROTOMO	Poroelastic Tomography by Adjoint Inverse Modeling of Data from Seismology, Geodesy, and Hydrology
REST	Regressive ESTimator (REST) autopicking package
ROP	Rate of penetration
RFF	Range Front Fault
RPPR	Research Performance Progress Report
SEF	San Emidio Fault
S_{HMax}	Maximum horizontal stress (reckoning compression positive)
S_{hmin}	Minimum horizontal stress (reckoning compression positive)
S_v	Vertical stress (reckoning compression positive)
SOPO	Statement of Project Objectives
TLA	Three Letter Acronym
TPM	Technical Performance Metric
TRL	Technology Readiness Level
UTC	Universal Time Coordinated
WHOLESCALE	Water & Hole Observations Leverage Effective Stress Calculations and Lessen Expenses
WOB	Weight on bit

Background

The goal of the WHOLESCALE project is to simulate the spatial distribution and temporal evolution of stress in a geothermal system. To reach this goal, the WHOLESCALE team proposed to develop a methodology that will incorporate and interpret data from four methods of measurement into a multi-physics model that couples thermal, hydrological, and mechanical (T-H-M) processes over spatial scales ranging from the diameter of a borehole (~0.1 m) to the extent of the entire field (~10 km) and temporal scales ranging from the duration of a microseismic event (~1 second) to the typical lifetime of a producing field (3 decades).

To do so, the WHOLESCALE team has taken advantage of the perturbations created by pumping operations to infer temporal changes in the state of stress in the geothermal system. This rheological experiment applied the key idea that increasing pore-fluid pressure reduces the effective normal stress acting across preexisting faults. The work included: (1) manipulating the stress field via hydraulic and thermal methods, (2) measuring the resulting response by geophysical methods, and (3) calculating the stress, strain, pressure, and temperature in the geothermal system using an open-source, numerical simulator named GEOS.

The WHOLESCALE team has applied this methodology at the San Emidio geothermal field, located ~100 km north of Reno, Nevada in the northwestern Basin and Range province. Figure 1 shows a conceptual model in vertical cross section. The geology, geophysics, and geothermics have been described previously (Matlick, 1995; Rhodes et al., 2010; Warren, 2010; Eneva et al., 2011; Moeck, 2011; Rhodes, 2011; Rhodes et al., 2011; Faulds, 2014; UNR, 2014; Teplow and Warren, 2015; Pulliam et al., 2019; Reinisch et al., 2019; Warren et al., 2019a; Feigl et al., 2020; Folsom et al., 2020; Folsom et al., 2021; Feigl et al., 2022b; Guo et al., 2022; Jahnke, 2022; Jahnke et al., 2022; Akerley et al., 2023; Jahnke et al., 2023; Sone et al., 2023).

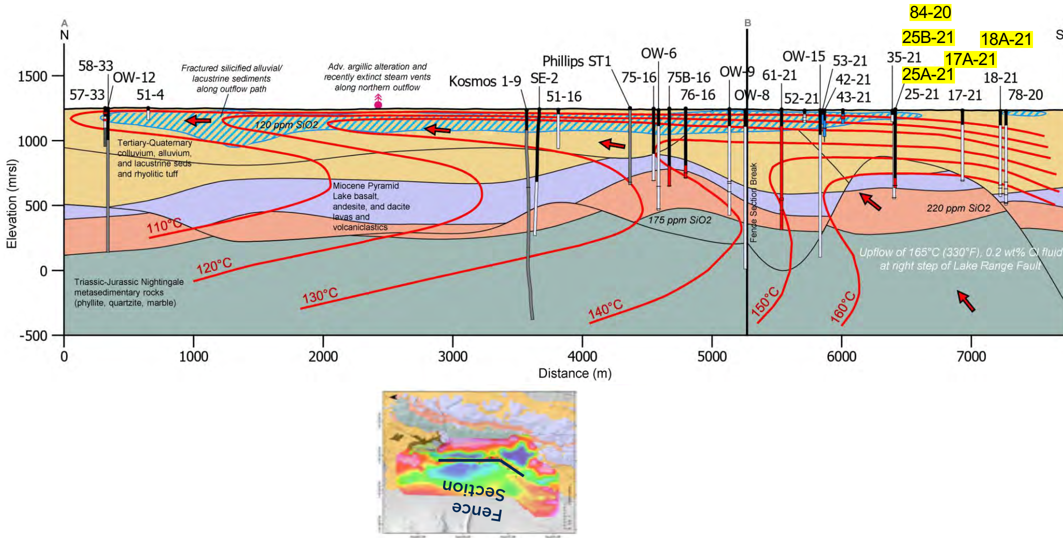

Figure 1: Vertical cross section of conceptual model of WHOLESCALE study area at San Emidio, showing geologic units (color), wells (vertical line segments, black where cased, white where open, red where tapping feed zone), and contours of "native state" temperature (red curves) (Folsom et al., 2020). The cross section follows the two black line segments shown in map view (lower panel) with a bend at point B. Names of wells are indicated (highlighted in yellow if drilled since 2020).

The San Emidio geothermal system occupies a right step in a North-striking, West-dipping, normal fault zone, as mapped in Figure 2 and Figure 3.

Minor dilation and high fault density within the right step likely produce the permeability necessary for deep fluid circulation (e.g., Eneva et al., 2011). Power was first produced in 1987 with a 3.6-MW binary plant, and average production increased to 9 MW (net) following commissioning of a new power plant in 2012. Production has ranged from less than 190 L/s to more than 280 L/s at temperatures of 140–148˚C. Drilling, geological, geophysical, and geochemical data sets collected since the 1970s help constrain controls on the geothermal resource and the structural setting.

At San Emidio, Ormat has provided access to four types of observational data collected by innovative techniques in seismology, drilling, geodesy, and hydrology. To interpolate and interpret these rich data sets, GEOS uses the finite-element method to solve the coupled differential equations governing the physics of a fractured, poroelastic medium under stress. The study site at San Emidio includes a volume with length of ~6 km, width ~5 km, and depth ~2 km. At each point within a mesh of this volume, the resulting numerical solution determines the complete stress tensor as a function of time as well as its sensitivity to perturbations in the input parameters. The numerical GEOS solution also calculates modeled values for each of the four types of observable quantities. By optimizing the goodness of fit between the observations and the modeled value calculated by the GEOS simulator, the methodology determines the model configuration that best fits the data and thus the best prediction of the spatial distribution and temporal evolution of the complete stress tensor.

The WHOLESCALE project should make an important impact because geothermal operators need quantitative information about the subsurface stress to successfully develop and sustainably manage a geothermal reservoir. The applied methodology has advanced capabilities “to directly measure or infer the stress state” which, as noted in the FOA, “are woefully inadequate, especially away from boreholes”. By reducing the uncertainty of in-situ stress estimates, the WHOLESCALE project should reduce the cost of geothermal energy.

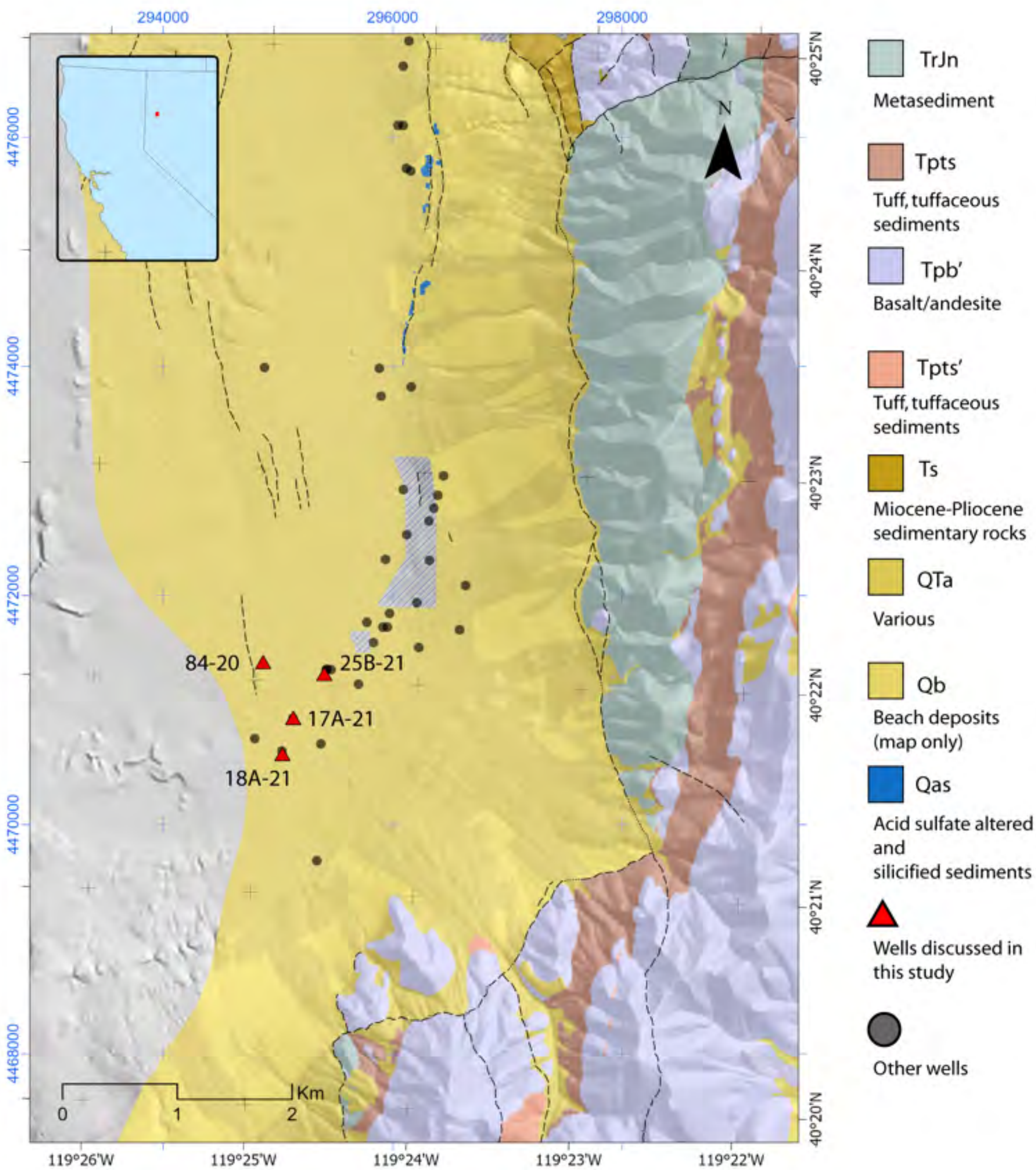

Figure 2. Geologic map of field area. As part of the North Valley Project in the San Emidio geothermal area, Ormat has drilled three new production wells (17A-21, 18A-21, and 25B-21) and two new injection wells (84-20 and 25-28), shown as red triangles. Geologic units simplified from earlier work (Rhodes, 2011; Rhodes et al., 2011) by Matt Folsom (2020). Black tick marks and labels on the east and south edges give geographic (WGS84) latitude and longitude, respectively in degrees and minutes. Blue ticks and labels on north and west edges give easting and northing coordinates, respectively, in meters in Zone 11 of the Universal Transverse Mercator (UTM) projection.

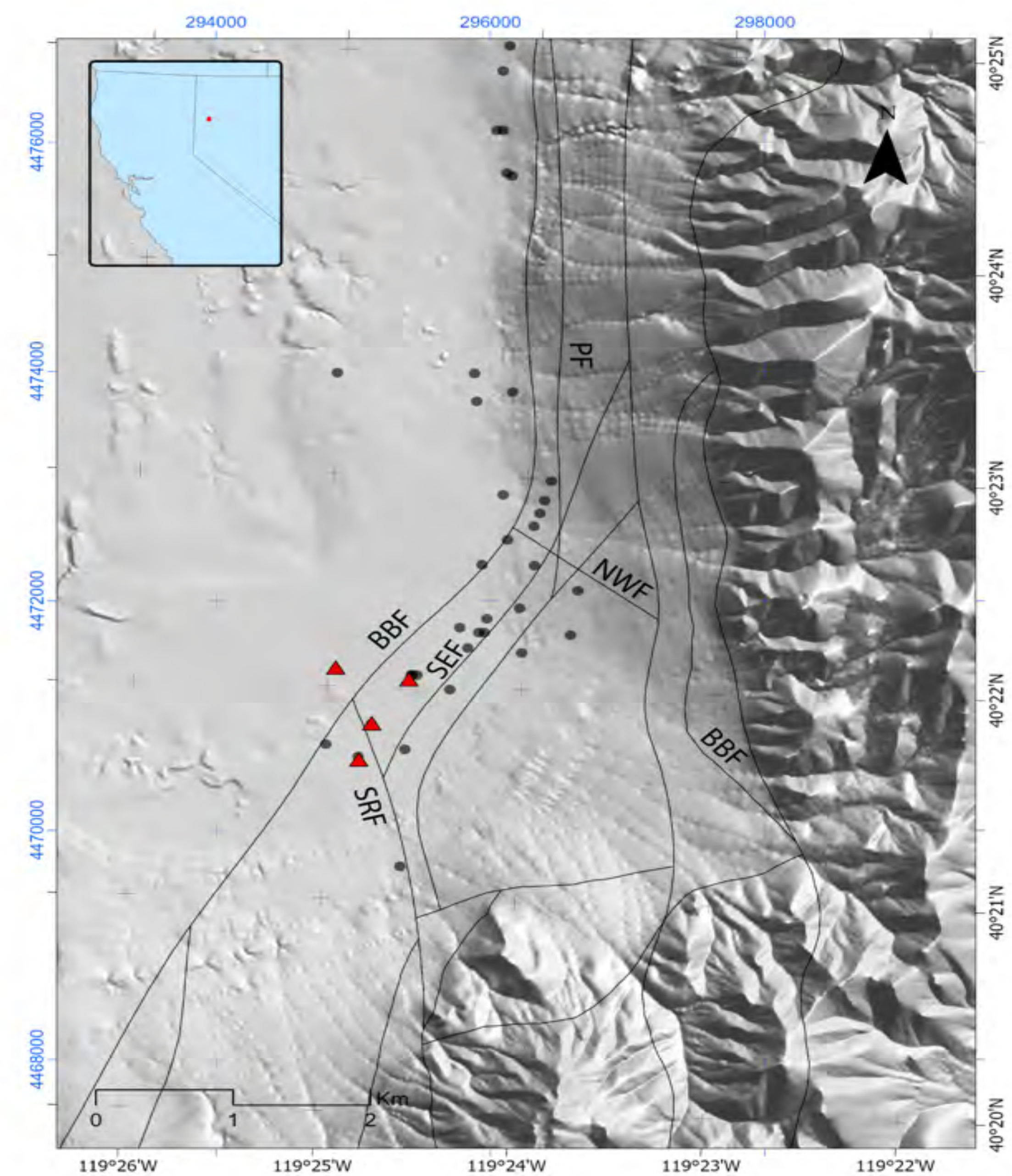

Figure 3. Map of the WHOLESCALE study area at San Emidio, showing fault traces in the geologic structural model updated in 2022 by Matt Folsom. The background gray image shows the topography. Fault names include: RFF, Range front fault; NF, Nightingale fault; FF, Fan fault; AF, Antithetic fault; SEF, San Emidio fault; BBF, Basin Bounding fault; PF, Piedmont fault; NWF, NW fault. Black tick marks and labels on the east and south edges give geographic (WGS84) latitude and longitude, respectively in degrees and minutes. Blue ticks and labels on north and west edges give easting and northing coordinates, respectively, in meters in Zone 11 of the Universal Transverse Mercator (UTM) projection.

Project Timeline and PERT

The WHOLESCALE project tasks and timeline are illustrated in Figure 4 (Phase I) and Figure 5 (Phase II) as charts according to the "program evaluation and review technique" (PERT). The project was completed in two phases that included three performance periods separated by two Go/No-go Stage Gate Reviews. Tasks were classified by data type (i.e., Geologic Structure, Borehole, Geodesy, Hydrology, Seismology, and Modeling).

The first phase of the project started July 31, 2020[4] and included ongoing project coordination (Task 1), a project kickoff (Task 2), analysis of existing data (Task 3), development of the initial stress model & deployment design (Task 4), and Go/No-go Decision Point #1 (Task 5). In this phase, the WHOLESCALE team demonstrated that the "expected goodness-of-fit measure will meet minimum requirement" (Figure 6) and was completed June 25, 2021 with an official "go" given August 25, 2021 .

Phase II began with implementing the 2022 deployment (Task 6) followed by Go/No-go Decision Point #2 (Task 7) which demonstrated "data were successfully collected according to plan" (Figure 7) which was completed June 22, 2022 with an official "go" given August 12, 2022. In May of 2022, the WHOLESCALE team requested and received approval in October 2022 for a 10-month extension of the Project Period through October 31, 2024[5]. The remainder of Phase II consisted of analyzing the data collected during the deployment (Task 8), calibrating the stress model on all observations (Task 9), and preparing the Final Review (August 23, 2024) & Final Technical Report (Task 10).

The team at UW-Madison coordinated twice-monthly teleconferences to ensure progress by exchanging information as well as identifying and resolving any technical difficulties. Minutes of teleconferences, including action items, were distributed to all team members. All of the WHOLESCALE team meetings held over the duration of the project are summarized in Table 1.

---

[4] The award document was signed on September 9th, 2020.
[5] Modification 004 extended the project period through October 31st 2024.

TASK CLASSIFICATION	**PHASE I** 2020/7/31* through 2021/07/31				
Task 1 **Coordination**	**Task 2** **Kickoff Meeting**	**Task 3** **Analyze existing data**	**Task 4** **Calibrate initial stress model with existing data & optimize deployment design**	**Task 5 (Go/No-go Decision Point #1): Completed 2021/06/25**	
1.1 Communications (Bradshaw, Feigl, ALL)					
1.2 Meetings (Feigl, Bradshaw)	**2.1 Host kickoff meeting** (Ormat, Bradshaw)	**Fortnightly teleconferences**	**Fortnightly teleconferences**		
1.3 Reporting (Feigl, Bradshaw, ALL)					
1. 4 Permitting (Ormat)					
1.5 Data management (Feigl, Bradshaw, ALL)					
1.6 Conceptual models (Cardiff, Sone, Wang, Feigl, Sherman)					
Geologic structure & material properties	**2.2 Conduct Field Trip to San Emidio** (Warren, Ormat)	**3. 1 Share Data & Models** (Ormat)	**4.1 Upscaling** (Hampton, Kleich, Sone)		
	2.3 Geologic Structure & Material Properties (Hampton, Folsom, Sone)	**3.2 Test Samples** (Hampton, Kleich, Sone)			
Borehole		**3.3 Interpret Regional Stress** (Warren, Sone)	**4.2 Define Prestress** (Sone, Jahnke)		
Geodesy	**2.4 Identify Locations for GPS Stations** (Kreemer, Feigl, Ormat)	**3.4 Collect & Analyze InSAR Data** (Feigl, Batzli, Kreemer)			
		3.5 Analyze GPS Data (Kreemer, Feigl, Ormat)			
Hydrology	**2.5 Visit Wells with Sensors** (Cardiff, Ormat)	**3.6 Compile Hydrologic Data** (Ormat, Cardiff)	**4.3 H-T Modeling** (Ormat, Cardiff, Roland)		
		3.7 Analyze Existing Hydrologic Data (Cardiff, Roland, Ormat)	**4.4 Design Network of Sensors for P, T, Q** (Cardiff, Roland, Ormat)		
Seismology	**2.6 Evaluate Conditions for Seismic Network** (Thurber, Guo, Heath, Lord, Ormat)	**3.8 Analyze Existing Seismic Data** (Thurber, Guo, Heath)	**4.5 Design Seismic Network** (Thurber, Guo, Heath, Lord)		
		3.9 Interpret PSET (Warren)			
Modeling		**3.10 Build Macroscale Configuration** (Sherman, Feigl, Tung, Sone)	**4.6 Calibrate Macroscale Stress Model** (Sherman, Tung, Feigl, Sone)		
		3.11 Build Mesoscale Configuration (Sherman, Morency, Wang, Tung)	**4.7 Calibrate Mesoscale Stress Model** (Sherman, Tung, Feigl, Cardiff)		

Figure 4. Tasks and schedules for Phase I of the WHOLESCALE project displayed as a PERT diagram.

TASK CLASSIFICATION	**PHASE II** 2021/08/01 through 2024/10/31**				
	2021/08/01 through 2022/07/31		**2022/08/01 through 2024/10/31****		
Task 1 **Coordination**	**Task 6** **Deploy Integrated technology at San Emidio**	**Task 7 (Go/No-go Decision Point #2): Completed 2022/06/22**	**Task 8** **Analyze Data collected during deployment**	**Task 9** **Calibrate stress model on observations**	**Task 10 Final review and reporting**
1.1 Communications (Bradshaw, Feigl, ALL)					
1.2 Meetings (Feigl, Bradshaw)	**Fortnightly teleconferences**		**Fortnightly teleconferences**	**Fortnightly teleconferences**	
1.3 Reporting (Feigl, Bradshaw, ALL)					
1. 4 Permitting (Ormat)					
1.5 Data management (Feigl, Bradshaw, ALL)					
1.6 Conceptual models (Cardiff, Sone, Wang, Feigl, Sherman)					
Geologic structure & material properties	**6.1 Coordinate Field Operations** (Ormat, Warren, Feigl, Lord, Bradshaw)		**8.1 Geologic Constraints and Interpretation** (Ormat, Warren, Sone)		
Borehole	**6.2 Mud Logging** (Ormat, Hampton, Wang)		**8.2 Lab Testing** (Hampton, Sone, Jin)	**9.1 Calibrate Mechanical Model on Borehole Observations** (Sherman, Sone, Wang)	
	6.3 Wireline Logging (Ormat, Sone, Wang)		**8.3 Geophysical Analysis of Well Logs** (Sone, Mudatsir)		
Geodesy	**6.4 Collect & Analyze InSAR Data** (Feigl, Batzli, Kreemer)		**8.4 Collect & Analyze InSAR Data** (Feigl, Batzli)	**9.2 Calibrate Mechanical Model on Geodetic Data** (Sherman, Feigl, Kreemer)	
	6.5 Collect & Analyze GPS Data (Kreemer, Feigl, Ormat)		**8.5 Collect & Analyze GPS Data** (Kreemer, Feigl, Ormat)		
Hydrology	**6.6 Install Additional P, T, Q Sensors** (Ormat, Cardiff)		**8.6 Quality Control, Interpretation of P,Q,T Data** (Ormat, Cardiff)	**9.3 Calibrate HT Model on Hydrologic Data** (Sherman, Cardiff)	
	6.7 Quality Control on Hydrologic Data (Ormat)				
Seismology	**6.8 Install and Operate Seismic Network** (Lord, Thurber, Feigl, Guo, Heath)		**8.7 Analyze Seismic Data** (Thurber, Guo, Cunningham, Lord)	**9.4 Calibrate HM Model on Seismic Data** (Sherman, Thurber, Sone)	
			8.8 Slip and Dilatation Tendency Analysis (Warren)		
Modeling	**6.9 Recalibrate Macroscale Stress Model** (Sherman, Feigl, Thurber, Sone)			**9.5 Calibrate THM Model on ALL Data** (Sherman, ALL)	
	6.10 Recalibrate Mesoscale Stress Model (Sherman, Feigl, Cardiff)				

*Figure 5. Tasks and schedules for Phase II of the WHOLESCALE project displayed as a PERT diagram (**Denotes the revised project end date.)*

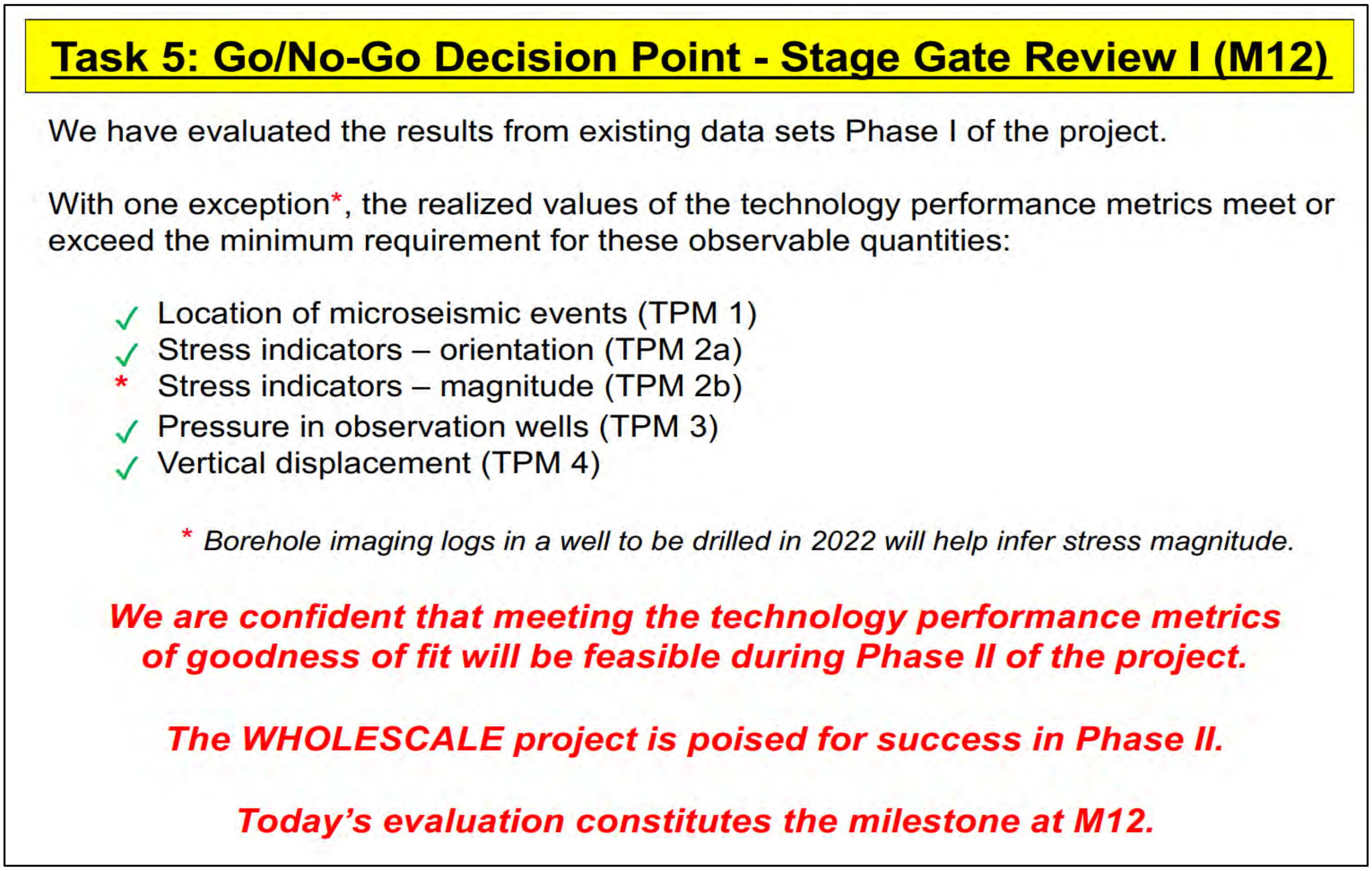

Figure 6. Summary slide for Task 5: Go/No-go Decision Point #1, demonstrating that “the expected goodness-of-fit measure will meet the minimum requirement.”

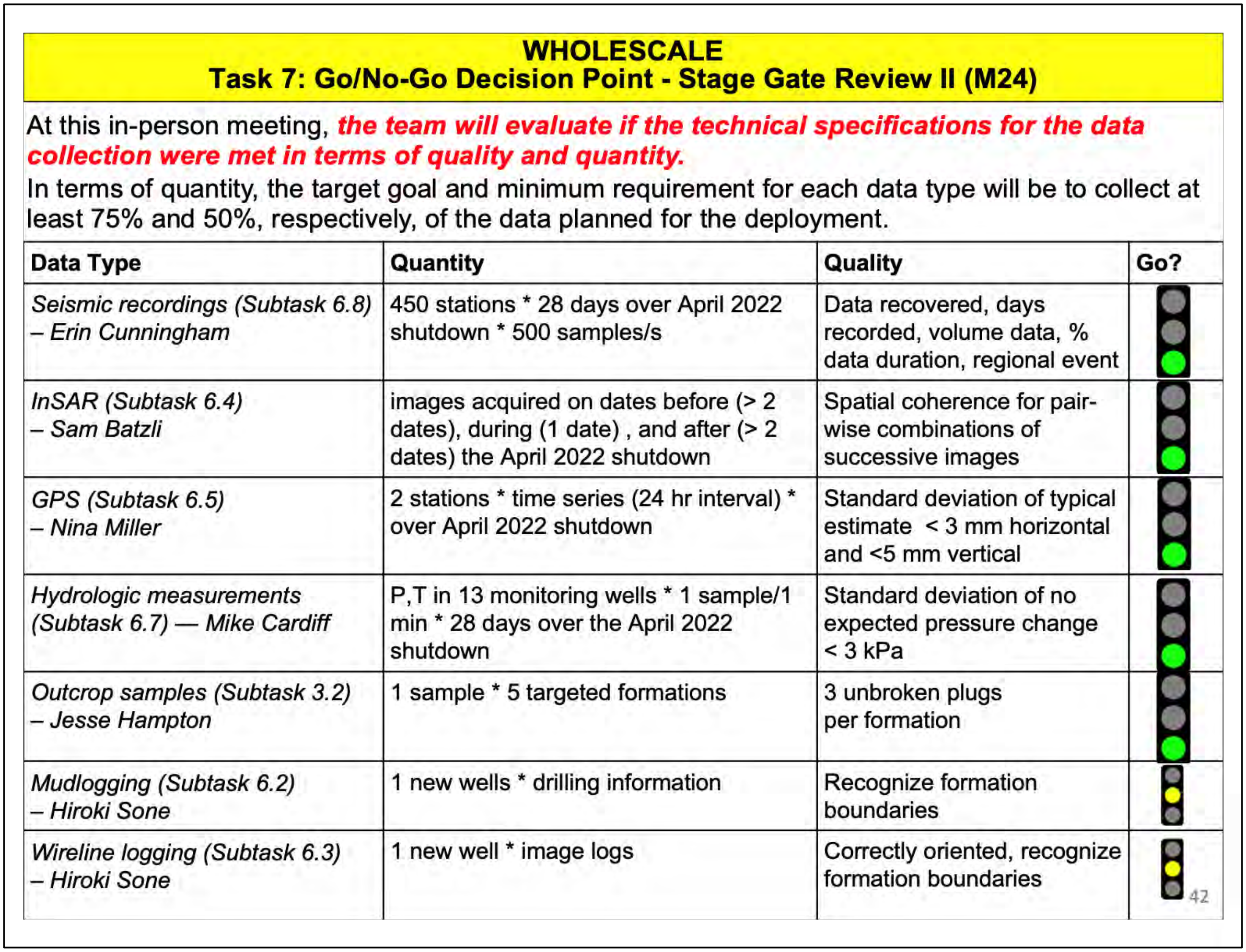

WHOLESCALE
Task 7: Go/No-Go Decision Point - Stage Gate Review II (M24)

At this in-person meeting, ***the team will evaluate if the technical specifications for the data collection were met in terms of quality and quantity.***

In terms of quantity, the target goal and minimum requirement for each data type will be to collect at least 75% and 50%, respectively, of the data planned for the deployment.

Data Type	**Quantity**	**Quality**	**Go?**
Seismic recordings (Subtask 6.8) – Erin Cunningham	450 stations * 28 days over April 2022 shutdown * 500 samples/s	Data recovered, days recorded, volume data, % data duration, regional event	
InSAR (Subtask 6.4) – Sam Batzli	images acquired on dates before (> 2 dates), during (1 date) , and after (> 2 dates) the April 2022 shutdown	Spatial coherence for pair-wise combinations of successive images	
GPS (Subtask 6.5) – Nina Miller	2 stations * time series (24 hr interval) * over April 2022 shutdown	Standard deviation of typical estimate < 3 mm horizontal and <5 mm vertical	
Hydrologic measurements (Subtask 6.7) — Mike Cardiff	P,T in 13 monitoring wells * 1 sample/1 min * 28 days over the April 2022 shutdown	Standard deviation of no expected pressure change < 3 kPa	
Outcrop samples (Subtask 3.2) – Jesse Hampton	1 sample * 5 targeted formations	3 unbroken plugs per formation	
Mudlogging (Subtask 6.2) – Hiroki Sone	1 new wells * drilling information	Recognize formation boundaries	
Wireline logging (Subtask 6.3) – Hiroki Sone	1 new well * image logs	Correctly oriented, recognize formation boundaries	

42

Figure 7. Summary slide for Task 7: Go/No-go Decision Point #2 demonstrating that the"data were successfully collected according to plan.

Table 3. List of WHOLESCALE team meetings.

Meeting #	Date	Meeting #	Date	Meeting #	Date
Teleconference #003	24-Jan-20	Teleconference #042	06-Aug-21	Teleconference #079	03-Feb-23
Teleconference #004	07-Feb-20	Teleconference #043	27-Aug-21	SWG In-Person	08-Feb-23
Teleconference #005	06-Mar-20	Teleconference #044	10-Sep-21	-Meeting #080a	
Teleconference #006	20-Mar-20	Teleconference #045	24-Sep-21	Teleconference #080	17-Feb-23
Teleconference #007	03-Apr-20	Teleconference #046	08-Oct-21	Teleconference #081	03-Mar-23
Teleconference #008	17-Apr-20	Teleconference #047	22-Oct-21	Teleconference #082	24-Mar-23
Teleconference #009	01-May-20	Teleconference #048	05-Nov-21	Teleconference #083	07-Apr-23
Teleconference #010	15-May-20	Teleconference #049	19-Nov-21	Teleconference #084	21-Apr-23
Teleconference #011	29-May-20	Teleconference #050	03-Dec-21	Teleconference #085	05-May-23
Teleconference #012	12-Jun-20	Teleconference #051	17-Dec-21	Teleconference #086	19-May-23
Teleconference #013	26-Jun-20	Teleconference #052	07-Jan-22	Teleconference #087	09-Jun-23
Teleconference #014	24-Jul-20	Teleconference #053	21-Jan-22	Teleconference #088	23-Jun-23
Teleconference #015	07-Aug-24	Teleconference #054	04-Feb-22	Teleconference #089	21-Jul-23
Teleconference #016	28-Aug-24	Teleconference #055	18-Feb-22	Teleconference #090	28-Jul-23
Teleconference #017	11-Sep-20	Teleconference #056	04-Mar-22	Teleconference #091	11-Aug-23
Teleconference #018	25-Sep-20	Teleconference #057	11-Mar-22	Teleconference #092	25-Aug-23
Teleconference #019	09-Oct-20	Teleconference #058	25-Mar-22	Teleconference #093	08-Sep-23
Teleconference #020	23-Oct-20	Teleconference #059	15-Apr-22	Teleconference #094	22-Sep-23
Teleconference #021	06-Nov-20	Teleconference #060	22-Apr-22	Teleconference #095	06-Oct-23
Teleconference #022	20-Nov-20	Teleconference #061	29-Apr-22	Teleconference #096	20-Oct-23
Teleconference #023	04-Dec-20	Teleconference #062	13-May-22	Teleconference #097	03-Nov-23
Teleconference #024	18-Dec-20	Teleconference #063	10-Jun-22	Teleconference #098	17-Nov-23
Teleconference #025	08-Jan-21	Teleconference #064	17-Jun-22	Teleconference #099	01-Dec-23
Teleconference #026	22-Jan-21	Teleconference #065	22-Jun-22	Teleconference #100	08-Dec-23
Teleconference #027	05-Feb-21	Teleconference #066	22-Jul-22	Teleconference #101	08-Jan-24
Teleconference #028	19-Feb-21	Teleconference #067	05-Aug-22	Teleconference #102	16-Jan-24
Teleconference #029	05-Mar-21	Teleconference #068	26-Aug-22	Teleconference #103	02-Feb-24
Teleconference #030	19-Mar-21	Teleconference #069	09-Sep-22	Teleconference #104	16-Feb-24
Teleconference #031	02-Apr-21	Teleconference #070	23-Sep-22	Teleconference #105	01-Mar-24
Teleconference #032	16-Apr-21	Teleconference #071	07-Oct-22	Teleconference #106	22-Mar-24
Teleconference #033	22-Apr-21	Teleconference #072	21-Oct-22	Teleconference #107	05-Apr-24
Teleconference #034	07-May-21	Teleconference #073	04-Nov-22	Teleconference #108	19-Apr-24
Teleconference #035	21-May-21	Teleconference #074	18-Nov-22	Teleconference #109	03-May-24
Teleconference #036	04-Jun-21	Teleconference #075	02-Dec-22	Teleconference #110	17-May-24
Teleconference #037	11-Jun-21	Teleconference #076	16-Dec-22	Teleconference #111	31-May-24
Teleconference #038	18-Jun-21	UW In-Person	06-Jan-23	Teleconference #112	14-Jun-24
Teleconference #039	25-Jun-21	-Meeting #076.5		Teleconference #114	19-Jul-24
Teleconference #040	09-Jul-21	Teleconference #077	13-Jan-23	Teleconference #115	02-Aug-24
Teleconference #041	23-Jul-21	Teleconference #078	27-Jan-23	Teleconference #116	16-Aug-24

SECTION III. FIELD WORK

Infrastructure

Major infrastructure operated at San Emidio from 2016 onward includes: (a) four production wells (75B-16, 76-16, 61-21, and – since 2018 – 25A-21) targeting depths from approximately 100 m to 930 m below land surface; and (b) three shallow wells (42-21, 43-21, and 53-21) where water is re-injected under ambient pressure. Other idle wells that access the reservoir are shown in black in Figure 8, and represent locations where reservoir pressure changes can be monitored. Pressure change data from pumping tests in 2016 and 2017 were recorded by Ormat independently, and provided as part of the WHOLESCALE project. Most recently, observed pressure changes were recorded at 13 idle wells in Spring 2022 as part of the WHOLESCALE project.

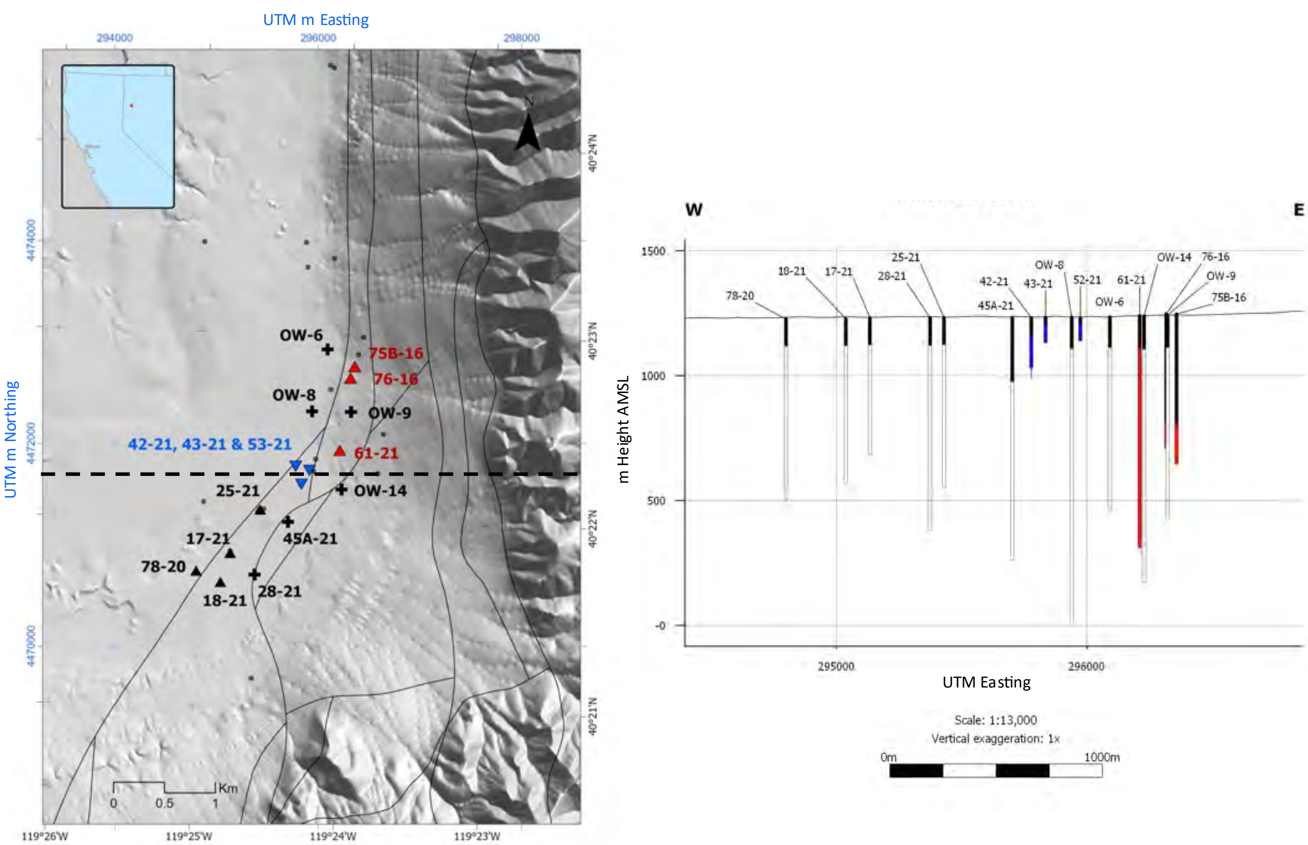

Figure 8. Infrastructure at San Emidio operating in 2016. Left: Map-view locations of all active wells relative to estimated fault traces. Right: Well locations, projected to a plane of UTM Zone 11T 4,471,700m N. Elevation H is orthometric height above mean sea level (WGS84 geoid).

2016 Deployment

The following section includes excerpts (some verbatim), from several sources (Warren et al., 2016b; Warren et al., 2018; Warren et al., 2019a; Warren et al., 2019b).

In 2016, passive seismic data were collected at San Emidio as part of the DOE-funded Subsurface Technology and Engineering R&D (SubTER) project to advance imaging and characterization of geothermal permeability (DE-EE0007698). Microseismic Incorporated (MSI) installed a seismic network consisting of 1302 stations with 6 wired geophones connected to OYO GXR recorders. They collected data for nearly 180 hours. The survey was designed to focus on a volume approximately 1700 m by 2200 m by 300 m (Figure 9).

The passive seismic data collected at the San Emidio site were processed using passive seismic imaging techniques based on beamforming of the high-frequency approximation of the wave equation. The first technique aims at identifying discrete events with an impulsive character using an algorithm known as Passive Seismic Emission Tomography (PSET) (Duncan and Eisner, 2010). In this case, the time window was 50 milliseconds. The direction of first motion and the observed amplitude across the array were used to derive focal mechanisms for several discrete events at San Emidio.

The second technique, Ambient Passive Seismic Imaging, is a close analog to the more conventional approach described above and accomplished using MSI's repetitive Passive Seismic Emission Tomography using a time window for imaging of 1 hour. The technique provides a holistic view of acoustic history using the long duration aggregation of multiple formed beams (Jeremic et al., 2016).

Magnetotelluric (MT) data collection started in late 2016; due to low natural signals the results were not satisfactory, and measurements over a portion of the survey area were repeated and completed in summer 2017. The MT data acquisition (250 Hz-0.001 Hz) was done by Quantec Geoscience USA Inc.

MSI delivered a catalog of microseismic events (MSEs) with locations and focal mechanisms. In analyzing the catalog, Ian Warren noticed that the number of events increased around the time that pumping operations were suspended for planned maintenance. MSI also delivered a PSET volume of acoustic energy transformed into Z-scores. The WHOLESCALE team submitted the metadata for the seismic survey[6] (Lord et al., 2016b), the raw seismic waveforms[7] (Lord et al., 2016a), and the PSET volume[8] (Warren et al., 2016a) to the Geothermal Data Repository (GDR)[9].

[6] https://doi.org/10.15121/1872549
[7] https://doi.org/10.15121/2008357
[8] https://dx.doi.org/10.15121/1924268
[9] Citations to data sets available on the GDR are dated with the date of collection, not submission.

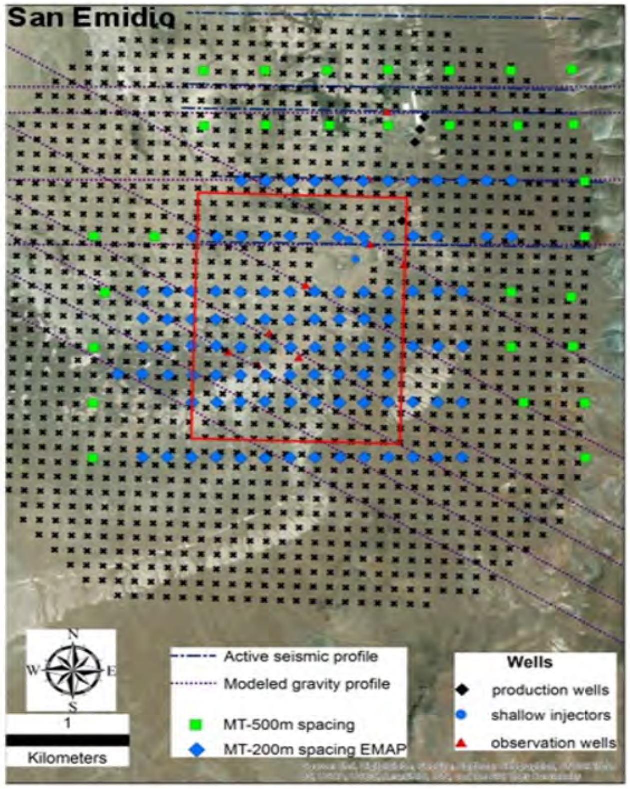

Figure 9. Map showing locations of passive seismic and electromagnetic data collections at San Emidio in 2016 and 2017. Red box shows the focus area. Figure and caption (Warren et al., 2018).

2021 Deployment

The WHOLESCALE team designed and deployed an "exploratory" seismic array in April 2021. The experiment was designed to monitor seismic activity before, during, and after the planned three-day plant maintenance shutdown April 19-21, 2021. Following permitting, postdoc Ben Heath visited the field site at San Emidio in April 2021 to install the temporary seismic instruments for the exploratory deployment. Seismic data was recorded using 37 tri-axial short-period seismographs that were deployed in a 1.8 km diameter cluster centered on 40.367278 N, 119.409019 W (Figure 10). The first data record started at 2021-04-06T07:09:10Z UTC and the last record ended at 2021-05-11T02:58:52Z UTC. The pumping stopped at 2021/04/19 12:51:45 UTC and resumed about 2021/04/21 21:00:00 UTC. The 37 stations included 29 SmartSolo IGU-16HR 3C all-in-one 5 Hz seismographs and 8 DataCube seismographs with 4.5 Hz HGS HG-6(B coil) tri-axial geophones. In May 2021, Neal Lord traveled to San Emidio to retrieve the seismic instruments. In total, the stations were deployed for more than 30 days. Recovered instruments show that data were recorded during the entire shutdown period (April 19 - 22, 2021) by all instruments, however some instruments stopped recording prior to retrieval due to discharged batteries. Three stations have one day's worth of data missing at the beginning of the deployment. These stations were retrieved after initial deployment as a "spot test" to ensure accurate data collection, and then redeployed. The experience and data from the exploratory deployment were used to provide guidance regarding site conditions to help plan the 2022 seismic array deployment (Figure 12).

Deploying the instruments in the field was straightforward because the vegetative cover is sparse, consisting mostly of low sagebrush rarely exceeding 60 cm in height. The soil is mostly loose sand and silt. Meteorologic conditions were dry, simplifying walking. During the deployment, several cattle were observed. During the recovery, footprints from cattle were observed near some of the instruments. The locations of cattle fences and gates were collected. This information was used to avoid external noise sources (such as cattle and vehicles) as well as to minimize the time required for the deployment and retrieval of seismic instruments in 2022.

Work on design of the seismic instrument deployment configuration mainly involved the examination of the data from the 2021 deployment. It provided critical information for planning the deployment in 2022. The 2021 deployment was configured to surround a relatively recently drilled injection well, 25A-21, anticipating that microseismicity would likely occur there during the planned April 2021 plant shutdown. Preliminary analysis of the 2021 seismic data suggested that in fact the microseismicity that followed the plant shutdown occurred in the same general area as during the December 2016 shutdown. Thus, we designed the 2022 deployment configuration encompass the region that experienced microseismicity in 2016, as well as encompassing Well 25A-21 in case microseismicity occurred there as well. We decided to increase the number of instruments to be deployed in 2022 to about 450 to achieve adequate coverage of the areas of interest.

The dataset entitled *WHOLESCALE: Seismic Survey Data from San Emidio Nevada 2021* (Lord et al., 2021b) is publicly available on the GDR[10]. The seismic data sets include: (a) raw format (level 0) data with 353 GB SmartSolo data sampled at 500 samples/second in native DLD format, (b) 113 GB DataCube data sampled at 400 samples/second in native DataCube format, (c) 3.4 GB of GPS data collected during the RTK GPS survey, and (d) 564 GB of (level 1) hourly files from all 37 instruments in SAC format. The dataset is hosted in an AWS data lake. The associated metadata, entitled *WHOLESCALE: Seismic Survey Metadata from San Emidio Nevada 2021* is also available on the GDR[11] (Lord et al., 2021a).

We have generated a preliminary catalog of microseismic events for only one day of the 2021 shutdown using the REST workflow (Comte et al., 2023; Yarce et al., 2023). Additional details on the REST workflow are provided in the section on analyzing the seismic data collected in 2022. We relocated these events using the triple-difference location method (Guo and Zhang, 2017). Two types of differential arrival time data, including the station-pair and double-pair P-wave differential time data, were constructed from the absolute P-wave arrival time data determined by REST. The station-pair differential time data from common events observed at pairs of stations can better constrain the absolute locations, although the accuracy of absolute locations is also dependent on the velocity model. The double-pair differential time data from pairs of events observed at pairs of stations can refine relative event locations by mitigating the effects of velocity model errors. During the inversion process, we initially weighted the station-

[10] https://gdr.openei.org/submissions/1478
[11] https://gdr.openei.org/submissions/1463

pair data more heavily to constrain absolute locations, and in later iterations, we weighted the double-pair data more heavily to refine relative locations. Figure 11 shows our relocation results for 574 events, which reveal multiple clusters of seismicity. The results show a more southerly distribution of seismicity than for the 2016 events, indicating that the 2022 field deployment should extend further to the south rather than simply surround our refined event locations from the 2016 Microseismic, Inc. event set.

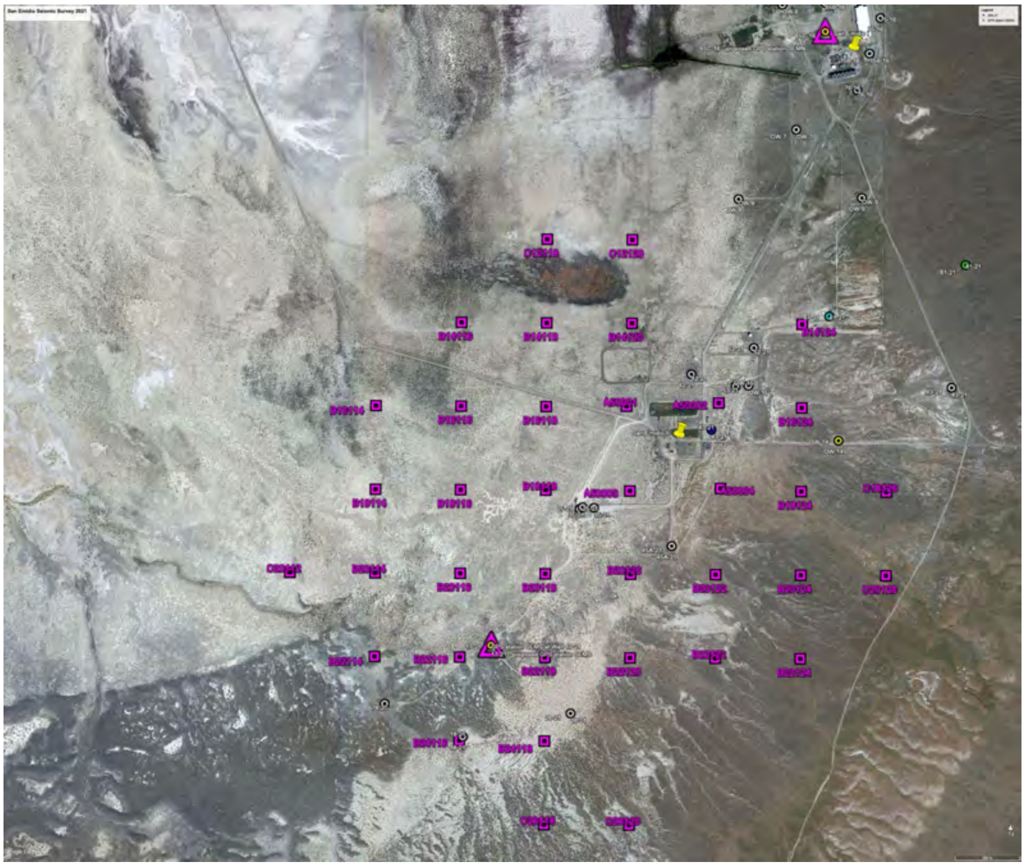

Figure 10. Map showing locations of seismic stations deployed in April 2021 (small triangles). Magenta triangles indicate GPS stations SEMN and SEMS to the north and south of the seismic array, respectively.

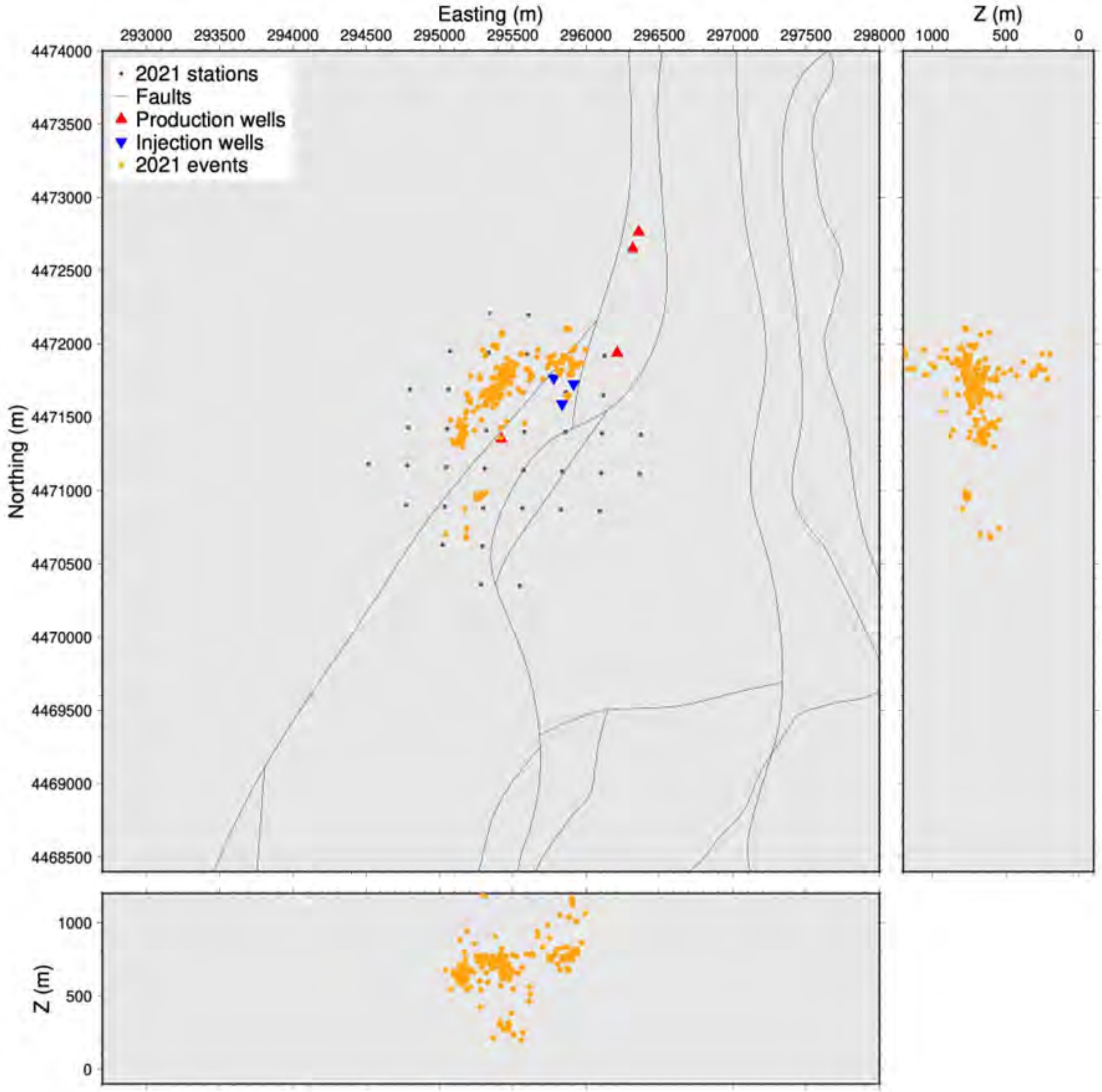

Figure 11. Map and cross sections showing moderate-precision relocations for 574 events (orange circles) on shutdown day in 2021, fault traces, injection wells (blue triangles), production wells (red triangles), and the location of the seismic stations deployed in 2021 (small black circles).

2022 Deployment

In the spring of 2022, the WHOLESCALE team deployed 450 SmartSolo seismic instruments at the San Emidio geothermal field in Nevada (Figure 13). The seismic instruments used were provided by EarthScope Consortium through the EarthScope Primary Instrument Center (EPIC) at New Mexico Tech. The deployment was executed in three phases: stakes were placed in the ground at locations using hand-held GPS receivers, seismographs were implanted next to the stakes, and seismographs were turned on to begin recording data in April. Three phases were necessary due to the combination of limits on the seismographs' battery life and personnel availability. This was the first project to use the low-power A-to-D mode instead of the standard high-resolution mode, which allowed a trade of a decrease in the digitizer's effective number of bits (from 21.8 to 21.5) for a 30% increase in battery life.

After approximately one month of observation, the seismographs were turned off, removed from the ground, and cleaned on May 6th (157 sites), May 7th (157 sites), and May 8th (136 sites). The data files were downloaded onto portable hard drives. The seismographs were then shipped to EPIC where the data were converted from the original (raw) SmartSolo (DLD) format to the more standard SAC format at UW and also at EPIC.

The methods for and results from evaluating the quality of the seismic data collected at San Emidio in 2022 are included in a GDR submission entitled, *WHOLESCALE: Seismic Waveform Data from San Emidio, Nevada 2022. United States*[12] (Lord et al., 2022). This GDR submission points to the raw seismic waveform data[13] (Feigl et al., 2022a) that are archived by EarthScope as part of the International Federation of Digital Seismograph Networks.

The quality and quantity of the data were assessed in Task 7. The analysis of these data is discussed below.

[12] https://gdr.openei.org/submissions/1610
[13] https://doi.org/10.7914/m5qt-mh37

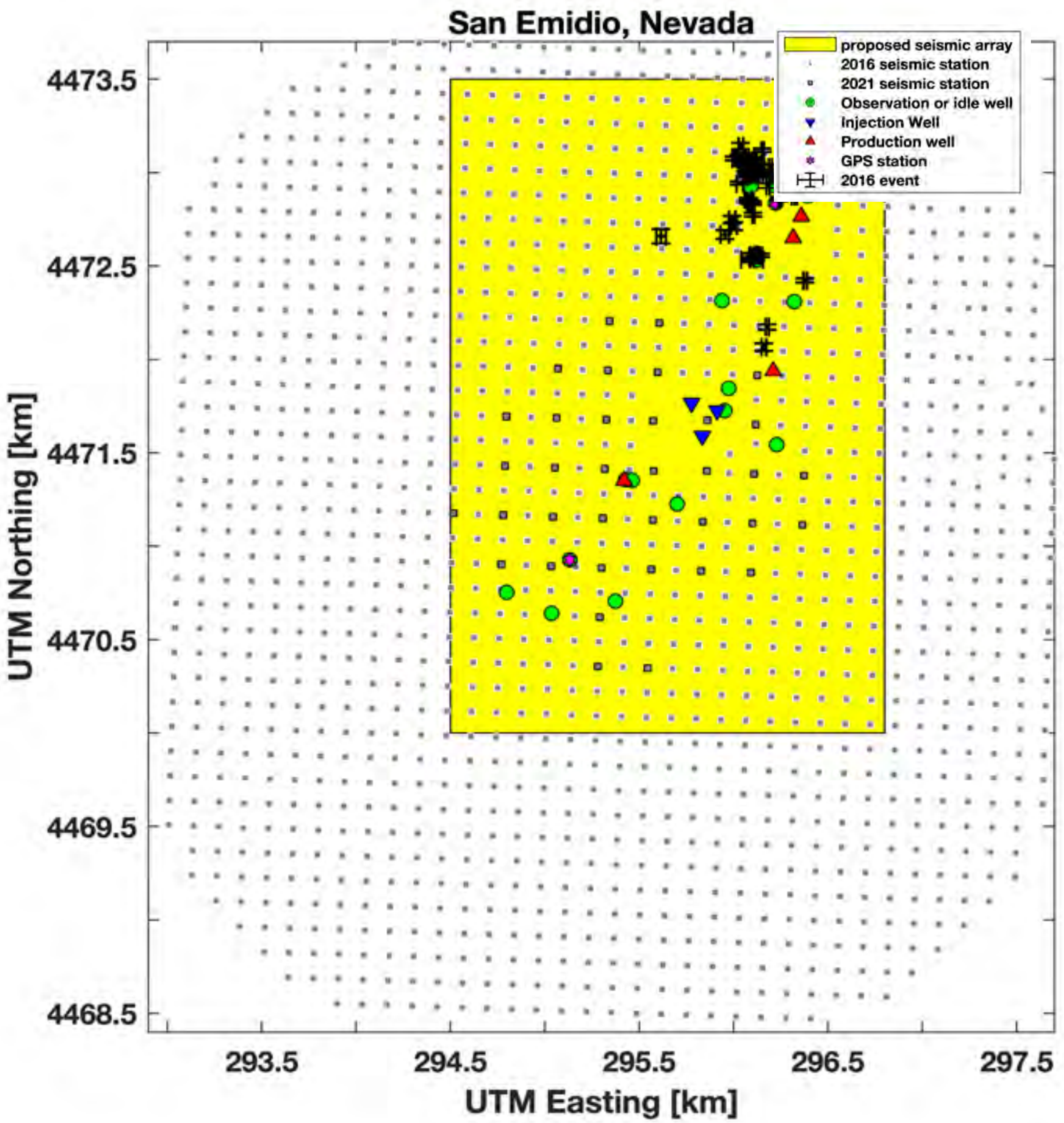

Figure 12. Map showing the planned location for the 2022 seismic array, based on locations of the microseismic events in 2016 (crosses), the seismic stations deployed in 2016 (small squares) and in 2021 (large squares).

414

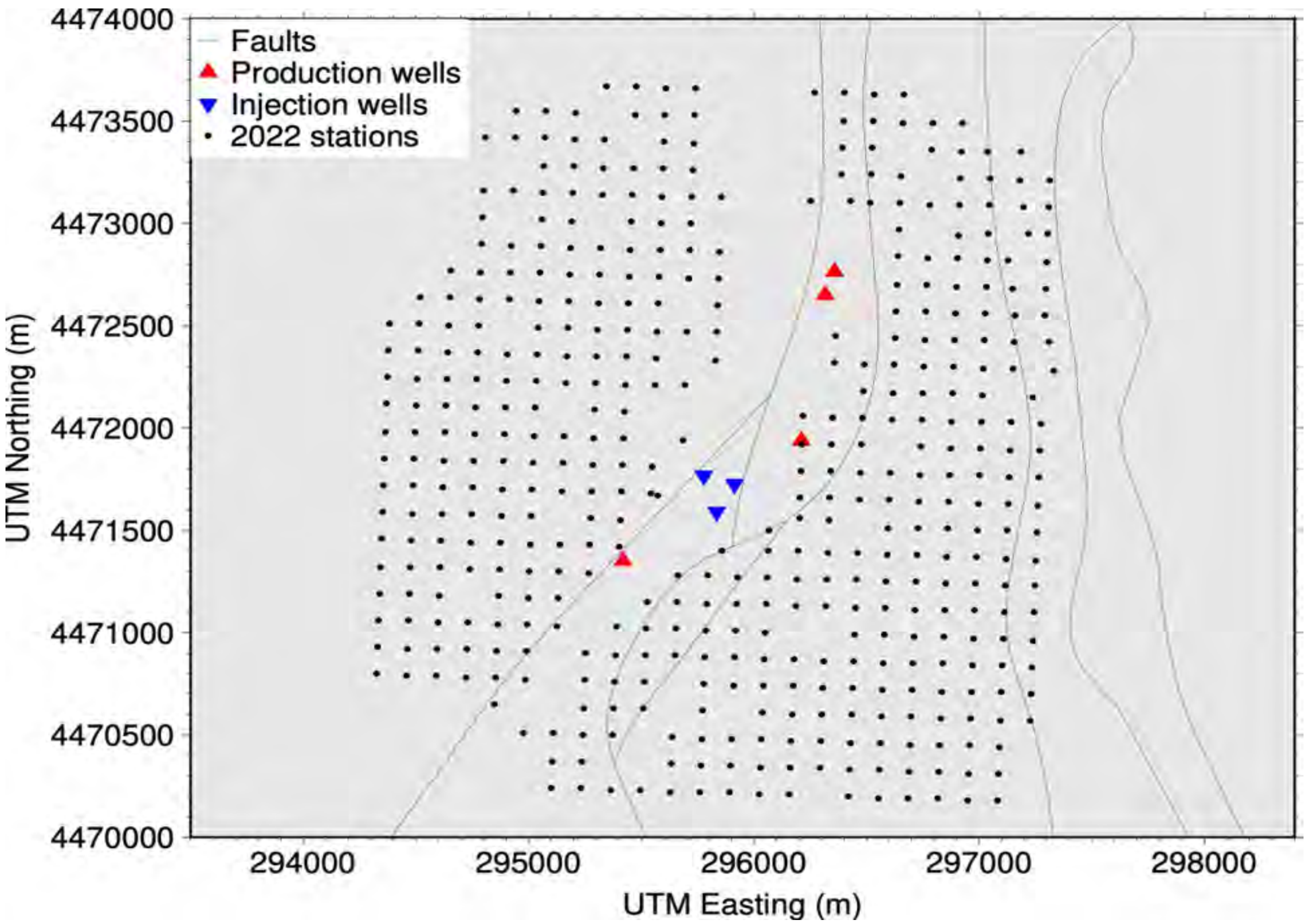

415 *Figure 13. Map of seismic stations deployed in April 2022. The gap running roughly*
416 *north-south through the area accommodates roads and pipeline construction.*

SECTION IV. DATA ANALYSIS

Geologic Structure

Mechanical and Poroelastic Rock Properties

The following section includes excerpts, some verbatim, from several sources (Hampton et al., 2022; Kleich et al., 2022a; Kleich, 2022a; Kleich et al., 2022b; Kleich et al., 2022c; Kleich, 2022b).

To better model the stress in the San Emidio geothermal reservoir, it is important to obtain mechanical and poroelastic rock properties of each lithologic unit (i.e., metasediment, basaltic andesite, etc.). To do this, we use oriented plug specimens from rock samples collected at the San Emidio geothermal site. To limit confusion, the sample scale will refer to the shoebox-sized rock samples collected from surface outcrops in the field and the plug specimen scale will refer to the 1-inch cylindrical specimens cored from these rock samples.

We can then measure the elastic stiffnesses and effective stress coefficients at the plug scale on each rock type which can be used to more accurately model stress in the geothermal reservoir. However, to properly determine the correct mechanical and poroelastic rock properties, the plug specimens must be categorized as either isotropic, anisotropic and/or containing heterogeneities. Our focus is on determining whether plug deformation is controlled by structural/textural anisotropy and/or heterogeneities, which is necessary for properly orienting strain instrumentation and stresses at the laboratory-scale to measure interpretable elastic stiffnesses and Biot coefficients.

Materials used in this study were collected from surface outcrops at the San Emidio geothermal site due to the absence of drill core. Therefore, collection of samples from the lithologic units within the area were limited to those that have surface expressions. As a result, these samples are not under the same state of stress as they otherwise would be in subsurface conditions and have been subjected to additional weathering, likely altering the physical properties of the rock materials, including strength and stiffness. Although sample collection and sample condition (i.e., weathering, heavy fracturing) limited the range of samples obtained, a majority of the subsurface lithologic units are represented within this testing suite.

The lithologic units of most concern for this study include QTa (Quaternary basin fill alluvium), Tpb' (Tertiary sparsely porphyritic basaltic andesite), Tpts (Tertiary tuffaceous and volcaniclastic sedimentary rocks), and TrJn (Triassic and Jurassic metasedimentary rocks) due to their location within the geothermal reservoir and their volumetric contribution to the model area. However, because of the lack of surface outcrops and/or integrity of the rock type, QTa and Tpts were not feasible for testing. Therefore, samples of Tpb' and TrJn, as well as Tss (Tertiary silicified sediments) are the primary lithologic units investigated during this study. Estimations of rock properties from wellbore logs, mineralogy, and elemental chemistry will aid in providing constraints for the unmeasured rock types, QTa and Tpts.

Before determining whether a sample was isotropic, anisotropic and/or contained heterogeneities, thin sections were made from numerous rock samples to examine any significant textural or structural features. Three thin sections were made for each rock sample at approximate orthogonal angles to one another (Figure 14). By determining whether one orientation had a more prominent feature than another, we could use this information when coring new samples or infer how this may affect the rock behavior when applying stress. Many of the orientations from each rock sample did not display any noticeable and/or quantifiable fabric.

Some orientations of TrJn samples contained plagioclase grains that aligned with one another in a linear fashion, whereas other quartz dominated TrJn samples contained a clear gradation from coarse-grained to fine-grained quartz. In addition, few orientations of TrJn contained structural joint patterns. Likewise, a limited number of orientations of Tpb' samples contained a well-defined lineation of plagioclase grains. For the Tss samples, there was a clear interlayering between quartz layers and a fine-grained matrix. However, the fabrics discussed in each of these cases could be dependent on scale and may not be ubiquitous throughout the entire rock sample (i.e., heterogeneity).

To measure mechanical and poroelastic properties of each lithologic unit, we first needed to obtain cylindrical core specimens from the rock samples collected in the field. If possible, three specimens were cored from the same rock sample at approximate orthogonal angles to one another depending on textural/structural information obtained from thin sections (Figure 14). The viability of coring a cylindrical specimen is based on the integrity of the rock samples; for example, degree of weathering, presence of surficial fractures, shape and size of the rock sample (i.e., jagged, small), and rock type. Samples that were heavily weathered, heavily fractured, too small or jagged, or rock types such as tuffaceous and volcaniclastic sedimentary rocks were deemed not feasible to obtain cylindrical specimens, as the preparation process would not result in a testable specimen. Samples considered to be in good condition were used to core cylindrical plug specimens that were 1-inch in diameter and between 1.5 inches to 2 inches in length. The surficial location of these plugs on the sample exterior was free of imperfections and relatively homogeneous. However, in many instances underlying imperfections such as voids and fractures often damaged the plug, rendering it useless, or were visible in the plug specimen. Once the sample is cored and cut to the desired length, each end of the sample is surface ground to achieve parallelism. Parallelism is essential to all types of testing to ensure stress is evenly applied to the sample ends and to inhibit bending of the sample.

Depending on the type of testing being conducted, specimens were jacketed accordingly (Table 5). Two different jacketing methods will be discussed: (1) radial velocity jacketing and (2) copper jacketing. For this study, the radial velocity jacket is used for radial velocity testing and the copper jacketing is used for static stiffness and Biot measurements. A section of viton tubing is used for the radial velocity jacket. This material is a pliable membrane that will contain the sample and prevent leakage of the external fluid used for confining pressure. Two holes are cut 180 degrees from one another in the viton tubing and replaced with radial velocity pucks (Figure 15). It is critical that the pucks sit flush against the specimen surface to properly measure the velocity across the diameter of the plug specimen, therefore curved titanium spacers are used to mate the velocity transducer to the specimens. Epoxy is used to connect the pucks to the viton jacket and fill in any gaps to block leakage. Lastly, each of the jacket ends is secured to the appropriate transducer using annealed steel wire to prohibit leaking. Copper jacketing is used for static stiffness and Biot measurements, as it is a pliable material that conforms to the sample and enables strain gauges to be glued directly to the copper. A piece of 0.13 mm-thick annealed copper sheet is wrapped around the plug specimen and soldered together. After filing down the excess solder, the specimen is placed inside a vessel where the copper is seated to the specimen by applying 13 MPa of hydrostatic confining pressure. Once the strain gauges are applied to the copper surface, the jacketed specimen can be attached to the source transducer and receiver transducer by using viton tubing and steel wire to prevent leaking of the external fluid and internal fluid, like that for the radial velocity jacket (Figure 15).

Using the viton jacketed sample with the radial velocity transducers, ultrasonic velocities were measured at 45-degree increments around the circumference of the cylindrical plug specimens (Figure 16). The specimens are tested in a high-pressure triaxial testing apparatus with 10 MPa confining pressure applied. A single compressional and two orthogonally polarized shear wave velocities are measured at each orientation to provide valuable information about the lithologic unit, and further compared to axial velocities taken during static mechanical testing. The implications of measuring the velocity at four different orientations pertains to quantifying any anisotropy and/or heterogeneities that may be present within the plug specimen. If the specimen is isotropic (i.e., has a physical property which has the same value when measured in different directions), then the velocity measurements will be approximately the same in all four orientations. If the specimen is anisotropic (i.e., has a physical property which has a different value when measured in different directions), then the velocity measurements would differ between orientations due to interactions with supposed layering, grain texture, fractures, etc.

The combination of qualitatively observing textural and structural anisotropy and/or heterogeneities and quantitatively measuring the radial velocity in four different orientations became useful for a number of reasons. First , geological and textural descriptions from thin sections were used to determine the direction to core the plug specimens. Secondly, by comparing velocity measurements to the thin section descriptions and photographs, we can see if the difference in velocity of a certain orientation is a result of observed fabric. Lastly, if the radial velocity data depicts anisotropy that is not in line with the currently plugged X-Y-Z orientations, we can quantify as necessary and re-core plug specimens in an orientation that would align with the anisotropy.

Using the copper jacketing preparation technique, a plug specimen can undergo differential stress, confining pressure, and pore pressure perturbations to measure the associated stiffnesses and Biot coefficients for each specimen. The number of independent elastic constants needed to characterize each rock type is dependent on the categorization made by the radial velocity data and geological/textural descriptions. If a sample is isotropic, only two independent elastic constants are needed to characterize that material (i.e., one Young’s modulus and one Poisson’s ratio). In contrast, if a sample is characterized as transversely isotropic (i.e., a material with physical properties that are symmetric about an axis that is normal to a plane of isotropy), five independent elastic constants are needed to characterize the material (i.e., two Young’s moduli and three Poisson’s ratios).

To conduct static mechanical testing, a sample is placed into the triaxial testing apparatus. A confining pressure of 20 MPa and a differential stress of 5 MPa is applied. The sample is then subjected to four different cycles to measure different moduli: (1) Bulk cycle to obtain bulk modulus K; (2) Unistress cycle to obtain Young’s modulus E and Poisson’s ratio ν; (3) Shear cycle to obtain shear modulus G; and (4) Hydrostatic cycle. The Bulk cycle modulates confining pressure only, the Unistress cycle will ramp differential stress only, and the Shear cycle and Hydrostatic cycle modulate both confining pressure and differential stress (Figure 17). Our focus is on measurements of Young's Modulus and Poisson's ratio. Using radial velocity data and the Unistress cycle data, we can respectively obtain dynamic and static E and ν for isotropic specimens.

Four radial velocity measurements were made on each cylindrical specimen at 45-degree increments around its circumference. Therefore, measurements were made at 0, 45, 90, and 135 degrees (Figure 16). An increment of 45 degrees was chosen as it provided an accurate representation of the possible velocity variations while maintaining a practical testing schedule. Picks of P-wave velocity, S1-wave velocity, and S2-wave velocity were chosen based on the head-to-head picks from a standard 1-inch aluminum sample, to accurately remove transit times within the titanium pucks when rock materials are tested. An example of ultrasonic waveforms with their corresponding velocity picks are displayed in Figure 18. Waveforms did not always result in a well-defined picking location, which can be attributed to the complexities and variations that come from using imperfect rock samples collected in the field. The ramifications and solutions for overcoming complications in velocity picking will be discussed later.

Table 6 provides a summary of radial velocity testing for specimens from lithologic units that were of prime interest to the San Emidio geothermal reservoir (i.e., Tpb', TrJn, and Tss) due to their volumetric component. Overall, most samples appear to be isotropic and display very few signs of anisotropy. This is quantified by the differences in velocity measurements between the four orientations tested. Samples that had velocity differences of 250 m/s or less between orientations were classified as isotropic. Samples that had velocity differences of greater than 250 m/s were flagged as potentially being anisotropic and/or containing heterogeneities. Using 250 m/s is a judgment call as it is approximately 6% of the observed velocity values, considering the overall average velocity value measured from all specimens was about 4,000 m/s. For example, if a P-wave velocity pick at the 0-degree orientation was 3,900 m/s and at the 45-degree orientation was 3,830 m/s, then this would be a difference of 70 m/s and classified as isotropic. If this difference was more than 250 m/s, say between velocities of 3,900 m/s and 4,300 m/s, then the sample would be further investigated for anisotropy and/or heterogeneities. Samples that are isotropic will have similar velocity values and thus, the shape of the radar chart will be more uniform and circular in shape. Samples that are anisotropic will have velocity values that significantly differ from one another and thus, the radar chart may be more irregular or oblong in shape. However, this is dependent on the scale being used to compare velocity measurements. In addition to comparing orientations from the same cylindrical specimen, a comparison of velocities can be made between different plug orientations (i.e., X, Y, Z) from the same rock sample. The same criterion of a difference of 250 m/s in velocity is used for comparing velocities across plug specimens.

One specimen was classified as having a velocity difference of greater than 250 m/s. Specimen 03-05, was slightly over a difference of 250 m/s with a P-wave velocity difference of about 256 m/s between the 0-degree orientation and the 90-degree orientation. However, the percent difference between the fastest and slowest velocity orientations was still very small. The percent difference between the fastest P-wave velocity and the slowest P-wave velocity was about 1.04% and therefore, the sample is still considered isotropic.

Between plug specimens from the same rock sample (i.e., specimens 03-03, 03-04, and 03-05 from sample 21KF03), a larger variation in velocities was found. Therefore, this may indicate anisotropy at the sample scale that is not apparent at the plug scale. Using velocity measurements displayed in Table 6, the largest differences between P-wave and S-wave velocities amongst all specimens from a rock sample (i.e., 21KF03) were considered. For sample 21KF03, a TrJn sample, the largest P-wave velocity difference was 363 m/s and the largest S-wave velocity difference was 512 m/s between three plugs in three different orientations: X, Y, and Z. For sample 21KF06, a Tpb' sample, the largest P-wave velocity difference was 986 m/s and the largest S-wave velocity difference was 507 m/s between two plugs in two different orientations: Y and Z. The large velocity differences between plug samples of the same rock type could indicate either anisotropy or heterogeneity at the rock sample scale. For sample 21KF20, a Tss sample, there was not a significant velocity difference between plugs from the same rock, thus indicating isotropy throughout the rock sample. The largest P-wave velocity difference was 134 m/s and the largest S-wave velocity difference was 246 m/s for three plugs in two different orientations: one in the X-orientation and two in the Y-orientation.

To confirm the presence of anisotropy within a sample with significant velocity differences, fabrics were analyzed within thin sections to compare to the measured velocity values. In rock samples 21KF03, 21KF06, and 21KF20 the results are quite interesting. Although the velocity differences are significant between plug orientations for samples 21KF03 and 21KF06, the thin sections do not display any quantifiable or noticeable fabric that can explain the apparent mechanical anisotropy. For sample 21KF03, the thin section is described as having equigranular quartz grains that are not elongated in any preferential direction and no layering is visible (Figure 19). For sample 21KF06, the thin section is described as having plagioclase grains that are rarely aligned with one another and many void spaces that are not elongated in any preferential direction (Figure 20). If plagioclase grains were lineated or quartz grains were elongated, this could explain the velocity differences. In contrast sample 21KF20, which had relatively consistent velocity measurements between plug orientations, does display evidence of a quantifiable fabric in thin sections. Although dependent on scale, the interlayering between quartz-grain layers and a finer-grained matrix could result in sample anisotropy for sample 21KF20, yet this is not indicated through velocity measurements (Figure 21).

However, as mentioned previously, there were often complications when picking velocities. Frequently, a waveform did not have a well-defined pattern or arrival pick location that resembled that of the head-to-head waveform. This could lead to errors in the velocity differences mentioned above and may over- or under-predict the velocity differences, thus altering the classification of isotropic or anisotropic. To quantify the error brought about by picking, velocities were picked at multiple locations representing possible arrival energy. This allowed us to give a range of possible velocities for each specimen rather than assigning it a single velocity value (Figure 22).

Using radial P-wave and average S-wave velocity measurements, dynamic E and ν can be calculated using the following two equations, respectively, for isotropic samples (Kuttruff, 1991).

$$E_d = \rho V_s^2 \left[\frac{3V_p^2 - 4V_s^2}{V_p^2 - V_s^2} \right] \tag{1}$$

where E_d, ρ, V_p, V_s are dynamic Young's Modulus, sample density, P-wave velocity, and average S-wave velocity, respectively.

$$v_d = \frac{V_p^2 - 2V_s^2}{2\left(V_p^2 - V_s^2\right)} \tag{2}$$

where v_d, V_p, V_s are dynamic Poisson's ratio, P-wave velocity, and average S-wave velocity, respectively.

An average value of P-wave and S-wave velocity from the four radial velocity measurements were used to obtain a single value of E and n for each plug specimen. Each sample was plotted to compare resulting values and compare amongst rock types (Figure 23 and Figure 24). TrJn samples had a dynamic Young's modulus E_d that ranged from about 78 GPa to 86 GPa and a dynamic Poisson's ratio v_d that ranged from 0.19 to 0.23. Tpb' samples had an E_d that ranged from about 28 GPa to 42 GPa and an v_d that ranged from 0.26 to 0.28. Tss has an E_d that ranged from 57 GPa to 58 GPa and a v_d that ranged from 0.24 to 0.25. Therefore, we see here that the lithologic unit, TrJn, has the highest Young's Modulus and the lithologic unit, Tpb', has the highest value of Poisson's ratio. Tpb' samples contain numerous voids of ranging sizes (Table 7).

Using the unistress cycle from static mechanical testing, static values of E and v are measured. Each sample was plotted to compare resulting values and compare amongst rock types (Figure 23 and Figure 24). TrJn samples had a static Young's modulus E_s that ranged from 52 GPa to 90 GPa and a static Poisson's ratio v_s that ranged from 0.14 to 0.17 based on measurements from three different plug sample of 21KF03. Tpb' samples had an Es of about 35 GPa and a v_s of about 0.21 based on measurements from one plug sample of 21KF06. Lastly, Tss samples had an E_s of about 71 GPa and a v_s of about 0.09 based on measurements from one plug sample of 21KF20. Therefore, we see here that the lithologic units, TrJn and Tss, have the larger values of Young's Modulus and the lithologic unit, Tpb', has the highest value of Poisson's ratio (Table 7).

Relatively large differences between static and dynamic elastic properties are observed but consistent with literature. Between static and dynamic E and v values of TrJn the largest difference of E is about 34 GPa and the largest difference of v is about 0.09. For Tpb' samples, the largest difference between static and dynamic values was about 7 GPa for E and about 0.07 for v. For Tss samples, the largest difference between static and dynamic values was about 14 GPa for E and about 0.16 for v.

By classifying these plug specimens before future data analysis, we can properly obtain the correct number of independent elastic constants needed to fully characterize each plug specimen. We also show the observed differences between static and dynamic moduli, which is important when the stress model incorporates dynamic well log estimations of elastic modulus.

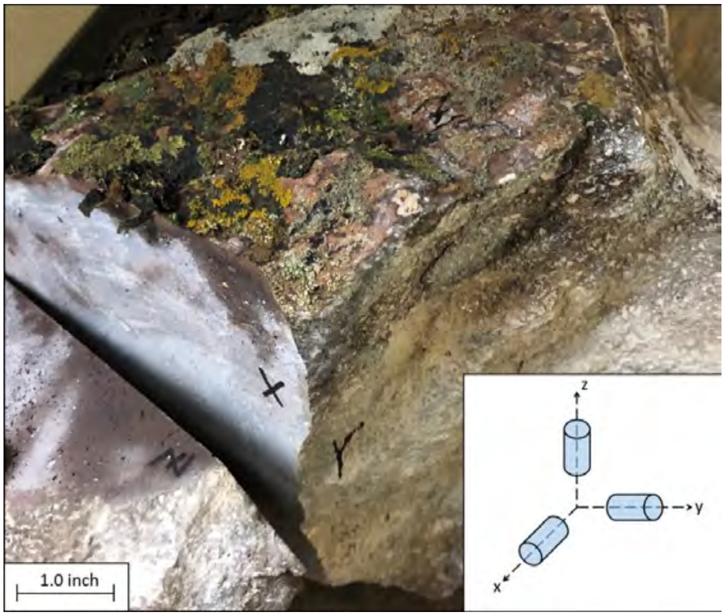

Figure 14. Image of 21KF06 Tpb' sample with markings of X-Y-Z orientations that are approximately orthogonal to one another. Thin sections taken from slabs of each orientation. The inset shows a schematic illustration of plug orientations retrieved from samples. It should be noted that plugs from all three orientations were not taken for every rock sample due to the feasibility of coring and specimen preparation.

663

Table 4. Three lithologic units of primary interest to this study that were capable of being plugged are shown within the table below. Three thin sections were taken at approximate orthogonal angles for each sample . Orientations (X-Y-Z) of each sample that had quantifiable fabric within its thin section are indicated by a check mark.

Sample ID	Formation (short name)	Formation (long name)	Thin Section Orientation (X/Y/Z)	Quantifiable Fabric from Thin Section
21KF03	TrJn	Triassic and Jurassic Nightingale	X	
			Y	
			Z	
21KF06	Tpb'	Tertiary Porphyritic Basaltic Andesite	X	
			Y	
			Z	
21KF20	Tss	Tertiary Silicified Sediments	X	
			Y	✓
			Z	✓

Table 5. Summary of sample testing. Check marks indicate that a specimen was tested using the method stated in the column heading. Radial velocity testing was conducted on a total of eight specimens discussed during this study. Static mechanical testing and Biot testing was conducted on a total of five specimens for this study.

Sample ID	Formation (short name)	Formation (long name)	Specimen ID	Specimen Orientation (X/Y/Z)	Radial Velocity Testing	Static Mechanical Testing	Biot Testing
21KF03	TrJn	Triassic and Jurassic Nightingale	03-03	X	✓	✓	✓
			03-04	Y	✓	✓	✓
			03-05	Z	✓	✓	✓
21KF06	Tpb'	Tertiary Porphyritic Basaltic Andesite	06-01	Y	✓	✓	✓
			06-02	Z	✓		
21KF20	Tss	Tertiary Silicified Sediments	20-01	X	✓		
			20-02	Y	✓	✓	✓
			20-03	Y	✓		

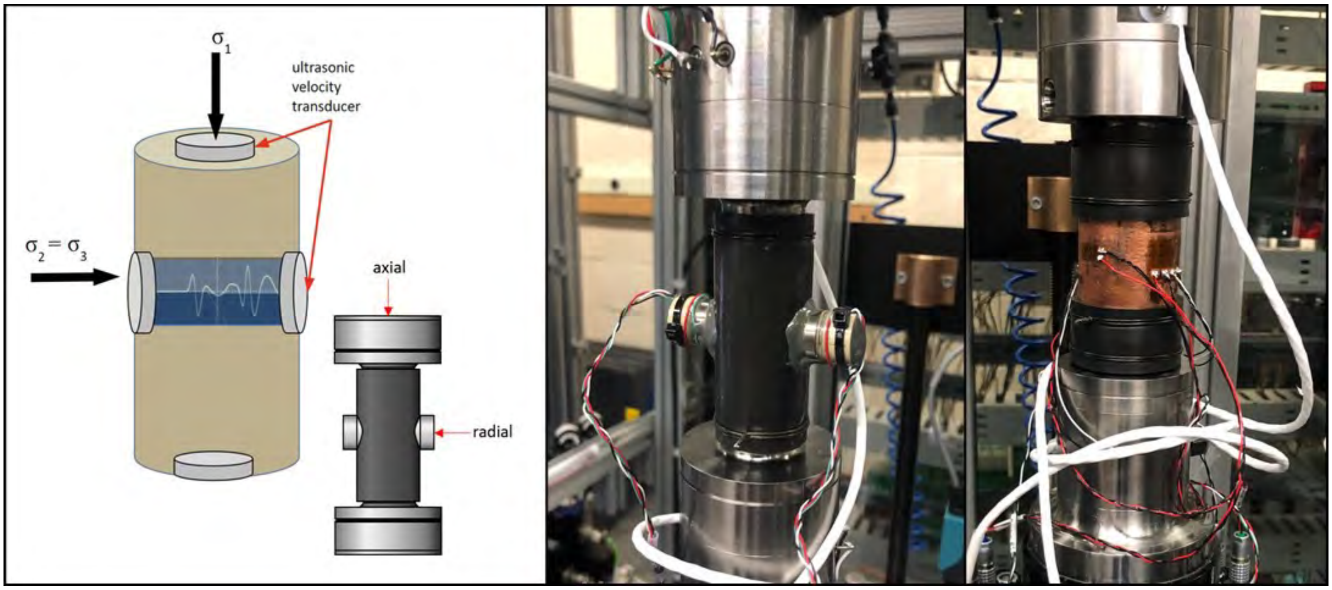

Figure 15. Schematic diagram of radial and axial velocity transducers where $\sigma1 = \sigma_2 = \sigma_3$ (left). Image of sample stack for conducting radial velocity tests (center). Radial velocity measurements were taken at 10 MPa confining pressure. Image of sample stack for static stiffness and Biot measurements (right).

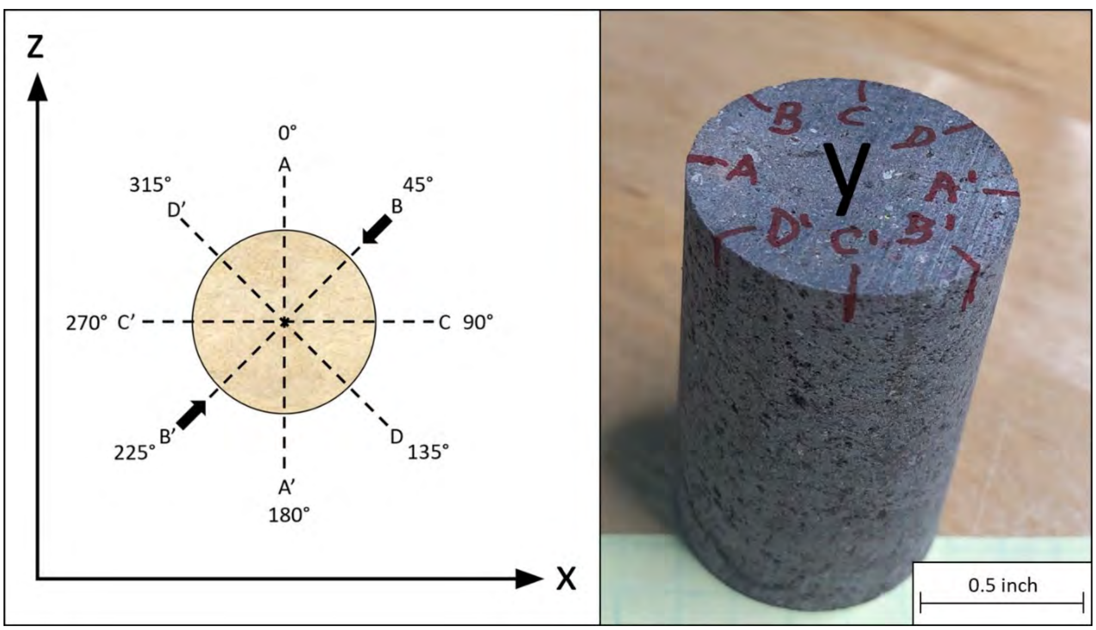

Figure 16 . Schematic illustration depicting orientation of radial velocity measurements (left). Image of Tpb' plug sample, 06-01, with markings indicating orientations for velocity measurements (A-A', B-B', C-C', D-D') (right). Plug specimen cored parallel to the y-axis. Four radial velocity measurements were made at 45-degree increments around the circumference of plug specimens.

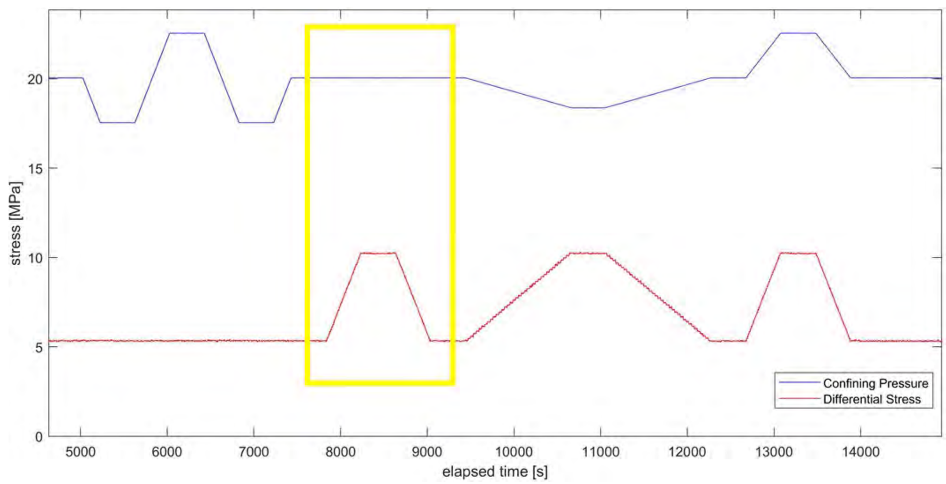

Figure 17. Protocol for static stiffness measurements. Unistress cycle used to obtain static E and v for isotropic specimens is highlighted in yellow. A ramp of 5 MPa differential stress is applied in this case.

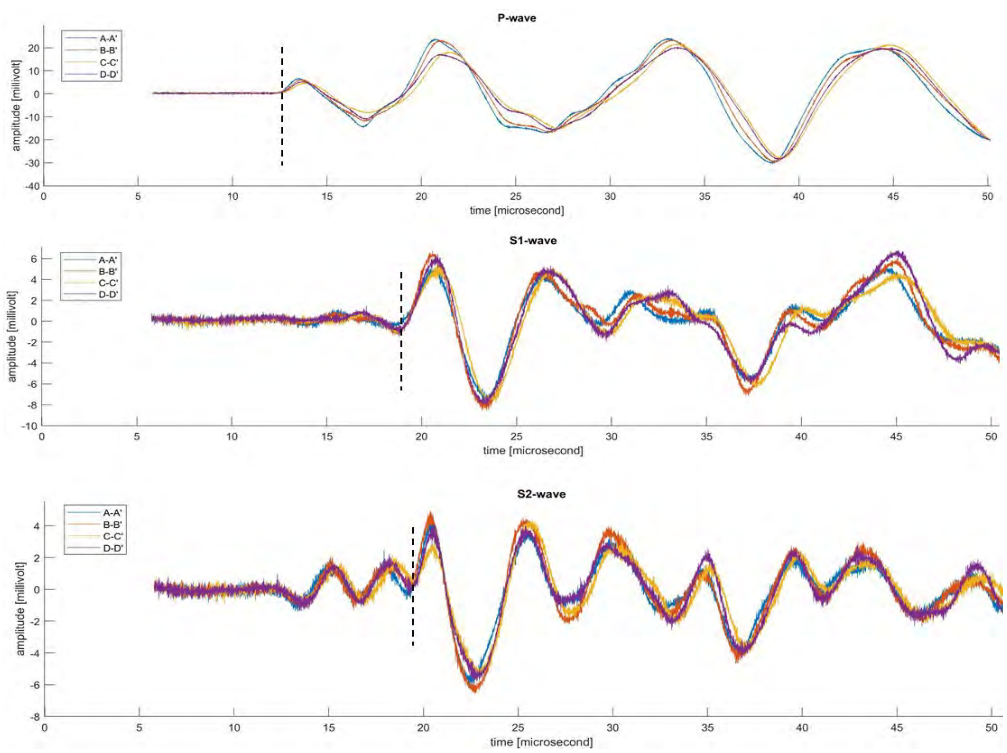

Figure 18. Example ultrasonic radial velocity waveforms of Tpb' specimen, 06-02. P-wave seismogram (top), S 1-wave seismogram (middle), and S 2-wave seismogram (bottom). Velocities taken at 45-degree increments around circumference of specimen in orientations A-A' (blue), B-B' (orange), C-C' (yellow), and D-D' (purple). Dotted black line indicates position of picked velocity. This test was conducted under a confining pressure of 10 MPa.

Table 6. Summary table of radial velocity testing of plug specimens. Table includes designation of specimen orientation, the ultrasonic velocity measurements at each direction (i.e., 0, 45, 90, 135), average radial velocities and standard deviations for each specimen, and the classification assigned on a plug-scale based on radial velocity measurements along with geological/textural descriptions. Averages and standard deviations are obtained from four ultrasonic velocity measurements made at each direction around the circumference of the specimen at one picking location on the seismogram.

Sample ID	Specimen ID	Specimen Orientation (X/Y/Z)	Angle [degrees]	P-wave [m/s]	S1-wave [m/s]	S2-wave [m/s]	P-wave Average [m/s]	P-wave Standard Deviation [m/s]	S1-wave Average [m/s]	S1-wave Standard Deviation [m/s]	S2-wave Average [m/s]	S2-wave Standard Deviation [m/s]	Specimen Classification (Isotropic/ Anisotropic)
21KF03	03-03	X	0	6013	3538	3671	5971	45	3508	30	3646	15	Isotropic
			45	6011	3538	3644							
			90	5959	3474	3633							
			135	5902	3482	3636							
	03-04	Y	0	5788	3582	3338	5797	58	3534	50	3333	21	Isotropic
			45	5893	3585	3334							
			90	5739	3501	3359							
			135	5766	3469	3302							
	03-05	Z	0	6102	3684	3812	5945	95	3601	69	3768	54	Isotropic
			45	5905	3542	3814							
			90	5846	3524	3767							
			135	5926	3653	3680							
21KF06	06-01	Y	0	4821	2535	2647	4701	73	2518	27	2643	19	Isotropic
			45	4668	2495	2643							
			90	4624	2488	2613							
			135	4690	2553	2667							
	06-02	Z	0	3912	2246	2197	3884	33	2247	12	2182	15	Isotropic
			45	3872	2263	2196							
			90	3835	2249	2160							
			135	3915	2229	2176							
21KF20	20-01	X	0	5238	2965	3106	5205	28	2981	12	3089	14	Isotropic
			45	5225	2977	3073							
			90	5190	2986	3078							
			135	5168	2996	3100							
	20-02	Y	0	5158	2938	3074	5213	51	2965	18	3116	42	Isotropic
			45	5292	2969	3183							
			90	5222	2988	3116							
			135	5182	2966	3089							
	20-03	Y	0	5193	2965	3057	5194	13	2969	7	3050	6	Isotropic
			45	5212	2968	3046							
			90	5194	2962	3055							
			135	5176	2981	3044							

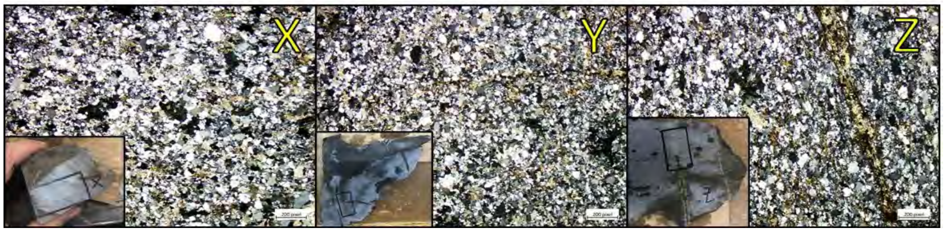

Figure 19. Thin section images from TrJn sample, 21KF03, at three approximate orthogonal orientations. X-orientation (left), Y- orientation (center), and Z-orientation (right). All orientations display fairly equigranular quartz grains with small masses of fine- grained biotite and muscovite throughout. Few cross-cutting fractures throughout thin sections.

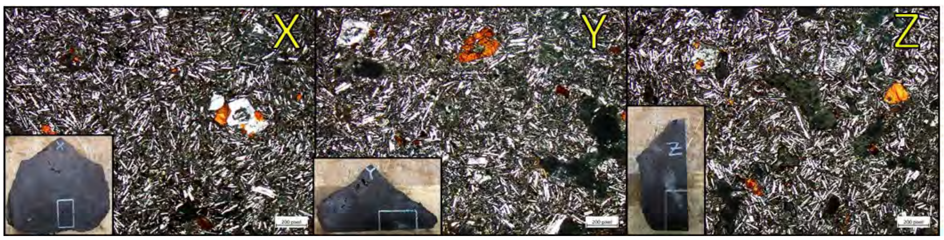

Figure 20. Thin section images from Tpb' sample, 21KF06, at three approximate orthogonal orientations. X-orientation (left), Y- orientation (center), and Z-orientation (right). All orientations display chaotic orientation of plagioclase grains with no clear lineated pattern. Many void spaces within thin section on account of being a vesicular basalt, but no preferential direction of elongation. Some larger plagioclase and clinopyroxene phenocrysts throughout thin section.

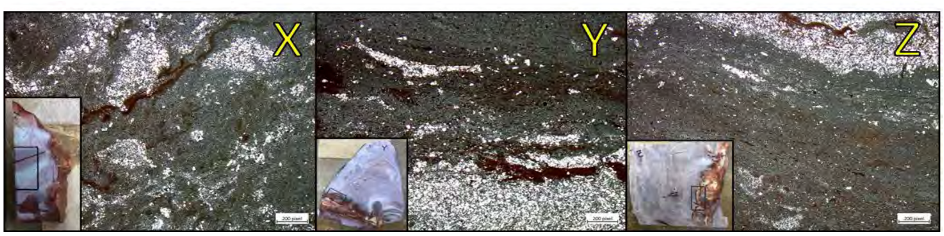

Figure 21. Thin section images from Tss sample, 21KF20, at three approximate orthogonal orientations. X-orientation (left), Y- orientation (center), Z-orientation (right). X-orientation displays clasts of fine-grained quartz within grey fine-grained matrix and some linear red iron-stained features. No clear elongation of grains or layering. Y- and Z- orientations both display interlayering between fine-grained quartz and grey/dark red iron-stained matrix. Although these linear features are present on the thin-section scale, they may not be representative or ubiquitous throughout the sample scale.

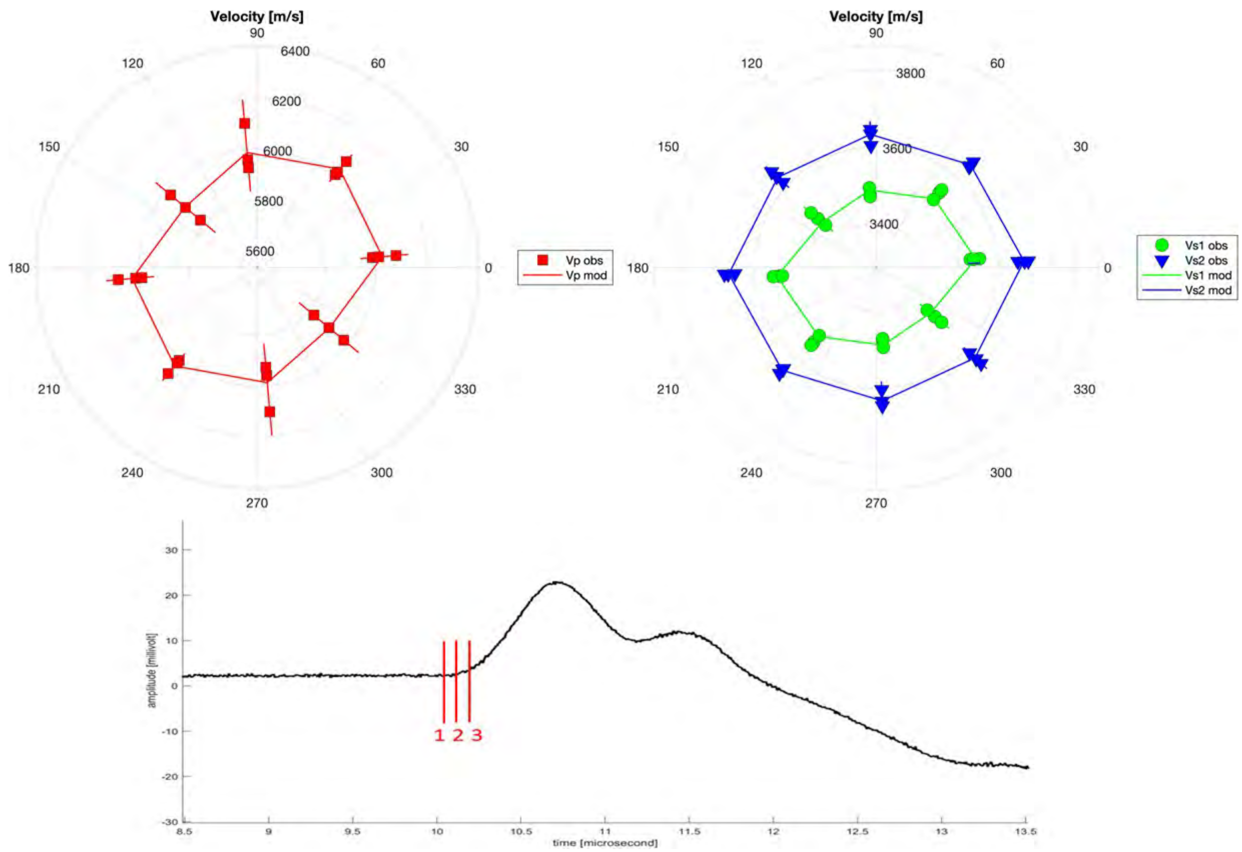

Figure 22. Polar plots of velocity picks from TrJn sample, 03-03. Observed P-wave velocity picks indicated by red squares (top left). Observed S1-wave velocity picks indicated by green circles and S 2-wave velocity picks indicated by blue triangles (top right). Error bars for each pick indicated by a line in top two figures. The straight lines connecting the observed velocity values at each orientation is the best fitting curve, not predictions. Example P-wave seismogram depicts three different locations for velocity picks (bottom). The range of error varies based on the two other velocity picks shown in red on the seismogram. The relatively circular shape shown above and the fact that velocities do not vary by more than 250 m/s between orientations, indicates that this sample is classified as isotropic.

Table 7. Summary table for dynamic and static Young's modulus E and Poisson's ratio ν values from three different velocity pick locations. Dynamic E and n values calculated using 1 and 2, respectively. Static E and ν values measured using unistress cycle from static mechanical testing. E values are in GPa and ν values are unitless. See Figure 23 (bottom seismogram image) for example of three ultrasonic velocity pick locations.

Specimen ID	Pick	Dynamic E [GPa]	Dynamic ν	Static E [GPa]	Static ν
03-03	1	84	0.22	57	0.14
	2	85	0.23		
	3	83	0.22		
03-04	1	78	0.23	90	0.17
	2	79	0.23		
	3	77	0.22		
03-05	1	86	0.19	52	0.16
	2	95	0.08		
	3	90	0.08		
06-01	1	42	0.28	35	0.21
	2	39	0.28		
	3	41	0.28		
06-02	1	28	0.26	N/A	N/A
	2	28	0.27		
	3	26	0.24		
20-01	1	58	0.24	N/A	N/A
	2	59	0.24		
	3	56	0.21		
20-02	1	58	0.24	71	0.09
	2	60	0.24		
	3	57	0.22		
20-03	1	57	0.25	N/A	N/A
	2	59	0.25		
	3	56	0.23		

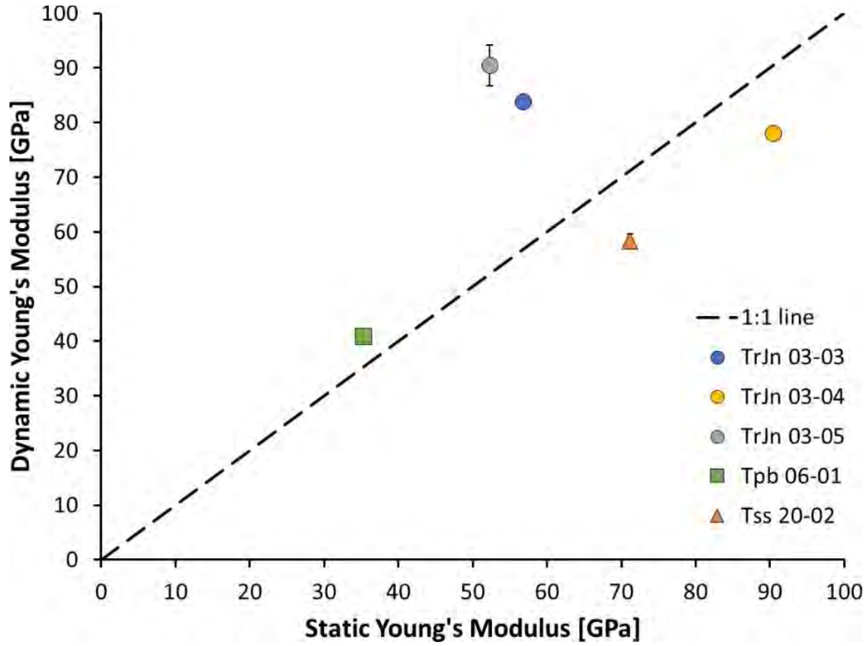

Figure 23. Average dynamic and static Young's modulus used for each plug specimen. Plug specimens are categorized by lithologic unit: circles indicating TrJn specimens, squares indicating Tpb' specimens, and triangles indicating Tss specimens. The dashed black line represents a static to dynamic ratio of 1. Samples that are over this 1:1 line have a dynamic E that is greater than the static E, and vice versa.

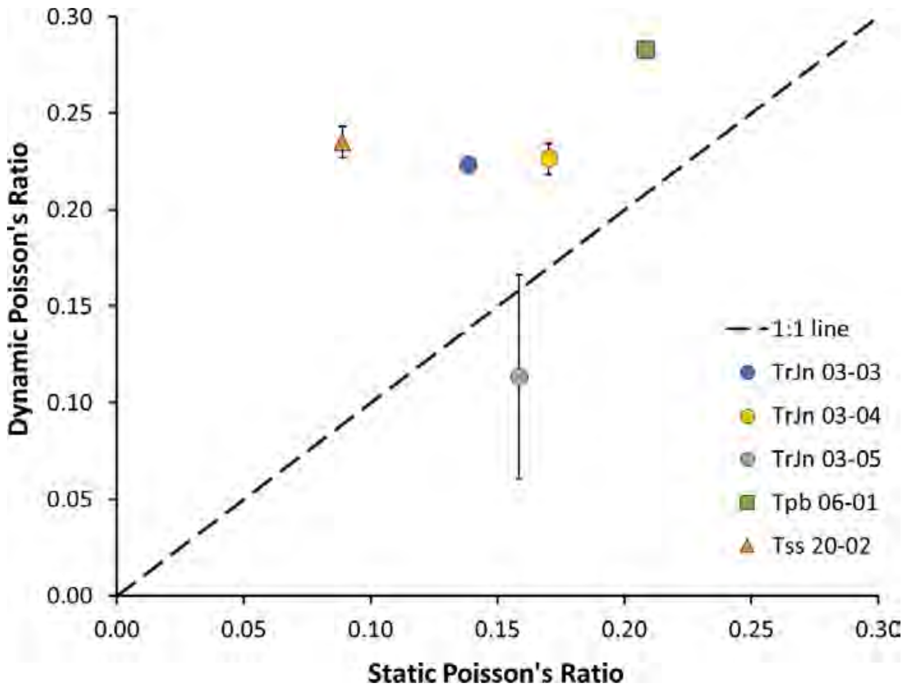

744 *Figure 24. Average dynamic and static Poisson's ratio used for each plug specimen.*
745 *Plug specimens are categorized by lithologic unit: circles indicating TrJn specimens,*
746 *squares indicating Tpb' specimens, and triangles indicating Tss specimens. The*
747 *dashed black line represents a static to dynamic ratio of 1. Samples that are over this*
748 *1:1 line have a dynamic v that is greater than the static v, and vice versa.*

Borehole Data (Subtasks 3.3 & 4.2)

Interpreting Regional Stress

The following section includes excerpts, some verbatim, from several sources (Jahnke, 2022; Jahnke et al., 2022; Jahnke et al., 2023).

Stress indicators within a ~175 km radius surrounding San Emidio were considered to reflect the background regional tectonic stress (Figure 25. The regional azimuth of greatest principal stress S_{Hmax}, was obtained from the World Stress Map (Heidbach et al., 2016) and wellbore indicators in the form of breakouts and drilling induced tensile fractures observed in nearby geothermal fields. Stress indicators from the World Stress Map primarily come from earthquake focal mechanisms, which indicated a maximum compressive horizontal stress azimuth near N10°E in a normal or strike-slip stress regime. Wellbore indicators from nearby geothermal fields at Astor Pass (Siler et al., 2016), Dixie Valley (Hickman and Zoback, 1998), and Desert Peak (Davatzes and Hickman, 2009; Hickman and Davatzes, 2010) indicated S_{Hmax} azimuths of N3°E ± 12°, N33°E ± 10°, and N24°E ± 17°, respectively. Additionally, the faulting regimes at Astor Pass, Dixie Valley, and Desert Peak are strike-slip, normal, and normal, respectively. Although not an indicator of stress, the direction of maximum contractional secular strain rate is N3°E at San Emidio (Kreemer et al., 2014), indicating that the background regional tectonic stress and strain rate directions appear to be subparallel.

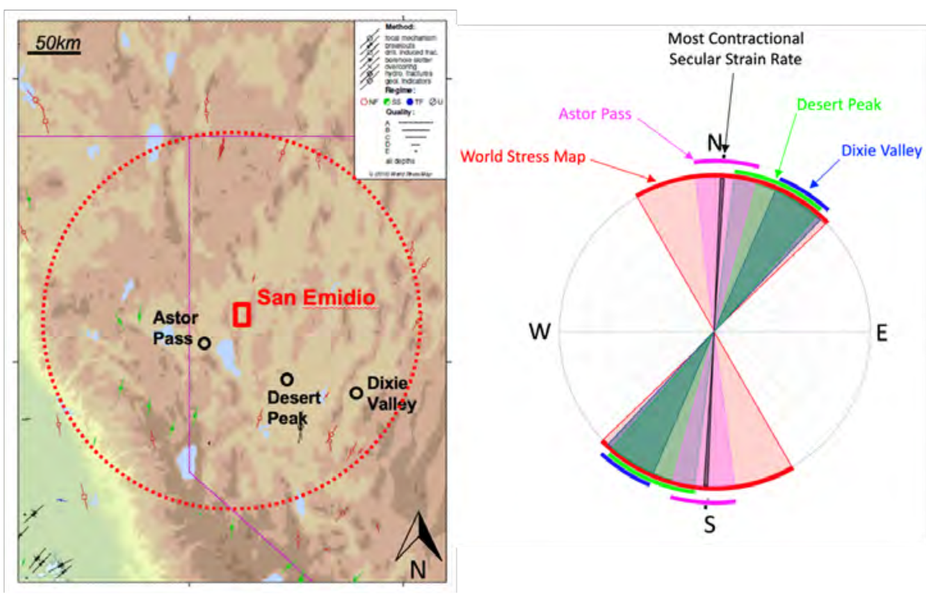

Figure 25. (Left) World Stress Map with locations of stress indicators within a ~175 km radius around San Emidio. Figure modified from World Stress Map (Heidbach et al., 2016). (Right) Summary of regional observations of S_{Hmax} azimuths (N10°E ± °40 with normal/strike-slip faulting regime).

In terms of more local observations, two microseismic with magnitude 3.52 and 3.80 occurred at a depth of 12 km in May 2016, to the west of the town of Gerlach, Nevada. Located to the north of the study site at San Emidio, these events provide additional inference of the local stress state. Each of the two events shows a strike-slip focal mechanism with a small normal-faulting component (Figure 26). Field observations of slickensides collected by Rhodes (2011) in the mountain range east of the study area were also used to infer the stress field. Although the analyses recovers the past stress state at the time of slickenside formation, the stress inversions indicates a normal faulting regime with S_{Hmax} in the N10°E ± 20° direction.

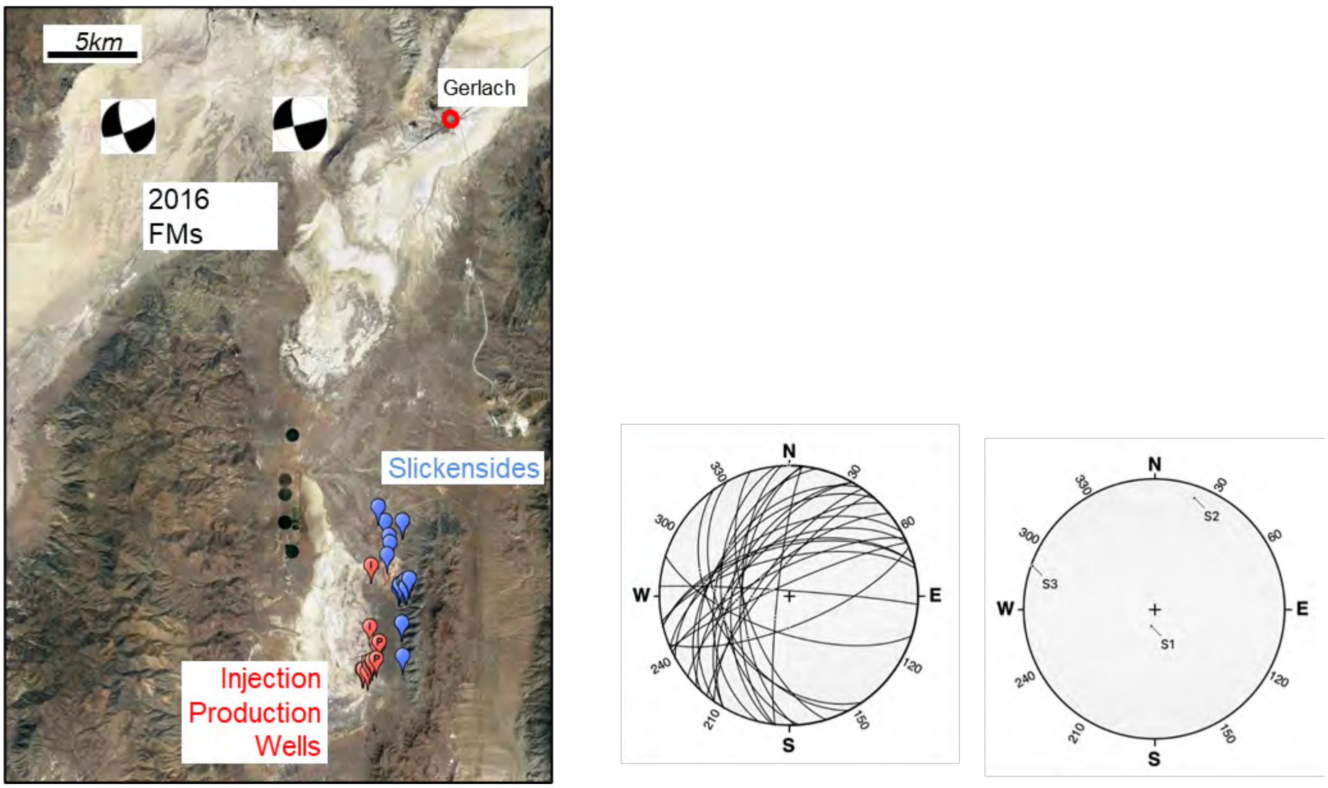

Figure 26. Focal mechanisms and fault slip for two earthquakes that occurred north of the study site, west of Gerlach, Nevada. Focal mechanisms from seismo.unr.edu and fault slip data from (Rhodes, 2011).

Table 8. Summary of data sources for interpreting regional stress at San Emidio.

Scale	Data Source	Faulting Regime	S_{Hmax} Direction
Regional	World Stress Map	NF/SS	N10ºE +/- 40º
	Nearby Geothermal Fields	NF/SS	N25ºE +/- 20º
Local	2016 Gerlach events	SS/NF	P-axis trend Nº25-30ºE
	Geological fault slip indicators (Rhodes, 2016)	NF	N20ºE

In-situ (preliminary)	2016 shut-in focal mechanism	NF	N-S on average, but ambiguous

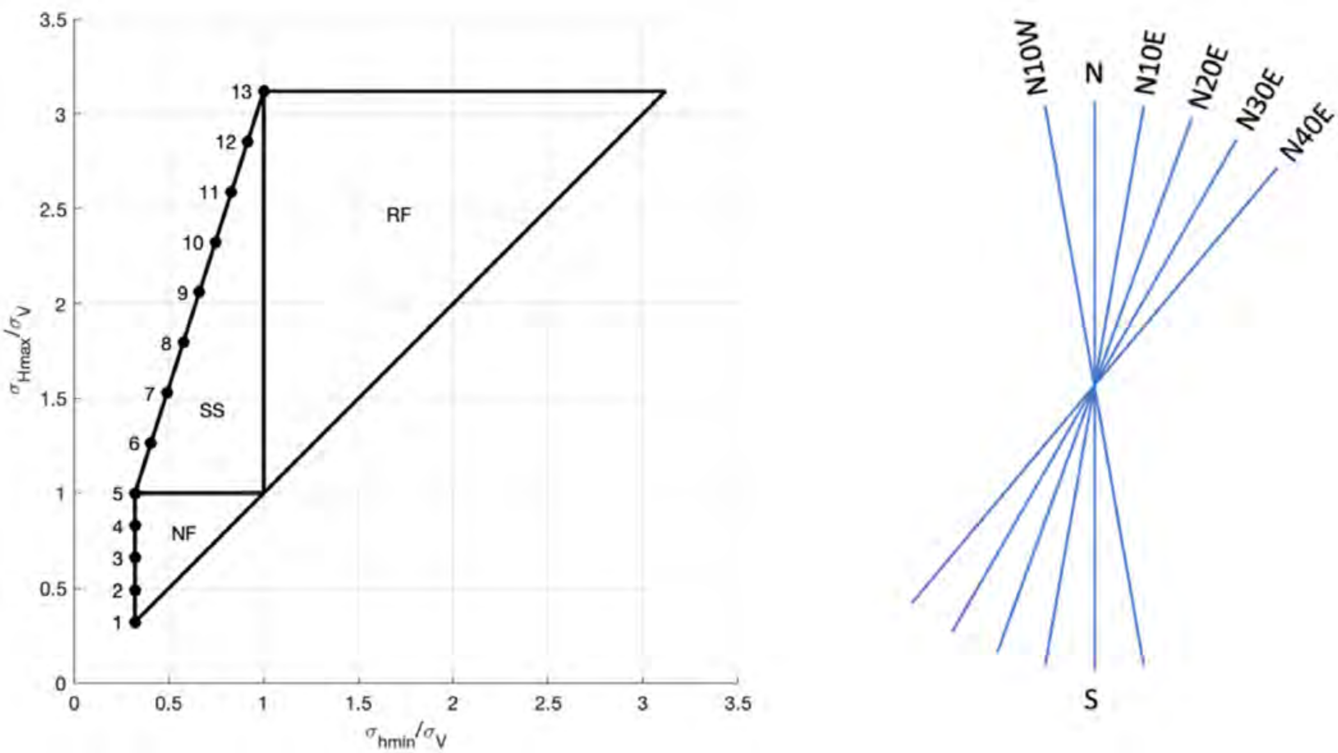

Figure 27. Assumption for regional stress interpretation.

Defining Prestress

The following section includes excerpts, some verbatim, from a peer-reviewed journal paper (Jahnke et al., 2023).

Stress profiles were estimated for 22 of the wells at San Emidio. An example of the stress profiles from the deepest well in the reservoir, Kosmos 1-9, is shown in Figure 28. The Kosmos 1-9 well reaches a maximum depth of 1636 m and penetrates three formations: QTa, Tpb', and TrJn. The stress profile in Figure 28 is generated for a transtensional stress regime, with a stress ratio $R = 0$. Vertical stress (S_v) is calculated from rock density (Figure 27) and horizontal stresses (S_{Hmax}, S_{hmin}) from frictional limits (μ=0.6). At the bottom of Kosmos 1-9, the magnitudes of total vertical stress, maximum horizontal stress, and minimum horizontal stresses were estimated to be 39.3 MPa, 39.3 MPa, and 23.5 MPa, respectively (Figure 28). Once such vertical profiles of the principal stress magnitudes were estimated for every location in the GEOS model honoring the lithological profiles the 22 wells, the domains in the model were allowed to equilibrate with adjacent elements to generate a mechanically equilibrated stress model. This process was repeated for each choice of S_{Hmax} azimuth and stress ratios (Figure 27) hypothesized based on the regional and local stress indicators summarized above. Based on the slip tendency values that project on the San Emidio and the Basin Bounding faults, Jahnke et al. (2023) suggested that the initial stress at San Emidio geothermal reservoir is characterized by a transtensional stress regime (S_v=S_{Hmax}>S_{hmin}) with an S_{Hmax} azimuth of N to N10°E.

Rock type	Abbr.	Model Density
Triassic metasediments (basement)	TrJn	2.67
Tertiary andesites and tuffaceous units	Tvu	2.6
Tertiary basalt	Tpb	2.8
Quaternary silicified sediments	Qas	2.4
Alluvial fill (0 - 200m deep)	Qal	2.02
Alluvial fill (0 - 200m deep)	Qal	2.12

Figure 27. Rock density values in g/cm^3 from Folsom et al. (2020) used to calculate vertical stress.

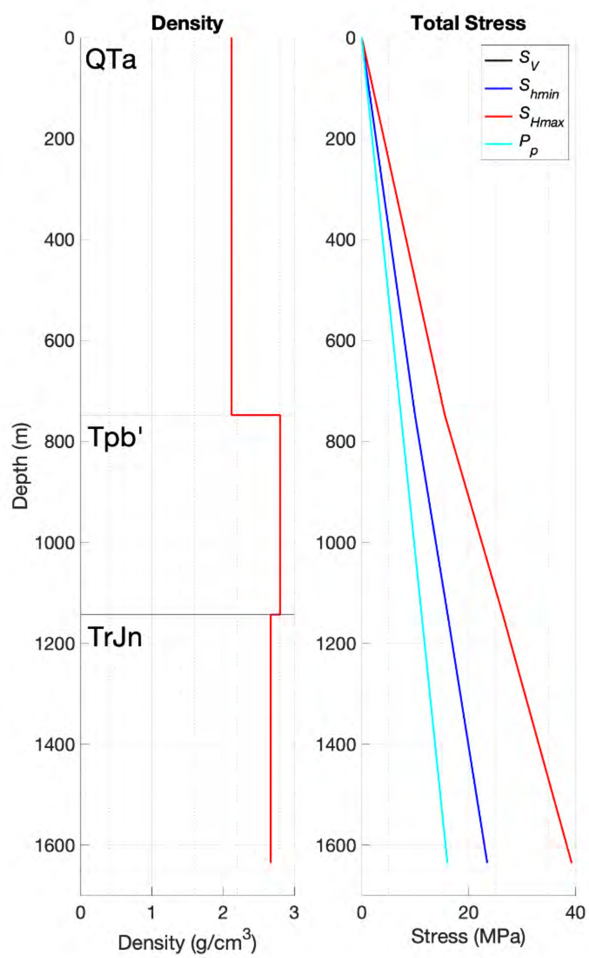

Figure 28. Profiles of density (left) and total stress (right) for the Kosmos 1-9 well. Since S_{Hmax} and S_V are assumed equal in magnitude, corresponding to a transitional normal faulting to strike-slip stress regime, S_V is not shown.

Borehole Data (Subtasks 6.2, 6.3, & 8.3)

Analysis of Wireline logging

The following section includes excerpts, some verbatim, from conference proceedings (Sone et al., 2023).

In summer 2022, multiple production and exploratory wells were drilled. Wells 17A-21, 18A-21, 25B-21 were drilled from the hanging wall of San Emidio fault (SEF), reaching 2000~2500 ft depths, and are expected to have penetrate the SEF. Well 84-20 was drilled from the hanging wall of the Basin Bounding fault (BBF), reaching 3400 ft depths and penetrating the BBF. In each well, drill cuttings were collected and examined every 10 ft of drilling to observe lithology changes and to construct a lithological column. Standard drilling parameters were also recorded which allowed us to identify drilling breaks and lost-circulation zones. In wells 17A-21, 18A-21, 25B-21, resistivity borehole image logs were collected in the open hole intervals covering the main reservoir in the Tertiary formations. In well 84-20, an acoustic borehole image log was collected, also in the open hole interval covering the Tertiary formations down to the metasediments.

In well 17A-21 only, a 3D Far-Field Sonic log (3DFFS) was run to capture the direct arrival of the acoustic waves and reflections from fractures within the formation. The 3DFFS log provides the compressional and shear wave slowness as well as the depth and orientation information of reflective fractures close to the borehole (Kumar et al., 2019).

Following drilling and the collection of downhole logs, the wells were cased with screened liner in their lower sections. They were then tested for permeability using a step-rate test while downhole pressure sensing equipment was hung near zones of inferred permeability (e.g., drilling losses). The precise locations of fluid feed zones were determined using flowing and static pressure, temperature and spinner logs (PTS). In the case of Well 84-20 this testing was performed under injection. For Wells 17A-21, 18A-21, and 25B- 21, testing was performed while flowing the wells to a sump.

The lithologic sequences encountered in each well roughly followed those expected from the regional geological map compiled by Rhodes et al. (2011). The Quaternary alluvium continued to about 400-600 ft depth, followed by a sequence of Tertiary claystones before entering the volcanic sequence. Although not identified in the geological map, the presence of the tuffaceous sediments and the andesite appears to be interlayered characterized by multiple appearances of these members, although depth precision of mud logs may not always be precise. Only the deepest well 84-20 reached the metasedimentary Nightingale formation at 2600 ft depth.

Some cuttings were also collected for the purpose of measuring wet densities of the formations. This was done to provide a better constraint on the density of the formations which are used to calculate the vertical stress profile in geomechanical analyses. For the Tertiary formation cuttings from Well 17A-21, the drilling mud was washed off using fresh water, then the excess water was removed from the surface. The mass was then measured on a precision balance and water-saturated volume measured using a helium porosimeter which utilizes the principles of the Boyle’s law to calculate sample volume. For the Quaternary sediments, collecting intact cutting specimens was much more challenging as the formation was likely not fully indurated. Nonetheless, some hand-picked intact fragments from Wells 18A-21 and 25B-21 were collected to measure the formation density, with the caveat in mind that these measurements may only serve as an upper limit value. Results are compared with the density values used to model gravity data in Folsom et al. (2020) in Figure 27. The depth trend in the tertiary formations in Well 17A-21 is also shown later in Figure 36 and Figure 39. The density profile reveals a gently increasing trend, with local perturbations caused by the anomalous presence of some light volcanic sediments (Figure 39).

Lost Circulation and Feed Zones from Drilling Records

Circulation losses were encountered at one or more depths in each well where the mud return flow was either partially or totally lost. Circulation losses can be caused by, for instance, the creation of open fractures in the formation when the mud pressure exceeds the minimum principal stress. But in a shallow, moderately-pressured reservoir like San Emidio, loss zones occur at depths close to high-permeability formations, such as unconsolidated sediments, porous lavas, highly fractured intervals, and fault damage zone (Winn et al., 2021). Circulation losses can also be accompanied by drilling breaks which are recognized as the sudden decrease of weight-on-bit (WOB) and increase of rate-of-penetration (ROP). These variables are indicative of the presence of incompetent formations, such as weak porous formations or fractured or brecciated rock masses. Following completion of drilling, image logs are run in open hole intervals before a screened liner is installed. Well testing is generally performed after the liner is installed.

Depths of loss circulation zones are listed in Table 9 and indicated together with the lithological column in In 18A-21, both partial and total loss circulation occur at 1900 feet and 1969 feet depths, respectively. In 17A-21 total loss circulation occurs at a depth of 2130 feet, which happens at the contact between tuff and andesite. We note, though, that this depth was quite different from the total loss encountered at 1766 ft depth in an adjacent well (17-21) that was drilled previously about 20 ft southwest (along-strike of SE) from Well 17A-21. In Well 25B-21 only partial losses are observed at 1963 feet and 2372 feet, and a partial gain at 2191 ft. In Wells 18A-21, 17A-21, and 25B- 21 all losses occur within the tuff or andesite intervals. However, in Well 84-20 losses occur at deeper intervals within metasedimentary rocks accompanied by frequent occurrence of drilling breaks. There were two partial losses and three total losses in this well. Note that multiple total losses are identified when a total loss of circulation recovers, but is lost again after hitting another loss zone resulting in another total loss of circulation. Such recovery likely occurs when open fractures are clogged by cuttings as drilling mud is lost into the formation. This may indicate limited aperture, extent, or connectivity of the fractures that were responsible for the total loss zones within the metasediments.

Feed zones are also listed in Table 9 and indicated in Figure 29. In wells 18A-21 and 17A-21, the major feed zone responsible for almost all of the flow rate corresponds to where total loss of circulation was encountered. However, in well 25B-21, no clear the feed zone was identified although two partial loss zones were found. Note that this is in stark contrast with a nearby well (25A-21) that was drilled about 100 ft away to the northeast (along-strike of SEF), which encountered a high permeability fracture causing total loss at 1932 feet depth. In well 84-20, multiple feed zones exist and they are more diffuse spanning over a range of depths. In the moderate and minor feed zones at shallower depths, these feed zones do not correlate with any loss zones although drilling breaks were observed. The major feed zone at the bottom of the well, however, overlaps with the two total loss circulation depths and drilling breaks. These observations could be interpreted that the BBF involves multiple fault strands rather than a single fault plane.

In summary, Wells 18A-21 and 17A-21 clearly intersected a fracture that is responsible for both total loss circulation and production flow rate. Well 25B-21 intersected only minor loss zones that may be contributing to some flow. Well 84-20, which is likely the only well that intersected the BBF, encountered numerous loss zones and drilling breaks, suggesting a rather distributed feed zone within the metasediments.

Image and Sonic Logs

Image logs highlight heterogeneous features on the borehole wall, allowing us to identify planer and linear structures. Resistivity image are scaled so that low-resistivity conductive rocks appear darker. The acoustic image is scaled so that spots with weaker reflection coefficients appear darker. In both types of borehole images, open, fluid-filled fractures appear as dark curved or linear features which correspond to natural fractures and drilling-induced tensile fractures (DITFs), respectively. Some examples of natural fractures and DITFs picked in the borehole images are shown in Figure 30 and Figure 31, respectively. The resistivity images also provide information about the relative resistivity of the formation which reflects the amount of fluid and/or clay minerals in the formation.

The dip angle, down-dip azimuth, and fracture density information from all picked fractures are summarized in Figure 32 and Figure 33. We recognize from the results that the down-dip azimuth can vary in all directions and the dip angle also varies widely between 20 and 90 degrees. However, the most frequent dip azimuth occurs in the northwest direction, consistent with the SW-striking, westward dipping orientation of the SEF and BBF close to the wells. Fractures in the conjugate orientation, dipping southeast, are also found in the Tertiary units.

The fracture density also varies along each well and among the wells. This reflects the inherent variation of the fracture density in the formation, as well as the uncertainty in our ability to pick fractures from the images. For instance, fractures are difficult to identify when the background formation is also conductive. The borehole also may not retain its original shape due to breakouts and washouts, which leads to low-quality out-of-focus images (Figure 32 and Figure 33). Both tend to occur at fault zones because fault rocks can have higher porosity and higher clay - content compared to the surrounding rock mass, and fault rocks are weaker and more prone to compressive rock failures. Taking into account these factors, it is possible to suggest that a typical fault zone architecture (Faulkner et al., 2003) is seen in these image logs where a fault core consisting of fault gouge and fault breccia is surrounded by a damage zone characterized by higher fracture density than the background fracture density in the host rock.

In Well 18A-21, there may be a fault core present at around 2060 ft characterized by low resistivity surrounded by high fracture density especially in the footwall. In Well 17A-21, a fault core may be present at around 1780 ft with high fracture density above. In Well 25B-21, the fault core may be present at 2090 ft with high fracture density above and below. It is interesting to note that these suggested fault cores do not correspond to the loss zones nor the feed zones. It is difficult to make similar inferences based on the acoustic images from well 84-20 because the reflection amplitude relates to the surface condition (i.e. roughness) of the borehole rather than petrophysical properties.

Numerous DITFs were also picked which can give information about the orientation of the horizontal principal stresses and constraints on the horizontal stress magnitudes (Figure 34). The azimuths at which the DITFs occur are consistently in the NNE-SSW direction in all wells which is consistent with the direction of the maximum horizontal stress inferred from the World Stress Map (Heidbach et al., 2016), fault slip indicators (Rhodes, 2011), and the inversion of focal mechanisms from microseismic events (Jahnke et al., 2023). When compared between formations, we find some variation in DITF azimuth with depth where the DITF azimuth in the shallow claystone and the deep metasediment appear in the NE-SW direction, whereas it is in the NNE-SSW direction in the tuff and andesite formations.

Sonic logs provide information about the stiffness of the formation. The acoustic slowness values shown in Figure 35 range from 60-120 μs/ft and 120-230 μs/ft, for compressional and waves, respectively, corresponding to seismic velocities of 2.5-5.1 km/s and 1.3-2.5 km/s, respectively. A notable anomaly is the low velocity seen at 1770-1800 ft depth, which is also where the low resistivity zone is observed. The natural gamma ray log also shows a broad peak at this depth. These observations are all consistent with the hypothesis that a relatively compliant, fluid-rich, and clay-rich fault rock exists at this depth interval, surrounded by damaged host rocks.

The 3DFFS log also detected numerous sonic waves reflected from fractures. The fracture orientation information and fracture density distribution recovered from the 3DFFS log is compared with the same information collected independently based on the resistivity image log in Figure 34. Note that fractures were picked manually from resistivity image logs, but were automatically picked using an algorithm from the 3DFFS log (Kumar et al., 2019). The comparison shows that less fractures are detected from the 3DFFS log, especially those fractures with low dip angles owing to the fact that subhorizontal fractures likely do not reflect back acoustic waves to the tool. However, the statistics of the dip direction shown in the Rose diagram and the fracture density distribution agrees quite well. Preferred dip directions generally match and peaks and troughs of fracture density also occur at the same depth range, confirming the validity of the interpretations made on the resistivity image logs.

Preliminary Stress Analysis Based on Borehole Data

Given the density information and the occurrence of DITFs in the image logs, we conduct a preliminary stress analysis. The vertical stress profiles were constructed from the formation densities described in Figure 36 and pore pressure was assumed to be hydrostatic (Figure 36). We also made an assumption that a leak-off pressure observed in a leak-off test from a nearby well resembles the minimum horizontal stress gradient, which is set at 13.7 MPa/km. Then by setting the frictional coefficient of the formation to be 0.6 (Byerlee, 1978), we can construct a stress polygon describing limits on the horizontal stress magnitude as shown in Figure 37 for a depth of 1973 ft. Because DITFs are observed in these wells, the in-situ stress state must lie along the red line and above the blue line in Figure 37, which suggests a trans- tensional faulting environment. This is consistent with the stress state inferred from slip tendency analyses (Jahnke et al., 2023).

Table 9. Fault plane depths as inferred from drilling events and testing results. Drilling losses describe intervals where circulating drilling muds were lost to the formation. Tested feed zone intervals follow from the results of flowing PTS logs that identify the precise intervals of permeability. These independent observations often correlate, with some notable differences.

Fault	***Well***	***Drilling Loss Depths [ft kb]***	***Drilling Loss Type***	***Tested Feed Zone Depth [ft kb]***	***Tested Feed Zone Type***
San Emidio Fault	17A-21	2130	Total loss of circulation	2130	Major feed zone
	18A-21	1900	Partial loss	1965	Major feed zone
		1969	Total loss of circulation		
	25B-21	1963	Partial losses	Uncertain depth	Moderate feed zone
		2191	Partial gain of pit volume		
		2372	Partial loss		
Basin Bounding Fault	84-20	2773	Partial losses	2620 – 2750	Moderate feed zone
		2794	Total loss of circulation	2845 – 2900	Minor feed zone
		3047	Partial losses	3152 – 4500	Major feed zone
		3194	Total loss of circulation		
		3353	Total loss of circulation		

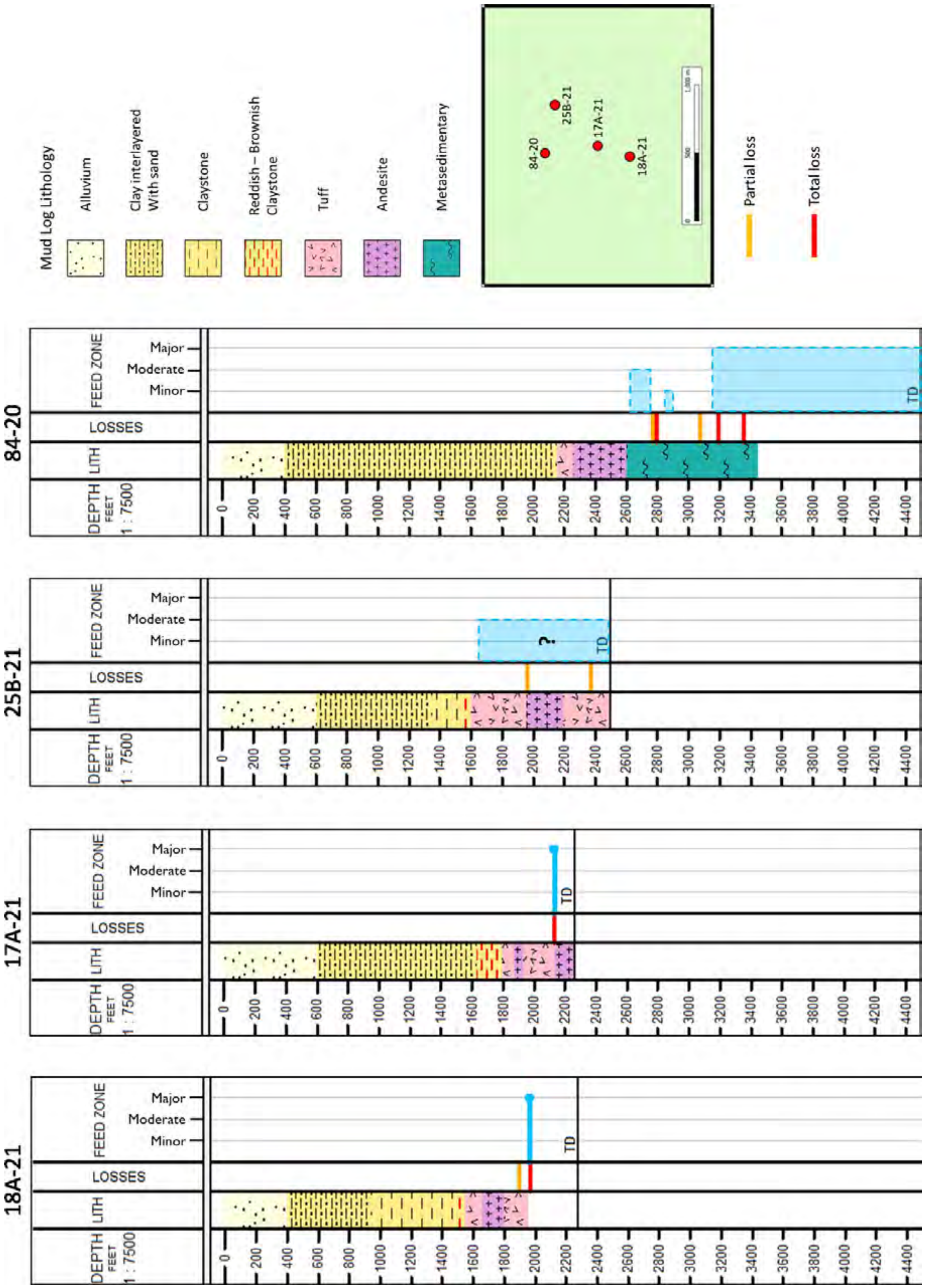
Mud Log Lithology
Alluvium
Clay interlayered With sand
Claystone
Reddish – Brownish Claystone
Tuff
Andesite
Metasedimentary
84-20
25B-21
17A-21
18A-21
Partial loss
Total loss
84-20
25B-21
17A-21
18A-21
FEED ZONE
Major
Moderate
Minor
LOSSES
LITH
DEPTH FEET 1 : 7500
TD
?

Figure 29. Lithological columns inferred from mud log cuttings observations and total/partial loss intervals in Wells 18A-21, 17A-21, 25B- 21, and 84-20. In Well 84-20 losses interval occur at metasedimentary interval meanwhile the other three occur at tuff and andesite intervals.

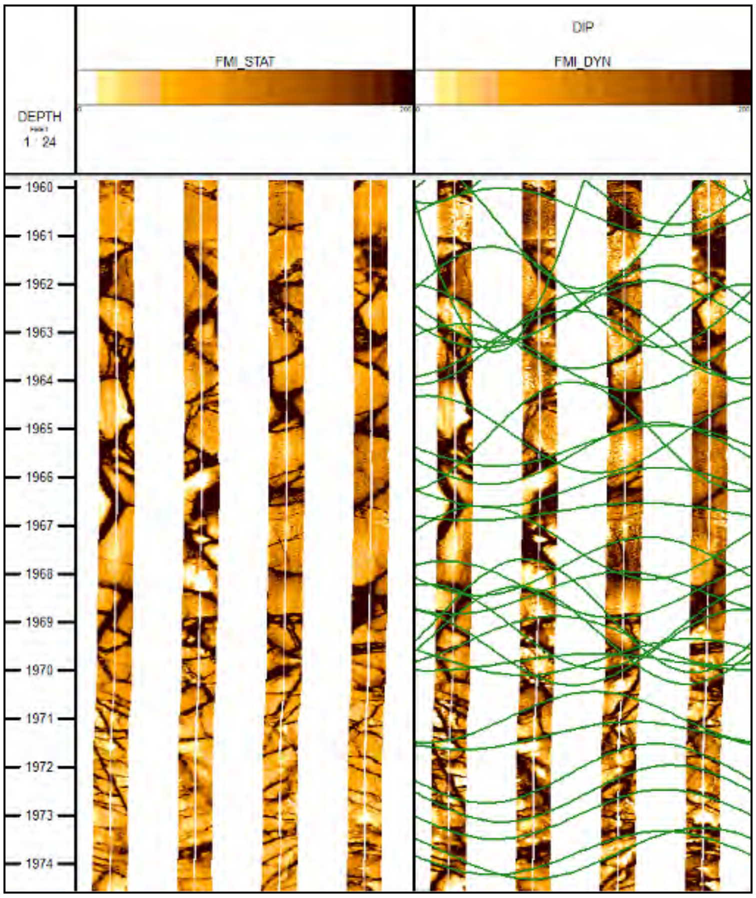

Figure 30. Resistivity borehole image from well 17A-21, showing example picks of conductive fractures (green curves).

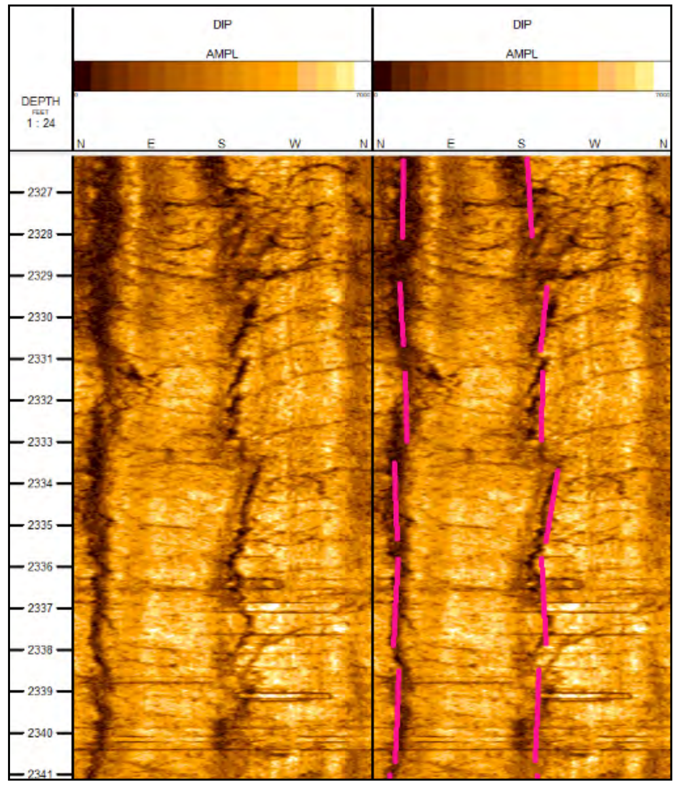

Figure 31. Acoustic borehole image from well 84-20, showing example picks of drilling-induced tensile fractures (magenta line segments).

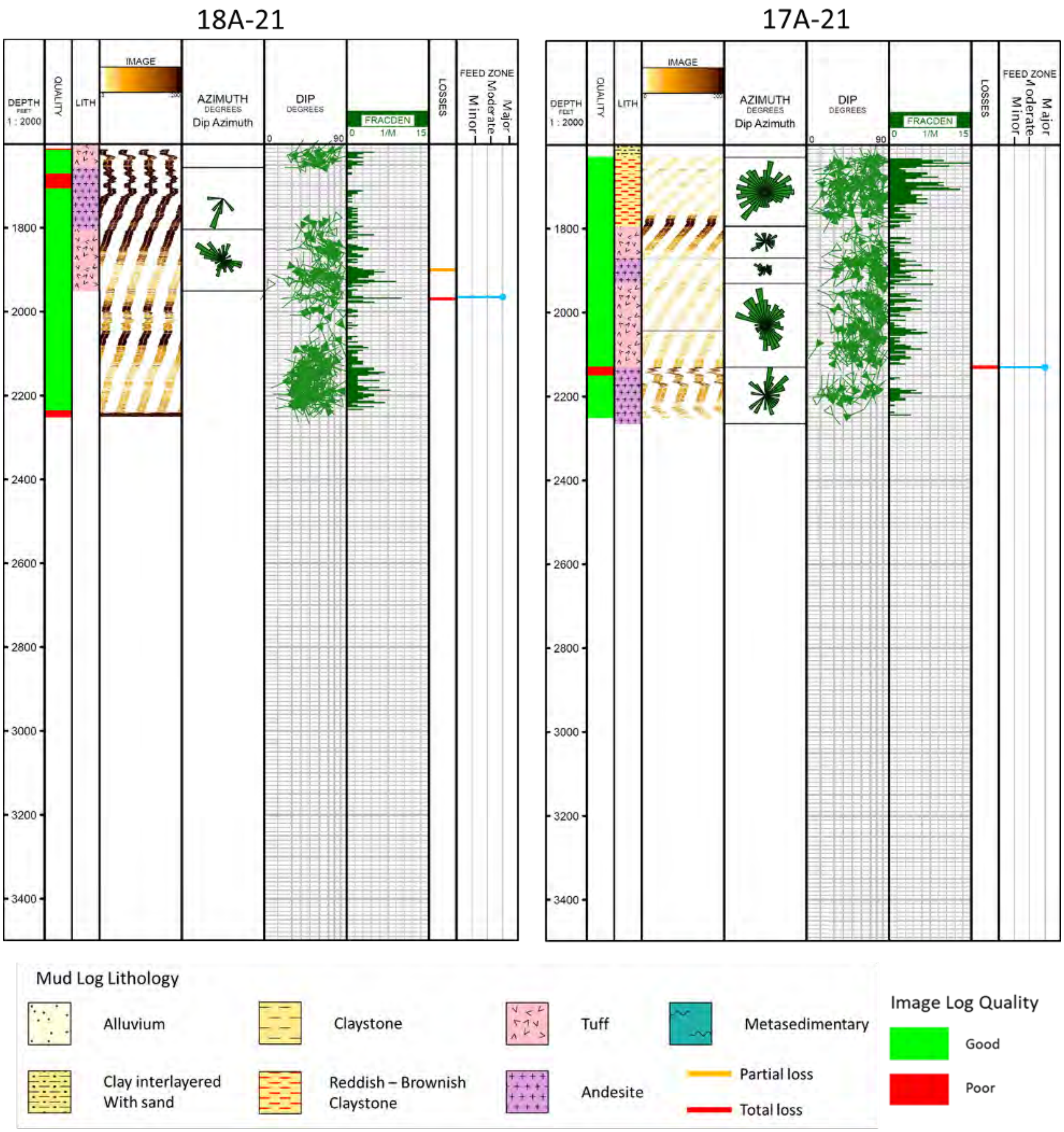

Figure 32. Borehole images of resistivity from wells 18A-21 and 17A-21 along with the orientation and distribution of fractures picked from image logs.

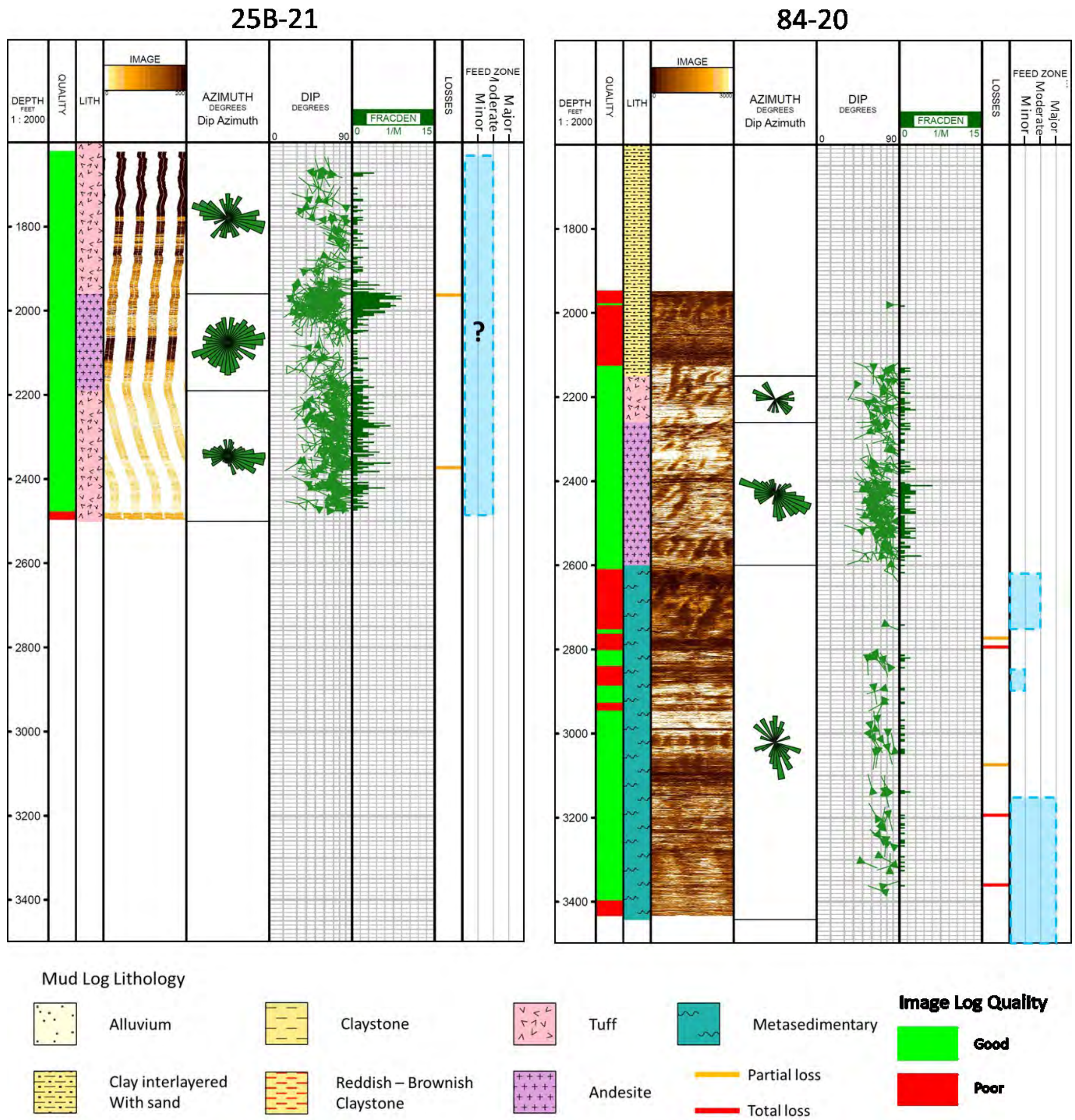

988 *Figure 33. Resistivity borehole image from well 25B-21 and acoustic borehole image*
989 *from well 84-20 along with the orientation and distribution of fractures picked from*
990 *the image logs.*

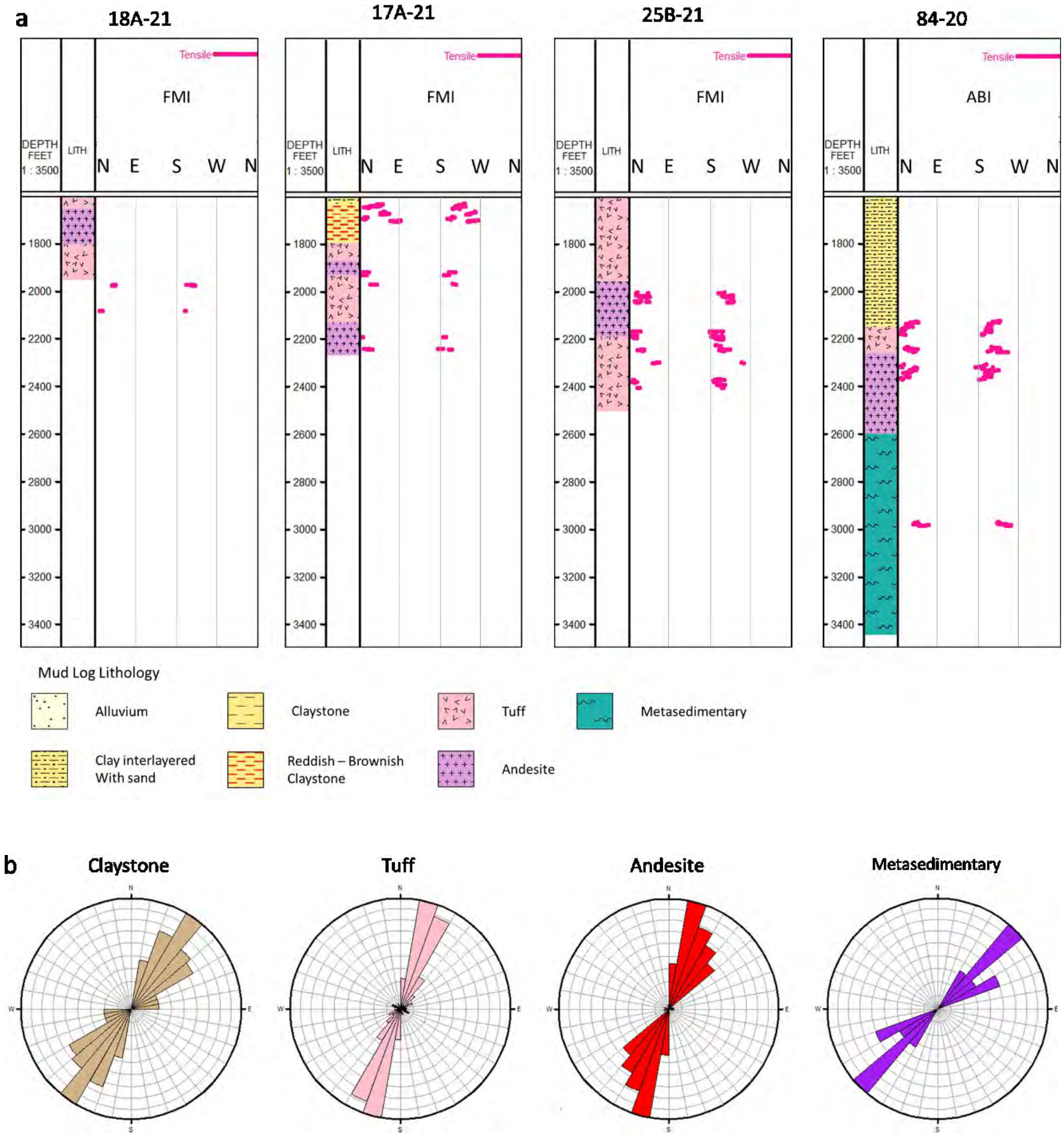

Figure 34. Interpretation of drilling-induced fractures (DITFs) in all wells. (a) DITF appears in all wells with the azimuth of NE - SW direction. (b) In tuff and andesite intervals DITF is consistent. In claystone and metasedimentary interval, the direction is slightly rotated to the east. The actual azimuth in claystone, tuff-andesite, and metasedimentary are N30E, N10E, and N40E, respectively.

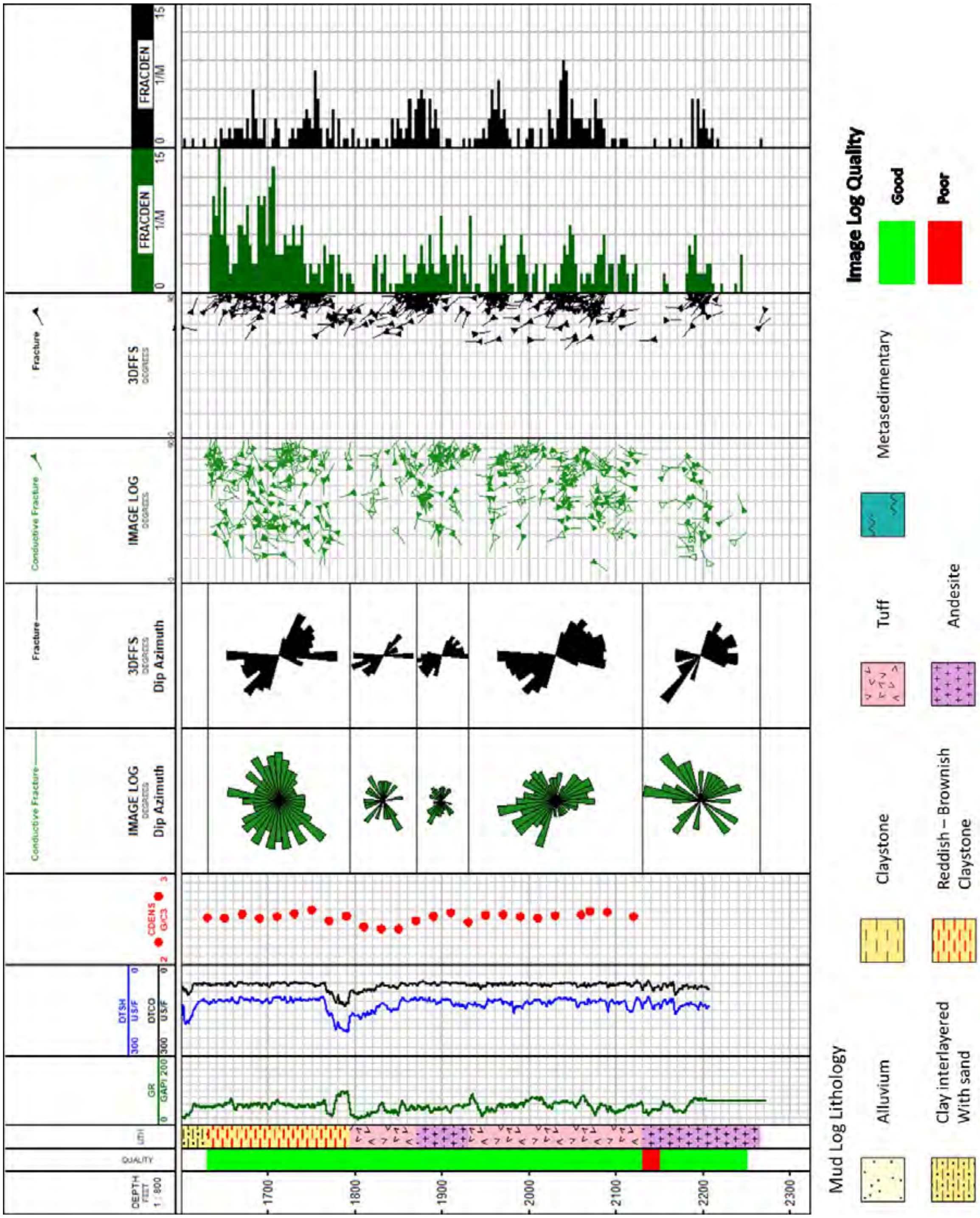

997 *Figure 35. Gamma ray, sonic log data, and comparison of fracture picks from*
998 *resistivity image log and 3DFFS sonic log data in well 17A-21.*

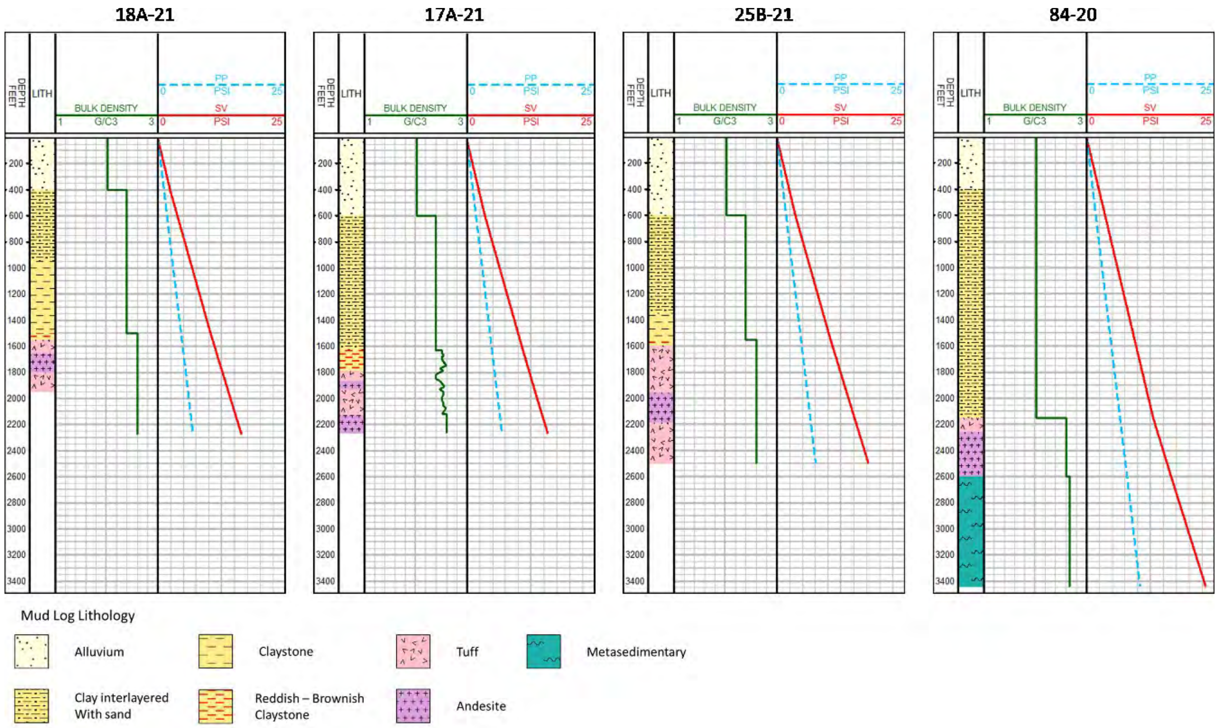

Figure 36. Bulk density profile inferred from the lithological column and also cutting mesurement for well 17A-21. Model density from Folsom et al. (2020).

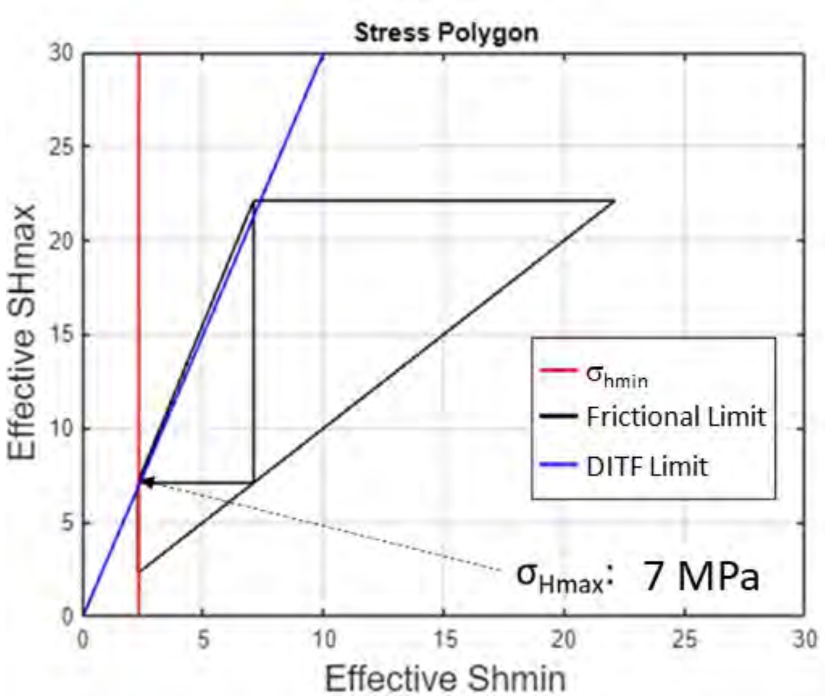

Figure 37. Limits on the magnitude of horizontal stresses at 1973 feet depth from well 18A-21 described in a stress polygon drawn with frictional coefficient 0.6.

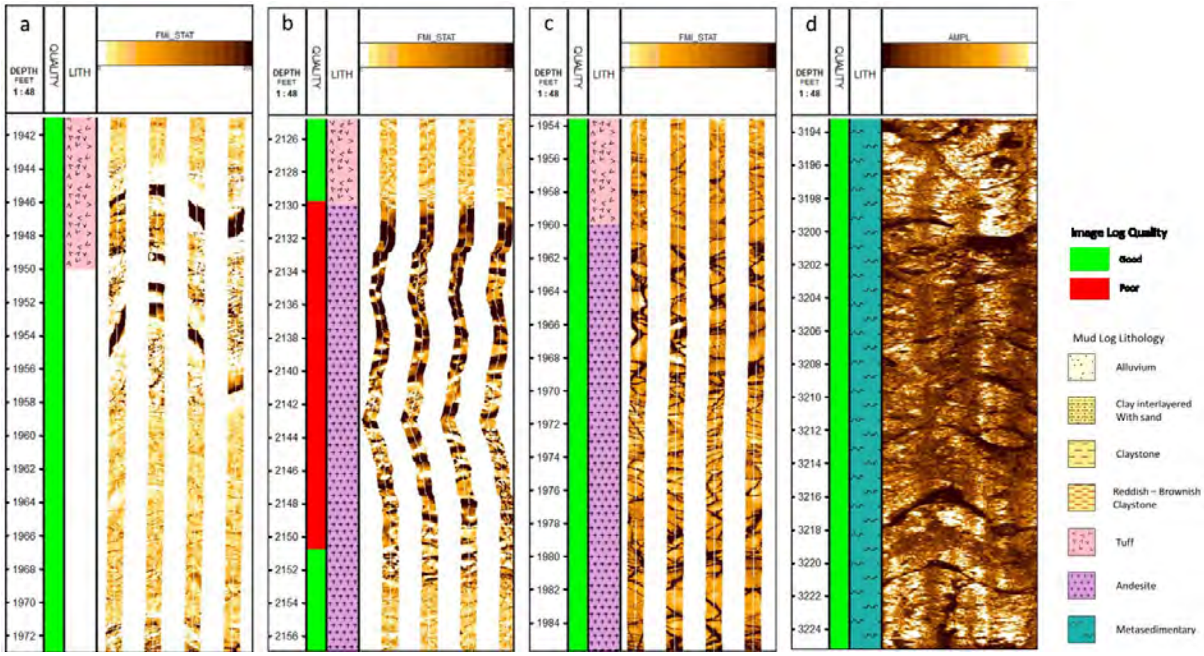

Figure 38. Enlargement of image logs showing the loss zones. (a) Total loss zone in well 18A-21, suggesting thick conductive sinusoid feature. (b) The total loss zone in well 17A-21 shows open pore structure. (c) Partial loss zone of 25B-21 coincides with highly fractured andesites. (d) Partial loss zone in 84-20 coincides with a high fracture density interval.

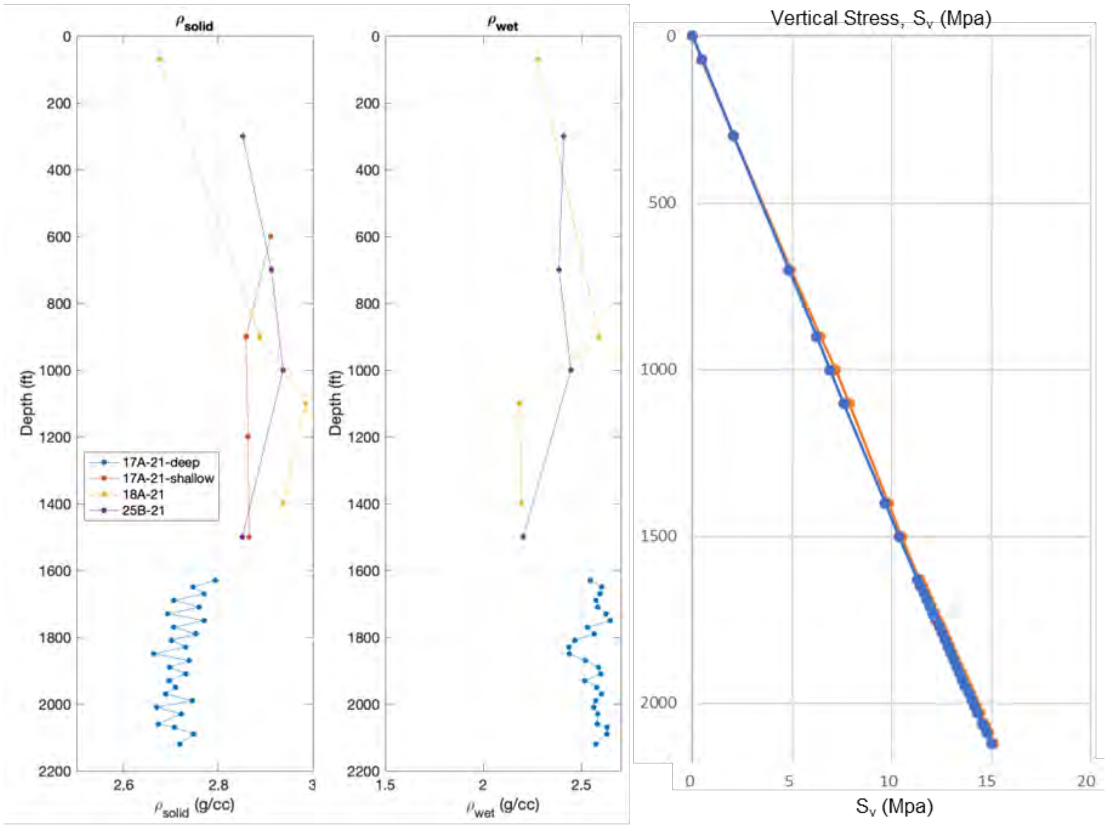

Figure 39. Profiles of density measurements from cuttings and estimated vertical stress profile.

Geodesy – InSAR

The following section includes excerpts, some verbatim, from several sources (Feigl et al., 2022b; Feigl et al., 2023; Feigl et al., 2024).

Interferometric Synthetic Aperture Radar (InSAR) data also measures ground deformation. The data set includes InSAR data collected by several satellite missions. The ERS-1/2 missions operated by the European Space Agency acquired image data covering San Emidio over two distinct time intervals 1992 to 2001 and 2003 to 2010, respectively (Eneva et al., 2011). These authors found relative rates of line-of-sight (LOS) displacement of the order of 5 mm/year at locations near the power plant at San Emidio. Assuming that the motion is purely vertically downward (subsidence) and dividing by the cosine of the incidence angle (~23°), we infer that the rate of vertical displacement is approximately 5.4 mm/year with respect to a location outside the geothermal field. By modeling the same two data sets, Reinisch et al. (2019) conclude that the rate of deformation was constant between 1992 and 2010.

A second InSAR data set consists of radar images acquired monthly beginning in 2019 by the TerraSAR-X (Pitz and Miller, 2010) and TanDEM-X (Krieger et al., 2007) satellite missions operated by the German Space Agency (DLR). To analyze these data, we have developed a high-throughput workflow using HT-Condor (Reinisch, 2018a; Reinisch, 2018b)to apply the GMT-SAR processing software (Sandwell et al., 2011; Sandwell et al., 2016).

We are also analyzing InSAR data from the SENTINEL-1 satellite mission (Salvi et al., 2012)operated by the European Space Agency (ESA). These data sets cover the site from late 2014 through the present. For the data acquired by the SENTINEL missions, we use the geocoded interferograms (standard InSAR displacement – GUNW – products) calculated by the Advanced Rapid Imaging and Analysis (ARIA) project (Bekaert et al., 2019).

To analyze the interferometric pairs as time series of displacement, we use the Miami INsar Time-series software in PYthon (MintPy) workflow (Yunjun et al., 2019). Figure 40, Figure 41, and Figure 42 show maps of the vertical displacement estimated from InSAR for three data sets acquired by the Sentinel-1 mission at different dates between 2016 and 2023. Each of the three data sets shows relative subsidence (blue colors) faster than 3 mm/year in absolute value in three areas:

Area A: Near the center of the geothermal field near GPS station SEMN (mapped as a yellow square), the deformation field shows a 3-km-by-2-km lobe of subsidence with a maximum rate of downward vertical displacement of ~5 mm/year in absolute value.

Area B: In the northwest corner of the map, deformation field shows a circular area approximately 1 km in radius where the maximum rate of downward vertical displacement is ~10 mm/year in absolute value. This feature is located within a kilometer of a circular "pivot sprinkler" irrigation system. We interpret the deformation as subsidence resulting from pumping groundwater from a shallow aquifer. Area B is not covered by the GEOS modeling.

Area C: Over the dry lake bed ("playa") to the west of GPS station SEMN, we see a lobe of subsidence centered at (X,Y) = (7, 16) [km]. Here, the displacement rate is significantly different from zero with 99% confidence only in Figure 40 and Figure 41.

Before attempting to simulate these observations quantitatively, we consider four possible interpretations.

In the first interpretation, the subsiding "bowls" observed near the irrigation system (Area A) and geothermal wells (Area B) are related to pumping fluids into or out of the wells. To explain the observed subsidence in Area B over an area roughly ~2 km in diameter, however, would require a "sink" that shrinks in volume at a depth of the order of a kilometer. Whether the volumetric contraction is due to the hydro-mechanical (H-M) processes or thermo-mechanical (T-M) processes is a question that we begin to address using numerical modeling below.

In the second interpretation, the signatures observed in the InSAR data could be related to changes in soil moisture (e.g., Zan et al., 2015; Ansari et al., 2017; Zheng et al., 2022). This effect could be pronounced on the dry lake bed (Area B) to the west of the geothermal field, where rainfall is rare. Considering a time series of Sentinel-1 data acquired near Bristol Dry Lake in the Barstow-Bristol Trough region of California, Zheng et al. (2022) write that "the bias time series of a pixel on the edge of the Bristol dry lake show clear correlation with precipitation and 'may' indicate the InSAR phase response to the drying process of soil after precipitation" (Zheng et al., 2022; emphasis theirs). Changes in soil moisture could affect the InSAR results near the agricultural fields around the circular irrigation system, as also noted around irrigated agricultural fields in the Imperial Valley of California (Gabriel et al., 1989).

In the third interpretation, the signatures observed in the InSAR results could be artefacts related to the time series analysis. In some cases, applying spatial averaging (so-called "multi-looking") to Synthetic Aperture Radar (SAR) images may cause a systematic bias in deformation modeling (e.g., Xu and Sandwell, 2020; Zheng et al., 2022).

In the fourth interpretation, the signatures observed in the InSAR data could be related to atmospheric effects. Heterogeneities in the atmosphere perturb the radar signals as they propagate along the "line of sight" between the sensor aboard the spacecraft in orbit to the ground and back again. As sketched by Massonnet and Feigl (1998) in their Figure 7, this effect produces a larger delay for a pixel located at a low elevation than for a pixel located at a high elevation. This effect has several nicknames, including "inverted barometer", "tropo-topo", and "height-correlation". To mitigate the effect of such atmospheric perturbations, we consider several different approaches. The first approach neglects atmospheric effects. In the second approach, we assume a horizontally stratified atmosphere, such that the delay is proportional to the difference in topographic elevation between two pixels in distinct locations. The algorithm (Berrada Baby et al., 1988) is implemented in MintPy with the "height_correlation" key word. The third approach uses weather data assimilated into meteorologic models from the European Centre for Medium-Range Weather Forecasts (ECWMF) to simulate the atmospheric delay. To trace rays through the atmospheric models, we use the Python based Atmospheric Phase Screen — PyAPS (Jolivet et al., 2015).

Which interpretation is correct? To address this question, we compare the InSAR results with time series of vector displacement at GPS stations. To minimize the effects of different reference frames, we consider differential displacement of GPS stations SEMN with respect to SEMS. To calculate the vertical component of displacement field from the InSAR results, we assume that the displacement is purely vertical. In other words, we divide the line-of-sight (LOS) displacements (and their rates) by the cosine of the incidence angle.

Figure 43 shows the time series of relative vertical displacement estimated from InSAR data for a pixel located near GPS station SEMN with respect to a pixel located near GPS station SEMS for InSAR data acquired in Sentinel-1 Tracks 64 and 42, respectively.

The time series of vertical component of displacement estimated from GPS data at station SEMN with respect to SEMS is also shown (identically) in each of these two panels. For the GPS data, we perform a weighted least-squares fit to estimate the rate of vertical displacement. For the InSAR data, we estimate the rate of vertical displacement using an unweighted least-squares fit as well as showing the average velocity estimated using MintPy. In each case, the quoted uncertainty in rate represents a formal estimate of one standard deviation scaled by the square root of the (weighted) mean squared error (WMSE). For Track 42, the rate of relative vertical displacement estimated from the InSAR data by MintPy is -7.5 ± 0.2 mm/year (downward). This estimate differs by less than 1 mm/year from the rate of -7.6 ± 0.4 mm/year estimated from the GPS data by a least-squares fit. For Track 144, the rate of relative vertical displacement estimated from the InSAR data by MintPy is -3.5 ± 0.1 mm/year (downward). This rate differs significantly from the rate estimated from the GPS data.

The quoted standard errors are formal. The procedure used to estimate the rate of vertical displacement from the GPS data does not account for temporal correlations between successive days of GPS measurements. Similarly, the procedure used to estimate the rate of vertical displacement from the InSAR data does not account for the correlation between two interferometric pairs that share a common acquisition date. These effects tend to increase the uncertainty of the estimated rates (e.g., Agram and Simons, 2015; Reinisch et al., 2016). The displacement rate of SEMN with respect to SEMS is –7.0 ± 2.3 mm/year estimated from the GPS data using the MIDAS robust trend estimator (Blewitt et al., 2016). Consequently, we consider that a more realistic estimate of the standard error of the vertical displacement rate is at least 2 mm/year.

We consider the InSAR results from Sentinel-1 Track 42 (Figure 40) to be the most reliable data set for interpretation because the rates of vertical displacement estimated from GPS agree more closely with the InSAR rates for Track 42 than for Track 64.

Which approach to mitigating atmospheric effects is most reliable? To address this question, we again compare the rates estimated from InSAR data to those estimated from GPS data. Figure 44 shows the comparison for each of the three approaches. The results using the height-correlation approach (-7.2 ± 0.2 mm/year, upper panel) insignificantly different from those estimated without accounting for atmospheric effects (-7.5 ± 0.2 mm/year, middle panel). The latter estimate differs by less than 0.1 mm/year from the rate of -7.6 ± 0.4 mm/year estimated from the GPS data by a least-squares fit. In contrast, however, using the PyAPS approach with meteorological data yields an estimated rate of 0.0 ± 0.1 mm/year (lower panel). Consequently, we consider only the displacement rate estimated without accounting for atmospheric effects in the subsequent interpretation.

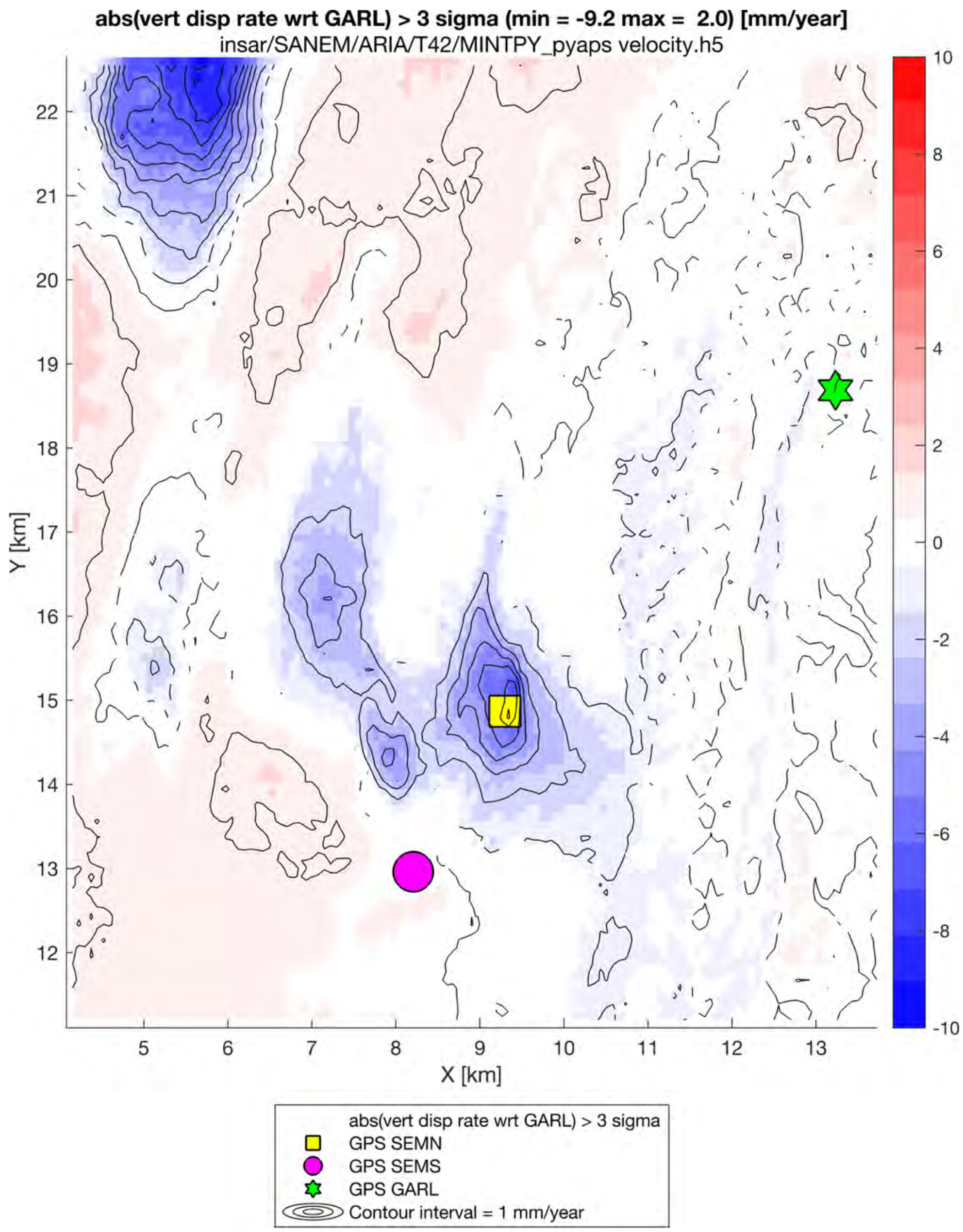

Figure 40. Map of the rate of vertical displacement estimated from InSAR data acquired between 2016 and 2022 by the Sentinel-1 satellite mission in Track 42. The rate of vertical displacement has been estimated using MintPy, neglecting atmospheric effects. The rates mapped in colors are referred to the median of the values for pixels located near GPS station GARL. Upward motion (relative uplift) appears as reddish colors, downward motion (relative subsidence) appears as blueish colors. Note the different color scales in each panel. Colors show only rates with an absolute value greater than 3 times their formal standard deviation. Symbols show GPS stations SEMS (yellow square), SEMN (magenta circle), and GARL (green star). Contour interval is 1 mm/year. Coordinates are in km with respect to an origin at UTM (Easting, Northing) = (286.924, 4457.967) [km].

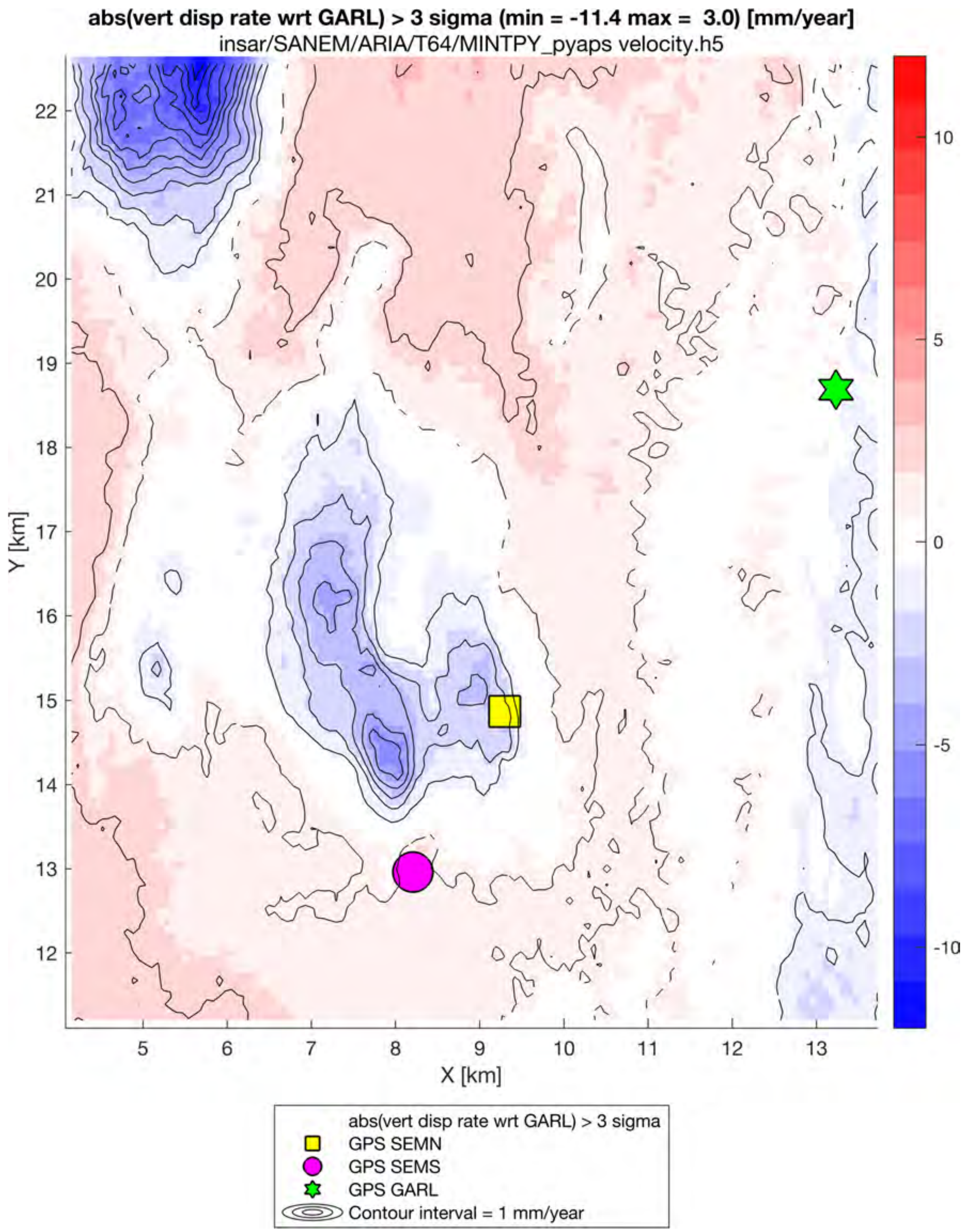

Figure 41. Map of the rate of vertical displacement estimated from InSAR data acquired between 2016 and 2022 by the Sentinel-1 satellite mission in Track 64. Plotting conventions as in previous figure.

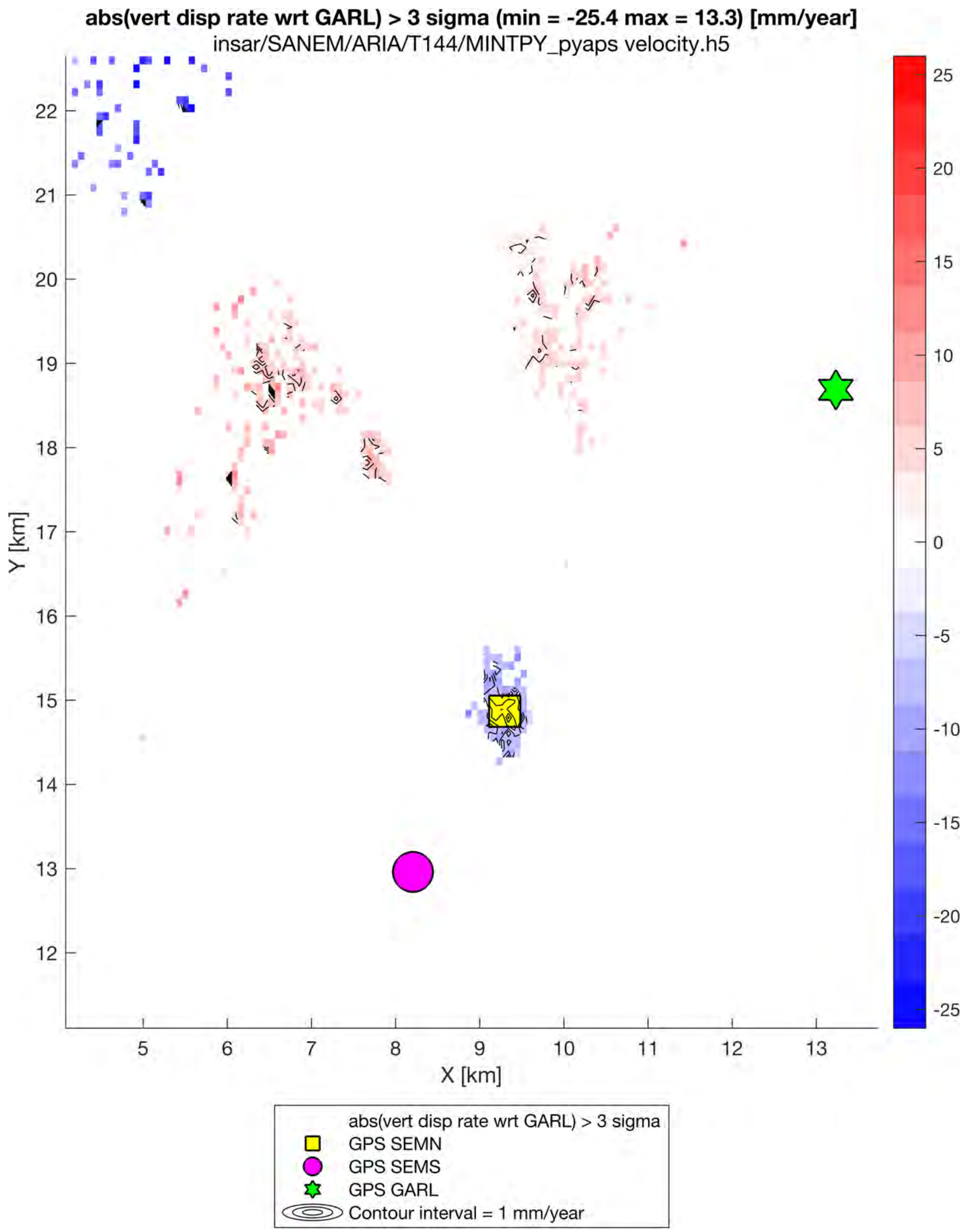

1145 *Figure 42. Map of the rate of vertical displacement estimated from InSAR data*
1146 *acquired between 2016 and 2022 by the Sentinel-1 satellite mission in Track 144.*
1147 *Plotting conventions as in previous figures.*

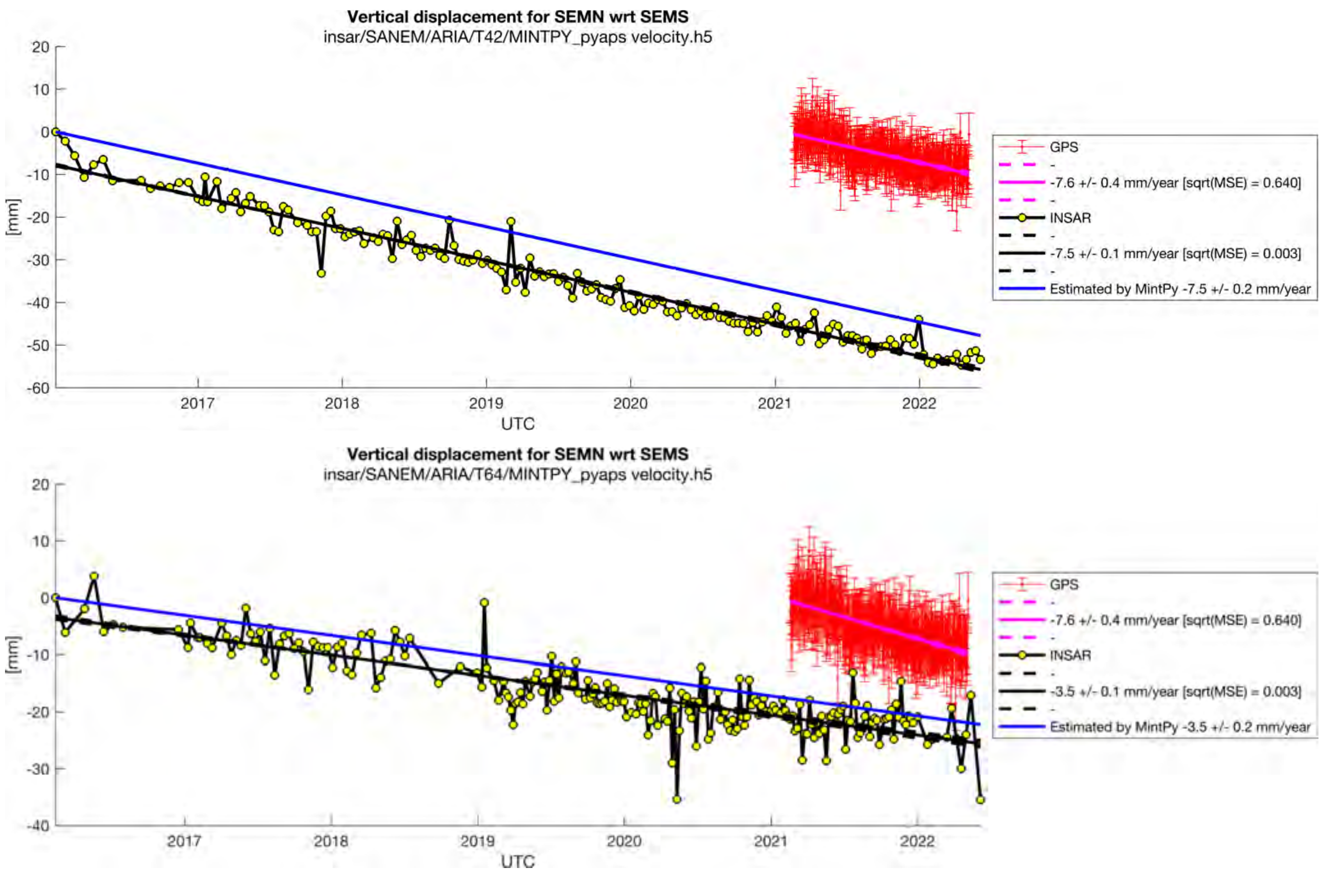

Figure 43. Time series of relative vertical displacement estimated from InSAR and GPS data for a point located near GPS station SEMN with respect to a point located near GPS station SEMS. The InSAR data were acquired by the Sentinel-1 satellite mission in Track 42 (upper panel) and Track 64 (lower panel). In each panel, the yellow circles connected by black line segments represented the displacement at the date of each InSAR acquisition. In each panel, the blue line best fit to the InSAR data estimated using unweighted least squares. The black line shows the rate of vertical displacement estimated from the InSAR data by MintPy, neglecting atmospheric effects. The red points with 1-σ error bars show the vertical component of displacement measured from GPS data analyzed by the Nevada Geodetic Laboratory at the University of Nevada-Reno (Blewitt et al., 2018; Kreemer et al., 2020). The magenta line shows the best fit to the GPS data estimated using weighted least squares. The GPS data and estimates are identical in both panels. The Y-intercepts of the GPS and InSAR data sets are arbitrary.

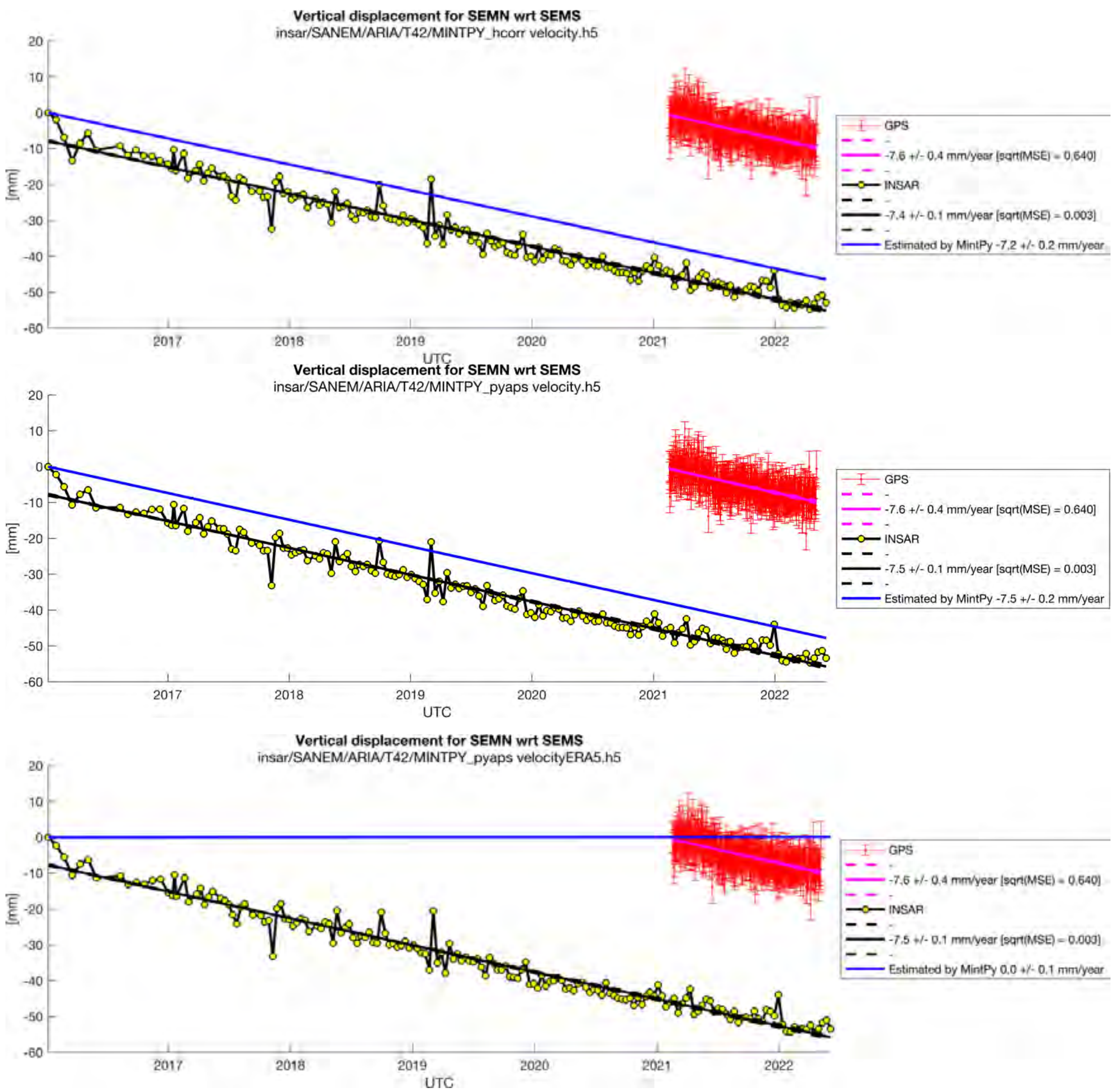

Figure 44. Time series of relative vertical displacement estimated from InSAR data acquired by the Sentinel-1 satellite mission in track 64 (yellow circles connected by black line segments). The three panels show results estimated using three different approaches for mitigating atmospheric effects: (upper panel) height-correlation; (middle panel) neglecting atmospheric effects, and (lower panel) PyAPS with meteorologic data. In each panel, the black line line best fit to the InSAR data estimated using unweighted least squares. The shows line shows the rate of vertical displacement estimated from the InSAR data by MintPy. The red points with 1-σ error bars show the vertical component of displacement measured from GPS data analyzed by the Nevada Geodetic Laboratory at the University of Nevada-Reno (Blewitt et al., 2018; Kreemer et al., 2020). The magenta line shows the best fit to the GPS data estimated using weighted least squares. The GPS data and estimates are identical in both panels. The Y-intercepts of the GPS and InSAR data sets are arbitrary.

Geodesy – GPS

Two continuously operating GPS stations, SEMS and SEMN, have been installed on monuments attached to idle wellheads within the geothermal field at San Emidio. GPS station SEMS was installed on the head of idle Well 17-21 at the southern edge of the geothermal field in January 2021 and then removed in April 2022. GPS station SEMN was installed on the head of idle Well 65C-16 near the power plant locate at center of the geothermal field in January 2021. The stations started collecting data on January 14 and February 17, 2021, respectively.

The last observations are from August 25 2024. Data completeness for SEMN is 99.31% and for SEMS it is only 48.43% because the original monument had to be removed after about one year due to nearby construction and was re-installed only two years later.

A third GPS station, named GARL, is located outside the geothermal area in the mountain range to the northeast of the power plant to provide a stable reference point.

At each station, raw GPS data are taken every 15 seconds. At the Nevada Geodetic Laboratory, we analyze the GPS data to calculate daily measurements of (relative) position coordinates in three dimensions that can be modeled as time series of displacement (Blewitt et al., 2018; Kreemer et al., 2020).

Time-series for SEMN can be found at:
http://geodesy.unr.edu/NGLStationPages/stations/SEMN.sta
Time-series for SEMS can be found at:
http://geodesy.unr.edu/NGLStationPages/stations/SEMS.sta
The SEMN and SEMS daily RINEX files have been posted at:
UNR: http://geodesy.unr.edu/magnet/rinex/ (up-to-date) and
UNAVCO data archive: https://data.unavco.org/archive/gnss/rinex/obs/

For this project, the position time-series of both stations are expressed relative to station GARL which is a very stable long-running GPS station in the mountain east of San Emidio. The position time-series are shown in Figure 45 and Figure 46.

Key metrics of SEMN and SEMS relative to GARL:
Average daily uncertainty (mm):
SEMN: 1.3 North, 1.0 East, 4.2 Up
SEMS: 1.3 North, 1.0 East, 4.1 Up
Velocity (mm/yr):
SEMN: 1.0±0.2 North, -4.7±0.3 East, -10.2±1.1 Up
SEMS*: 2.4±0.2 North, -2.0±0.2 East, -3.8±0.8 Up
RMS Repeatability (mm):
SEMN: 1.0 North, 1.5 East, 4.3 Up
SEMS*: 1.1 North, 1.7 East, 4.2 Up
* We accounted for an offset due to the dismantling and re-installation of the monument. Offset was estimated as part of the least-squares fit estimating the rate.

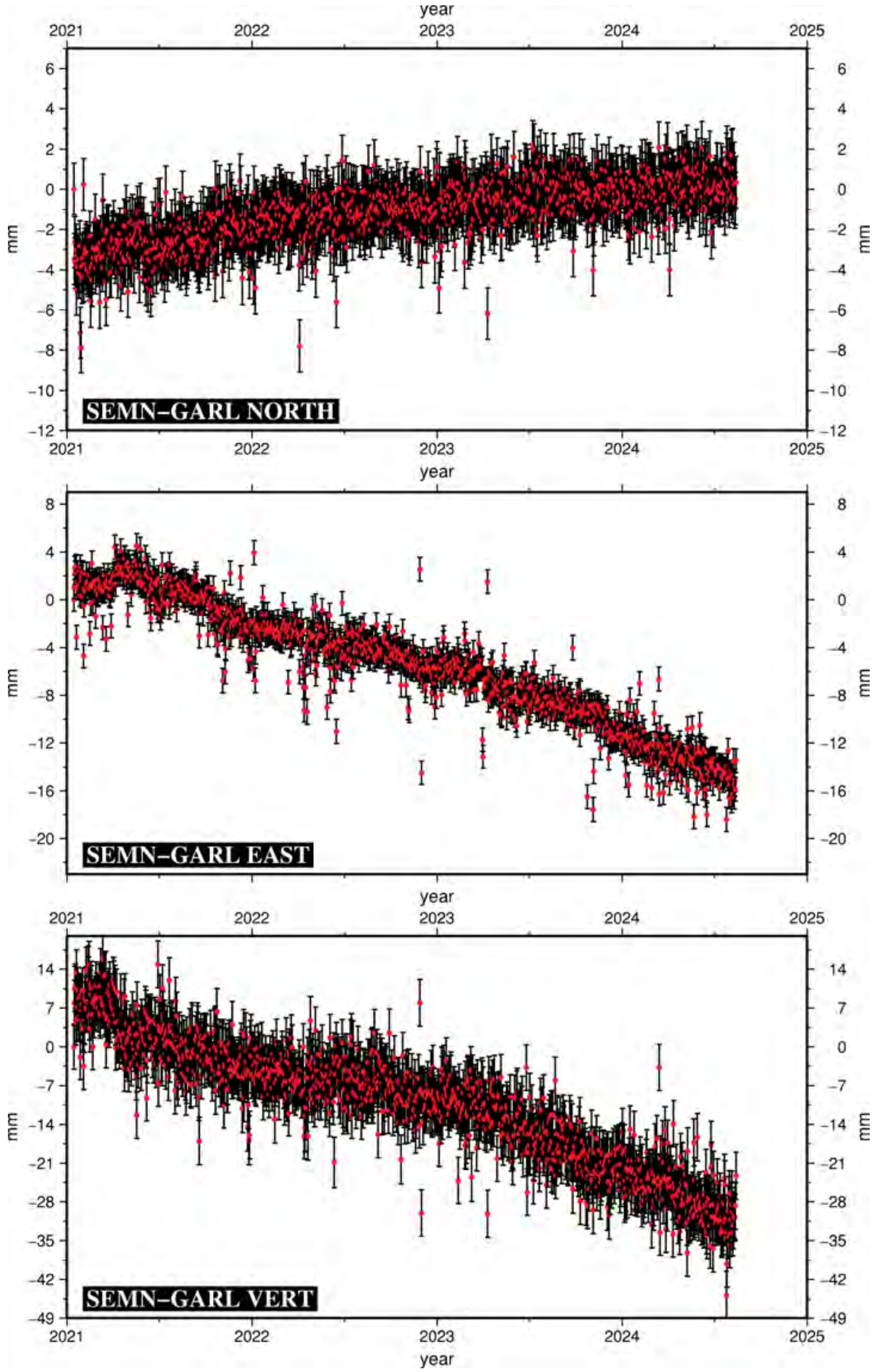

1218 *Figure 45. Time series of daily estimates of position of GPS station SEMN relative to*
1219 *GARL.*

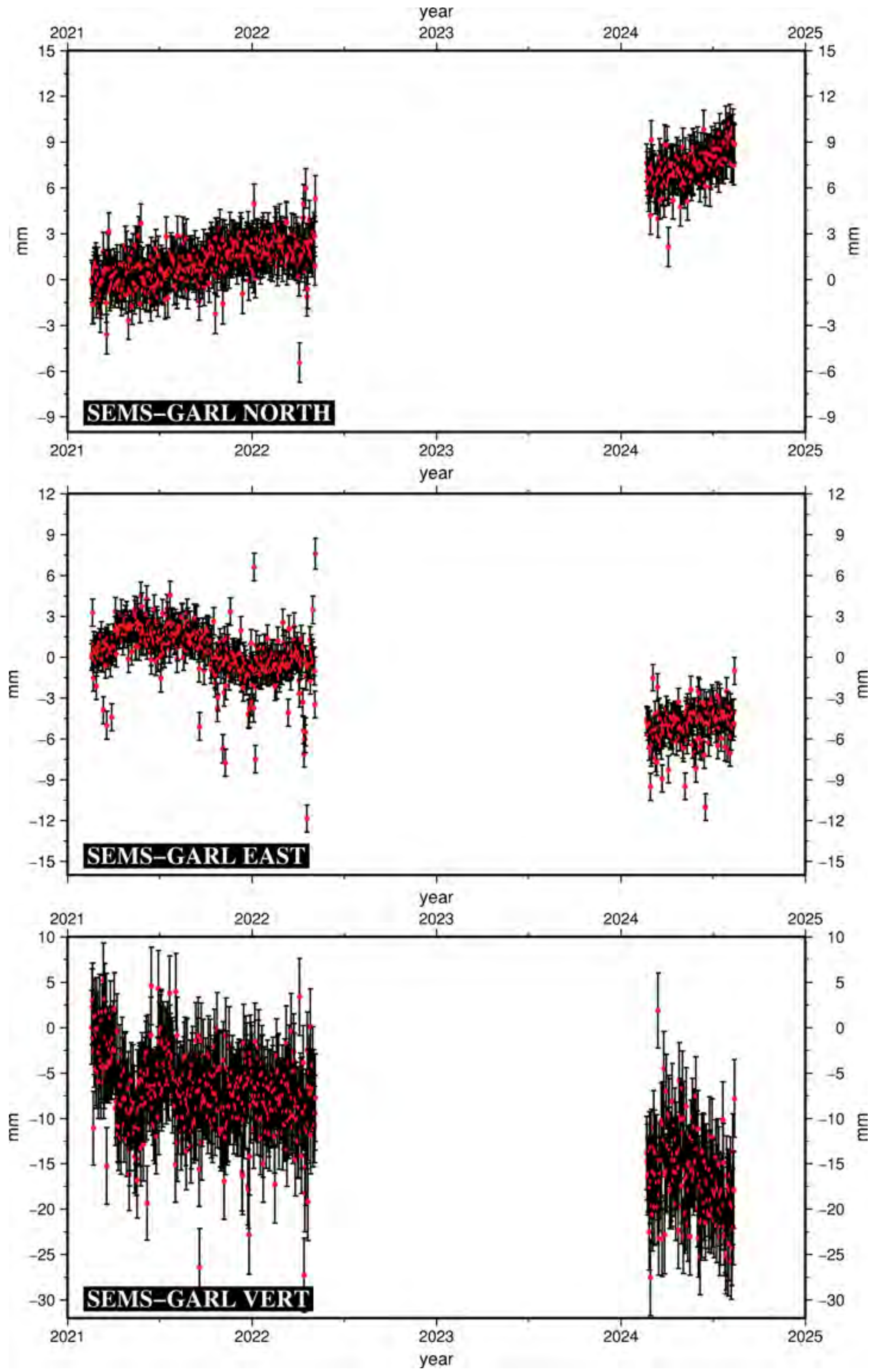

Figure 46. Time series of daily estimates of position of GPS station SEMS relative to GARL. Note that the monument at SEMS removed in 2002 and then re-installed in 2024, causing an offset. The offset is removed from the plot and was estimated as part of a least-squares fit estimating the rate.

Hydrology

The following section includes excerpts, some verbatim, from several sources (Cardiff et al., 2023).

Ormat has shared information with the project team, including well assemblies, current site operations and pumping rates, and a conceptual model that represents the 3-D geometry of the San Emidio system (Figure 8). We analyze the existing pumping test data from San Emidio, as provided by Ormat, to estimate spatially variable subsurface permeability. The geologic structural model contains the key stratigraphic units and fault structures identified via geologic and geophysical analysis of the region. We pursue multiple conceptual models for the dominant drivers of permeability variability through alternative parameterizations of subsurface structures represented in this model. Using the pumping test data sources, we perform forward modeling using the COMSOL Multiphysics finite element modeling platform, and estimate – through inverse modeling – the permeability of key geologic structures. The results of forward and inverse modeling are used to simulate pressure changes expected during plant shutdowns in 2016, 2021, and 2022. These pressure changes alter the effective stress on faults.

The geologic conceptual model of the subsurface provided by ORMAT was developed using the Leapfrog Geothermal software, and includes geometric elements that define key volumes (lithology), surfaces (faults and lithologic boundaries) and curves (wellbore profiles). Five key stratigraphic units are defined (Figure 47, left), as documented by Folsom et al.(2020) – from deepest to shallowest, they are: (1) Triassic and Jurassic Nightingale metasedimentary rocks (TrJn) consisting of phyllite, quartz, and marble; (2) Tertiary andesites and tuffaceous units (Tvu); (3) Tertiary basalt (Tpb); (4) Quaternary alluvial fill (Qal); and (5) Altered and silicified Quaternary alluvial sediments (Qas) that represent the shallow north-trending geothermal outflow zone (Rhodes, 2011; Rhodes et al., 2011; Folsom et al., 2020). Key faults that are thought to be important contributors to fluid flow in the region (Figure 47, right) are the San Emidio Fault (SEF) and Basin Bounding Fault (BBF), which were parameterized as permeable through all units except the Nightingale basement material (TrJn). This geologic conceptual model was imported into the COMSOL Multiphysics models and translated to the WHOLESCALE coordinate system described above.

Information provided by Ormat for each well at the site included the UTM coordinates at land surface, the total depth of drilling, and the range of depths over which the well is open to the surrounding formation (either via a perforated interval or open hole). For pumping tests performed in 2016 and 2017, flow rates at all pumping wells and pressure responses at a subset of site wells representing observation wells were provided. For site shutdowns, flow rate data from all operational (i.e., producing and injecting) wells was provided. A summary of the pressure data utilized is found in Table 10, and an example of the 2017 testing data is shown in Figure 48. Before importing into the COMSOL model, all pumping data was converted to mass estimates by assuming a fluid density for water at 100°C. Pressure change observations were baselined to assume zero pressure change before pumping changes began, and then resampled to hourly time steps.

Once all geometry, hydraulic forcing, and observational data were imported to COMSOL, the model domain was discretized using tetrahedral finite elements using COMSOL's automatic meshing routines. Several meshes were created, and the mesh used depended on the time period being simulated. For the experimental pumping tests, the mesh was refined near wells 17-21, 18-21, and 78-20 as these represented the location of pumping and thus the steepest expected head gradients. For later modeling of site shutdowns (described later), the mesh was refined in the vicinity of all operational wells. The mesh is conformal with the geologic boundaries shown in Figure 47, and is also refined in the vicinity of all operational wells to have a maximum dimension of 50 m.

After validating the numerical model through mass balances and other solution checks, the COMSOL model was used to perform inverse modeling for the internal permeability structure. Other model parameters – including stratigraphic unit porosity, effective matrix compressibility, fluid viscosity, fluid density, and fluid compressibility – were assumed constant, based on either prior site data or (where unavailable) literature estimates. Permeability was parameterized according to a series of alternative conceptual models, following the approach of multiple working hypotheses (Chamberlin, 1890). In conceptual model 1 (CM1), which is used as a baseline, the reservoir assumes a homogeneous, anisotropic permeability value throughout the region. For conceptual models 2 through 4 (CM2 – CM4), stratigraphic and structural permeability variations are successively included. In CM2, we estimated permeability values for each stratigraphic unit (TrJn, Tvu, Tpb, Qal, and Qas), along with a vertical anisotropy coefficient for all units (representing the ratio of horizontal to vertical permeability). In conceptual model 3 (CM3), an additional permeability value was added to represent the San Emidio Fault (SEF) as a fault plane with its own permeability and assumed fault zone of 1 m width. In conceptual model 4, we include both the mapped San Emidio Fault (SEF) and basin bounding fault (BBF) as units with their own defined permeability values, each also with 1-meter widths. All individual forward-run simulations required less than 10 minutes on a 2.5 GHz, 28-core Intel Xeon W computer with 96GB of RAM. At present, the model simulates fluid flow only, though COMSOL is capable of coupled thermal-hydraulic modeling.

All observations of pressure change during the 2016 and 2017 pumping tests were fit via inversion using nonlinear least squares. We minimized the least squares objective function using an iteratively linearized Gauss-Newton method, which approximates the objective function as quadratic in the vicinity of current parameter estimates (e.g., Aster et al., 2005). To ensure non-negativity of input permeability, all inverse modeling was performed on log-transformed parameter values, which were converted back into native units following convergence. During each inversion iteration, the elements of the model Jacobian matrix – representing the sensitivity of all simulated observations to all model parameters – were estimated via a finite difference method that successively altered each parameter by 30%. Iteration in the inversion included a line-search between current parameter estimates and the update step calculated via Gauss-Newton. Convergence was declared when the maximum relative parameter change was less than 0.1% or when the relative objective function change was less than 0.1% at the end of a linearization iteration. Full inversion runtimes for each conceptual model were several days each.

Different production and injection wells were operating during the 2016 site shutdown, and at larger flow rates than those recorded during the 2016 and 2017 pumping tests.

Results for all inversions are summarized in Table 10*: Testing data utilized within COMSOL finite element numerical model.*

	2016 Testing	2017 Testing	2016 Site Shutdown
Time Period Imported	2016-10-05 – 2016-10-13	2017-09-19 – 2017-09-27	2016-12-07 – 2016-12-15
Pumping Flow rates	17-21, 25-21	17-21, 18-21, 78-20	61-21, 75B-16, 76-16 (Production) 42-21, 43-21, 53-21 (Injection)
Pressure Observations	OW-6, OW-8, OW-9	OW-6, OW-8, OW-9, 25-21, 28-21, 45A-21	None

Table 11, including the root mean squared error (RMSE) misfit between hourly-resampled observations of pressure changes and model-simulated pressure changes. Analyses of data from periods when site operations do not change had an average standard deviation of 1.4 kPa; this value is thus assumed as a reasonable proxy for inherent "measurement error" associated with unmodeled processes including sensor noise, systematic drift, and secular signals including atmospheric temperature fluctuations that affect instrument response.

While overall RMSE for each model is of the same order of magnitude as sensor error, plots of drawdown curves for individual observation wells indicate potential structural errors in all conceptual models. For both the 2016 and 2017 pumping tests, pumping took place toward the southern end of the wellfield. Field data indicates that pressure response at northern well OW-6 was similar in magnitude and timing to pressure response at well 28-21 in the south (Figure 49). Another northern well, OW-8, experienced very small pressure variation despite its proximity to OW-6. All inverse modeling results, however, simulated small pressure changes at northern well OW-6. These observations taken together suggest that flow conduits connecting the southern field to OW-6 at its open interval may be present that are currently not represented in the geologic conceptual structure.

All heterogeneous conceptual models show improvement in reducing data misfit relative to the homogeneous base case (CM1). Though it does not include any fault-based permeability, CM2 is consistent with other observations from prior studies at San Emidio, including: (1) Qas (silicified alluvium) has been previously identified as unit that likely has substantial permeability relative to other basin-fill materials; and (2) the permeability anisotropy ratio of approximately 3 for all geologic units is within a reasonable range for natural sediment and rock formations.

In contrast, CM3 includes the San Emidio Fault (SEF) and estimates high permeability for this feature, but: (1) Qas is optimized as having lower permeability than surrounding materials, which is not consistent with other observations; and (2) The anisotropy ratio, which implies a >1000-fold decrease in vertical hydraulic conductivity, is significantly more extreme than even those observed in shales over a range of pressure conditions (Bhandari et al., 2015; Pan et al., 2015).

Finally, CM4 includes both the San Emidio Fault (SEF) and Basin Bounding Fault (BBF) as separate permeable units. This conceptual model is able to obtain a similar level of misfit to CM2 and CM3, and we deem this model to be more plausible than CM3 due to: 1) a high permeability estimated for Qas, as in CM2; and 2) A more reasonable estimated anisotropy ratio.

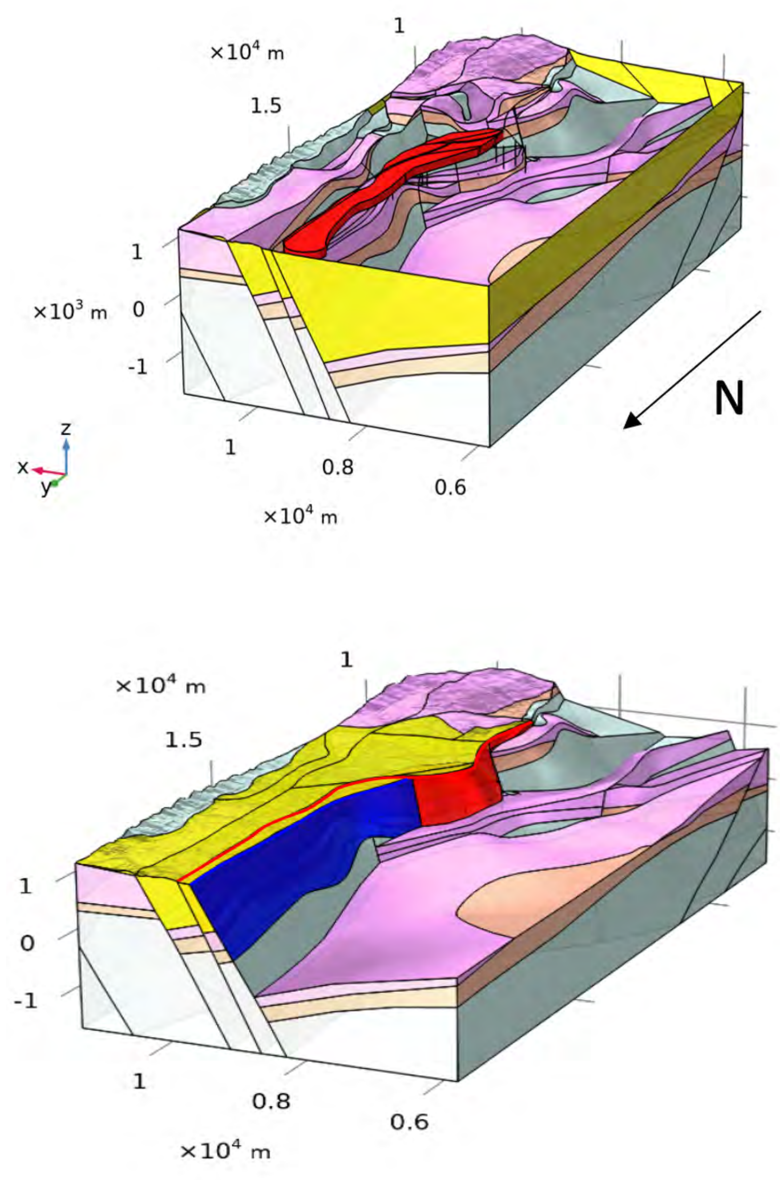

Figure 47. Two views of geologic conceptual model (camera is from the northwest) provided by Ormat. Upper panel: Stratigraphic geologic units are from top to bottom: Qal (yellow, with land surface removed), Qas (red), Tbp (pink), Tvu (orange) and TrJn (teal). Lower panel: Fault planes considered as permeable segment SEF (red) and BBF (blue).

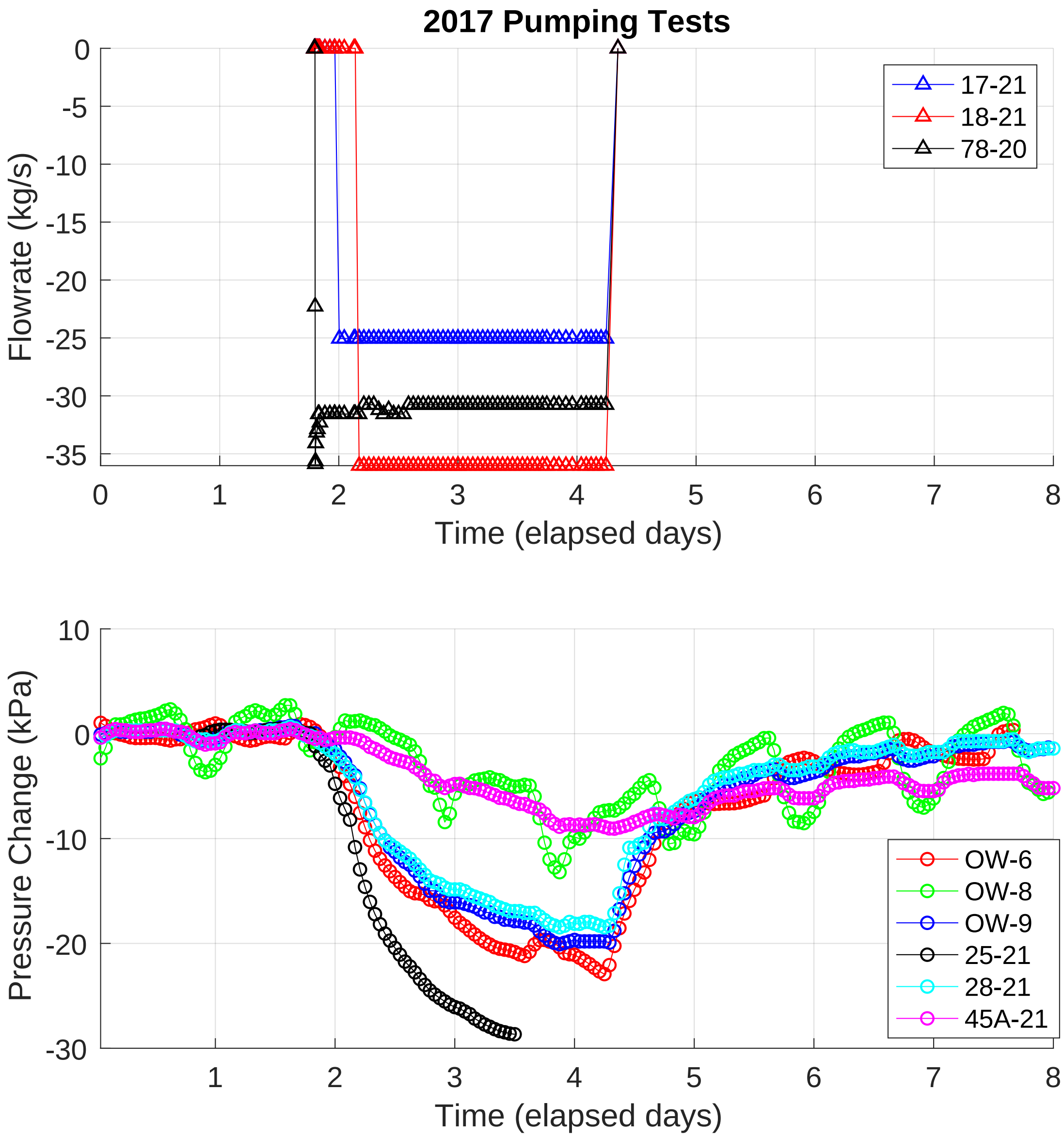

Figure 48. 2017 flow rate (positive flowrate is injection, negative is production) and pressure data provided by ORMAT, after units conversion and baselining. Elapsed days are days after 2017-09-19.

Table 10: Testing data utilized within COMSOL finite element numerical model.

	2016 Testing	**2017 Testing**	**2016 Site Shutdown**
Time Period Imported	2016-10-05 – 2016-10-13	2017-09-19 – 2017-09-27	2016-12-07 – 2016-12-15
Pumping Flow rates	17-21, 25-21	17-21, 18-21, 78-20	61-21, 75B-16, 76-16 (Production) 42-21, 43-21, 53-21 (Injection)
Pressure Observations	OW-6, OW-8, OW-9	OW-6, OW-8, OW-9, 25-21, 28-21, 45A-21	None

Table 11: Results of inverse modeling from all 4 conceptual models.

	*CM1**	*CM2*	*CM3*	*CM4*
RMSE Misfit $[kPa]$	5.8	5.2	5.3	5.3
Qal $k_x [m^2]$	2.9×10^{-12}	1.5×10^{-13}	1.9×10^{-13}	1.5×10^{-13}
Qas k_x $[m^2]$	2.9×10^{-12}	6.2×10^{-11}	5.0×10^{-15}	4.3×10^{-11}
Tpb k_x $[m^2]$	2.9×10^{-12}	1.3×10^{-13}	2.0×10^{-13}	1.7×10^{-12}
Tvu k_x $[m^2]$	2.9×10^{-12}	5.2×10^{-11}	1.4×10^{-10}	2.4×10^{-11}
TrJn k_x $[m^2]$	2.9×10^{-12}	4.4×10^{-14}	4.4×10^{-14}	3.1×10^{-14}
Anisotropy kx/kz	2.0	3.5	1,300	140
SEF k $[m^2]$	–	–	1.7×10^{-10}	4.4×10^{-11}
BBF k $[m^2]$	–	–	–	3.7×10^{-9}

*Permeability for all stratigraphic units (Qal, Qas, Tpb, Tvu, TrJn) was estimated as a single parameter in CM1

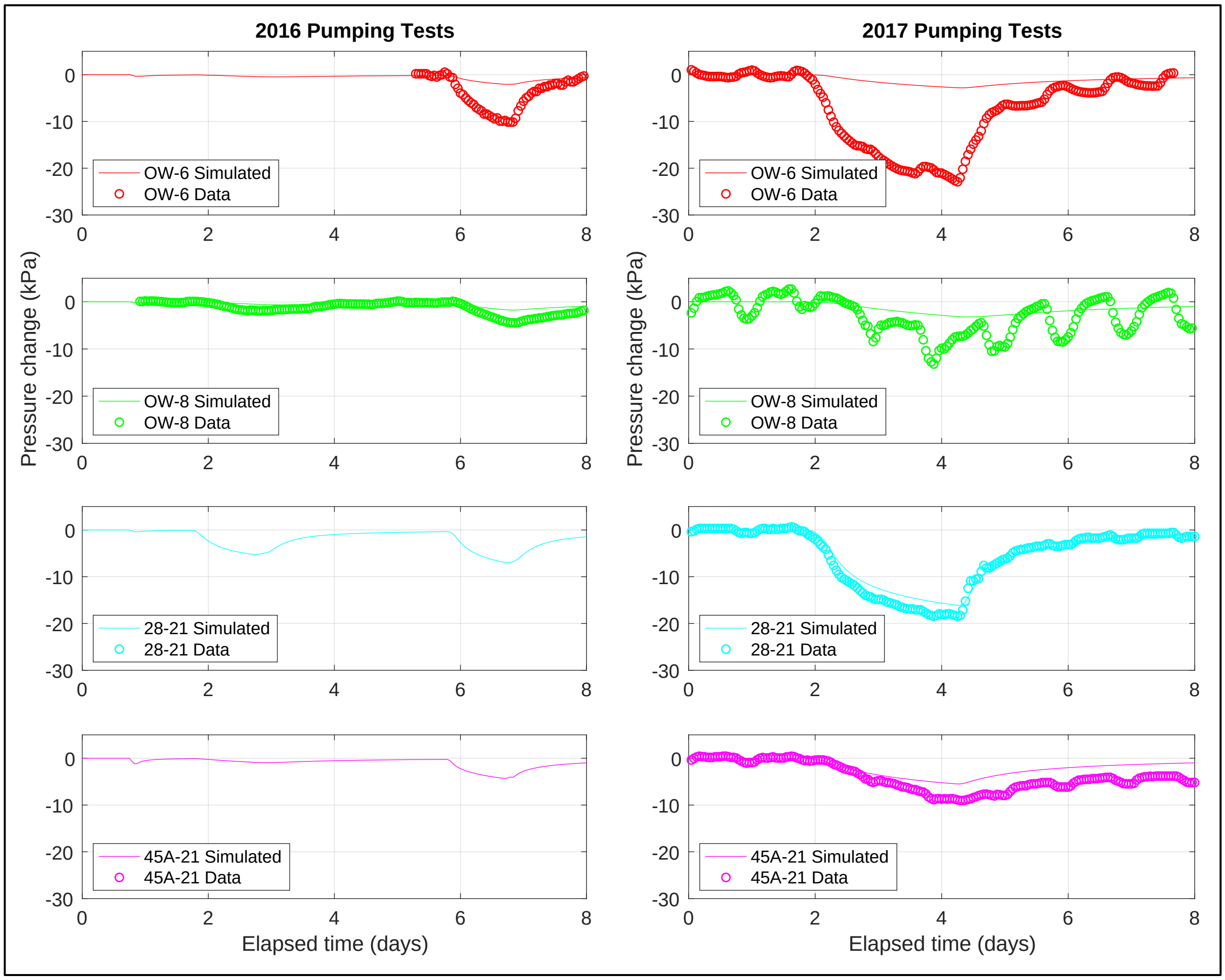

Figure 49. Simulated pressure changes from CM2 (lines) and resampled pressure observations (symbols) for subset of pressure data from 2016 and 2017 pumping experiments. Impacts from atmospheric temperature fluctuations on observations is prominent in 2017 OW-8 observations. Elapsed days represent days after start of time period described in Table 1.

2016 Shutdown (~100 Events)

The following section includes excerpts, some verbatim, from several sources (Feigl et al., 2023; Guo et al., 2023; Thurber et al., 2024)

Increases in microseismicity (magnitude less than 3) have been associated with the temporary cessation of pumping at production wells in geothermal fields. This phenomenon was recently reported at the Brady Hot Springs geothermal field, Nevada, USA (Cardiff et al., 2018). The basic hypothesis is that fluid extraction during normal power plant operation inhibits fault slip by reducing pore pressure (P_p) and thereby increasing the effective normal stress on faults, whereas short-term cessations of production promote fault slip by increasing P_p and decreasing the effective stress. Similar correlations between microseismicity and production pumping cessation during planned shutdowns have also been observed at the Kakkonda geothermal field, Japan (Tosha et al., 1998), the Blue Mountain geothermal field, Nevada, USA (Templeton et al., 2017; Gonzalez et al., 2022), and the San Emidio geothermal field, Nevada, USA (Warren et al., 2018; Feigl et al., 2022, 2023).

In December 2016, a dense passive seismic array was deployed at the San Emidio geothermal field for about one week and 123 microseismic events (MSEs) were detected by Warren et al. (2018) (Figure 50). Temporal evolution of the MSEs shows a substantial increase in microseismicity during a ~20-hour-long shutdown of pumping at all production and injection wells (Figure 50 & Figure 51). A majority of the MSEs occurred adjacent to two production wells in the northeastern part of the seismic array (Figure 50), suggesting a direct connection between the MSEs and the cessation of pumping at the production wells.

To understand the spatial distribution and temporal evolution of the stress field at San Emidio, the WHOLESCALE project began in 2020 (Feigl et al., 2022). As a part of the WHOLESCALE project, we have performed a detailed analysis of the 2016 December microseismic event data set developed by Microseismic, Inc., including: (1) determining high-precision hypocentral locations, magnitudes, and focal mechanisms for observed MSEs; (2) developing a P-wave tomographic velocity model; (3) inferring a local stress tensor for the site with focal mechanisms. In this study, we present our seismic and stress analysis results that advance the characterization of material properties, distribution of seismically active faults/fractures, and stress state in the reservoir. In the following sections, we first briefly introduce the geologic setting and operation history at San Emidio, the 2016 seismic data set, and the methodology of our analysis, and then present and discuss our results.

Several geophysical surveys have been performed in the field to investigate the subsurface structure (e.g., Warren et al., 2018; Folsom et al., 2020). Warren et al. (2018) mapped geothermal permeability using a passive seismic emission tomography method. Folsom et al. (2020) performed a 3-D inversion of magnetotelluric (MT) data. They also forward-modeled gravity data informed by geology, drilling, MT, and other results. Their results helped them to construct a conceptual block model of the subsurface including the 3-D distribution of fault surfaces and inferred stratigraphic contacts.

From 2016-12-08 19:33 to 2016-12-09 15:00 UTC, the San Emidio power plant was shut down for 19.45 hours for maintenance (dark gray shading in Figure 51a). There are three vertical production wells and three vertical injection wells (red and blue triangles in Figure 50), which all stopped operating during the shutdown, except for a short resumption (Figure 51b). A dense passive seismic array with 1,302 vertical-component seismographs, spaced approximately 80 m apart, was deployed at San Emidio during December 5-11, 2016 (Figure 50) (Lord et al., 2016a; Lord et al., 2016b; Warren et al., 2018). The primary aim was to advance the characterization of permeability using passive seismic emission tomography (PSET), a back-projection type technique (Sicking et al., 2012; Warren et al., 2018). In addition, 123 MSEs were detected, most of which were located within the northeastern part of the seismic array (Figure 50) (Warren et al., 2018). In addition to the MSEs, one string shot on December 8, 2016 was also recorded by the seismic array (Figure 50).

We cut event waveforms for the MSEs in the catalog of Warren et al. (2018) and the string shot, which were then processed by removing the mean and trend. We then performed bandpass filtering between 5 and 50 Hz based on the visual inspection of signal-to-noise ratio (SNR) from the spectra of several events. We picked P-wave arrivals for the catalog events using an automatic arrival picking code (Guo et al., 2018), which is based on Akaike Information Criteria (Maeda, 1985). The arrivals were picked within preset time windows, which are 0.6 s before and 0.6 s after the theorical arrivals calculated with the catalog locations and an existing velocity model from Warren et al. (2018). For each arrival pick, we scored its quality based on the SNR (the ratio of the root-mean-square amplitudes of the phase and noise windows). After picking arrivals, we removed the MSEs that had few or bad picks or had picks with large azimuth gaps, leaving 110 MSEs and one string shot to be used for the following analysis.

To estimate the magnitudes of the seismic events, we calculated the coda duration magnitude (M_c), a common approach for small seismic events (e.g., Lee et al., 1972; Herrmann, 1975). We followed the approach used by the University of Utah Seismograph Stations (Pechmann et al., 2006; Koper et al., 2020). We first took the envelope for each successfully picked waveform. The logarithm of the waveform envelope was used for coda windowing, starting near the maximum amplitude after the theoretical S-wave arrival and ending at twice the pre-P noise level. We then linearly fit the windowed coda and defined the duration as the time of the end of coda (when the best-fit line fell below a fixed cutoff value) minus the P-wave arrival time. Defining coda duration relative to a fixed cutoff value, instead of relative to the pre-P noise level, can mitigate the influence of temporal variations in ambient seismic noise (Koper et al., 2020), e.g. day versus night and during shutdown versus before and after shutdown. The fixed cutoff value we used is the median value of the pre-event noise levels during shutdown, which were calculated as the mean of the log10 envelope of the noise window within 1 s before P-wave arrival on each station for each event. The station magnitude M_c was then calculated based on the empirical magnitude-duration formula:

$$M_c = 2.65 \log_{10}(\tau) - 1.7 \quad (3)$$

where τ is duration in seconds. This formula is used by the Nevada Seismological Laboratory for the Nevada region. The final event magnitude was defined by taking the median of the M_c values from at least three stations. We successfully calculated magnitudes for 91 of our relocated events, which are all very small ranging from –2.2 to 0, as shown in Figure 51a and Figure 52a–b.

We relocated catalog events and determined a 3-D model of P-wave velocity (V_p) using the triple-difference seismic location and tomography algorithm tomoTD (Guo & Zhang, 2017; Guo et al., 2021). tomoTD is an arrival-time based tomography technique that was modified from the double-difference tomography algorithm tomoDD (Zhang & Thurber, 2003, 2006). The tomoTD algorithm is able to combine absolute arrival times with station-pair, event-pair, and double-pair differential arrival times to invert for event locations and a 3-D velocity model simultaneously. The three types of differential time data have their respective advantages in determining event locations and velocity model (Guo & Zhang, 2017; Guo et al., 2021). The station-pair differential time data from an event to pairs of stations are more sensitive to absolute event locations and the velocity model beneath the stations. The event-pair differential time data from pairs of events at a station are more sensitive to relative event locations and the velocity model of the source region. The double-pair differential time data from pairs of events at pairs of stations have similar benefits as the event-pair data but can further remove the effect of origin time errors. tomoTD solves a linearized inversion system, which is stabilized by damping and smoothing constraints.

We constructed event-pair, station-pair, and double-pair catalog differential time data from our picked absolute arrival times (note that our picked arrival time data are called catalog data). Constructing event-pair and double-pair catalog differential time data relies on relative locations between events. Since the relative event locations are not well constrained in the original catalog, we first conducted a preliminary inversion to improve the event locations and then used the event relocations to reconstruct the differential time data. We also measured P-wave waveform cross-correlation (WCC) differential times from pairs of events separated by 1 km or less, following the time-domain WCC method of Schaff et al. (2004). The measurements with WCC coefficients below 0.7 were discarded. The event-pair WCC differential time data were used to construct the double-pair WCC differential time data. In total, our final input P-wave data set includes 34,008 absolute arrivals, 1,092,974 station-pair catalog differential times, 247,856 event-pair catalog differential times, 554,912 double-pair catalog differential times, 103,847 event-pair WCC differential times, and 382,107 double-pair WCC differential times.

Our tomographic inversion uses the Universal Transverse Mercator (UTM) coordinate system and has a velocity model grid spacing of ~0.2-0.3 km in the Easting, Northing, and vertical directions in the regions where there are event and station coverage. We started from the catalog event locations and the V_p model from *Warren et al.* (2018). As mentioned previously, the catalog events were detected and located using PSET, a beamforming type technique (*Warren et al.*, 2018). The V_p model of *Warren et al.* (2018) was guided by one seismic imaging profile along an active-source line at a Northing of ~4471.7 km and modified to fit the arrivals of downhole string shot data.

We selected the optimal smoothing by testing a range of smoothing values and chose the one that balanced the model smoothness and data residual reduction. We selected the damping value to constrain the condition number of the inversion within a reasonable range around 100-200. After the inversion, the root-mean-square (RMS) data residual decreased from 0.128

s to 0.079 s for the catalog data and from 0.096 s to 0.031 s for the WCC dt data. We performed bootstrap analysis, a statistical method (Efron and Gong, 1983; Efron and Tibshirani, 1986), to estimate event location uncertainties following *Guo and Zhang* (2017). We conducted noise-free and noise-added checkerboard tests with varying checkerboard sizes to assess model resolution. At shallow depths (above 0.8 km elevation), the model is well resolved in the northern and central parts of the study area, whereas at greater depths (below 0.8 km elevation) only the seismically active region in the northeastern part is well resolved.

After the inversion, 106 of 110 events are relocated successfully. Figure 53b shows the horizontal and cross-section views of our relocations, which are much more concentrated compared to the catalog locations shown in Figure 53a. Most events are within 600 m to the northwest of the two northern production wells. On the E-W cross-section, event relocations generally dip to the west and the majority are between 0.4 and 0.85 km elevation. The main seismicity cluster at ~296 km Easting, ~4473 km Northing, and ~0.4-0.6 km elevation forms a westward dipping lineation with ~60° dip angle, which we consider to be reliable given the small location uncertainty estimates represented by the crosses in Figure 53b. There are only 2 events located near the injection wells.

Figure 54 and Figure 55 show the depth slices and cross-section of our new V_p model. Note that in Figure 54 and Figure 55c, we show the V_p model perturbation in percentage relative to the 1D model calculated by averaging velocities at each depth. The well-resolved parts of the model as estimated by the resolution tests are outlined. It is noteworthy that the initial model embodies some large-scale structure features, including the velocity contrast on the two sides of the Range Front fault at an Easting of ~297.5 km and the stair-step (half-graben) structure going from east to west. Compared to the initial model, our new model refines the shallow structure beneath the seismic array and the structure of the seismically active parts of the reservoir (Figure 54, Figure 55b), as suggested by the resolution tests. The velocity contrast characterizing the range front at an Easting of ~297 km becomes sharper and more continuous from north to south (Figure 54).

The SEF, Piedmont Fault (PF), and Basin Bounding Fault (BBF), along which the geothermal reservoir is developed, are associated with low-velocity anomalies at 0.3-0.8 km elevation (Figure 55-c). The SEF and PF are delineated by a strong velocity contrast from high velocity on their eastern side to low velocity on their western side (Figure 55b). To the west of the PF and SEF, there is a zone from ~1.8 to ~3.3 km distance along the AA' profile at 0.3-0.8 km elevation, as outlined in Figure 55c, with negative velocity perturbations as low as –25%, much lower than the zone just above. The BBF cuts through this extremely low-velocity zone. It is also located to the west of the production wells 75B-16 and 76-16 (note the perforated sections of the wells are in contact with PF and SEF) (Figure 55b-c). All the events to the northwest of wells 75B-16 and 76-16 occurred on the BBF and in the area between the PF and BBF, which are contained within this low velocity zone (Figure 55a-c). The other MSEs are distributed in the low-velocity zone bounded and/or crossed by the BBF, SEF, PF, and NWF and tapped by the nearby production wells, except for a few deeper events to the west of the BBF (Figure 55b-c). Figure 56 zooms in our MSE relocations and V_p model in the region where the main seismicity cluster and all the MSEs before plant shutdown and after plant restart occurred. Most MSEs before shutdown and after restart occurred in a very localized zone at the top of the seismicity cluster, which is associated with lowest V_p values (2.8-3.0 km/s).

We computed first-motion focal mechanisms for catalog MSEs using the HASH algorithm (Hardebeck and Shearer, 2002). P-wave first-motion polarities were automatically identified for our arrival picks using a method similar to that of Chen and Holland (2016). This was done by first searching for a local maximum or minimum after the arrival pick and then calculating the signal-to-noise ratio (SNR). The SNR values were then used to decide which polarity picks to be used. In general, higher SNR thresholds eliminate more wrong polarity picks at the cost of losing more correct polarity picks, whereas smaller SNR thresholds provide more polarities but include more incorrect polarities. After testing a set of SNR thresholds, we set the threshold value to SNR=5. This value yields the most high-quality focal mechanisms while providing relatively small fault plane uncertainties.

HASH searches for a set of acceptable focal mechanisms for each event, accounting for possible errors in earthquake locations, velocity model, and polarity observations. We input azimuth and takeoff angle computed with our final relocations and 3-D V_p model. The average of the acceptable mechanisms is the preferred mechanism and the uncertainty is calculated based on the distribution of acceptable mechanisms. Kilb and Hardebeck (2006) found that the average of the fault and auxiliary plane uncertainty was the best indicator of mechanism quality, with values less than 35° indicating the best mechanisms. We defined quality A and B mechanisms such that the average fault plane uncertainty is less than 25° and 35°, respectively.

One concern regarding focal mechanism inversion is whether the station polarities sample the focal sphere well, depending on the event depth and station distribution. In general, the polarities are well distributed on the focal sphere for the high-quality mechanisms. Owing to the wide distribution of stations compared to the very shallow depths of events, P waves recorded on the stations near event epicenters leave sources in the upward direction whereas for the ones recorded on the stations far from the event epicenters they leave sources downward. Thus, the upgoing and down-going ray paths sample the focal spheres well. Most of the polarities locate in the expected quadrants although there are some misfits. The misfits are likely due to a combination of error sources: (1) incorrect polarity picks; (2) the assumption of pure double couple mechanism, which may not be appropriate for all the events; (3) errors in the inverted focal mechanisms. We tried higher SNR thresholds to exclude more wrong polarity data at the cost of losing more correct data but the inverted focal mechanisms are not significantly changed.

Figure 57a and Figure 57b show our high-quality focal mechanism results for 36 events (3 quality A and 33 quality B), from which we identified two clusters (C1 and C2) with at least 10 mechanisms. Most events are dominated by normal slip but also show strike-slip components except for the events in C2, many of which are dominated by strike slip (Figure 57b). The orientations seen from the focal mechanisms have a large variability, but appear more similar among each individual cluster, especially C1 and C2. Figure 57c-e enlarge C1 and C2. The events in C1 are dominated by normal slip with strike and dip angles generally consistent with the seismicity lineation (Figure 57c-d). The events in C2 form an elongated zone striking NNE and one of the nodal planes for each strike-slip event is generally aligned in a similar direction (Figure 57e).

We estimated the stress-field orientation from the focal mechanisms using the MSATSI algorithm (Martínez‐Garzón et al., 2014a) which is based on the SATSI algorithm (Hardebeck and Michael, 2006). MSATSI is a robust, linearized method that uses damped least-squares optimization to invert for the principal stress axis orientations and the ratio *R* of their relative magnitudes:

$$R = (\sigma_1-\sigma_2)/(\sigma_1-\sigma_3) \quad (4)$$

where σ_1, σ_2, and σ_3 represent the maximum, intermediate, and minimum principal stresses, respectively. The bootstrap resampling method is applied to the input focal mechanism data for estimating uncertainties. Figure 58 shows the stress inversion results, including the final stress tensors (Figure 58b, d, f) and 1,000 bootstrap solutions Figure 58a, c, e), using all high-quality (quality A and B) focal mechanisms (Figure 58a-b) and the mechanisms in C1 (Figure 58c-d) and C2 (Figure 58e-f) only. The other clusters are not analyzed separately due to the limited mechanisms available.

The entire northeastern part of the seismic array where the focal mechanisms are located (Figure 57a) shows a normal faulting dominated stress regime (Figure 58b). The fairly concentrated solutions from the bootstrap inversions for each principal stress direction indicate the robustness of the final solution (Figure 58a). The stress tensor is generally aligned with the geometry of the normal faults SEF, BBF, and PF in the northeastern part of the seismic array (Figure 57a and Figure 58a-b): σ_1 is essentially vertical, σ_2 is close to horizontal and trends north-south, parallel to the strike of those faults, and σ_3 is close to horizontal and trends east-west, normal to the strike of those faults. The R value is 0.44. As noted by *Jahnke et al.* (2023), this overall reservoir stress state is consistent with other stress indicators, including the World Stress Map (Heidbach et al., 2018), slickenlines, wellbore stress indicators from nearby geothermal fields, and secular strain rate measurements.

However, the local stress states in C1 and C2 are markedly different (Figure 58c-f), indicating stress heterogeneity in the reservoir. C1 has a normal faulting environment with σ_1 close to vertical, σ_2 close to horizontal and trending SSW, and σ_3 close to horizontal and trending WNW (Figure 58d). Given this stress state, the ideal orientation of the failure plane is the one striking to NNE and dipping ~60º, consistent with the geometry of the BBF and the seismicity observations (Figure 57a, c-d). C2 has a trans-tensional stress regime dominated by strike slip with some normal slip component (Figure 58f), consistent with the resolved focal mechanisms (Figure 57b, e). The R values for C1 and C2 are 0.62 and 0.45, respectively.

Using a preliminary set of our focal mechanisms determined with preliminary event locations and a 1-D velocity model, Jahnke et al. (2023) conducted stress inversions using the method of Vavryčuk (2014) and calculated slip tendency for each inferred fault plane given a set of potential initial stress models. In general, we have better constraints on the stress tensor orientation and relative stress magnitude due to more and higher-quality focal mechanisms available owing to more accurate predictions of azimuth and take-off angle for each event-station pair with the finalized event locations and 3-D velocity model.

The catalog of Warren et al. (2018) shows enhanced seismicity during plant shutdown (Figure 51a). However, changes in the rate of the detected seismicity may be caused by the varying ambient noise during different periods. Using the same methodology as described above, we calculated the level of noise preceding each event. We then compared the pre-event noise levels before, during, and after shutdown. The result shows that the noise level is lower during shutdown. As shown in Figure 51a, almost all of the smaller events below magnitude -1.1 were detected during shutdown (blue dots), which is likely due to the lower noise level. Above magnitude -1.1, the detection capability is likely comparable during all periods. There are 9 events of magnitude -1.1 and above during the 80 hours before shutdown (0.11 events per hour), 34 during the 19.45 hours of shutdown (1.75 events per hour), and 7 events in the 40 hours after restart (0.18 events per hour) (Figure 51a). This indicates the enhanced microseismicity during shutdown is a reliable observation.

The broad distribution of seismicity clusters in map view and the very small event magnitudes suggest that the MSEs in different clusters happened on small, isolated fault patches and fractures (Figure 52-Figure 56). MSE relocations and focal mechanisms suggest that the main cluster C1 to the northwest of the production wells 75B-16 and 76-16 occurred on a small patch of the BBF at an elevation of 0.4 to 0.7 km (Figure 55a-b, Figure 56, and Figure 57c-d). This cluster forms a linear structure on the fault surface, striking to the northwest, as seen from the horizontal and cross-section views (Figure 55a-b and Figure 56). Such microseismic lineations, i.e., streaks, aligned in the slip direction have been observed in tectonic fault zones and are interpreted to be structural or compositional in origin (e.g. Rubin et al., 1999; (Waldhauser et al., 2004). The seismicity lineation and the nodal planes of the strike-slip mechanisms in cluster C2 suggest a previously unmapped strike-slip fault, striking approximately NNE (Figure 57e). The other MSEs between the BBF, PF, SEF, and NWF probably occurred on small-scale fractures within the damage zones associated with the individual faults (Figure 55a-b, Figure 57a-b).

Our V_p model and event relocations show that the BBF and the area between the BBF, PF, SEF, and NWF, where most MSEs occurred, are within a low-velocity body with a length of ~1 km at 0.3-0.8 km elevation (Figure 55c). This zone has negative velocity perturbation values as low as –25%, much lower than that in the zone just above, which indicates that the extremely low velocity values in this zone are not due only to varying lithology from west to east (Figure 55e). In comparison, the overlying zone at 0.8-1.2 km elevation that has lower velocities compared to the eastern region (Figure 55b-c) may simply reflect a change in lithology from west to east.

According to theoretical and experimental studies, V_p is related to the bulk modulus, shear modulus, and bulk density of the rock, as well as its pore properties (e.g., Hutchings et al., 2019; Winkler & Nur, 1979). For a liquid-dominated geothermal reservoir, the main mechanism for decreasing its V_p is likely due to decreased bulk and shear modulus caused by increased rock damage (i.e., more cracks and fractures) and high fluid-filled porosity (e.g., Hutchings et al., 2019). The extremely low-velocity body is also characterized by high temperature and low resistivity (Folsom et al., 2020) and is in contact with the perforated sections of the nearby active production wells (Figure 55). Note that the production wells were perforated at these depths due to the geology (permeable fractures). The spatial coincidence of the high-temperature, low-velocity, low-resistivity zones with the fault patches and fractures delineated by the MSEs indicates this part of the geothermal reservoir around the production wells is fractured and presumably permeable such that fluids can flow through the BBF, PF, SEF, and NWF, and the fractures in between them. The stress regime at San Emidio is dominated by normal faulting (Figure 58a-b). However, local variations in fracture orientations and stress distribution can be expected for such a fractured, fluid-filled reservoir, as is evident by the diverse focal mechanisms with a wide range of orientations (Figure 57b) and the spatial variation in local stress state between different clusters (Figure 58c-f).

During plant shutdown, most of the MSEs occurred on the BBF and the fractures between BBF, PF, and SEF near the perforated sections of the production wells. Although pumping at the injection wells also stopped during plant shutdown (Figure 51), the microseismicity is not likely to be caused by the cessation of injection pumping. The MSEs observed during shutdown are much closer to the production wells than to the injection wells (Figure 53b). As shown in Figure 52c-d, the larger magnitude events during shutdown tend to be located closer to the production wells.

In summary, we have performed detailed seismic and stress analysis with data from a dense seismic array to characterize the geothermal reservoir at San Emidio, Nevada, where a substantial increase in microseismicity during a plant shutdown in December 2016 was observed. The seismic events are very small with coda duration magnitudes ranging from -2.2 to 0. Our MSE relocations show that the main seismicity cluster is linearly distributed on the westward dipping BBF and most of the other MSEs likely occurred on small-scale fractures near and between existing normal faults. Our tomographic V_p model shows that the fault patches and fractures delineated by MSEs are within a low-velocity body, which is in contact with the perforated sections of nearby active production wells. Focal mechanisms are dominated by normal faulting with some strike-slip components and have a wide range of orientations, consistent with the normal faulting stress regime. Given the local stress state, the BBF hosting the main seismicity cluster is optimally oriented for failure.

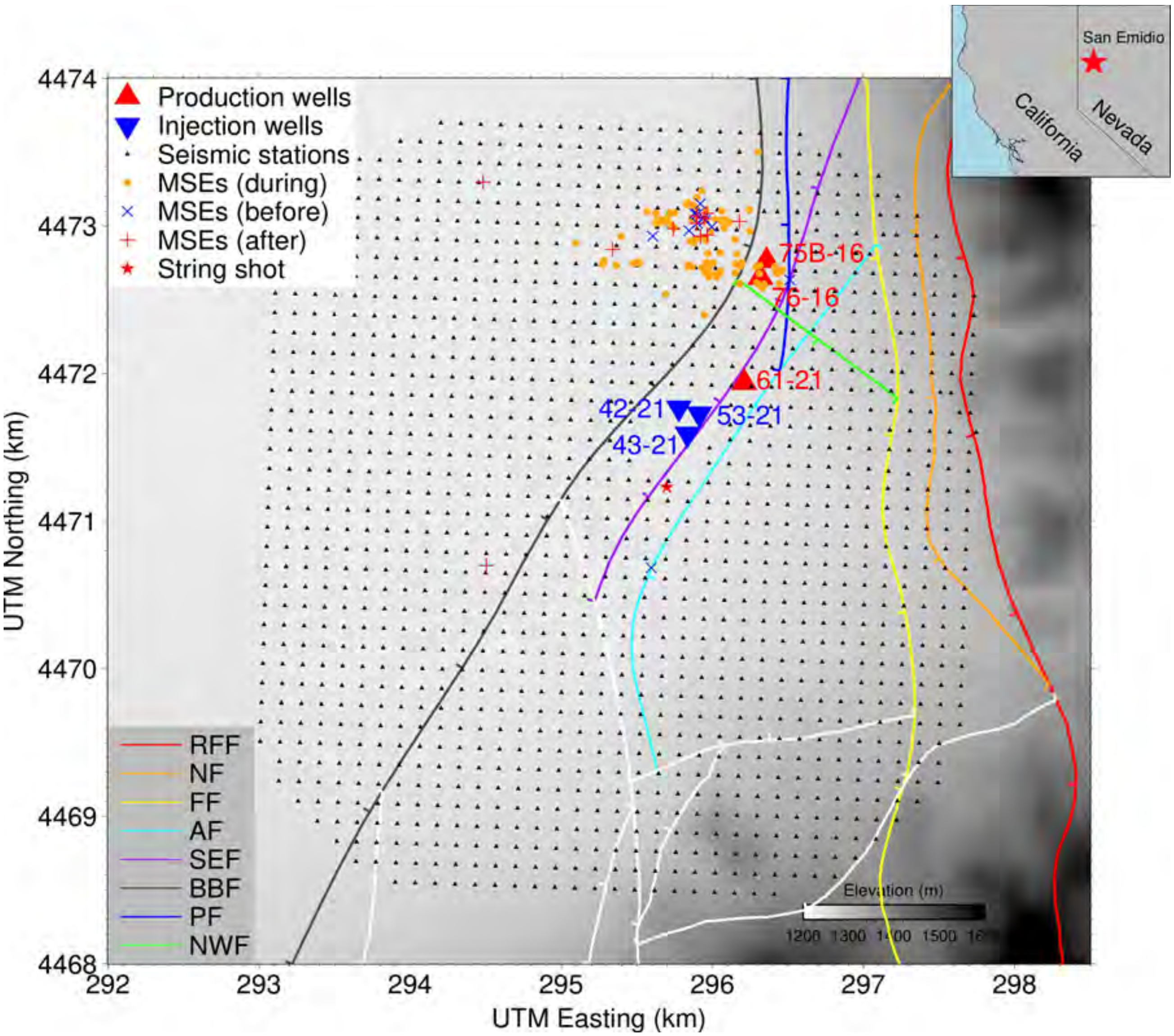

Figure 50. Map view of microseismicity and seismic station deployment in December 2016 at San Emidio. Blue crosses, orange dots, and red pluses represent catalog microseismic events (MSEs) before shutdown, during shutdown, and after restart, respectively. The Easting and Westing coordinates are in the Universal Transverse Mercator (UTM) coordinate system (zone 11 T). Black dots, seismic stations; red star, string shot event; lines, fault traces at surface. Red and blue triangles represent active production and injection wells in 2016, respectively. The background gray image shows the topography. RFF, Range front fault; NF, Nightingale fault; FF, Fan fault; AF, Antithetic fault; SEF, San Emidio fault; BBF, Basin Bounding fault; PF, Piedmont fault; NWF, NW fault. All the other faults in the southern part are shown as white lines. Tick marks on fault traces represent dip directions. The fault model has been updated from Folsom et al. (2020). The inset map on the top right shows the geographic location of San Emidio (red star).

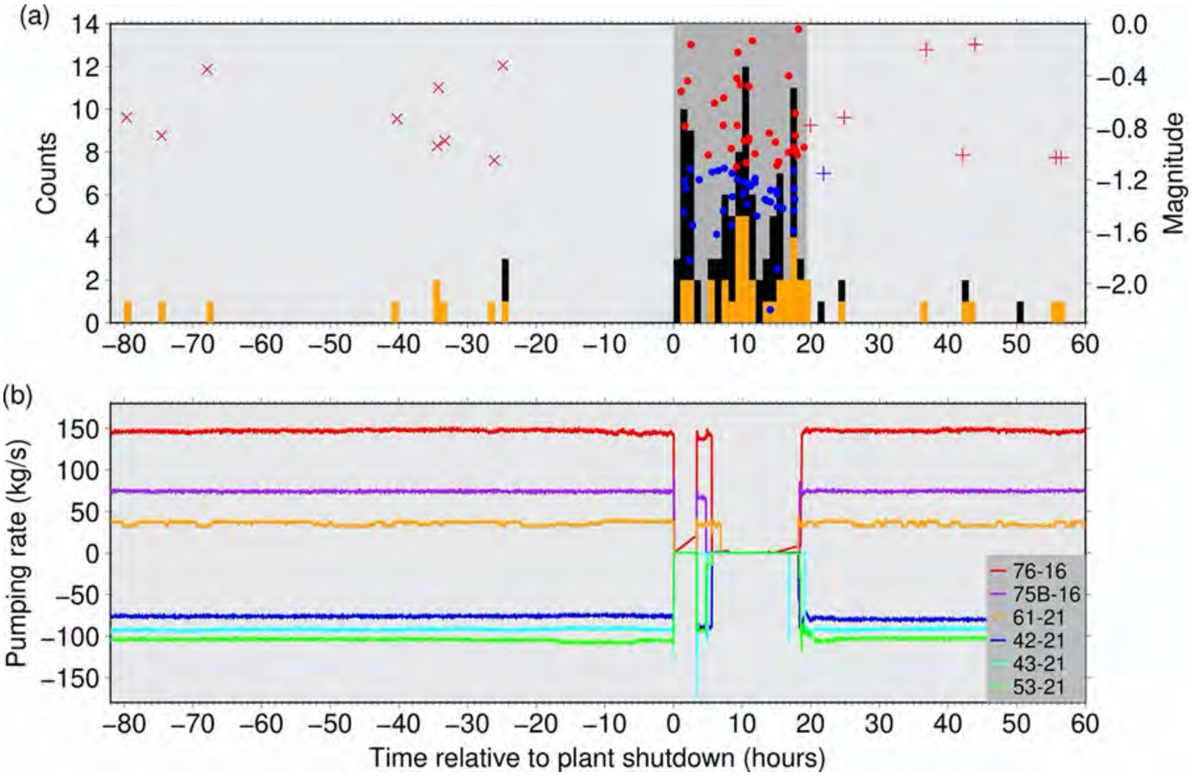

Figure 51. Temporal evolution of seismicity and pumping rates of production and injection. (a) Seismicity. The plant shutdown period (t = 0 to 19.45 hours) is shaded. The plant shutdown began at 2016-12-08 19:33 UTC. The number of MSEs per hour is shown as black and orange bars with the vertical axis shown on the left. The black bars are for all the events in the catalog. The orange bars are for the events above magnitude -1.1. Note that some black bars are completely covered by orange bars. Crosses, dots, and pluses show magnitudes (vertical axis on the right) of the events before shutdown, during shutdown, and after restart, respectively. These symbols are colored in red and blue for the events above and below magnitude -1.1, respectively. (b) Pumping rate (positive, production; negative, injection). The red, purple, and orange lines show the pumping rate evolution for the three production wells. The blue, cyan, and green lines are for the three injection wells. There is no pumping at all the wells during shutdown except for a short resumption within the 3 to 6 hour time window.

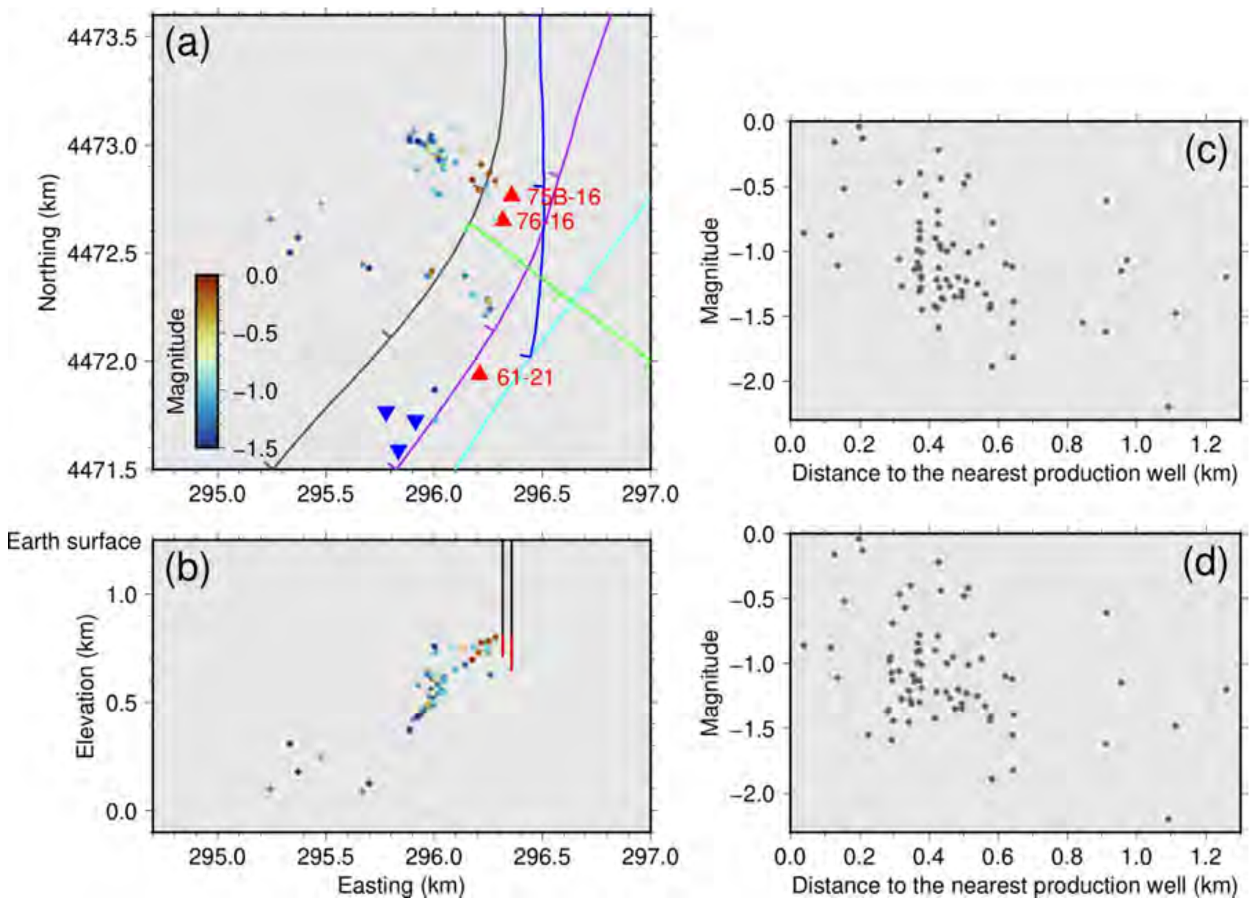

Figure 52. (a) Map view and (b) cross-section of event locations showing magnitudes. 91 of our relocated events with magnitude estimates are shown as dots colored by magnitudes. Red and blue triangles, active production and injection wells, respectively; Lines, fault traces at the surface (gray: BBF; purple: SEF; blue: PF; green: NWF; cyan: AF). Note all the wells are vertical. On the cross-section, the two vertical lines are the depth trajectories of production wells 75B-16 and 76-16, and the red segments of the lines are the perforated sections. (c) Magnitude versus the distance from hypocenter to the nearest production well (75B-16 or 76-16) for the events during shutdown. (d) Same as (c) except that the southern production well 61-21 is also used for calculating distances.

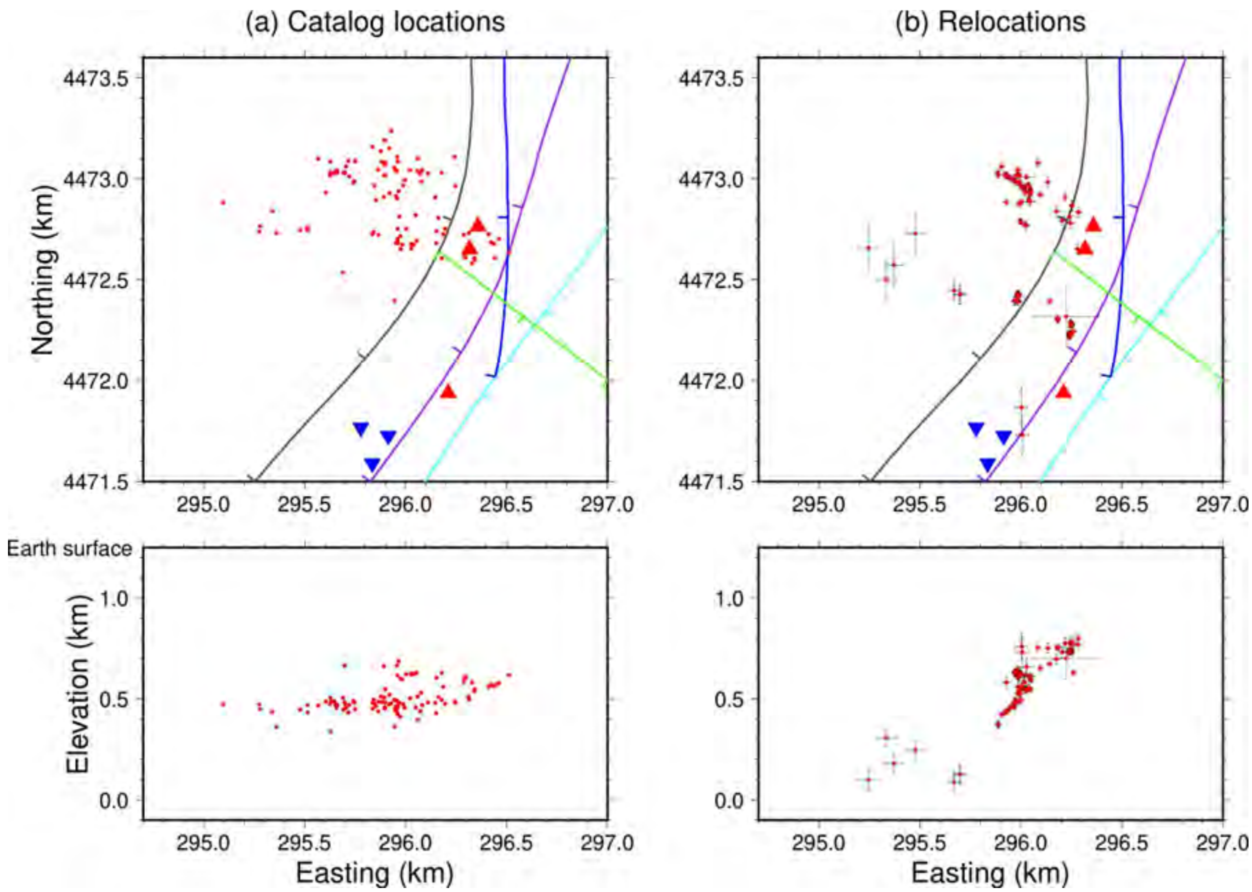

Figure 53. Comparison of (a) catalog event locations and (b) our relocations in map view and cross-section. Lines, fault traces at surface (gray: BBF; purple: SEF; blue: PF; green: NWF; cyan: AF); red and blue triangles, active production and injection wells, respectively. In (b), the error bars represent the event location uncertainty estimates using bootstrap analysis.

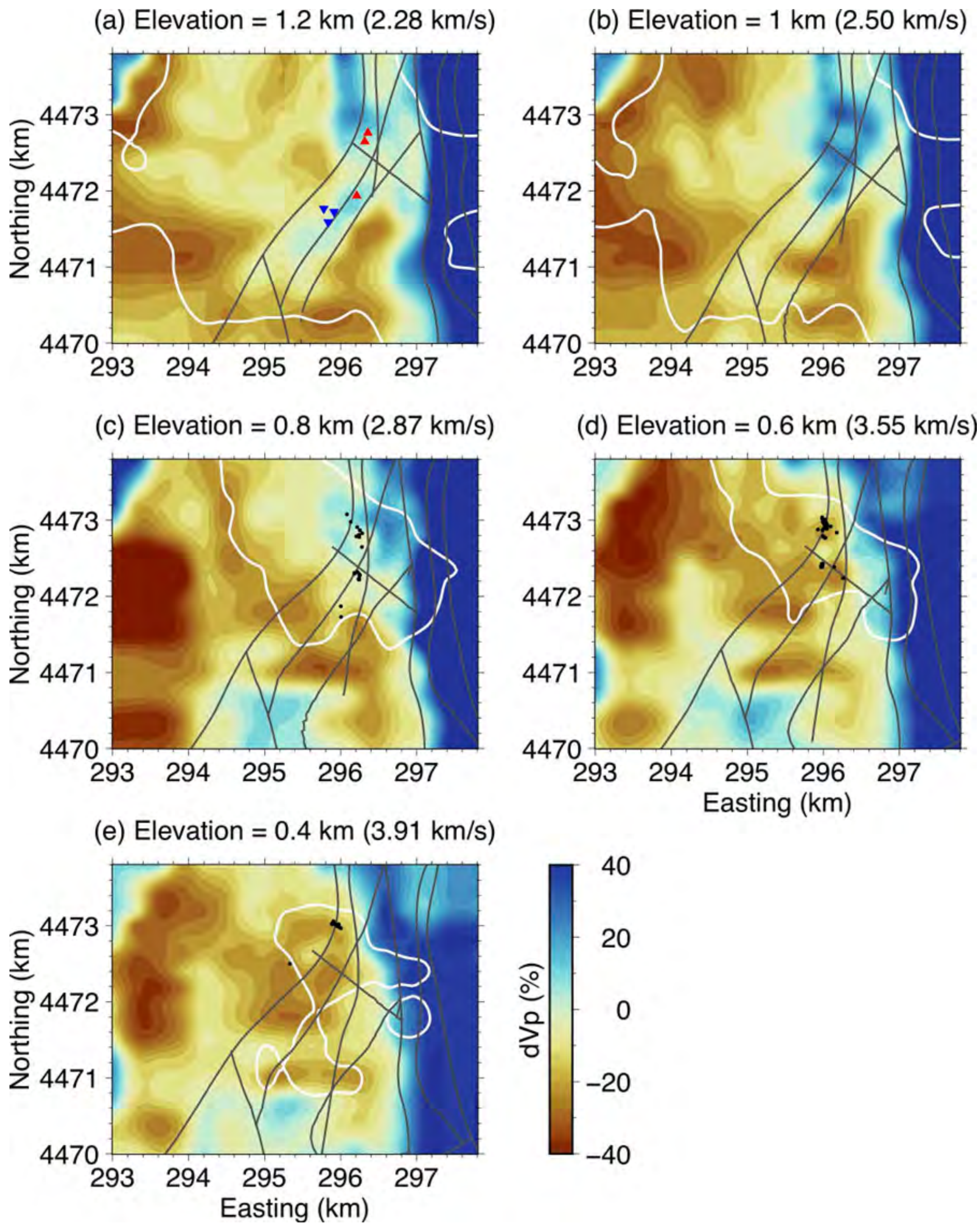

Figure 54. Depth slices of the inverted V_P model perturbations in percent relative to the 1-D average model at each depth (given in the panel titles). Black dots represent the MSEs within 0.1 km of each slice. Gray lines represent the fault traces at each depth. The red and blue triangles in (a) represent active production and injection wells, respectively. The white lines represent the model resolvability contour of 0.7, estimated from the 3-by-3-by-3 checkerboard resolution test, outlining the well resolved regions.

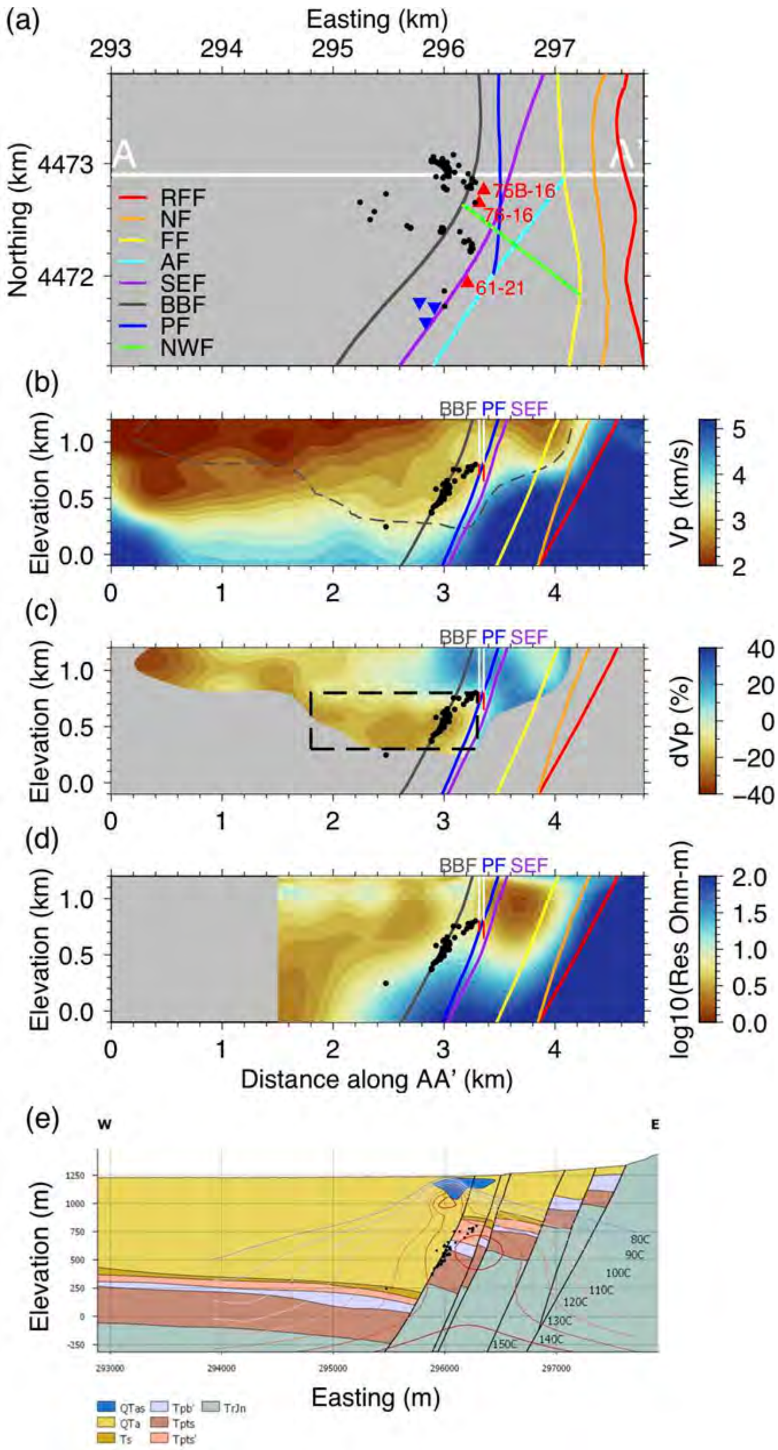

Figure 55. Cross-sections of the MSE relocations and V_p, resistivity, temperature, and geologic models, and well trajectory along profile AA' shown in (a). (a) Map view of MSE locations (dots) and fault trace at surface (colored lines), and active production (red triangles) and injection (blue triangles) wells. Note all the wells are vertical. The white line shows the profile AA'. (b) V_p model. The depth trajectories of wells 75B-16 and 76-16 (white-to-red lines with the red segments representing the perforated sections) and fault traces at depth (colored dipping lines) are projected. The dashed gray lines represent the model resolvability contour of 0.7, estimated from the 3-by-3-by-3 checkerboard resolution test, outlining the well resolved region (but note the small gray circle is likely an artifact of the resolvability estimation). (c) V_p model perturbation in percentage relative to the 1-D depth-averaged model. The low-resolution regions are masked. (d) Resistivity model from Folsom et al. (2020). The region where there is no MT station at surface is cut. (e) Geologic and temperature models. Iso-temperature curves (80^{o}C-150^{o}C) are shown. QTas, silicified sediments; QTa, Alluvium is further subdivided by grain size and clay content; Ts, Late Miocene siltstones, tilted and indurated; Tpb', Upper basaltic andesite; Tpts, Lower tuffs; Tpts', Upper tuffs and tuffaceous sediments; TrJn, Nightingale. The temperature model is from Folsom et al. (2020). The geologic model has been updated from Rhodes (2011) and Folsom et al. (2020). In (b-e), the MSEs within 0.2 km of the cross-section are shown as black dots.

1736

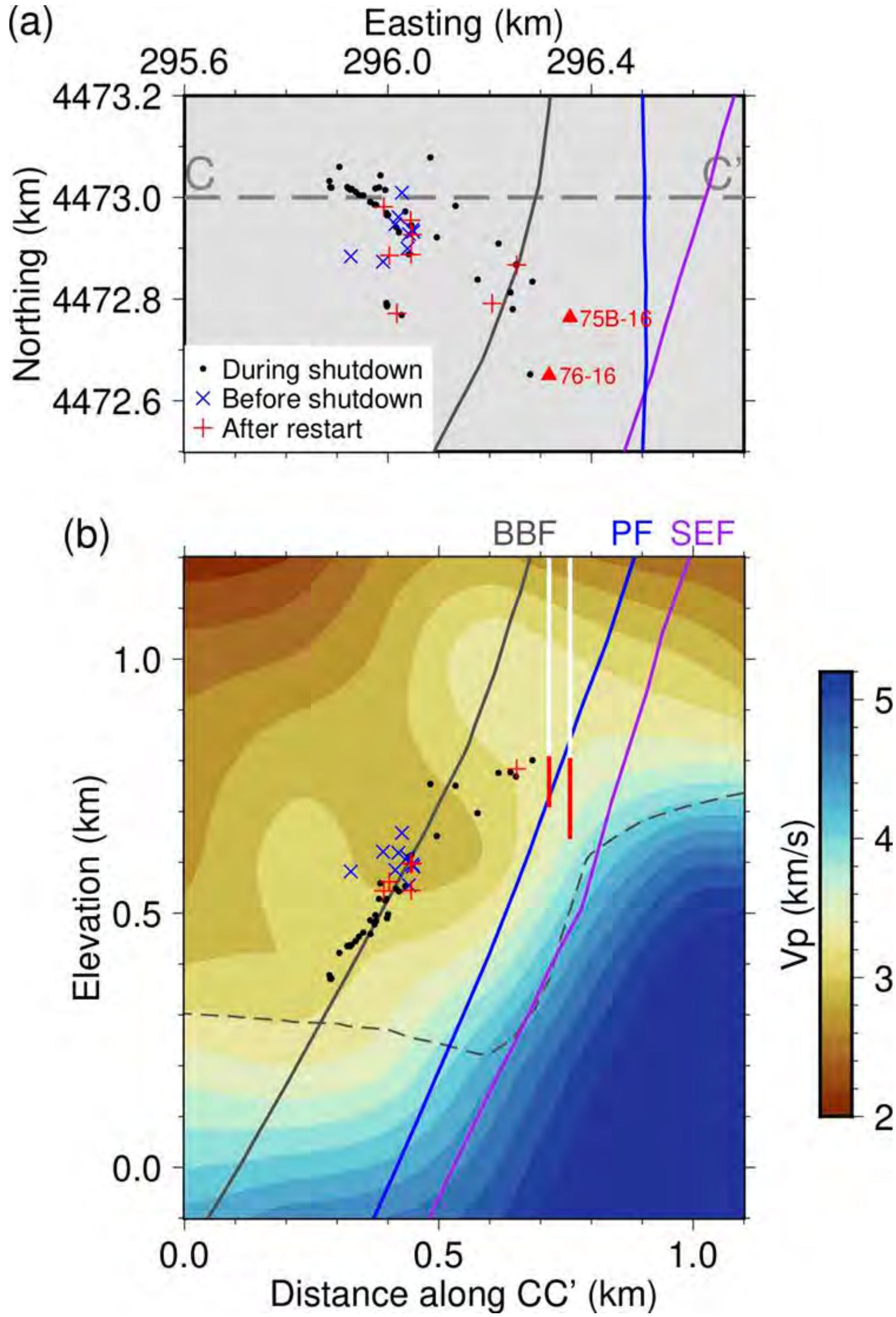

Figure 56. (a) Map view of MSE locations (crosses, before shutdown; dots, during shutdown; pluses, after restart) and fault traces at the surface (gray line, BBF; blue line, PF; purple line, SEF), and production wells (red triangles). (b) The V_p model cross-section along the profile CC' shown in (a). The depth trajectories of the two production wells (white-to-red lines with the red segments representing the perforated sections) and fault traces at depth (colored dipping lines) are projected. The dashed gray line outlines the well resolved region.

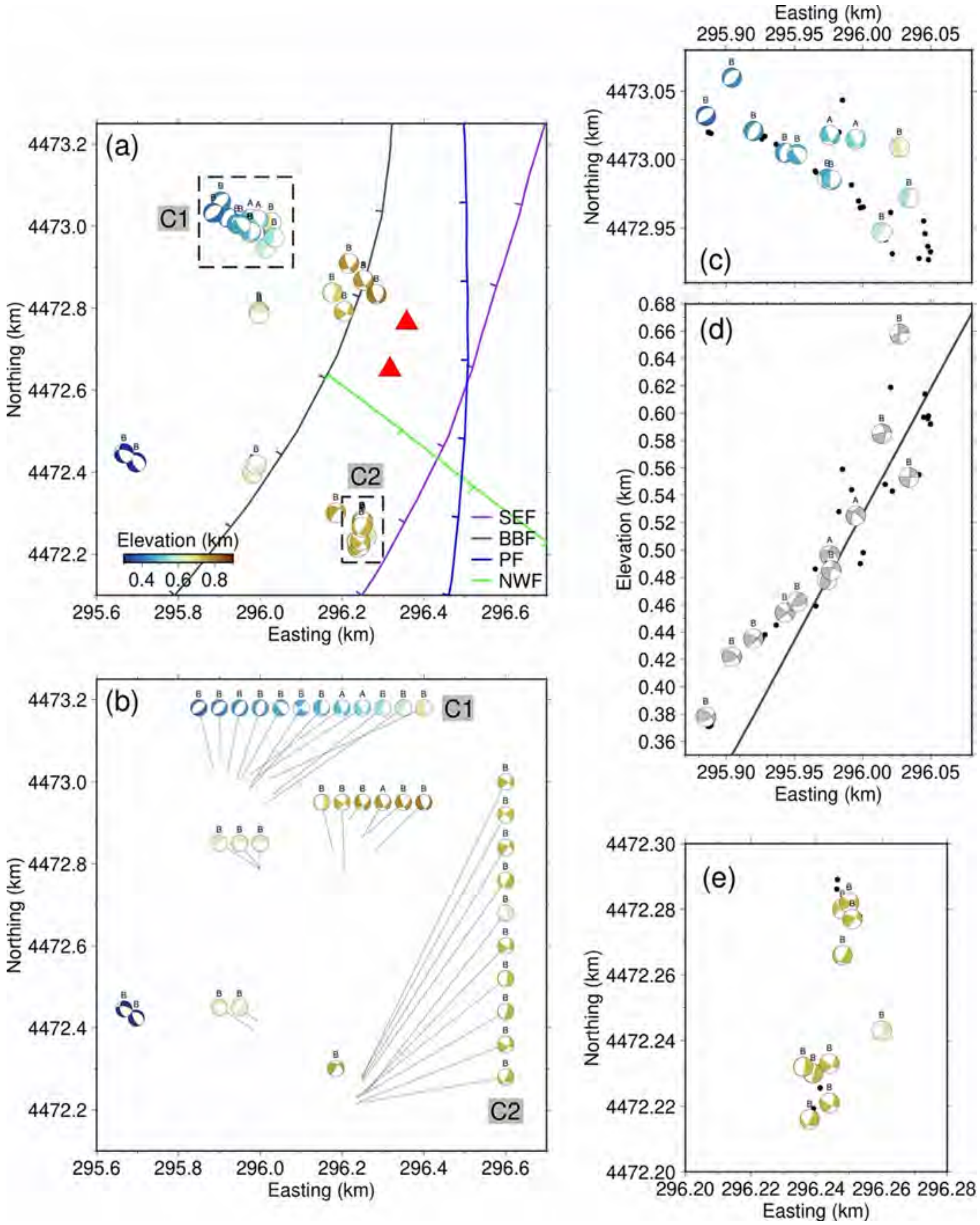

Figure 57. MSE focal mechanisms. (a) Map view of all the inverted focal mechanisms (lower hemisphere beach balls). Dashed rectangles outline the two clusters C1 and C2 that are zoomed in (c) and (e). (b) Same focal mechanisms as in (a). All the mechanisms are plotted separately from each other and connected with event epicenters. (c-d) Zoom-in map view and cross-section of C1. Note that in (d) the mechanisms are rotated to the E-W cross-section view. (e) Zoomed-in map view of C2. Black dots in (c-e) show the events that do not have focal mechanism results. The focal mechanism quality (A or B) is labeled above each beach ball.

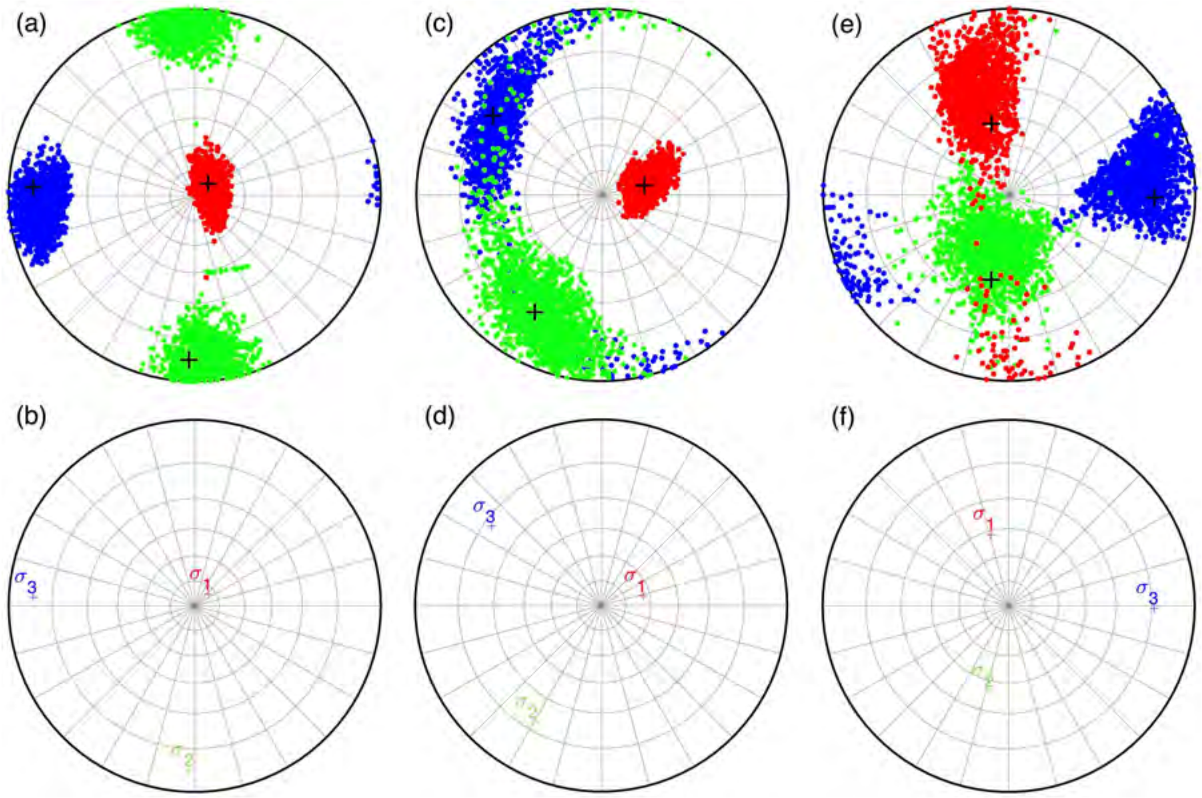

Figure 58. Stress inversion results. (a, c, e) 1000 bootstrap solutions (dots) and (b, d, f) the best solution (pluses) using high-quality focal mechanisms (a, b) in the whole study area and in the clusters (c, d) C1 and (e, f) C2 only. In the top panels, red, green, and blue dots represent the maximum (σ_1), intermediate (σ_2), and minimum (σ_3) principal stresses, respectively; black pluses represent the best solution, the same as that shown in the bottom panels. The relative stress magnitude R values for (b), (d), and (f) are 0.44, 0.62, and 0.45, respectively.

2016 Shutdown (>1000 Events)

The following section has been excerpted from a manuscript in preparation by Cliff Thurber et al .

The discovery of hundreds of microseismic events on just one day in 2021 and over a thousand during the 2022 shutdown compared to not many more than 100 in the Microseismic, Inc. catalog for the 2016 shutdown led us to think that there might be many more events in the 2016 data. Visual inspection of the shutdown day records confirmed that many obvious microseismic events were present in the data that were not included in the Microseismic, Inc. catalog. Therefore, we proceeded to assemble the seismic data for the entire 2016 deployment and began to process the data in the same manner as for the 2022 data (described in next section), but with one change. The processing flow is: (1) seismic event detection, picking, and preliminary locations with REST; (2) event magnitude estimation; (3) arrival time repicking and waveform cross-correlation (WCC) measurement of differential times; and (4) location of the events in the 3-D velocity model from the analysis of the 2022 data. The resulting locations are shown in Figure 59, and in Figure 65, we plot both the 2016 and 2022 events in map view. The main differences are the greater westward extent of microseismicity in 2016 and the greater southward extent of microseismicity in 2022.

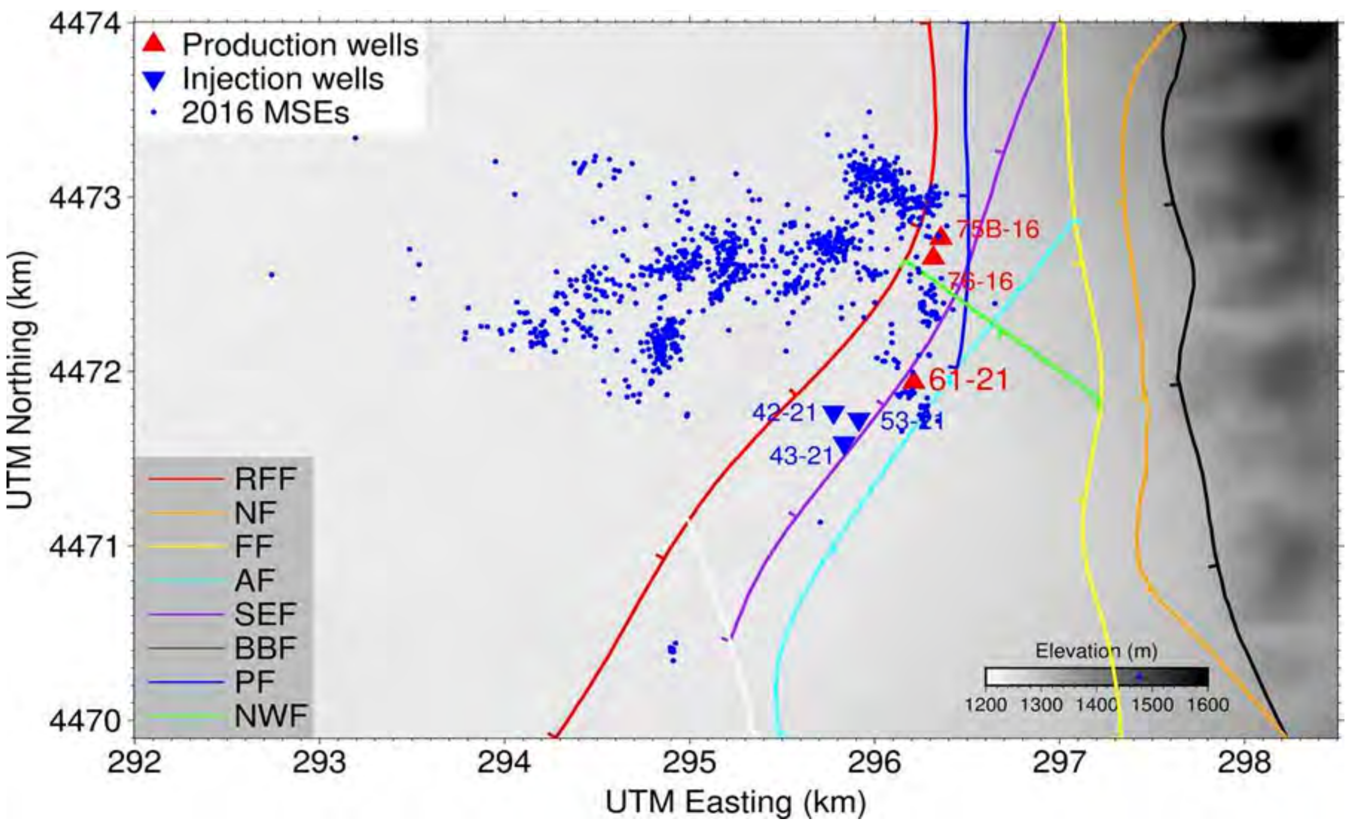

Figure 59. Precise locations of microseismicity determined by a re-analysis of the data set collected by Microseismic, Inc. in 2016. The events were detected and located using a workflow similar to that used for the 2022 data set.

2022 Shutdown

The following section has been excerpted from a manuscript review {Guo, submitted 2024/08/22 to Geophys. Res. Lett. #50537}.

In this section, we focus on a planned, 82-hour-long power plant shutdown at the San Emidio geothermal field, Nevada, USA from ~13:00 UTC on April 18 to ~22:42 UTC on April 21, 2022 (Figure 60). All the pumping wells, including three vertical production wells and three vertical injection wells (Figure 60), stopped operating during the shutdown (Figure 61). To monitor the stress perturbations in the reservoir associated with this shutdown, the WHOLESCALE team deployed a comprehensive observation system integrating seismology, hydrology, geodesy, and well logging and collected rich data sets (Feigl et al., 2023), including data from a dense seismic array (Figure 60).

Unlike the 2016 December shutdown studied by Guo et al. (2023), it is noteworthy that the 2022 April shutdown involved a new production well (25A-21), installed in the southern part of the field, in addition to two long-running production wells in the northern part (75B-16 and 76-16) (Figure 60). These wells were surrounded by the seismic array (Figure 60). The involvement of this new well and the integrated observation system provide an excellent opportunity to better understand how the power plant operations perturb the reservoir and modulate seismicity.

We conducted a series of seismic analyses to develop a comprehensive seismic event catalog and a high-resolution three-dimensional (3-D) velocity model, using the dense seismic array data and state-of-the-art techniques. Through these analyses, we determined the spatiotemporal evolution of seismicity, the distribution of activated faults, and the material properties in the reservoir. These results, combined with hydrologic and field operational data, provide key physical constraints for understanding how the reservoir responds to changes in power plant operations and the factors controlling the underlying physical processes that induce seismicity during the shutdown. These analyses are described here in detail.

The WHOLESCALE team deployed a dense seismic array in the field for one month from April 6 to May 7, 2022 to coincide with the 2022 April shutdown (Feigl et al., 2023) (Figure 60). This array consisted of 450 three-component nodal stations, spaced approximately 100-200 m apart (Figure 60), which well covered all the active production and injection wells (Figure 60). With this dense array data set, we have developed a seismic event catalog and a 3-D P-wave velocity (V_p) model using an advanced seismic analysis workflow. As described next, our workflow involves: (1) seismic event detection, (2) event magnitude estimation, (3) arrival time repicking and waveform cross-correlation (WCC) measurement of differential times, and (4) joint tomographic inversion of event locations and 3-D velocity model. We did not analyze S-wave data due to the small S-wave amplitudes of most events, severely limiting our ability to pick S-wave arrivals.

We built the initial event catalog using a processing workflow consisting of a seismic wave arrival detection algorithm, arrival association, and iterative repicking and relocation. The combined algorithm is known as REST (e.g., Comte et al., 2019; Yarce et al., 2023). It first utilizes an autoregressive estimation approach on continuous seismic data for signal detection and onset estimation (Pisarenko et al., 1987; Kushnir et al., 1990). A detection is declared when the autoregressive model of the waveform series differs from a background estimate by a given threshold. Onsets are defined as the sample point at which the difference between the autoregressive models before and after the prospective arrival is maximized. Onsets (picks) are then associated into potential events based on a specified time window length, and the continuous seismic data are windowed about these picks. The next stage involves repicking in successively smaller windows and location of potential events using a grid search approach (Roecker et al., 2006) in the velocity model provided, followed by further steps of repicking and relocation. A valid event is declared if the picks are consistent with a plausible event location.

We then refined P-wave arrival picks using an automatic picking code developed by Guo et al. (2018) based on Akaike Information Criteria (Maeda, 1985). We also measured P-wave differential times for pairs of events observed at common stations using a waveform cross-correlation (WCC) code developed by Guo & Thurber (2021) based on the time-domain WCC algorithm (e.g., Schaff et al., 2004). The absolute arrival times and WCC differential times are used for our subsequent tomographic inversion.

We determined event locations and a 3-D V_p model using the triple-difference seismic tomography algorithm tomoTD (Guo and Zhang, 2017; Guo, 2019; Guo et al., 2021). tomoTD uses absolute arrival time data and three types of differential time (dt) data, including station-pair, event-pair, and double-pair dt data. By combining these data types, tomoTD can simultaneously determine high-precision absolute and relative event locations and image high-resolution velocity structure in both earthquake generation zones and the zones beneath seismic stations.

We estimated event magnitudes with the coda duration magnitude method, an effective way for estimating magnitudes for small events, using a code developed by Guo et al. (2023) based on the method described in Koper et al. (2020). The general idea of this method is first to estimate coda duration on each station for each event and then use an empirical formula to relate the estimated coda duration with magnitude. The formula we employed here is the one used by the Nevada Seismological Laboratory for the Nevada region.

We detected and successfully located 1,761 seismic events, 134 of which occurred before shutdown, 1,575 during shutdown, and 52 after restart (Figure 60 and Figure 62). All these events have small magnitudes, ranging from –3 to 1 (Figure 62). The two largest events with magnitudes of 1.08 and 1.11 occurred 52 hours after shutdown.

Seismic event detection is influenced by ambient noise. At San Emidio, the noise level during shutdown, when no pumping operations occurred, is systematically lower than before shutdown and after restart, which could cause varying detection capability. By applying a constant noise level to define the end of coda and calculate coda duration, the calculation of coda duration magnitudes is not biased by varying noise (Pechmann et al., 2006; Koper et al., 2020), allowing us to assess the effect of varying noise on detection. We defined a magnitude threshold to be –1.3, above which the detection capability is comparable in all periods and below which the smaller events are only reliably detected during shutdown when the noise level is lower (Figure 62). Above magnitude –1.3, there are 121 events (0.4 events per hour) before shutdown, 790 events (9.7 per hour) during shutdown, and 40 events (0.1 per hour) after restart, indicating a significant increase in microseismicity during shutdown.

Microseismicity also varies with time during shutdown. There is an apparent fluctuation from day to night, whereby microseismicity during the night is generally more abundant than during the day (Figure 62). This pattern is likely due to the higher noise level during the day resulting from the construction activities related to a new production well during the 2022 April seismic deployment.

We estimated MSE location uncertainties using a bootstrap analysis and assessed the V_p model resolution using checkerboard resolution tests. In the vertical cross-sections that are approximately perpendicular to fault strikes (Figure 63), the events with location uncertainties larger than 50 m along each direction are excluded.

Our high-precision event relocations effectively delineate the seismically active volume and detailed seismicity structures. Most events occurred in a region bounded by the two northern production wells 75B-16 and 76-16 and the southern production well 25A-21 (Figure 60). Most MSEs are located on or around the Basin Bounding Fault (BBF) or in the areas between the BBF, Piedmont Fault (PF), and San Emidio Fault (SEF), based on the fault model of Folsom et al. (2020) (Figure 60 and Figure 63). The MSEs form multiple clusters and exhibit linear structures in both map and cross-section views (Figure 60 and Figure 63). In map view, the seismicity lineations to the west of 295.6 km Easting strike from NNE to SSW or from north to south, aligning with the strike directions of the BBF and SEF (Figure 60). To the east of 295.6 km Easting, there are another two clusters at shallow depths, both of which trend SSE to NNW (Figure 60). One of them is to the NNW of the two northern production wells and the other is to the WSW of these two wells. It is noteworthy that the former cluster occurred in the same area where a seismicity cluster occurred during the 2016 December shutdown (Guo et al., 2023). In the cross-sections perpendicular to the strike of the BBF and SEF, most of the clusters dip approximately 60°, generally consistent with the dip angles of the BBF and SEF (Figure 63). The cluster to the WSW of the two northern production wells is located very close to the depth extension of the NWF. It is important to point out that although in map view the microseismicity distribution appears quite complex, if viewed obliquely from the southeast, the distribution is nearly planar (Figure 64). We also note that we find no systematic seismicity migration following the shutdown. However, migration did occur within several small-scale clusters.

Our V_p model reveals high-resolution structures at both large and small scales. At the larger scale, the model shows high velocities below the Lake Range in the eastern part of the model (east of the Fan Fault) and low velocities below the basin in the western part of the model (Figure 63), consistent with the geologic model (Folsom et al., 2020). More importantly, at a smaller scale, our model reveals lateral velocity contrasts in the reservoir at elevations of -0.5 to 0.8 km from about 2 to 3 km distance along cross-sections perpendicular to the strike of the BBF and SEF, as shown in Figure 63. The most obvious velocity contrasts are the ones where the linearly distributed MSEs are located. Another notable feature in our model is that most MSEs occurred within extremely low velocity zones (LVZs), with velocities reduced by up to -40% relative to the depth-average velocity and even more if compared to the high velocities to the east (Figure 63). This low velocity structure is distributed along the BBF and is in direct contact with the perforated sections of the nearby production wells (Figure 63).

Although small offsets exist between the MSE locations and the modeled faults of Folsom et al. (2020), the close spatial proximity and generally consistent orientations (strike and dip) between the seismicity lineations and the modeled faults indicate that most MSEs likely occur on patches along the pre-existing normal faults BBF and SEF, with additional MSEs occurring on the PF and NWF (Figure 63). The small (< 200 m) offsets may be partially attributed to uncertainties in the fault model, which was constructed without seismicity constraints (Folsom et al., 2020), as well as errors in the MSE absolute locations. The BBF and SEF faults are not only delineated by MSE locations but also characterized by strong velocity contrasts in our velocity model, transitioning from high velocity in the east to low velocity in the west (Figure 63).

Most MSEs are contained within LVZs, which are distributed along the BBF (Figure 63). These LVZs spatially coincide with high-temperature bodies to the west of the BBF and SEF (Folsom et al., 2020), and are in direct contact with the production wells (Figure 63). It is likely that these LVZs are filled with geothermal fluids migrating toward these wells through permeable fault zones, especially the BBF and SEF faults, and the fractures in between the faults (Figure 63). V_p is influenced by the bulk and shear modulus, density, and pore properties (e.g., Hutchings et al., 2019). The decreasing bulk and shear modulus due to the varying lithology from east to west can result in a decrease in velocities from east to west. However, the negative velocity perturbations in these LVZs are much lower than those in the zones just above (shallower than 0.8 km depth), as evident in all cross-sections in Figure 63. A change in lithology from east to west alone may explain the moderately low velocities in the overlying zones but cannot account for the extremely low velocities in these LVZs. Due to the spatial coincidence of these LVZs and the fault patches and fractures delineated by the MSEs, these LVZs can be attributed to decreased bulk and shear modulus due to faulting and fracturing, high porosity and the filling of pore spaces and cracks with geothermal fluids.

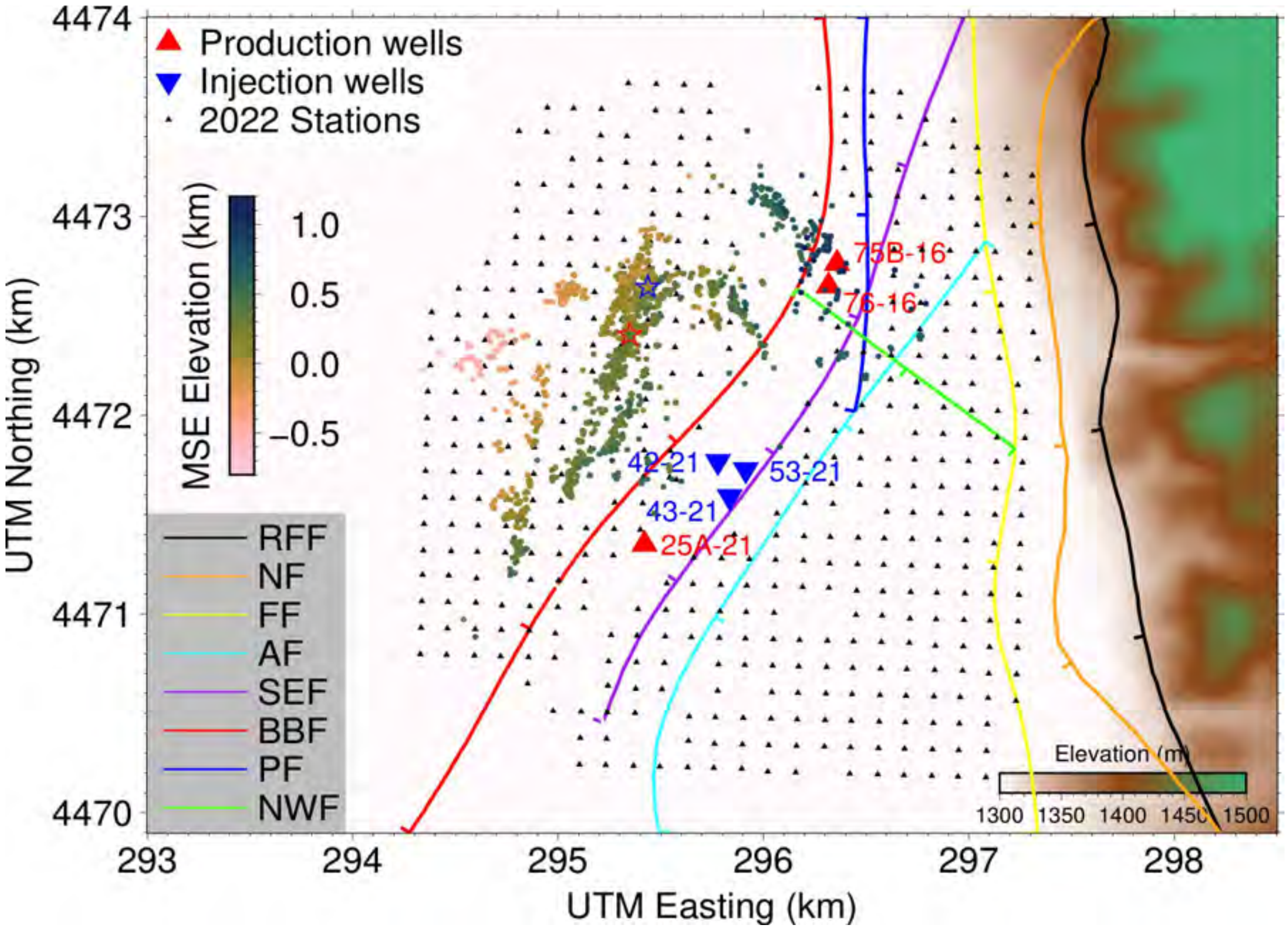

Figure 60. Map view of MSE relocations, seismic deployment, pumping wells, and the fault system. Dots, MSE epicenters colored by depth (positive above sea level); blue star, M1.08 event; red star: M1.11 event; black triangles, seismographs; red triangles, production wells; blue triangles, injection wells; lines, surface fault traces with tick marks representing dip directions. RFF, Range Front Fault; NF, Nightingale Fault; FF, Fan Fault; AF, Antithetic Fault; SEF, San Emidio Fault; BBF, Basin Bounding Fault; PF, Piedmont Fault; NWF, NW Fault. The background image shows the topography.

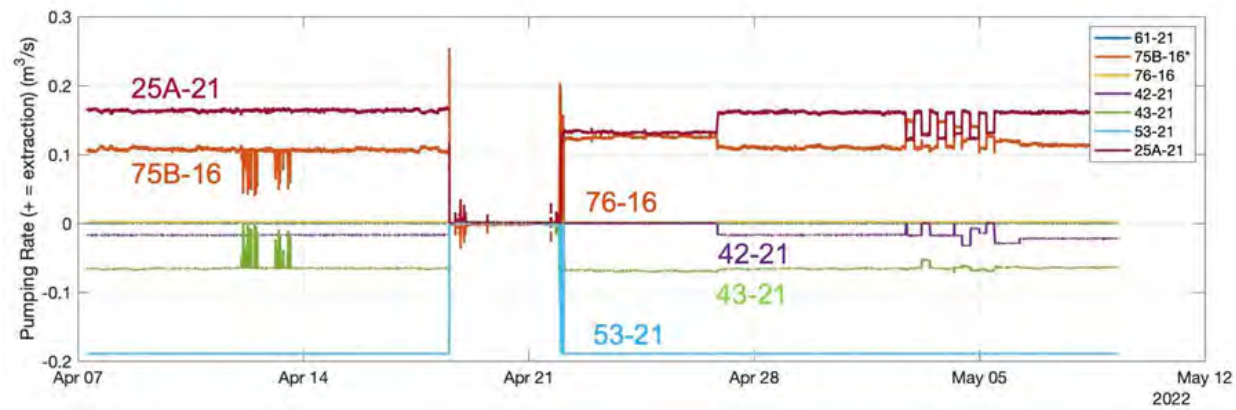

Figure 61. Pumping history before, during, and after the 2022 shutdown. Production wells are in hot colors and have generally positive values, whereas injection wells are in cool colors and have generally negative values.

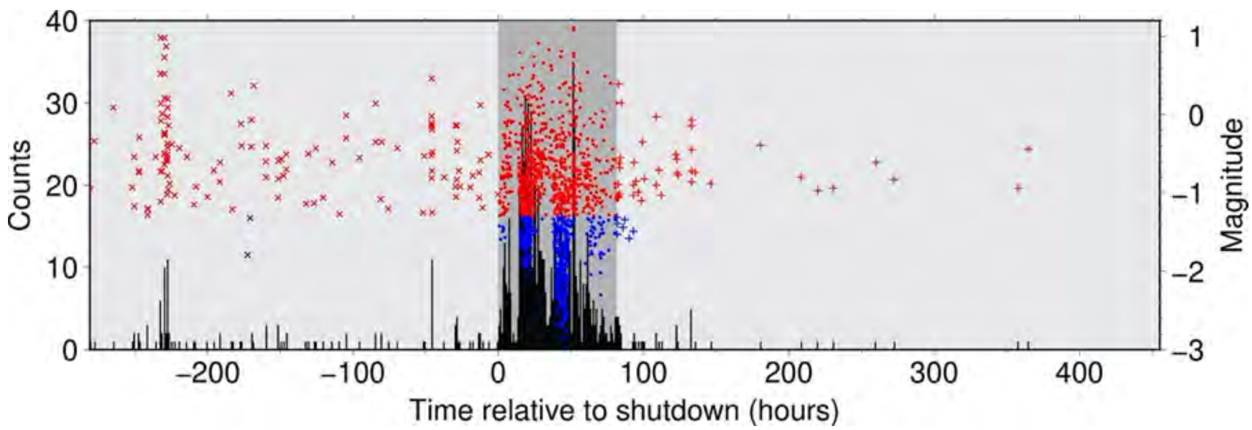

Figure 62. Temporal evolution of microseismicity throughout the period of the seismic array deployment. Time is relative to the start of shutdown (UTC 13:00 on April 18, 2022). Black bars show the number of events with magnitude > -1.3 per hour (left vertical axis). Crosses, dots, and pluses show magnitudes (right vertical axis) for the events before, during, and after the shutdown period (dark gray shaded area), respectively. Events with magnitudes below -1.3 are colored blue, and those above -1.3 are colored red.

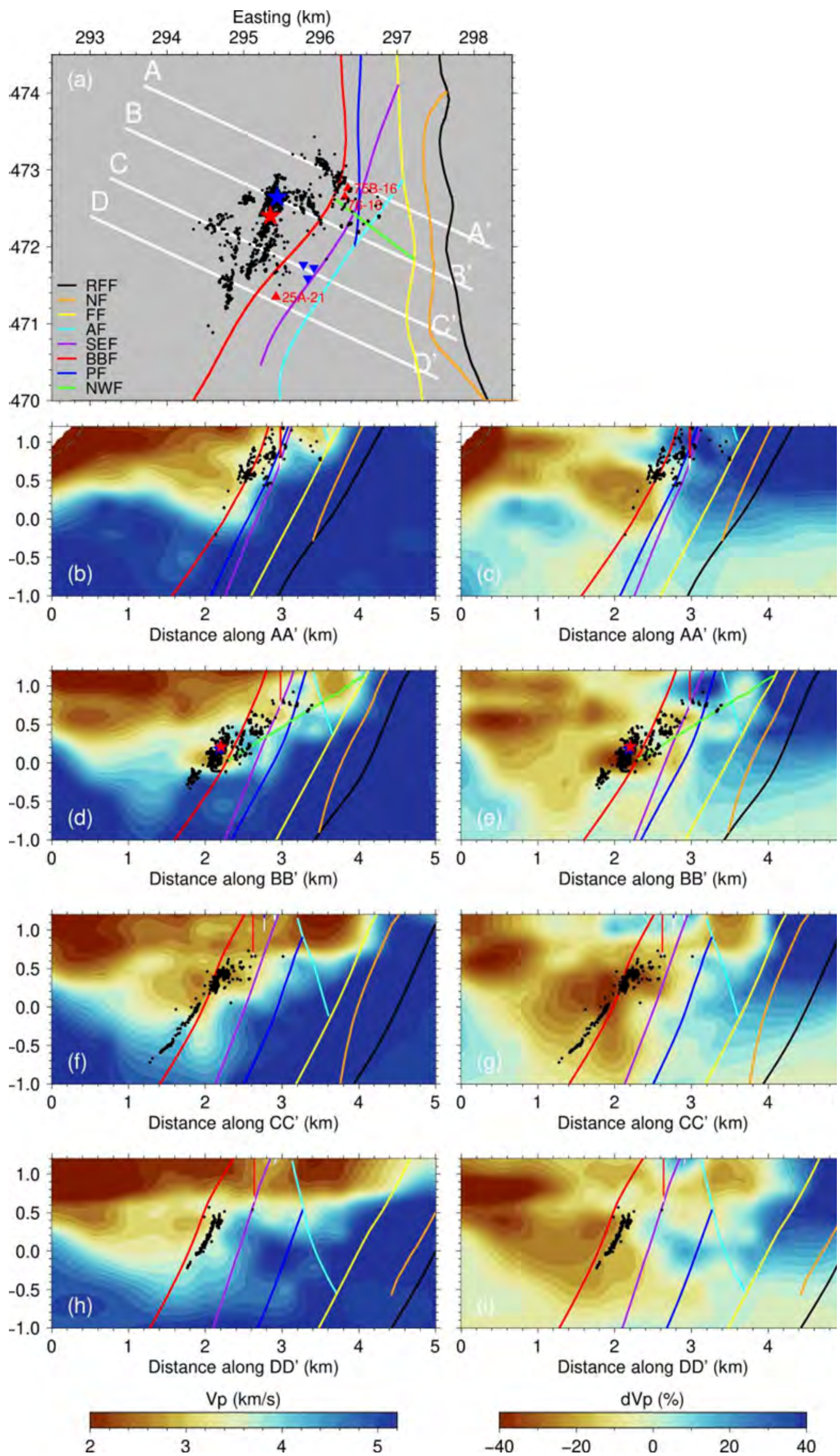

Figure 63.Map view and vertical cross-sections of event relocations (black dots) and the V_p model along four profiles that are approximately perpendicular to the main fault strikes. (a) Map of the microseismicity and four profiles (white lines). (b, d, f, h) V_p model. (c, e, g, i) V_p model perturbation (in percentage) relative to the depth-averaged 1-D model. Blue star (M1.08) and red star (M1.11) are the two largest events during shutdown. Red triangles, production wells; blue triangles, injection wells. Faults traces at the surface and at depth are showed as colored lines. In the cross-sections, the red-to-white and blue-to-white lines denote the depth trajectories of the production and injection wells, respectively, with the white parts at the bottom representing the perforated segments.

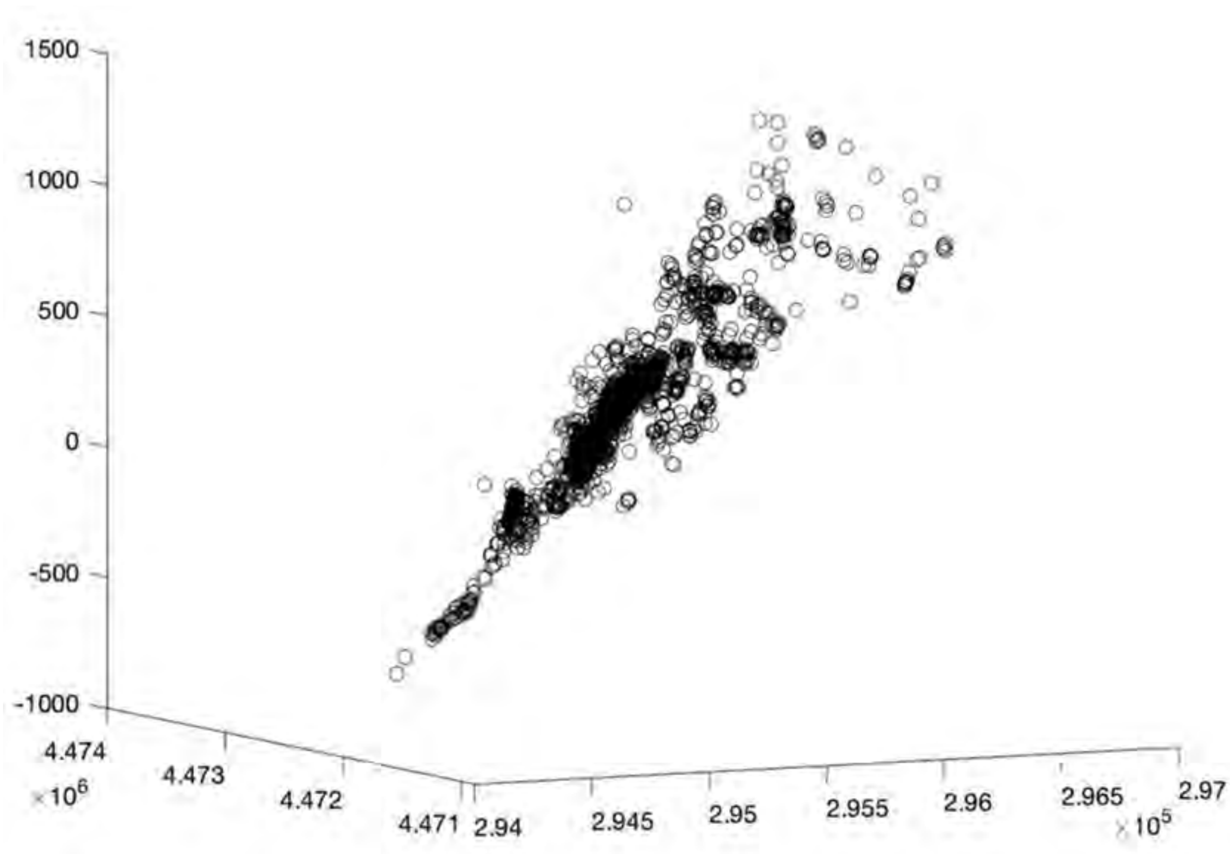

Figure 64. Perspective view of the 3-D distribution of microseismicity in the 2022 data set. Note the near planarity of the distribution, despite the complex appearance in map view. Coordinates in meters are vertical (elevation H above sea level), UTM Northing (to the left), and UTM Easting (to the right).

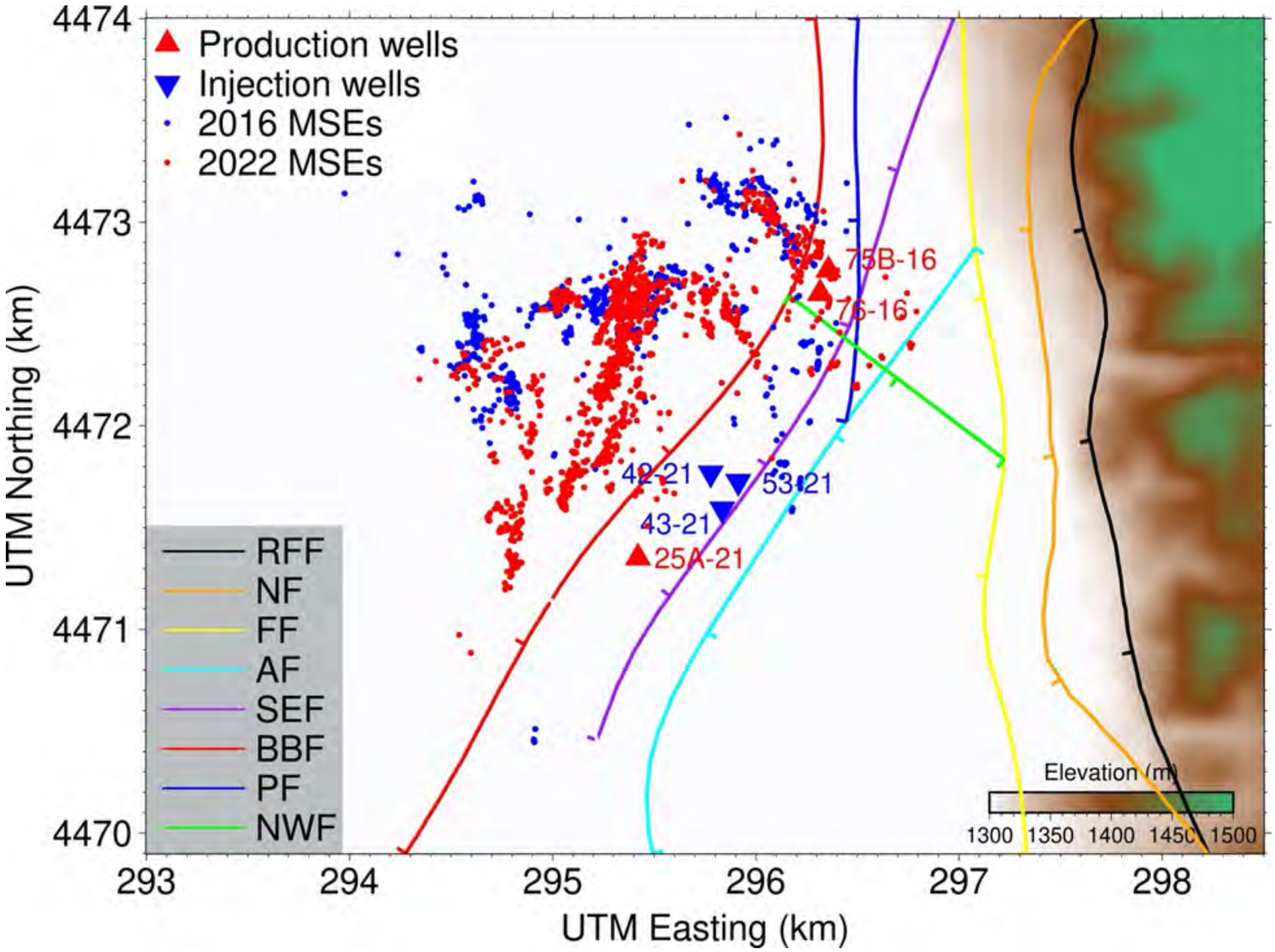

Figure 65. Comparison of the precise locations of microseismicity in 2016 (blue dots) and 2022 (red dots). The main differences are the greater westward extent of microseismicity in 2016 and the greater southward extent of microseismicity in 2022. Only events with location uncertainties less than 50 m are plotted here.

SECTION V. CALIBRATING STRESS MODELS ON OBSERVATIONS

We have calibrated stress models of the San Emidio geothermal system using available data. To do so, we use the GEOS code as a common framework to calculate modeled values of several observable quantities. The mesh for the GEOS modeling appears in Figure 66. The boundary conditions are listed in Table 12. The material properties are listed in Table 13.

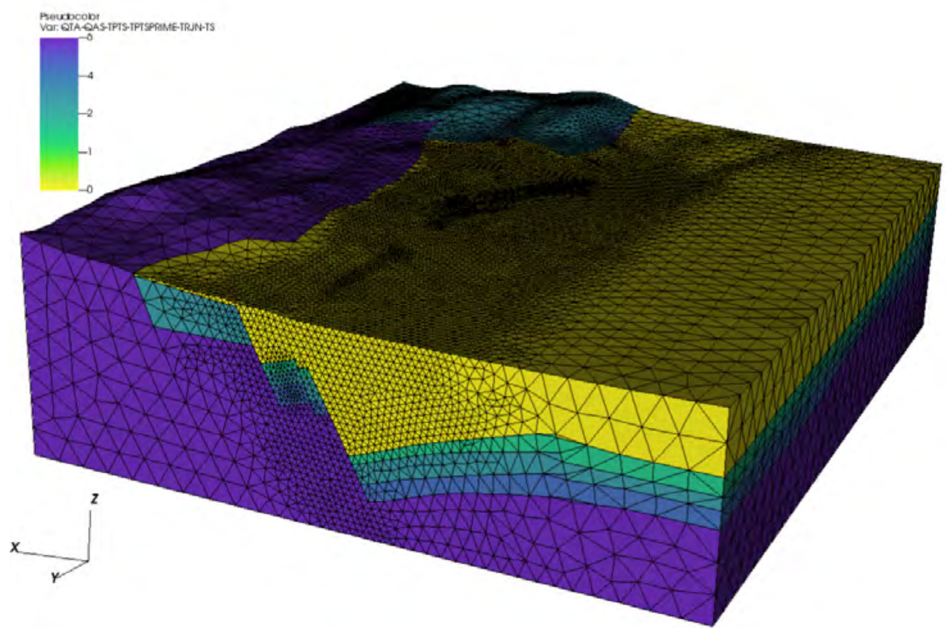

Figure 66. Mesh used for T-H-M and H-M modeling (view from northwest) showing blocks (element sets) of material properties corresponding to geologic units (from top to bottom): Qal (yellow), Qas (light green, hidden), Tpts (green), Tpts' (teal), TrJn (blue), and Ts (purple) (Luo et al. 2024; Feigl et al. 2024).

Table 12. Boundary conditions for H, T, and M.

# name	fieldName	component	setNames	scale	units	functionName
xconstraint	totalDisplacement	0	xneg;xpos;yneg;ypos	0	m	NA
yconstraint	totalDisplacement	1	xneg;xpos;yneg;ypos	0	m	NA
zconstraint	totalDisplacement	2	zneg	0	m	NA
edge_pressure	hydrostatic	.	yneg;ypos	.	.	edge_pressure
edgeTemperature	relative temperature	.	yneg;ypos	0	degC	NA
faultTemperature	relative temperature	.	fault_se_zneg	0	degC	NA
well_42_21_temperature	relative temperature	.	well_42_21	-94.3	degC	NA
well_43_21_temperature	relative temperature	.	well_43_21	-94.3	degC	NA
well_53_21_temperature	relative temperature	.	well_53_21	-94.3	degC	NA
well_25A_21	mass flux	.	well_25A_21	987	kg/s	well_25A_21
well_75B_16	mass flux	.	well_75B_16	926	kg/s	well_75B_16
well_76_16	mass flux	.	well_76_16	931	kg/s	well_76_16
well_42_21	mass flux	.	well_42_21	-987	kg/s	well_42_21
well_43_21	mass flux	.	well_43_21	-987	kg/s	well_43_21
well_53_21	mass flux	.	well_53_21	-987	kg/s	well_53_21
well_61_21	mass flux	.	well_61_21	923	kg/s	well_61_21

Table 13. Material properties for each set of elements.

# name	unit	fieldName	component	scale
permeability_x_QTA	m^2	rockPerm_permeability	0	1.50E-12
permeability_y_QTA	m^2	rockPerm_permeability	1	1.50E-12
permeability_z_QTA	m^2	rockPerm_permeability	2	1.07E-14
porosity_QTA		rockPorosity_referencePorosity	NA	3.00E-01
permeability_x_QAS	m^2	rockPerm_permeability	0	4.30E-11
permeability_y_QAS	m^2	rockPerm_permeability	1	4.30E-11
permeability_z_QAS	m^2	rockPerm_permeability	2	3.07E-13
porosity_QAS		rockPorosity_referencePorosity	NA	3.50E-01
permeability_x_TPTS	m^2	rockPerm_permeability	0	1.70E-12
permeability_y_TPTS	m^2	rockPerm_permeability	1	1.70E-12
permeability_z_TPTS	m^2	rockPerm_permeability	2	1.70E-12
porosity_TPTS		rockPorosity_referencePorosity	NA	5.00E-02
permeability_x_TPTSPRIME	m^2	rockPerm_permeability	0	2.40E-11
permeability_y_TPTSPRIME	m^2	rockPerm_permeability	1	2.40E-11
permeability_z_TPTSPRIME	m^2	rockPerm_permeability	2	2.40E-11
porosity_TPTSPRIME		rockPorosity_referencePorosity	NA	1.00E-01
permeability_x_TRJN	m^2	rockPerm_permeability	0	3.10E-14
permeability_y_TRJN	m^2	rockPerm_permeability	1	3.10E-14
permeability_z_TRJN	m^2	rockPerm_permeability	2	3.10E-14
porosity_TRJN		rockPorosity_referencePorosity	NA	5.00E-02
permeability_x_TS	m^2	rockPerm_permeability	0	3.10E-14
permeability_y_TS	m^2	rockPerm_permeability	1	3.10E-14
permeability_z_TS	m^2	rockPerm_permeability	2	3.10E-14
bulk_modulus_QTA	Pa	rock_bulkModulus	NA	7.40E+09
shear_modulus_QTA	Pa	rock_shearModulus	NA	4.50E+09
density_QTA	kg/m^3	rock_density	NA	2.12E+03
bulk_modulus_QAS	Pa	rock_bulkModulus	NA	5.70E+09
shear_modulus_QAS	Pa	rock_shearModulus	NA	4.30E+09
density_QAS	kg/m^3	rock_density	NA	2.40E+03
bulk_modulus_TPTS	Pa	rock_bulkModulus	NA	1.55E+10
shear_modulus_TPTS	Pa	rock_shearModulus	NA	1.26E+10
density_TPTS	kg/m^3	rock_density	NA	2.12E+03
bulk_modulus_TPTSPRIME	Pa	rock_bulkModulus	NA	1.74E+10
shear_modulus_TPTSPRIME	Pa	rock_shearModulus	NA	1.41E+10
density_TPTSPRIME	kg/m^3	rock_density	NA	2.67E+03
bulk_modulus_TRJN	Pa	rock_bulkModulus	NA	2.04E+10
shear_modulus_TRJN	Pa	rock_shearModulus	NA	1.66E+10
density_TRJN	kg/m^3	rock_density	NA	2.67E+03
bulk_modulus_TS	Pa	rock_bulkModulus	NA	2.86E+10
shear_modulus_TS	Pa	rock_shearModulus	NA	2.15E+10
density_TS	kg/m^3	rock_density	NA	2.80E+03
biot_QTA		rockPorosity_biotCoefficient	NA	3.60E-01
biot_QAS		rockPorosity_biotCoefficient	NA	3.60E-01
biot_TPTS		rockPorosity_biotCoefficient	NA	3.60E-01
biot_TPTSPRIME		rockPorosity_biotCoefficient	NA	3.60E-01
biot_TRJN		rockPorosity_biotCoefficient	NA	3.60E-01
biot_TS		rockPorosity_biotCoefficient	NA	3.60E-01
fault_se_permeability_x	m^2	rockPerm_permeability	0	1.50E-12
fault_se_permeability_y	m^2	rockPerm_permeability	1	1.50E-12
fault_se_permeability_z	m^2	rockPerm_permeability	2	1.07E-14
porosity_TS		rockPorosity_referencePorosity	NA	5.00E-02

To quantify the performance of the models, we consider four different technical performance metrics (TPMs), as summarized in the columns of Table 14. The rows indicate different levels of performance. Specifically, each numerical value represents the misfit equal to the mean absolute deviation of the residual differences between the observed values U_{obs} and modeled values U_{mod}:

$$misfit = \text{mean}(\text{abs}(U_{obs} - U_{mod})) \tag{5}$$

This definition of the misfit was specified for the state of the art in 2020 (row 1 in Table 14), the minimum requirement for success (row 2), and the target level (row 3) in the SOPO. Row 4 in the table shows the level of performance that was realized and evaluated in 2021 as part of Task 6. Row 5 shows the level of performance that has been realized using the data sets used to calibrate the GEOS models in Task 9. Row 6 shows the level of performance remaining to be determined (TBD) in Subtask 9.5 using auditing data sets.

In the following sections, we discuss the calibration of the models in Subtasks 9.1, 9.2, 9.3, and 9.4, to evaluate TPMs 2, 4, 3, and 1, respectively.

Table 14. Technical performance metrics (TPMs) for four types of observable quantities (columns) at several levels of performance (rows).

	TPM 1a Microseismic Events: location		TPM 1b Microseismic Events: time		TPM 2a Stress indicators: Orientation		TPM 2b Stress indicators: Magnitude		TPM 3 Pressure in observation wells		TPM 4 Vertical displacement	
Current state of the art in 2020	Location	250 m				20 deg		10 MPa		50 kPa	GPS-InSAR	10 mm
Minimum requirement from SOPO	location	250 m				20 deg		10 MPa		50 kPa		10 mm
Target level from SOPO	location	100 m				10 deg		5 MPa		20 kPa		5 mm
Realized in 2021 from existing data (Task 5)	2016 shutdown	72 m	—	—	Observations are stress inferred from redigional inidcators, nearby wells, and focal mechanisms from 2016 MSE. Model is GEOS equilibrium solution. [Jahnke et al., 2023]	10 deg	No borehole breakouts were observed in Well 25A-21, providing an upper bound on input to GEOS model. [Jahnke et al., 2023]	*	Observed pressure in 6 wells during 2017 flow test. Model is Theis H-only (on each well individually)	2 kPa	Vz(INSAR) – Vz(GPS) for SEMN w.r.t. SEMS	2 mm/y
Realized 2024 on calibration data set (Task 9)	Position residual is defined as the minimum distance between the observed event location during 2016 shutdown and the modeled contour ΔCFS = 0	TBD	Percentage of events during 2016 shutdown that occur when ΔCFS > critical	60%	SHmax azimuth in Well 17A-21. Observation is DITF. Model is GEOS long-term THM solution. Metric mean(abs(mod-obs)	TBD	Szz magnitude in 1 well model:GEOS long-term THM obs: from density of cuttings	TBD	Observed pressure in 6 wells during 2017 flow test. Model is short-term GEOS H-M. Metric is total RMS of residuals over 6 wells	37 kPa	Vz at SEMN wrt SEMS. Obs is InSAR and GPS. Model: long-term THM GEOS.	obs=7±2mm/y mod~28mm/y
Realized 2024 on auditing data set (Subtask 9.5)	*MSEs during 1-month deployment before, during, and after 2022 shutdown*	TBD	Percentage of events during 2022 shutdown that occur when ΔCFS > critical	85%	*Tune temperature in input to GEOS. Consider BCs in T.*	TBD	*Tune temperature in input to GEOS. Consider BCs in T.*	TBD	*Observed pressure in 13 observation wells before, during, and after 2022 shutdown. Model is short-term*	TBD	*Time dependent displacement at SEMN wrt SEMS. Obs is InSAR and GPS. Model: long-term THM GEOS*	TBD

Cells shaded in green indicate that the TPM successfully met the specification. Cells shaded in yellow indicate caveats discussed in the narrative. Magenta-colored text indicates quantities to be determined (TBD).

Calibration of long-term T-H-M model on borehole observations (Subtask 9.1 & TPM 2)

In Subtask 5.1, we calibrated the macroscale model to match the orientation and magnitude of various stress indicators, as described above. Specifically, the "pre-stress" initial condition for the long-term T-H-M model was set to match the orientation of the maximum compressive horizontal stress S_{Hmax} at an azimuth of N10°E, as selected by Jahnke et al. [2023] based on regional stress indicators.

To evaluate the orientation of the stress field (TPM 2a), we plan to consider the orientation of maximum compressive horizontal stress S_{Hmax} at specific locations. To do so, we plan to use the observed data set consisting of the azimuths of the drilling-induced tensile fractures (DITFs) picked at several depths from the borehole image log in Well 17A-21 when it was drilled in July 2022. The modeled values of S_{Hmax} will be computed using the long-term T-H-M model. The mean of the absolute value of residual (misfit) will be compared to the minimum requirement of 20.0 degrees specified in the SOPO.

To evaluate the magnitude of stress in TPM 2b, we plan to consider the magnitude of the vertical component of stress, i.e. $|\sigma_{zz}|$ conventionally abbreviated S_V. The observed values are derived from a vertical profile constructed from density measurements of cuttings returned to the surface while drilling Well 17A-21. The modeled values will be calculated from the long-term T-H-M model computed by GEOS.

Table 15. Technical performance metrics (TPMs 2a and 2b) for stress indicators (columns) at several levels of performance (rows).

	TPM 2a Stress indicators: Orientation	TPM 2b Stress indicators: Magnitude
Current state of the art in 2020	20 deg	10 MPa
Minimum requirement from SOPO	20 deg	10 MPa
Target level from SOPO	10 deg	5 MPa
Realized in 2021 from existing data (Task 5)	Observations are stress inferred from redigional inidcators, nearby wells, and focal mechanisms from 2016 MSE. Model is GEOS equilibrium solution. [Jahnke et al., 2023] 10 deg	No borehole breakouts were observed in Well 25A-21, providing an upper bound on input to GEOS model. [Jahnke et al., 2023] *
Realized 2024 on calibration data set (Task 9)	SHmax azimuth in Well 17A-21. Observation is DITF. Model is GEOS long-term THM solution. Metric mean(abs(mod-obs) TBD	Szz magnitude in 1 well model:GEOS long-term THM obs: from density of cuttings TBD
Realized 2024 on auditing data set (Subtask 9.5)	*Tune temperature in input to GEOS. Consider BCs in T.* TBD	*Tune temperature in input to GEOS. Consider BCs in T.* TBD

Cells shaded in green indicate that the TPM successfully met the specification. Cells shaded in yellow indicate caveats discussed in the narrative. Magenta-colored text indicates quantities to be determined (TBD).

Calibration of long-term T-H-M model on geodetic observations (Subtask 9.2 & TPM 4)

To describe the geodetic data analyzed in previous tasks, we are developing a fully coupled, thermo-hydro-mechanical ("T-H-M") numerical model using the open-source GEOS code developed at Lawrence Livermore National Laboratory (e.g., Liu et al., 2018; Settgast et al., 2018). To constrain the modeling effort, the WHOLESCALE team is analyzing multiple types of observational data at San Emidio. Our long-term T-H-M modeling uses the same set of finite elements in the tessellated mesh of tetrahedral elements (Luo et al., 2024). For the mechanical and hydrologic aspects of the model, we use the same material properties, initial conditions, and boundary conditions as assumed for the short-term H-M model (Luo et al., 2024). The modeled viscosity of water is assumed to be constant, i.e. it does not vary with temperature. For the thermal aspects of the modeling, the material properties are listed in Table 13 and the boundary conditions are listed in Table 12. The initial conditions are set to the "natural state" temperatures before production began shown as red contours in Figure 1 (Folsom et al., 2022). The modeling results in terms of vertical displacement rate are shown in map view (Figure 67).

We have calibrated the long-term T-H-M model using geodetic observations from InSAR and GPS in Subtask 9.2.

To evaluate TPM 4, we consider vertical displacement and its temporal derivative, velocity. In the latter case, the observed value is the mean vertical velocity (in mm/year) from 2016 to 2022 as measured by InSAR. The modeled values are calculated from the long-term T-H-M model implemented in GEOS. The difference of these two values is the residual difference. The three fields appear in map view in Figure 67. The absolute values of the residuals are plotted as a histogram in the lower-right panel of Figure 67. The misfit statistic, i.e. the mean absolute value of the residual difference, is 1.1 mm/year for the pixels where the observed velocity is at least twice its estimated standard deviation in absolute value.

Another calibration considers the relative velocity of a point located near the center of the subsiding bowl at GPS station SEMN with respect to a point located at the edge of the subsiding bowl at GPS station SEMS. As shown in Figure 43, this velocity is 7 ± 2 mm/year as observed by GPS over an 18-month interval and (also) 7 ± 2 mm/year as observed by InSAR from 2016 to 2022. In terms of the rate of vertical displacement, however, the T-H-M simulations are greater than the GPS and InSAR observations by a factor of ~4.

Following the presentation of the geodetic measurements of deformation as observed by InSAR and GPS and the modeling results from GEOS, we compare the latter to the former.

In Area C, on the playa to the west of the production wells, the modeled deformation field (Figure 67c) differs markedly from the deformation field observed by InSAR (Figure 41). The observed deformation field shows a velocity gradient greater than 1 mm/year per kilometer where the modeled displacement field is essentially uniformly less than 2 mm/year.

In Area A, near the production wells, the shape of the modeled subsidence "bowl" Figure 67c) roughly mimics that observed by InSAR in Sentinel-1 Track 42 (Figure 41). The modeled rate of vertical displacement, however, is significantly higher than the observed rate. To quantify this difference, we consider the (relative) vertical displacement of a point located in the center of the geothermal field (near GPS station SEMN) with respect to a point located at the southern edge of the geothermal field (near GPS station SEMS). This rate is –28.2 ± 0.1 mm/year in the model. The InSAR estimate is –7.5 ± 0.2 mm/year, as estimated from InSAR data acquired between 2016-01-07 and 2022-06-04 in Sentinel-1 Track 42 without accounting for atmospheric effects (yellow circles in upper panel of Figure 44). The InSAR estimate agrees well with the value of –7.6 ± 0.4 mm/year estimated from the GPS data between January 2021 and April 2022 by a least-squares fit (red points with error bars Figure 44). A realistic estimate of the uncertainty on both geodetic rates is more likely to be of the order of 2 mm/year.

The shape of the modeled displacement field agrees approximately with that observed by InSAR near the producing wells at the center of the geothermal field. The modeled rate of vertical displacement, however, agrees with that estimated from GPS and InSAR data only to within a factor of four. Further tuning of the model parameters, especially spatial permeability, will be required to match the geodetic observations.

Table 16. Technical performance metric (TPM 4) for vertical displacement (columns) at several levels of performance (rows).

	TPM 4 Vertical displacement	
Current state of the art in 2020	GPS-InSAR	10 mm
Minimum requirement from SOPO		10 mm
Target level from SOPO		5 mm
Realized in 2021 from existing data (Task 5)	Vz(INSAR) – Vz(GPS) for SEMN w.r.t. SEMS	2 mm/y
Realized 2024 on calibration data set (Task 9)	Vz at SEMN wrt SEMS. Obs is InSAR and GPS. Model: long-term THM GEOS.	obs=7±2mm/y mod~28mm/y
Realized 2024 on auditing data set (Subtask 9.5)	*Time dependent displacement at SEMN wrt SEMS. Obs is InSAR and GPS. Model: long-term THM GEOS.*	TBD

Cells shaded in green indicate that the TPM successfully met the specification. Cells shaded in yellow indicate caveats discussed in the narrative. Magenta-colored text indicates quantities to be determined (TBD).

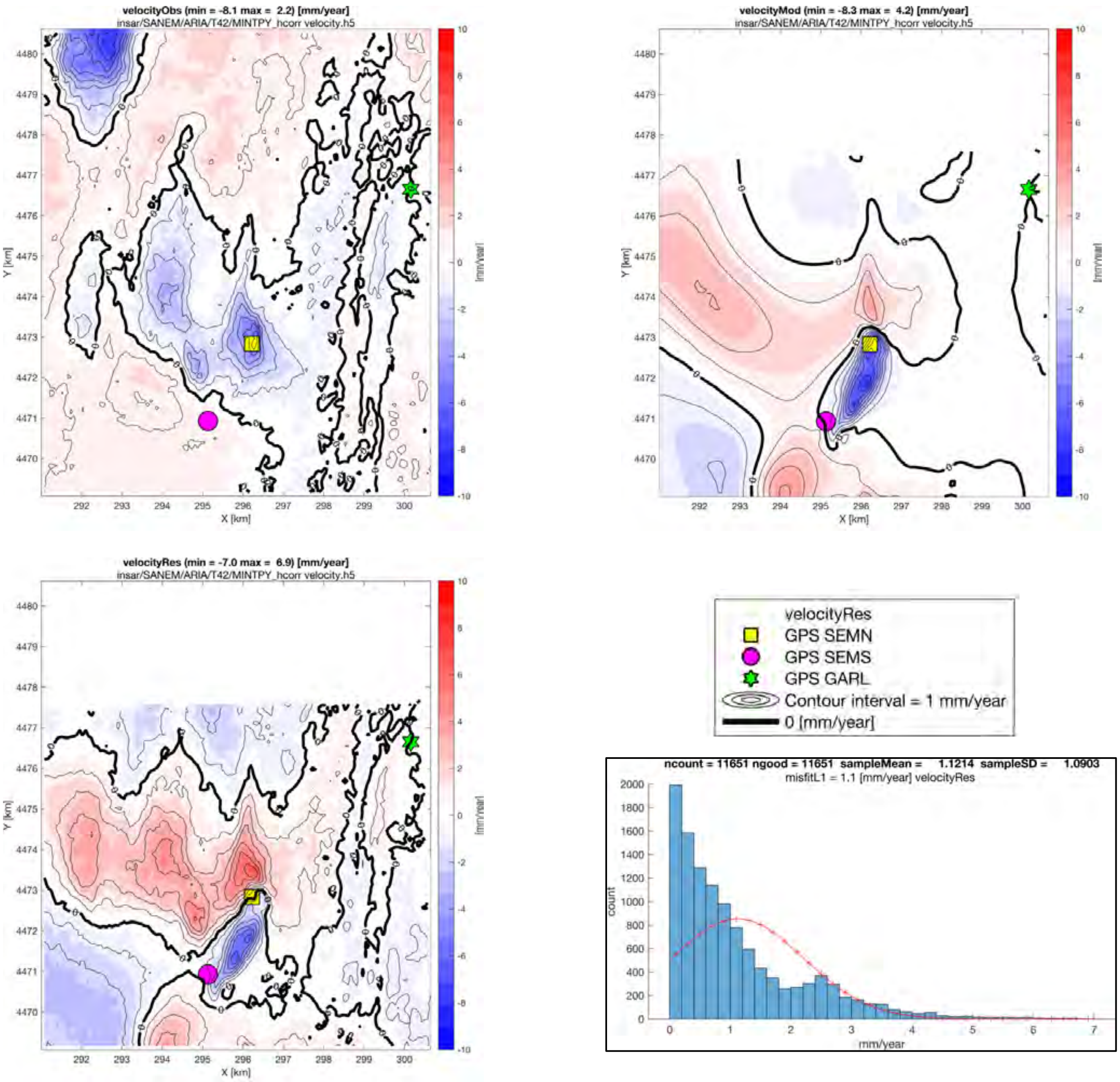

Figure 67. Map view of the mean vertical velocity (in mm/year) from 2016 to 2022 as observed by InSAR (upper left panel), as modeled by the long-term T-H-M solution in GEOS (upper right), and displayed as the residual difference of the modeled minus the observed fields (lower left). The map coordinates are Easting and Northing in the UTM cartographic projection. A legend for the three maps appears in the upper part of the lower-right panel. A histogram of the absolute values of the residual differences appears in the lower half of the lower-right panel.

Calibrating the H-M model on hydrologic observations (Subtask 9.3 & TPM 3)

The following section includes excerpts, some verbatim, from several sources (Feigl et al., 2022b; Feigl et al., 2023; Feigl et al., 2024; Luo et al., 2024). It also includes new material in preparation for a manuscript entitled WHOLESCALE modeling of hydro-mechanical processes at San Emidio, Nevada, U.S. on time scales of days: December 2016 by Xi Luo, Chris Sherman, Kurt L. Feigl, John Murphy, John Akerley, Hiroki Sone, Michael A. Cardiff, Jesse Hampton,, Hao Guo, Clifford H. Thurber, and Herbert F. Wang.

We have calibrated the short-term H-M model using pressure measurement from a flow test conducted in 2017. To evaluate TPM 3, the observed data set consists of pressure measurements recorded in six wells over eight days in 2017. The modeled values are calculated from a short-term H-M simulation computed using GEOS. For this calibration, the metric is the root-mean-square (RMS) of residuals accumulated over all six wells.

In this type of modeling, permeability is an extremely important parameter. In Subtask 9.3, we considered many different combinations of permeability for the various regions in the short-term H-M simulation, as shown in Table 18. The RMS statistics for the different sets of input permeabilities are shown as a bar graph in Figure 68. For our preferred solution (case 40), the RMS of the residual pressure values is 40.9 kPa.

Table 17. Technical performance metric (TPM 3) for pressure in observation wells (columns) at several levels of performance (rows).

	TPM 3 Pressure in observation wells	
Current state of the art in 2020		50 kPa
Minimum requirement from SOPO		50 kPa
Target level from SOPO		20 kPa
Realized in 2021 from existing data (Task 5)	Observed pressure in 6 wells during 2017 flow test. Model is Theis H-only (on each well individually)	2 kPa
Realized 2024 on calibration data set (Task 9)	Observed pressure in 6 wells during 2017 flow test. Model is short-term GEOS H-M. Metric is total RMS of residuals over 6 wells.	**37 kPa**
Realized 2024 on auditing data set (Subtask 9.5)	*Observed pressure in 13 observation wells before, during, and after 2022 shutdown. Model is short-term GEOS H-M.*	TBD

Cells shaded in green indicate that the TPM successfully met the specification. Cells shaded in yellow indicate caveats discussed in the narrative. Magenta-colored text indicates quantities to be determined (TBD).

2104 *Table 18. Summary of permeability of rock formations for GEOS model input cases.*

case number	TRMS [kPa]	QTA	QTA	QTA	QAS	QAS	QAS	TPTS	TPTS	TPTS	TPTSPR	TPTSPR	TPTSPR	TRJN	TRJN	TRJN	TS	TS	TS	fault_se	fault_se	fault_se	fault_se	fault_se	fault_se	fault_bd	fault_bd	fault_bd
permeability	[m2]	kx	ky	kz	kx	ky	kz	kx	ky	kz	kx	ky	kz	kx	ky	kz	kx	ky	kz	kx	ky	kz	kx	ky	kz	kx	ky	kz
1	**51.8**	1.5E-12	1.5E-12	1.1E-14	4.3E-11	4.3E-11	3.1E-13	1.7E-12	1.7E-12	1.7E-12	2.4E-11	2.4E-11	2.4E-11	3.1E-14	3.1E-14	3.1E-14	3.1E-14	3.1E-14	3.1E-14									
2	**61.6**	1.5E-12	1.5E-12	7.5E-13	4.3E-11	4.3E-11	2.2E-11	1.7E-12	1.7E-12	1.7E-12	2.4E-11	2.4E-11	2.4E-11	3.1E-14	3.1E-14	3.1E-14	3.1E-14	3.1E-14	3.1E-14									
3	**60.3**	1.5E-12	1.5E-12	5.0E-13	4.3E-11	4.3E-11	1.4E-11	1.7E-12	1.7E-12	1.7E-12	2.4E-11	2.4E-11	2.4E-11	3.1E-14	3.1E-14	3.1E-14	3.1E-14	3.1E-14	3.1E-14									
4	**39.8**	1.5E-13	1.5E-13	4.3E-14	6.2E-11	6.2E-11	1.8E-11	1.3E-13	1.3E-13	3.7E-14	5.2E-11	5.2E-11	1.5E-11	4.4E-14	4.4E-14	1.3E-14	4.4E-14	4.4E-14	1.3E-14									
5	**55.4**	1.5E-13	1.5E-13	4.3E-14	6.2E-11	6.2E-11	1.8E-11	1.3E-13	1.3E-13	3.7E-14	2.4E-12	2.4E-12	6.9E-13	4.4E-14	4.4E-14	1.3E-14	4.4E-14	4.4E-14	1.3E-14									
6	**50.5**	1.5E-13	1.5E-13	4.3E-14	6.2E-11	6.2E-11	1.8E-11	1.3E-13	1.3E-13	3.7E-14	5.2E-11	5.2E-11	1.5E-11	4.4E-15	4.4E-15	1.3E-15	4.4E-14	4.4E-14	1.3E-14									
7	**54.0**	1.5E-13	1.5E-13	4.3E-14	6.2E-11	6.2E-11	1.8E-11	1.3E-13	1.3E-13	3.7E-14	5.2E-11	5.2E-11	1.5E-11	4.4E-15	4.4E-15	1.3E-15	4.4E-15	4.4E-15	1.3E-15									
8	**41.0**	1.5E-13	1.5E-13	4.3E-14	6.2E-11	6.2E-11	1.8E-11	1.3E-14	1.3E-14	3.7E-15	5.2E-11	5.2E-11	1.5E-11	4.4E-14	4.4E-14	1.3E-14	4.4E-14	4.4E-14	1.3E-14									
9	**53.4**	1.5E-13	1.5E-13	4.3E-14	6.2E-11	6.2E-11	1.8E-11	1.7E-12	1.7E-12	1.7E-12	1.3E-13	1.3E-13	3.7E-14	4.4E-14	4.4E-14	1.3E-14	4.4E-14	4.4E-14	1.3E-14									
10	**45.4**	1.5E-13	1.5E-13	4.3E-14	6.2E-11	6.2E-11	1.8E-11	1.7E-12	1.7E-12	1.7E-12	1.3E-13	1.3E-13	3.7E-14	4.4E-14	4.4E-14	1.3E-14	4.4E-14	4.4E-14	1.3E-14	1.5E-10	1.5E-10	1.5E-10	1.5E-10	1.5E-10	1.5E-10			
11	**45.3**	1.5E-13	1.5E-13	4.3E-14	6.2E-11	6.2E-11	1.8E-11	1.3E-13	1.3E-13	3.7E-14	1.3E-13	1.3E-13	3.7E-14	4.4E-14	4.4E-14	1.3E-14	4.4E-14	4.4E-14	1.3E-14	1.5E-10	1.5E-10	1.5E-10	1.5E-10	1.5E-10	1.5E-10			
12	**45.1**	1.5E-13	1.5E-13	4.3E-14	6.2E-11	6.2E-11	1.8E-11	1.3E-14	1.3E-14	3.7E-15	1.3E-13	1.3E-13	3.7E-14	4.4E-14	4.4E-14	1.3E-14	4.4E-14	4.4E-14	1.3E-14	1.5E-10	1.5E-10	1.5E-10	1.5E-10	1.5E-10	1.5E-10			
13	**44.8**	1.5E-13	1.5E-13	4.3E-14	6.2E-11	6.2E-11	1.8E-11	1.7E-12	1.7E-12	1.7E-12	1.3E-13	1.3E-13	3.7E-14	4.4E-14	4.4E-14	1.3E-14	4.4E-14	4.4E-14	1.3E-14	1.5E-11	1.5E-11	1.5E-11	1.5E-11	1.5E-11	1.5E-11			
14	**52.2**	1.5E-12	1.5E-12	4.3E-13	6.2E-11	6.2E-11	1.8E-11	1.7E-12	1.7E-12	1.7E-12	1.3E-13	1.3E-13	3.7E-14	4.4E-14	4.4E-14	1.3E-14	4.4E-14	4.4E-14	1.3E-14	1.5E-11	1.5E-11	1.5E-11	1.5E-11	1.5E-11	1.5E-11			
15	**120.1**	1.5E-13	1.5E-13	4.3E-14	6.2E-11	6.2E-11	1.8E-11	1.3E-13	1.3E-13	3.7E-14	5.2E-11	5.2E-11	1.5E-11	4.4E-14	4.4E-14	1.3E-14	4.4E-14	4.4E-14	1.3E-14	1.5E-12	1.5E-12	1.1E-14	1.5E-12	1.5E-12	1.1E-14	1.5E-10	1.5E-10	1.5E-10
16	**47.9**	1.5E-13	1.5E-13	4.3E-14	6.2E-11	6.2E-11	1.8E-11	1.3E-13	1.3E-13	3.7E-14	5.2E-11	5.2E-11	1.5E-11	4.4E-14	4.4E-14	1.3E-14	4.4E-14	4.4E-14	1.3E-14	1.5E-12	1.5E-12	1.1E-14	1.5E-12	1.5E-12	1.1E-14	1.5E-11	1.5E-11	1.5E-11
17	**49.2**	1.5E-13	1.5E-13	4.3E-14	6.2E-11	6.2E-11	1.8E-11	1.3E-13	1.3E-13	3.7E-14	5.2E-11	5.2E-11	1.5E-11	4.4E-14	4.4E-14	1.3E-14	4.4E-14	4.4E-14	1.3E-14	1.5E-12	1.5E-12	1.5E-12	1.5E-12	1.5E-12	1.5E-12	1.5E-11	1.5E-11	1.5E-11
18	**47.9**	1.5E-13	1.5E-13	4.3E-14	6.2E-11	6.2E-11	1.8E-11	1.3E-13	1.3E-13	3.7E-14	5.2E-11	5.2E-11	1.5E-11	4.4E-14	4.4E-14	1.3E-14	4.4E-14	4.4E-14	1.3E-14	1.5E-12	1.5E-12	1.5E-13	1.5E-12	1.5E-12	1.5E-13	1.5E-11	1.5E-11	1.5E-11
20	**38.0**	1.5E-13	1.5E-13	4.3E-14	6.2E-11	6.2E-11	1.8E-11	1.3E-13	1.3E-13	3.7E-14	5.2E-11	5.2E-11	1.5E-11	4.4E-14	4.4E-14	1.3E-14	4.4E-14	4.4E-14	1.3E-14	1.5E-12	1.5E-12	1.5E-13	1.5E-12	1.5E-12	1.5E-13	1.5E-12	1.5E-12	1.5E-12
21	**38.1**	1.5E-13	1.5E-13	4.3E-14	6.2E-11	6.2E-11	1.8E-11	1.3E-13	1.3E-13	3.7E-14	5.2E-11	5.2E-11	1.5E-11	4.4E-14	4.4E-14	1.3E-14	4.4E-14	4.4E-14	1.3E-14	1.5E-12	1.5E-12	1.5E-13	1.5E-12	1.5E-12	1.5E-13	1.5E-13	1.5E-13	1.5E-13
22	**39.6**	1.5E-13	1.5E-13	4.3E-14	6.2E-11	6.2E-11	1.8E-11	1.3E-13	1.3E-13	3.7E-14	5.2E-11	5.2E-11	1.5E-11	4.4E-14	4.4E-14	1.3E-14	4.4E-14	4.4E-14	1.3E-14	1.5E-12	1.5E-12	1.0E-14	1.5E-12	1.5E-12	1.0E-14	1.5E-13	1.5E-13	1.5E-12
23	**88.7**	1.5E-13	1.5E-13	4.3E-14	6.2E-11	6.2E-11	1.8E-11	1.3E-13	1.3E-13	3.7E-14	5.2E-11	5.2E-11	1.5E-11	4.4E-13	4.4E-13	1.3E-13	4.4E-14	4.4E-14	1.3E-14	1.5E-12	1.5E-12	1.0E-14	1.5E-12	1.5E-12	1.0E-14	5.0E-11	5.0E-11	5.0E-11
24	**46.8**	1.5E-13	1.5E-13	4.3E-14	6.2E-11	6.2E-11	1.8E-11	1.3E-13	1.3E-13	3.7E-14	5.2E-11	5.2E-11	1.5E-11	4.4E-13	4.4E-13	1.3E-13	4.4E-14	4.4E-14	1.3E-14	1.5E-12	1.5E-12	1.0E-14	1.5E-12	1.5E-12	1.0E-14	5.0E-12	5.0E-12	5.0E-12
25	**38.5**	1.5E-13	1.5E-13	4.3E-14	6.2E-11	6.2E-11	1.8E-11	1.3E-13	1.3E-13	3.7E-14	5.2E-11	5.2E-11	1.5E-11	1.4E-14	1.4E-14	1.3E-14	4.4E-14	4.4E-14	1.3E-14	1.5E-12	1.5E-12	1.0E-14	1.5E-12	1.5E-12	1.0E-14	8.0E-12	8.0E-12	8.0E-12
40	**36.8**	1.5E-13	1.5E-13	4.3E-14	6.2E-11	6.2E-11	1.8E-11	1.3E-14	1.3E-14	3.7E-15	1.2E-10	1.2E-10	4.1E-11	1.4E-14	1.4E-14	3.3E-15	4.4E-14	4.4E-14	1.3E-14	1.5E-12	1.5E-12	1.5E-13	1.5E-12	1.5E-12	1.5E-13	1.5E-10	1.5E-10	1.5E-13

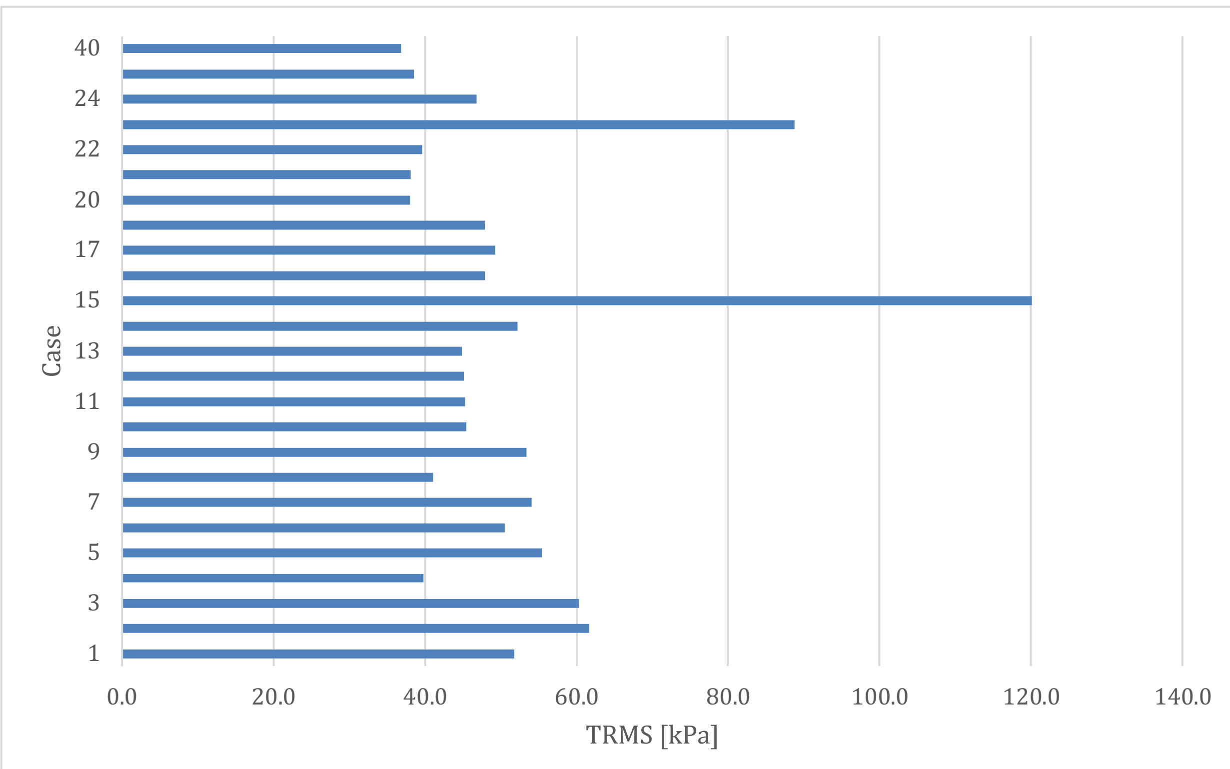

2105 *Figure 68. Overall ("total") RMS of residual pressure in kPa for each permeability.*

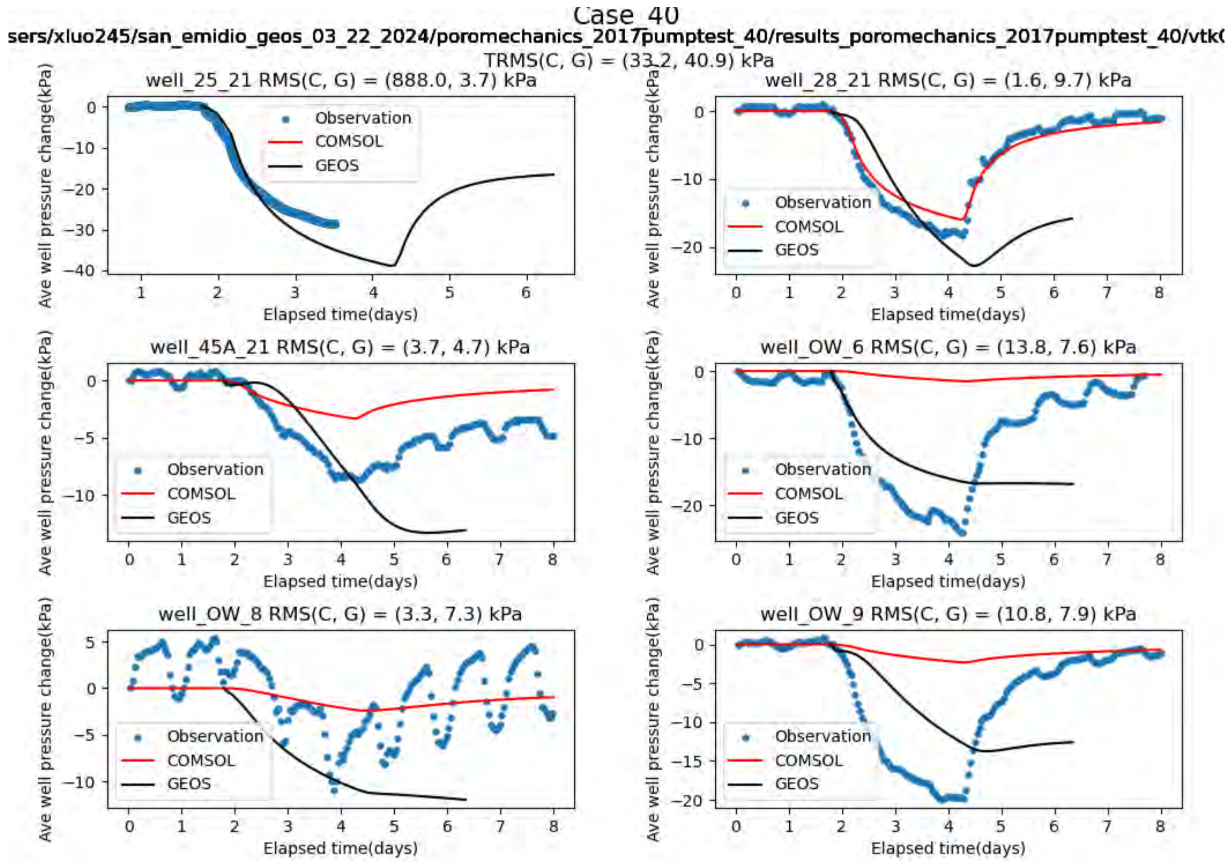

Figure 69. Pressure changes in observation wells during a flow test in 2017, showing observed pressure as blue dots, simulated pressure calculated using a hydrology-only model with COMSOL (Cardiff et al., 2023) as red curves, modeled pressure calculated using the hydro-mechanical simulation with GEOS (case 40) as black curves. The title and subtitles give the total root-mean-square (TRMS) and root-mean-square (RMS) residual difference between observed and simulated pressure values for the COMSOL (C) and GEOS (G) models respectively.

Calibration of short-term H-M model on seismic observations (Subtask 9.4 and TPM 1)

In Subtask 9.4, we have calibrated the short-term H-M model using the timings, locations, and focal mechanisms for microseismic events recorded before, during and after the shutdown in December 2016. To evaluate TPM 1, we evaluate the Coulomb failure criterion on sets of planes using the simulated stress field calculated by a GEOS solution. We assume that the rock is critically stressed during normal operations.

Following equation (3) of Oppenheimer et al. (1988), we write the proximity of a rock volume to failure as a Coulomb failure function $F = |\tau_p| - \mu(\sigma_p - p) - S_0$,where |τP| is the magnitude of the shear traction vector, σP is the normal traction (a scalar) and p is the fluid pore pressure within the rock. We assume that the internal friction coefficient μ = 0.6 and that cohesion S0 = 0. We follow more recent conventions and denote the value of F as CFS and temporal changes in F as ΔCFS. Since the magnitude of the shear stress is always positive, CFS does not distinguish between dextral and sinistral shear. Similar notational conventions appear elsewhere (e.g., Vavryčuk, 2014; Kusumawati et al., 2021). Oppenheimer et al. (1988) also note that "a physical assumption implicit in the criterion is that the quantity σP – p [effective stress] be greater than zero; otherwise different modes of failure will occur", citing Jaeger and Cook (1979, p. 96). To follow this sign convention, as used in rock mechanics, we multiply each component of the stress tensor from GEOS by –1.

The ΔCFS values are calculated with respect to an (arbitrary) reference value CFS(tref) at time tref. In other words, at time ti, the change in Coulomb failure stress ΔCFS(ti) =CFS(ti) – CFS(tref). Since we assume critically stressed conditions at the reference time tref, a positive value of ΔCFS > 0 implies that failure is favored.

Here, we consider only the 32 microseismic events for which Guo et al. (2023) calculated a focal mechanism from seismic data. Each event includes two possible fault planes specified by their strike, dip, and rake (Figure 70). The Coulomb Failure Stress ΔCFS is positive for 28 of the 32 events (88%). This result is sensitive to the permeability values assumed in the modeling. For example, decreasing the permeability values in the X- and Y- directions by a factor of 10 increases the number of events for which ΔCFS is positive from 28 to 29 of 32.

Next, we calculate the modeled change ΔCFS in Coulomb failure stress on the (hypothetical) optimally oriented plane at each grid point in a 3-dimensional grid with a spacing of 100 m. The model calculates ΔCFS at each 1-hour time step in the model.

To evaluate the timings of the microseismic events in TPM 1a, we extract the modeled change ΔCFS at the grid point nearest the precise location of each microseismic event at the corresponding time step in the model. Figure 72 and Figure 73 show results as time series for the shutdowns in 2016 and 2022, respectively. Of the ~1000 events during each shutdown, a majority occur when the modeled value of ΔCFS is above critical.

To evaluate the locations of the microseismic events in TPM 1b, Figure 74 and

UTM Easting [km]

Figure 75 show the results in map view the shutdowns in 2016 and 2022, respectively. In each case, most of the events occur in areas where the modeled value of ΔCFS is positive.

Table 19. Technical performance metrics (TPMs 1a and 1b) for microseismic events (columns) at several levels of performance (rows).

	TPM 1a Microseismic Events: location		TPM 1b Microseismic Events: time	
Current state of the art in 2020	Location	250 m		
Minimum requirement from SOPO	location	250 m		
Target level from SOPO	location	100 m		
Realized in 2021 from existing data (Task 5)	2016 shutdown	72 m	—	—
Realized 2024 on calibration data set (Task 9)	Position residual is defined as the minimum distance between the observed event location during 2016 shutdown and the modeled contour ΔCFS = 0	TBD	Percentage of events during 2016 shutdown that occur when ΔCFS > critical	**60%**
Realized 2024 on auditing data set (Subtask 9.5)	*MSEs during 1-month deployment before, during, and after 2022 shutdown*	TBD	Percentage of events during 2022 shutdown that occur when ΔCFS > critical	**85%**

Cells shaded in green indicate that the TPM successfully met the specification. Cells shaded in yellow indicate caveats discussed in the narrative. Magenta-colored text indicates quantities to be determined (TBD).

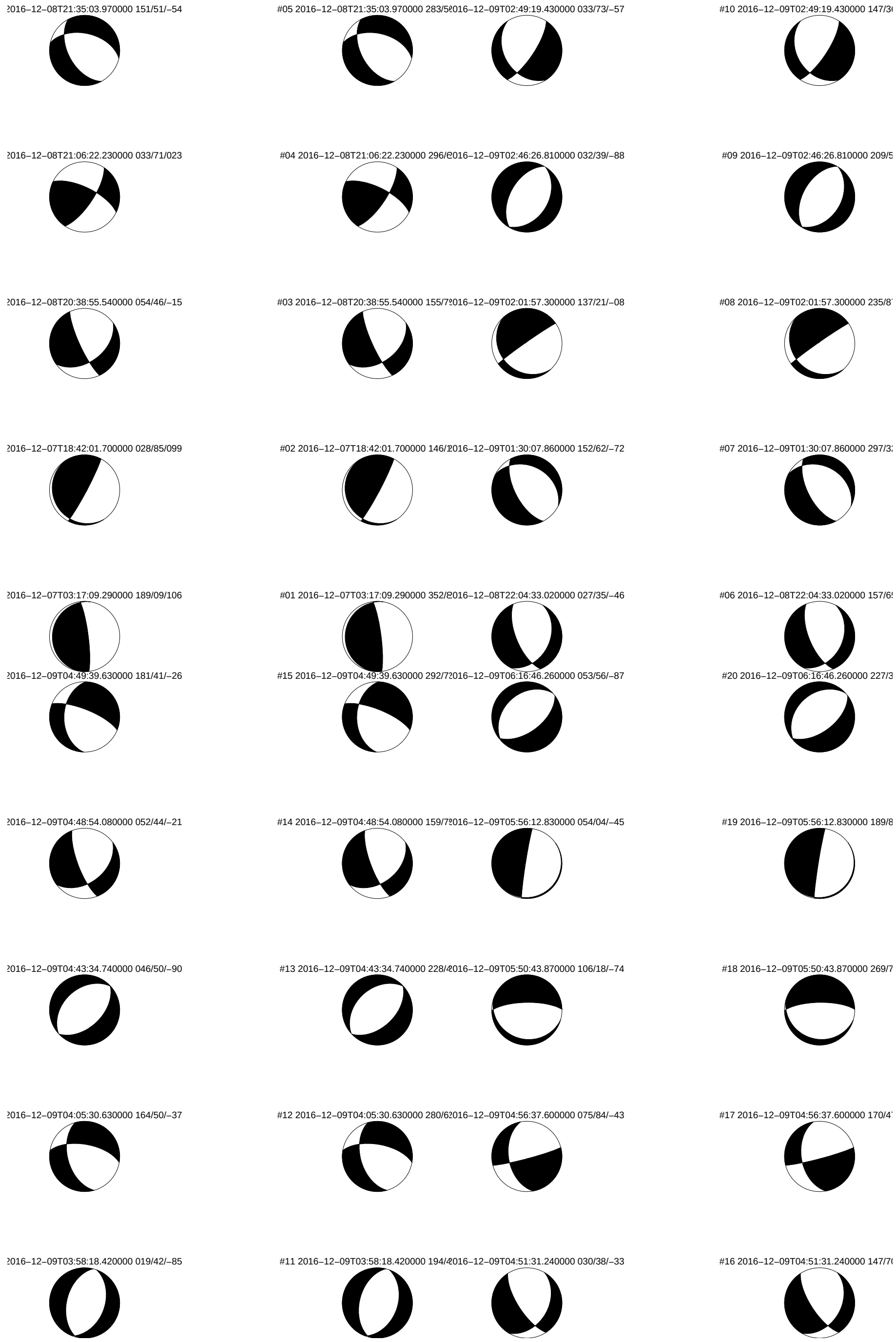

Figure 70. Fault plane solutions for microseismic events in December 2016 listing time of event as well as strike/dip/rake for each of the two possible fault planes (Guo et al., 2023).

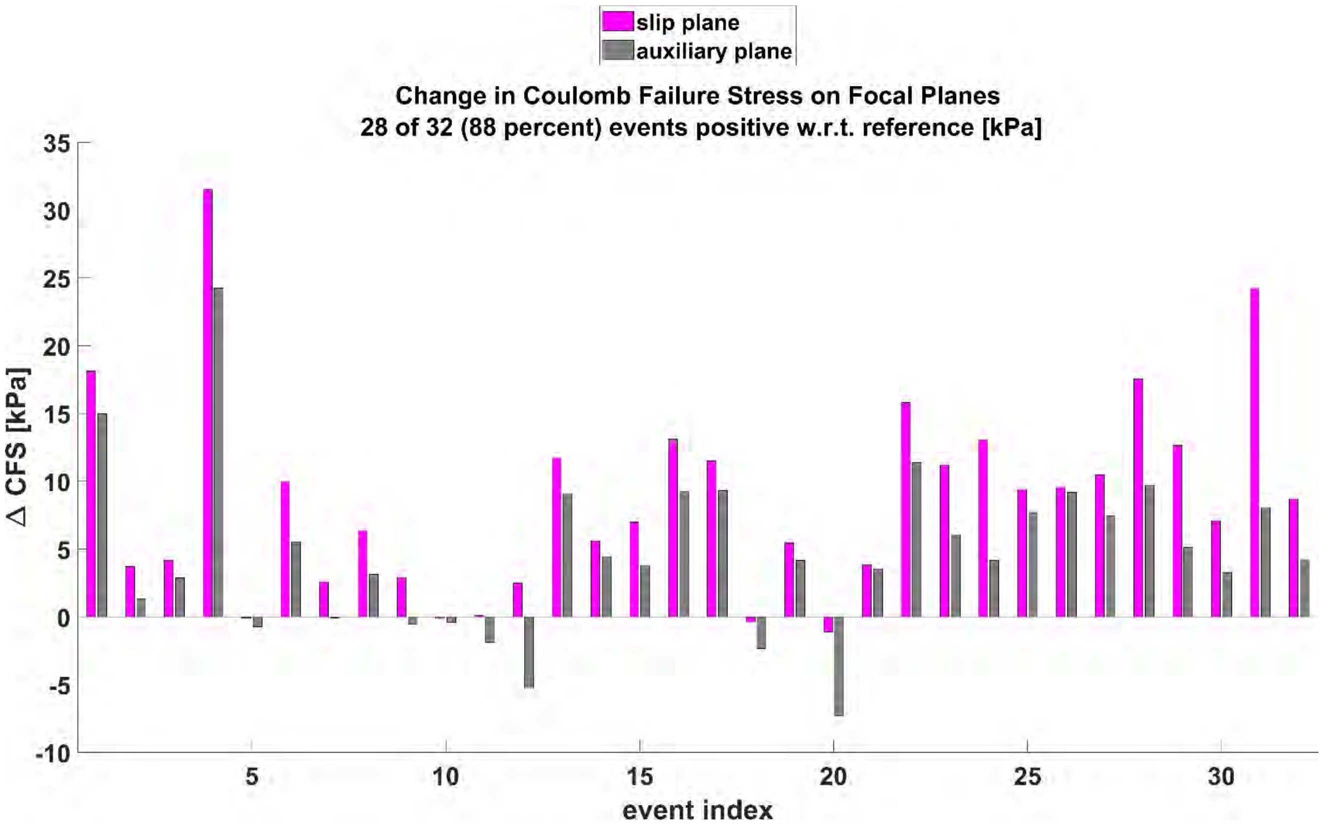

Figure 71. Modeled change in Coulomb Failure Stress (ΔCFS) calculated on fault planes inferred from seismic data in December 2016 {Guo, 2023 #50405}. For each event, the magenta bar corresponds to ΔCFS in kPa to the fault plane, the gray bar to the auxiliary plane. According to the sign convention used in rock mechanics, positive values of ΔCFS indicate conditions favorable to fault slip. The ΔCFS values are calculated with respect to a reference time of 2016/12/08 19:23 UTC, i.e., ten minutes before the shutdown began.

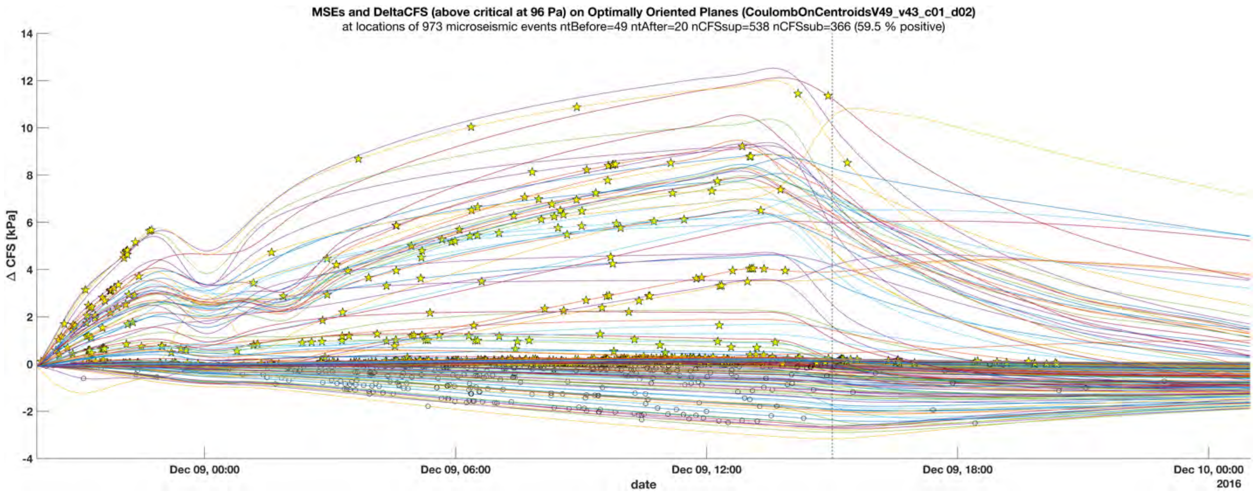

Figure 72. Time series of the change in Coulomb failure stress ΔCFS on hypothetical optimally orientated planes. The calculation includes the microsesmic events during the 2016 shutdown that have been precisely relocated using the REST workflow described above (Thurber et al. 2024; m.s. in preparation).

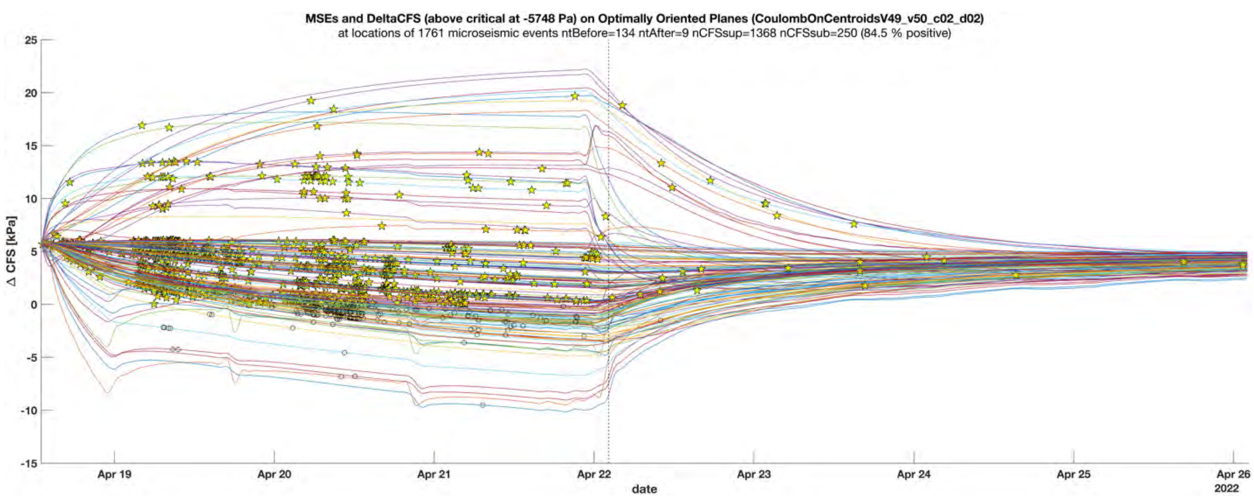

Figure 73. Time series of the change in Coulomb failure stress ΔCFS on hypothetical optimally orientated planes. The calculation includes the microsesmic events during the 2022 shutdown for which precise locations are available (Guo et al., submitted 2024/08/22 to Geophys. Res. Lett.).

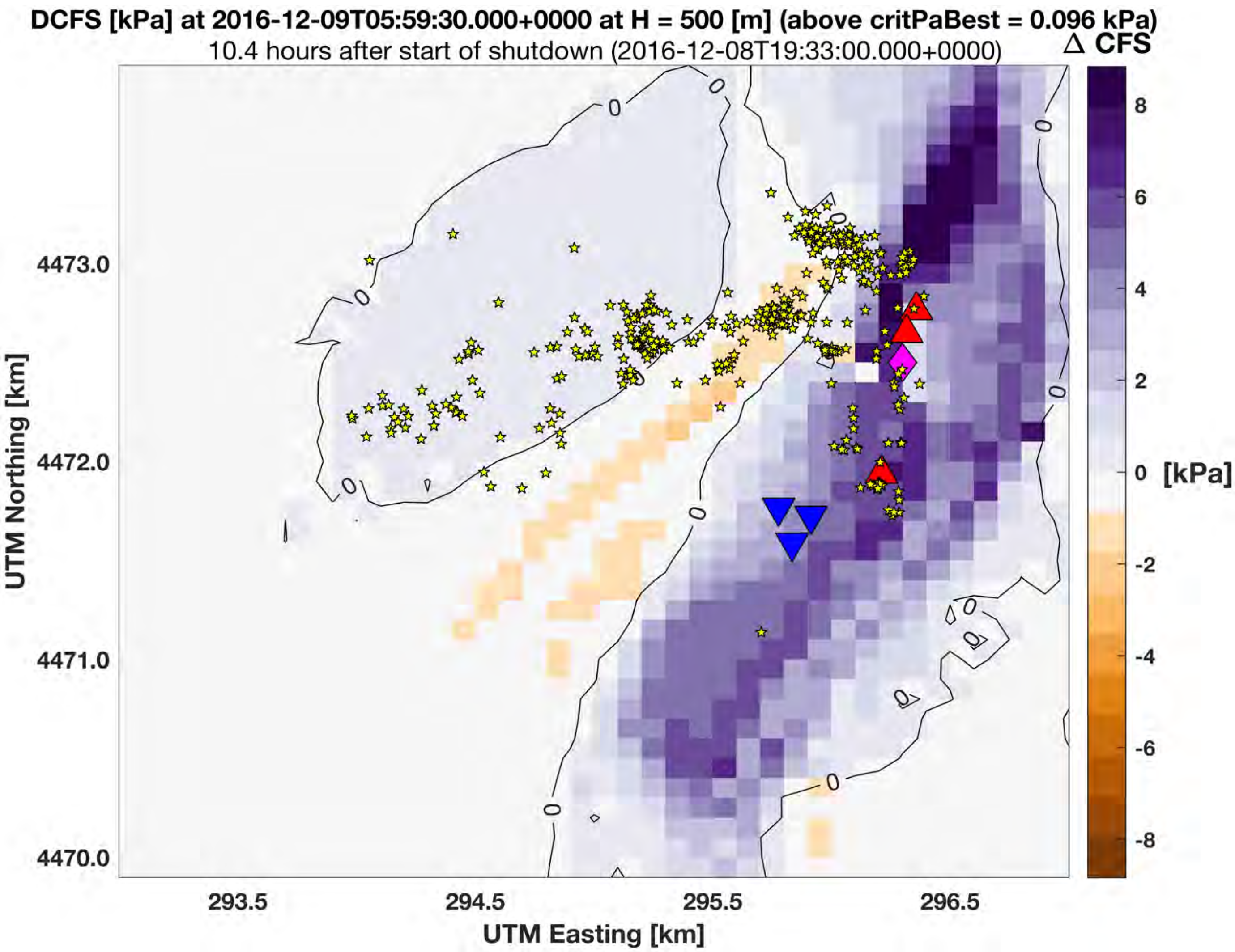

Figure 74. Numerical solution for changes ΔCFS in Coulomb failure stress on a 3D field in response to the shutdown of reservoir operations in December 2016. The map shows the modeled values of ΔCFS calculated at t_i = 2016/12/09 00:59:30 UTC, i.e. 5.4 hours after the shutdown began. The reference time is t_{ref} = 2016/12/08 18:33 UTC, i.e., one hour before the shutdown began. Yellow stars indicate precise locations of microseismic events which occurred during the time interval $t \in [t_{ref}, t_i]$ as determined using the REST workflow described above (Thurber et al. 2024; m.s. in preparation). The modeled values of ΔCFS at an elevation H = 500 m above the WGS84 geoid, i.e. depths of approximately 700 m below the ground surface. Triangles indicate wells: red for production, blue for injection. The magenta lozenge indicates the location of a representive point located near the primary production wells.

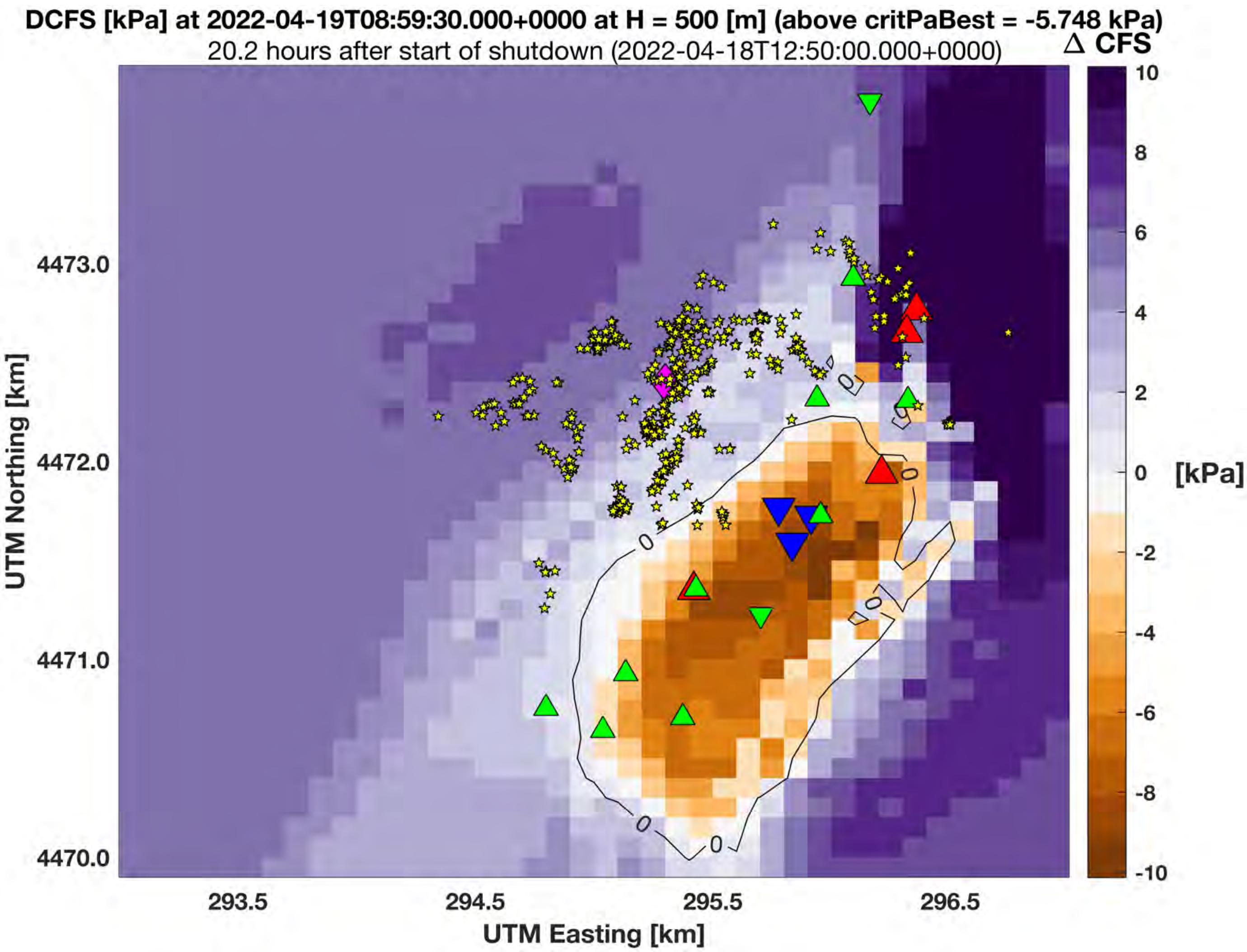

Figure 75. Numerical solution for changes ΔCFS in Coulomb failure stress on a 3D field in response to the shutdown of reservoir operations in April 2022. The map shows the modeled values of ΔCFS calculated at t_i = 2022/04/19 00:59:30 UTC, i.e. 20.2 hours after the shutdown began. The reference time is t_{ref} = 2022-04-18 12:50:00, i.e., when the shutdown began. Yellow stars indicate precise locations of microseismic events which occurred during the time interval $t \in [t_{ref}, t_i]$ (Guo et al., submitted 2024/08/22 to Geophys. Res. Lett.). The modeled values of ΔCFS at an elevation H = 500 m above the WGS84 geoid, i.e. depths of approximately 700 m below the ground surface. Triangles indicate wells: red for production, blue for injection, green for observation. The magenta lozenge indicates the location of a representive point located at the epicenter of an microseismic event.

Calibration on All Observations (Subtask 9.5)

After calibrating the macroscale and mesoscale stress models of the geothermal system against the four key datasets (borehole, geodetic, observation well, and microseismic event locations) individually, we plan to incorporate the results into a consistent, fully-coupled, multi-scale model of the geothermal system.

SECTION VI: DISCUSSION –IMPROVING CONCEPTUAL MODELS

The vertical cross section in Figure 76 summarizes the structure of the geothermal system at San Emidio.

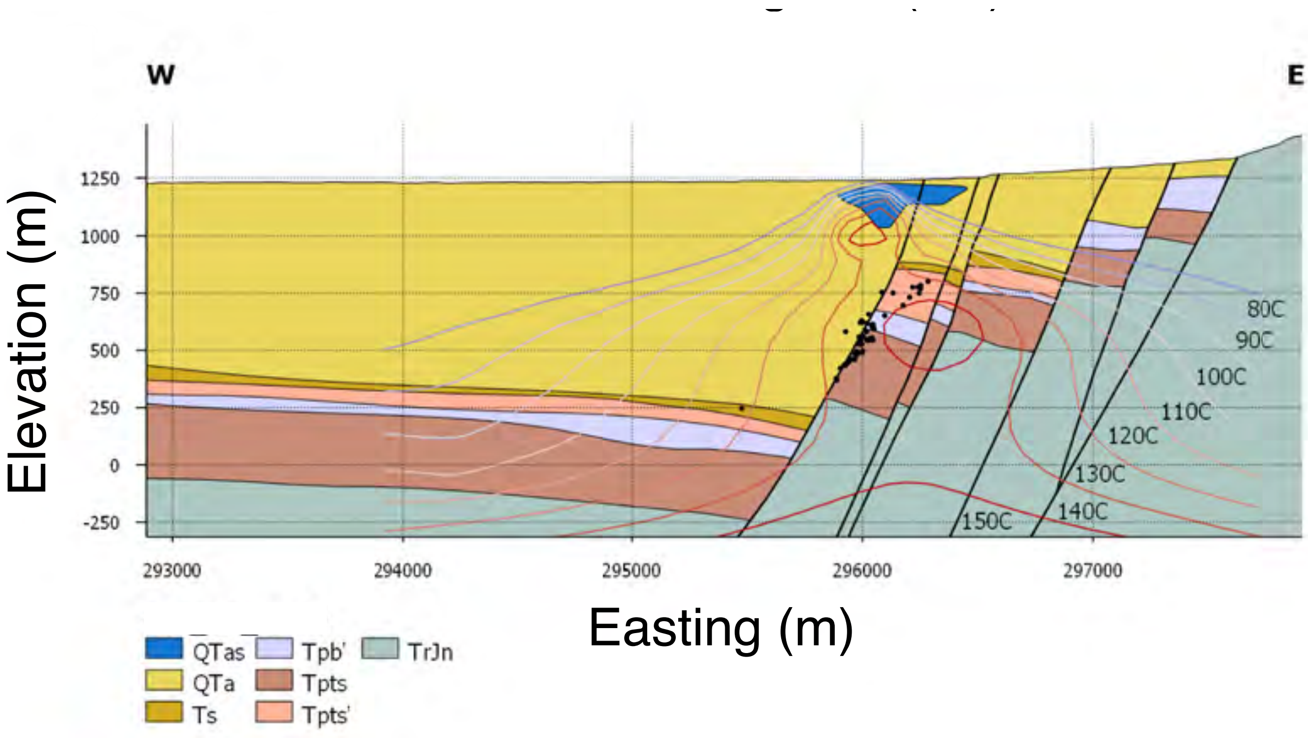

Figure 76. Geologic cross section, showing primary lithologic units, wells, and faults, as updated in 2022 with geologic units consistent with those mapped in the field (Rhodes et al., 2010; Rhodes, 2011; Rhodes et al., 2011). Color codes denote geologic units: QTas, silicified sediments; QTa, alluvium further subdivided by grain size and clay content; Ts, Late Miocene siltstones, tilted and indurated; Tpb', Upper basaltic andesite; Tpts, Lower tuffs; Tpts', Upper tuffs and tuffaceous sediments; TrJn, Nightingale formation. Vertical plane is an E-W transect at UTM Northing coordinate 472,900 m Red contour lines show the "natural state" temperature ranging from 80 °C to 150°C (Folsom et al., 2020). Relocated microseismic events (Guo et al., 2023) are shown as black dots. They and the faults have been projected from 200 m onto the vertical plane. Most of the hypocenters are located between the San Emidio Fault (SEF) and the Basin Bounding Fault (BBF). Horizontal axis shows Easting coordinate in meters. Vertical coordinate axis shows elevation above mean sea level (WGS 84 geoid) in meters.

Simple Conceptual Model

How can we explain the observation that the microseismic events tend to occur when the power plant is NOT operating, neither producing nor injecting? We hypothesize that it has something to do with the wells, or at least the fluids around them. We first observed this phenomenon at Brady Hot Springs during the PoroTomo experiment. We hypothesized a mechanism in 2018 by publishing a peer-reviewed paper by Cardiff et al. that includes many of the WHOLESCALE team members as co-authors. As sketched in Figure 77, the basic idea is that production causes drawdown. When pumping stops, the fluid pressure recovers. Let's look at a point at a specific depth near a production well. During normal operations, the drawdown creates a so-called "cone of depression" around the production well. At our observation point, the pore-fluid pressure is low, the effective normal stress is high, and a potential fault is clamped. Once the pumping at the production well stops, though, the fluid level recovers, the pore pressure increases, the slip tendency increases, and microseismic events are more likely. The bottom line is that fluid pressure recovers when production stops.

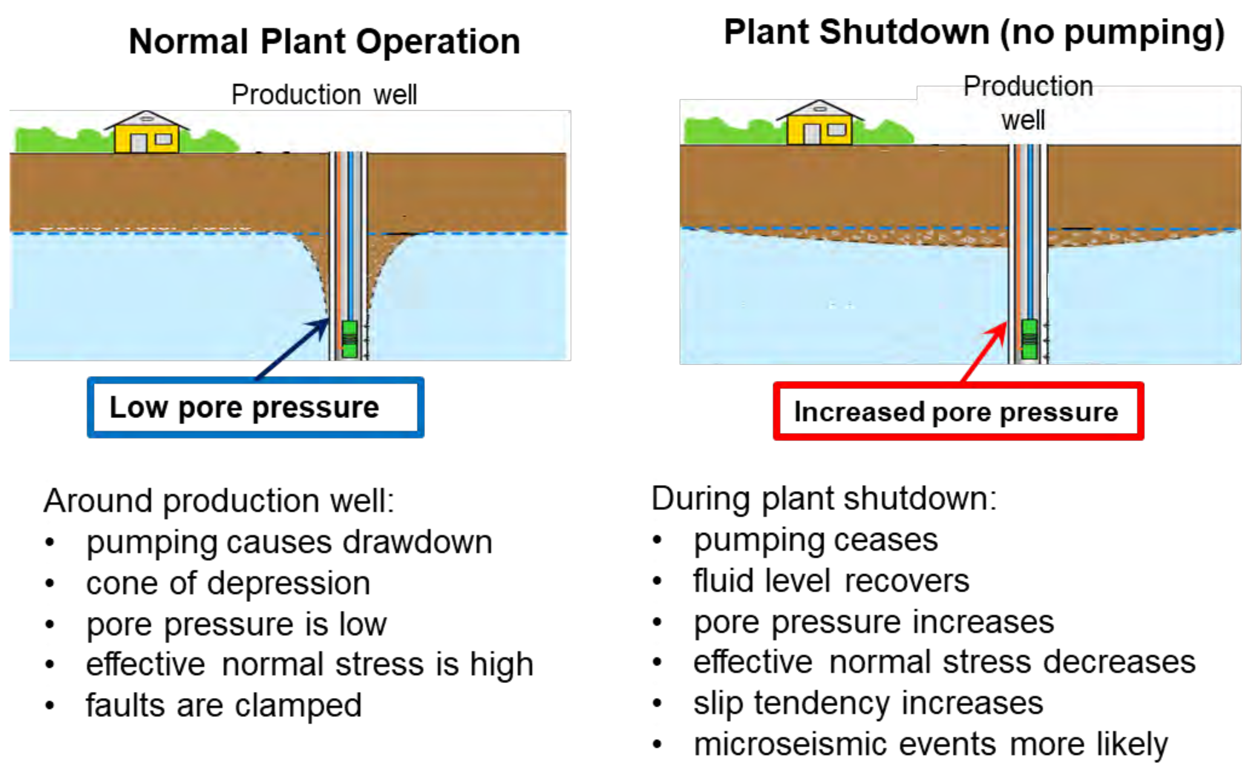

Figure 77. Visualization of changes in pore pressure and effective stress near a production well during normal plant operations (left) and during a shutdown (right). In both panels, the upper edge of the blue-shaded area is a heuristic representation of the hydraulic head, e.g., the so-called "water table".

Critical value of pore-fluid pressure

The following section is excerpted, nearly verbatim, from a peer-reviewed paper (Guo et al., 2023).

We propose a conceptual model for the microseisms associated with the cycle of plant operations. As sketched in Figure 78, this model describes how the pore-fluid pressure P_p (blue curve) and critical pore pressure P_{crit} (red curve) evolve over time due to changes in plant operations and reservoir stress, . As defined in reservoir geomechanics (e.g., Zoback, 2007), the critical pore pressure P_{crit} is the magnitude of pore pressure above which faulting is induced, which depends on the reservoir stress state and frictional strengths of faults. Here we describe how P_{crit} is related to the reservoir stress state and fault strength.

First, we clarify the underlying assumptions and the mechanical setting. In this discussion, compressional stresses are reckoned positive. As constrained by Guo et al. (2023) and Jahnke et al. (2023), the faulting environment is either normal faulting ($S_v > S_{Hmax} > S_{hmin}$) or trans-tensional ($S_v = S_{Hmax} > S_{hmin}$), where S_v, S_{Hmax}, and S_{hmin} are vertical, maximum horizontal, and minimum horizontal principal stresses, respectively. We assume the vertical stress S_v to equal the maximum principal stress σ_1 because secular strain rates from GPS show areal dilation at San Emidio, according to Kreemer et al. (2012). Consequently, the minimum principal stress σ_3 equals the minimum horizontal stress S_{hmin}. If we consider failure on optimally oriented fault planes, which is the case for the normal faults in San Emidio, then the relation between the magnitudes of the principal stresses and the pore pressure P_p at failure can be described using the Coulomb criterion as:

$$S_v - P_p = (S_{hmin} - P_p)(1 + \sin\varphi)/(1 - \sin\varphi) \tag{6}$$

where φ is the friction angle. From equation (6), we can derive the expression for P_{crit} by solving for P_p,

$$P_{crit} = [(1 + \sin\varphi)/2\sin\varphi]\, S_{hmin} - [(1 - \sin\varphi)/2\sin\varphi]\, S_v \tag{7}$$

This equation provides the magnitude of P_p required to induce slip, given knowledge about the principal stress magnitudes. Because S_v does not change due to reservoir cooling or local tectonics considered here, the *change* ΔP_{crit} the critical pressure is influenced only by the change ΔS_{hmin} in the minimum compressive horizontal stress.

$$\Delta P_{crit} = [(1+\sin\varphi) / 2\sin\varphi]\, \Delta S_{hmin} \tag{8}$$

If we assume a friction angle φ = 30 degrees, typical of crustal materials, then equation (8) shows that the change ΔP_{crit} in the critical value is a factor of 1.5 greater than ΔS_{hmin}.

Next, we discuss qualitatively how ΔS_{hmin} and ΔP_{crit} evolve over time during plant operation. Before the beginning of production, we assume that the crust is critically stressed such that P_p and P_{crit} are at the same level. During normal operations, pumping at production wells decreases pore pressure P_p. At the same time, a combination of thermoelastic contraction and tectonic loading could decrease the minimum horizontal principal stress S_{hmin} and thus P_{crit} according to equation (8). As a result, P_p remains below P_{crit} and seismicity is inhibited.

During the shutdown time interval (shaded in gray in Figure 78), the pore pressure P_p recovers rapidly and exceeds P_{crit}, inducing microseismicity. After production resumes, P_{crit}

decreases at a similar rate as before the shutdown due to reduced S_{hmin} whereas P_p decreases more quickly to a value less than P_{crit} and thus inhibits microseismicity.

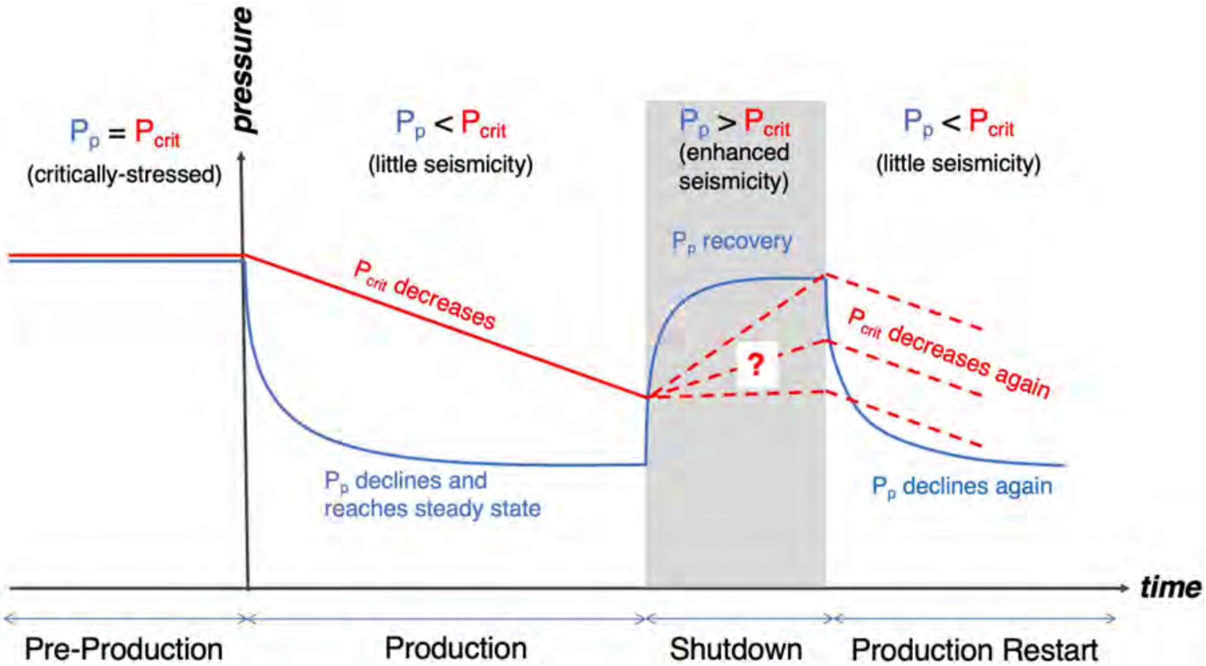

Figure 78. Schematic diagram of mechanism for inducing microseismicty during the production pumping cessation at San Emidio. The time axis divides reservoir behavior into four operational periods: Pre-Production, Production, Shutdown, and Production Restart. The interplay of critical pore pressure P_{crit} (red curve) and reservoir fluid pressure P_p (blue curve) illustrates the mechanism for induced microseismic events (Guo at al., 2023). The shutdown at San Emidio in December 2016 (gray shaded area) continued for about one day.

Cyclic behavior

This section is excerpted essentially verbatim from the proceedings of a conference (Wang et al., 2024).

Extraction of heat from geothermal reservoirs requires a working fluid circulating in hot rock. Efficiently managing the resource must consider how fundamental physical variables of temperature and fluid pressure control reservoir stresses. Simulating thermal-hydrologic-mechanical (T-H-M) processes in heterogeneous rock is typically approached using numerical models calibrated and validated from field observations. T-H-M models are based on conceptual models and idealized physics. The WHOLESCALE project at the San Emidio Geothermal Field uses Lawrence Livermore's GEOS code to model the three-dimensional stress field through time (Feigl et al., 2024; Luo et al., 2024). The code allows for geometric flexibility, heterogeneity, and coupling between thermal (T), hydrologic (H), and mechanical (M) processes as well as limited chemical (C) but not biological (B) processes. Although T-H-M codes are indispensable tools for understanding reservoir behavior for reservoir management, their complexity and detail can obscure the controlling processes. Another difficulty is choosing an appropriate mesh and time step that are numerically reasonable because observations may span many orders of magnitude in space and time, e.g., deformation over months and years associated with InSAR and rapid microseismic events too small to be captured by InSAR.

The WHOLESCALE project is a case study of the stress evolution of a geothermal reservoir. Focus was placed on approximately annual maintenance shutdowns when all injection and production pumping ceased and rapid changes of fluid pressure occurred. Seismic networks were in place near production wells for a few days before and after shutdowns in December 2016 (Warren et al., 2018), March 2021 (Thurber et al., 2022), and April 2022 (Thurber et al., 2024). Microseismic event clusters occurred for each of these years immediately following pumping cessation in the same small region and few microseismic events occurred before or after the shutdown. The 2021 array of 37 three-component nodes was a preliminary experiment for the larger deployment in 2022 of 450 three-component nodes. The 2022 data are still being analyzed. Therefore, the analysis in this paper is based on microseismic events detected in 2016 by 1302 vertical-component seismographs with 80-meter spacing (Guo et al., 2023).

The semi-quantitative analysis consists of three detailed WHOLESCALE studies conducted for the 2016 shutdown – seismic analysis of microseismic events for locations, focal mechanisms, and coda magnitudes (Guo et al., 2023), hydrologic simulation (Cardiff et al., 2023), and geomechanical stress inversion of focal mechanisms (Jahnke et al., 2023). Guo et al. (2023) interpreted their observations with a scenario in which microseismic events are the result of time-varying changes in reservoir fluid pressure (Figure 78).

An almost universally adopted assumption underlying their scenario is that slip occurs on shear discontinuities when the Coulomb Failure Stress *CFS* exceeds some critical value. As defined above, this definition involves the shear stress, the coefficient of friction, the normal stress, and the pore-fluid pressure.

We address three aspects of Figure 78: (1) the numerical values for the axes, (2) choosing among the three dashed-line paths for the critical value of pore pressure P_{crit} during the shutdown period, and (3) the recurrence of microseismic events in the same general area. The field Kaiser effect in crystalline-rock geothermal reservoirs will be invoked as part of the interpretation. The

Kaiser effect is the empirical observation that faults/fractures have a “memory” of the maximum stress state at which they previously experienced failure (Zang et al., 2014).

In the sections that follow, we first establish the state of stress using a simple hydro-geomechanical model of fluid extraction near a normal fault. Then we consider the different operational periods by focusing on the six days of microseismic activity around the shutdown that began on December 8, 2016. We then consider the production periods before and after the shutdown period. Finally, we discuss the modeling choices and assumptions that produced a microseismic event cycle.

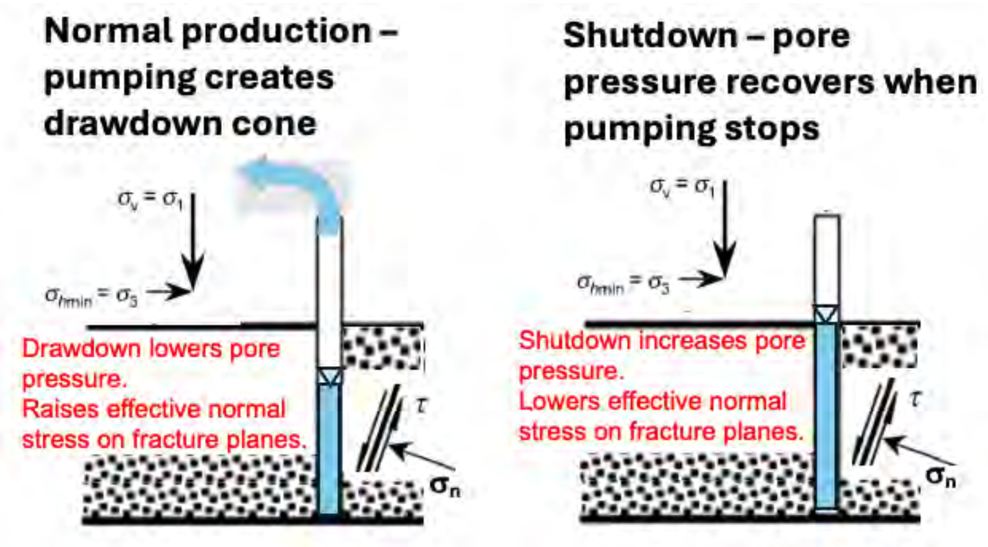

Figure 79. Sketch of conceptual hydro-mechanical response to production versus cessation of pumping. During production effective normal stress increases on nearby dipping failure planes. When pumping stops, effective normal stress decreases on nearby failure planes to trigger microearthquakes (adapted from Dusseault et al., 2001).

State of Stress

The geologic model (Figure 76) used by the WHOLESCALE team portrays the San Emidio geothermal reservoir as hot permeable rock within a zone of north-striking, west-dipping, normal faults in the Basin and Range Province (e.g., Rhodes et al., 2011; Folsom et al., 2020; Feigl et al., 2024; Luo et al., 2024). Jahnke et al. (2023) found S_{Hmax} to be oriented at N10°E (i.e., nearly parallel to the overall strike of the normal fault system) by considering the World Stress Map, slickenlines, wellbore stress indicators from nearby geothermal fields, and the secular strain rate. This stress state is used to define the “pre-stress” in the numerical modeling (Luo et al., 2024; Feigl et al. 2024). Microseismic events with coda magnitude less than zero were recorded in the northeastern part of the field between the San Emidio Fault (SEF) on the east and the Basin Bounding Fault (BBF) on the west at depths between 500 m and 800 m below surface (Guo et al., 2023). Figure 55 shows that the microseismic events are located along two distinct planes – the deeper one with the majority of events dipping ~60° and the shallower one with fewer events dipping ~40°.

Based on the geologic and finite-element models, we adopted the simple hydro-mechanical H-M model sketched in Figure 79 for first-order estimates of stress changes caused by poroelastic and thermal processes. Although Figure 79 represents normal faulting, the same Mohr-circle analysis applies for strike-slip because the vertical stress $S_v \cong S_{Hmax}$, where S_{Hmax}, the axis of maximum horizontal stress, is in the direction of strike (Jahnke et al., 2023). Similarly, the geometry of Figure 79 applies to heat extraction as well as fluid extraction, albeit with different boundary conditions.

Pressure Over Shutdown Cycle

We consider the two time intervals that establish a Thermal-Hydrologic-Mechanical (T-H-M) cycle of stress and pore pressure changes: 1) The 20-hour shutdown of plant operations for annual maintenance and 2) The 364 days of geothermal energy operations through fluid injection and production. We begin by focusing on the 20-hour shutdown period on December 8, 2016 because the microseismic events that occurred immediately after cessation of pumping and pore pressure increase near production wells are the observations from which our conceptual model can be analyzed semi-quantitatively. We then proceed to the subsequent production period that begins after normal injection-production pumping resumes. We used self-consistent values for the initial condition at shutdown, which lead back to the same values at the end of a year to explain recurring microseismic activity associated with maintenance shutdowns. In this way, we backtrack to the production period preceding shutdown but do not consider the pre-production period

We assume the reservoir is in a critical stress state at the start of shutdown at a depth of 700 meters where microseismic events occur. Therefore, the reservoir fluid pressure is set equal to the critical fluid pressure, that is, $P_p = P_{crit} = 7000$ kPa for a slip plane dipping 60° (Table 20). The flow rate of 0.3 m^3/sec (nearly 5000 gal/min) just prior to December 8, 2016 went suddenly to zero. Cardiff et al. (2023) simulated fluid pressure recovery in the near-well region due to the sudden cessation of pumping using hydrologic properties obtained from earlier pumping tests. Within hours, increases of approximately 40 kPa occurred at lateral distances of several hundred meters from the pumping wells, which decreased to 10 kPa at distances of one kilometer. Significantly, the simulated rapid pore pressure recovery occurred in the region near the production wells where microseismic events were located. Similarly, pore pressure increases of ~150 kPa were measured and modeled during a plant shutdown at the geothermal field at Brady Hot Springs, Nevada (Patterson et al., 2017; Cardiff et al., 2018). Under the assumption of an initial critical stress state in the fault zone, these small pressure increases were sufficient to trigger microseismic events.

Guo et al. (2023) obtained locations and coda magnitudes of ~100 microseismic events over several days before, during, and after the plant shutdown (Figure 80). Only minor microseismic activity occurred before or after the shutdown period. During the 20 hours of shutdown, three broad clusters of events occurred. Microseismic activity leads to a redistribution of stresses to re-establish equilibrium of the rock mass plus a small hysteretic strengthening according to the Kaiser effect (Zang et al., 2014). We treat the strengthening as a linear increase of P_{crit} from its initial value to a value 50 kPa larger over 20 hours.

This brings us to the end of the shutdown period, when we have $P_{crit} = P_p = 7050$ kPa. The transient response of P_{crit} and P_p to microseismic activity and hydrologic recovery is summarized in Figure 81a. The changes in fluid pressures from first-order simple stress calculations are consistent with finite-element modeling of *changes* in pore and critical pressure by Luo et al. (2024). As shown in Figure 71, the change in Coulomb failure stress ΔCFS was between 10 and 50 kPa for 28 of 32 microseismic events during the shutdown period for which focal mechanisms were determined by Guo et al. (2023). The Coulomb Failure Function increases are generally smaller than Kaiser-effect strengthening in other studies. However, Liu et al. (2011) estimated values as small as 10 kPa, although they more typically found values of several hundred kPa for a series of four earthquakes of increasing magnitude between 2 and 4 at the Danjiangkou Reservoir in Hubei Province, China, which were interpreted to be a stress-memory sequence.

Given the small magnitudes of the San Emidio microseismic events, a speculative but plausible explanation is that the triggering threshold scales with the size of discontinuity that is activated.

The initial condition for the production period after the pumps restart is that at the end of the shutdown period, $P_{crit} = P_p = 7050$ kPa (Figure 81a). Resumption of pumping leads to sudden, rapid drawdown of P_p near the production wells that brings pore pressure back to its pre-shutdown value. This rapid drawdown period is approximately one day in duration whereas the production period is on the order of a year. The different transient responses of P_p and P_{crit} reflect different T-H-M processes over these different time spans. The short time scale of one day after production resumes is dominated by the transient drawdown of P_p near the production wells whereas the reservoir gradually cools at an estimated rate of one degree Celsius per year over the longer time scale of one year. The resulting reservoir contraction decreases P_{crit}, that is, it increases the tendency for slip on the normal faults SEF and BBF.

An estimate of the effect of cooling on P_{crit} can be made from the mathematical equivalence of the constitutive equations of poroelasticity and thermoelasticity. Equating volumetric strain due to a change in pore-fluid pressure ΔP_p with that due to a change in temperature ΔT gives

$$(1/H)\Delta P_p = \alpha \Delta T \tag{9}$$

where H is the poroelastic expansion coefficient and α is the volumetric thermal expansion coefficient (Wang, 2000). The term H is equal the Biot-Wills coefficient K/α_{BW} is

$$\alpha_{BW} = 1 - K/K' \tag{10}$$

where K is the drained bulk modulus of the porous medium, and K' is the bulk modulus of the solid constituents. The Biot-Willis coefficient will have a value of about $a_{BW} = 0.75$ at reservoir depth. The caveat in this analogy between poroelastic and thermal effects is that the boundary conditions differ. For example, a Coulomb Failure criterion might be applied on a basin bounding normal fault whereas a Newton's law-of-cooling or specified temperature profile condition might be applied in the thermal model.

Next, we consider an order-of-magnitude estimate of the changes in fluid pressure and temperature. Using plausible values for the expansion coefficients suggests that the ratio ΔP/ΔT is between 10 and 100 kPa/°C (Table 20. Principal stresses, hydrostatic fluid pressure, P_{hydro}, resolved shear and normal stress on fault planes, and critical pore pressure at depths where microseismic events occur. The values are from the stress inversion by Janke et al. (2023) for the 1636-m deep Kosmos 1-9 well.

Depth, m	$S_V \cong S_{Hmax}$, MPa	S_{hmin}, MPa	P_{hydro}, MPa	Fault dip, degrees	Shear stress, MPa	Normal stress, MPa	P_{crit}, MPa
500	12.0	7.2	3.5	60	2.1	8.4	4.9
				40	2.4	10.0	6.0
600	14.4	8.6	4.2	60	2.5	10.0	5.8
				40	2.9	12.0	7.2
700	16.8	10.1	4.9	60	2.9	11.8	7.0
				40	3.3	14.0	8.5

Table 21). In other words, a temperature decrease of 1°C means that the same strain would result from a fluid pressure decrease of 100 kPa for values in the first row and 10 kPa for values in the second row. A temperature decrease of 0.5°C and a thermal expansion coefficient α of 5 × 10^{-5} would be equivalent to a decrease in P_{crit} of 50 kPa for the values in the first row. These estimates imply that temperature decline over a year would decrease P_{crit} by approximately the same amount as the strengthening from the Kaiser effect during the shutdown period (Figure 81b).

In summary, a plausible explanation for the repeating pattern of microseismic events from shutdown-to-shutdown is that the combination of Kaiser-effect strengthening and temperature weakening offset each other between shutdowns. If this hypothesis is correct, then we would expect that "older" geothermal reservoirs are likely to see decreases in seismicity as the temperature field stabilizes.

We now consider the production period for the year *preceding* the December 2016 shutdown. In Section 3.2 we described the rapid post-shutdown decline of P_p in response to resuming operations and the gradual lowering of reservoir temperature over the year. The net result was that P_{crit} and P_p at the end of a full-year production period returned, by design, to exactly the same initial values chosen for them at the start of the shutdown period. We assume the shutdown production period is equivalent to the shutdown production period, therefore being consistent with a scenario in which microseismic events recur repeatedly.

To review, the three sets of observations that facilitated a semi-quantitative analysis of pore pressure and critical pressure during the shutdown period and post-production period were:

1. Coda magnitudes and focal mechanisms of ~100 microseismic events obtained from an array of 1302 geophones operating for six days that bracketed December 8, 2016.
2. Principal stress directions obtained from inverting the microseismic focal mechanisms and other stress indicators.
3. Pressure changes simulated using parameters obtained by modeling pumping tests. Pressures measured in the reservoir during shutdown allowed us to validate these order-of-magnitude modeled pressure changes.

These observations were combined with a hydro-geomechanical model of slip occurring on small fractures aligned with regional geologic structure and a hypothetical average annual reservoir temperature decline of the order of ~1 °C/yr.

Discussion

The hypothesized sequence of reservoir changes in fluid pressure, microseismic activity, and temperature results in an cyclic sequence of microseismic events (Figure 82). The argument can be critiqued for its fine-tuned balance of processes that weaken and strengthen meter-scale fractures. Uncertainties of at least a factor of two are likely for the *changes* in P_{crit} and P_p at each step in Figure 82, and, therefore, the net-zero change of critical pressure could as easily have been several hundred kPa. Thus, some selective choices were made to present a heuristic, semi-quantitative justification of the T-H-M scenario.

In the remainder of this section, we address several uncertainties and assumptions that challenge the delicate balance of small stress changes in the closed-loop T-H-M scenario presented in Figure 82. Although we can dismiss some, others are problematic. Specifically, we consider the: (1) decadal-scale tectonic changes that modify stresses in the geothermal field, (2) net changes in reservoir fluid content, (3) diverse nature of hydrologic, microseismic, and stress field data in terms of spatial and numerical uncertainties, (4) slip-patch size, (5) magnitude of stress drop of microseismic events, and (6) Kaiser stress-memory effect

We estimated that reservoir cooling of 1°C per year was approximately equivalent to a stress relaxation on the bounding faults between 10 and 100 kPa depending on our choice for thermal expansion. Here we consider the magnitude of stress relaxation due to a tectonic strain rate in the northern Basin and range of 10 nanostrain/year (Bennett et al., 2003). Using a modulus of 20 GPa converts the strain rate to a stress change of 20 Pa/year, well below the Coulomb Failure Function change of 50 kPa due to pumping recovery. Therefore, the tectonic strain rate is considered negligible.

The geothermal plant operates with an above-ground, closed-loop system that transfers heat from the geothermal brine (from the production wells) to the motive fluid in the power plant. Then the cooled brine is pumped to separate injection wells. Therefore, we expect no significant reservoir contraction from the loss of subsurface brines. We also assume no significant recharge at reservoir depths.

The hydrologic, microseismic, and stress inversion results were integrated into the Coulomb Failure Function for the simple hydro-geomechanical model of the San Emidio fault zone (Figure 79). The hydrologic data were pumping test data whose changes were in the tens of kilopascals and whose spatial resolution was tens of meters. These data were appropriate for the T-H-M scenario. The microseismic events were generally located along a planar feature near the

BBF that was approximated by the simple hydro-geomechanical model applied to tiny slip patches of 1 to 10 meters (Figure 66 and Figure 79). The stress-inversion results from focal mechanisms would realistically only be quantitative at the megapascal level. Nonetheless, the values at 700-meter depth worked surprisingly well. After these choices were made for numerical values of initial stresses and pore pressure, the rest of the scenario's Coulomb Failure Function changes were rooted in the hydrologic data. The numerous assumptions mean that the model is a plausible, but not definitive, explanation for the recurrence of microseismic activity in the same region.

The size of a microseismic slip patch can be estimated from the seismic moment $M_o = GAU$, where G is shear modulus, A is fault area and U is mean slip. The moment is related to the seismic moment magnitude through the relationship (Hanks and Kanamori, 1979)

$$M_w = (2/3)\, log\, M_o - 10.7 \text{ (in cgs units)} \quad (11)$$

Taking $G = 20\ GPa$, the same as the poroelastic expansion coefficient in Table 2, a $M_w = 0$ earthquake can be viewed as occurring on a patch area $A = 100$ m^2 with displacement $U = 0.5$ *mm* and a $M_w = -2$ earthquake as having $A = 1$ m^2 and $U = 0.05$ mm. In other words, a rectangular or circular slip patch would have length dimension between 1 and 10 meters. Thus, the size of the slip patches is small relative to the assumption of a uniform stress field in the fault zone where microseismic events occurred. Magnitudes between -2 and zero have been classified as "nano" earthquakes by Bohnoff et al. (2010).

The underlying assumption for microseismic events immediately after shutdown is that the fault zone contains many discrete slip patches with a distribution of orientations centered around the maximum principal stress direction. Individual patches might also have a distribution of frictional strength centered around a value of 0.6. Sudden failure on a small slip patch within the fault zone is presumed to be the source of microseismic events. Stress redistribution due to the slip event is spatially limited. Negligible stress interaction among slip patches is plausible given their small size.

Stress drops reported for shallow earthquakes are typically between 1 and 100 megapascals (Yamada et al., 2007; Abercrombie, 2021; Shearer et al., 2022). Stress drops appear to be largely independent of magnitude for $M > 6$, but with a tendency to decrease for smaller magnitudes. Stress drops of several megapascals are obtained for seismic events with magnitude less than one. Even a one-megapascal stress drop is 50-100 times the pore pressure increase during shutdown. If stress drops are several megapascals for the triggered microearthquakes at San Emidio, it is most likely that each small magnitude event occurs on a patch that had not slipped previously, obviating the need to rebuild the fault stress on a particular slip surface from one shutdown to the next.

Goertz-Allmann et al. (2011) measured stress drops for about 1000 earthquakes during hydraulic stimulation at the Basel geothermal site. The median $\Delta\sigma$ was 2.3 MPa. This value turns out to be almost perfectly consistent with the definition of seismic moment $M_o = GAU$ and Kostrov's (1974) stress drop equation $\Delta\sigma = GU/(cA^{1/2})$, where c is a geometric factor for patch shape (c=1 for a circle or square). Combining these two equations gives $\Delta\sigma = (G/c)(U/A^{1/2})$. If U scales with the linear dimension $A^{1/2}$, i.e., patch length, then $\Delta\sigma$ is scale independent. Based on the values for patch dimensions in Section 4.1, $\Delta\sigma$ = 2.5 MPa for both M_w = 0 and M_w = -2, that is, stress drop is invariant by the theory.

Given the small patch sizes computed from the moment magnitudes of the San Emidio microearthquakes, it seems most likely that they occur on individual patches (Kostrov, 1974). After a slip event, stresses redistribute in the fault zone and bring other favorably oriented patches into play for slip, either immediately (cascading) or at a future time, based on some statistical distribution of frictional strength. For a patch model, the magnitude of the stress drop is not an important factor for a cluster of microearthquake recurrence in the fault zone.

Alternatively, it is possible that mean stress drops might be less than one megapascal. Goertz-Allmann et al. (2011) observed that stress drop decreased by a factor of five as the pore pressure perturbation propagated radially. They found it plausible that this decrease could occur because effective stresses are decreased. Another explanation is that stress drops during shutdown at San Emidio are lower than predicted by the Kostrov (1974) theory. In Brune's (1970) model, stress drop for a given M_o is smaller for larger patch radius.

$$\Delta\sigma = 7M_0 /(16\, r^3) \quad (4)$$

Figure 83 is a plot of Eqn. (4) from Abercrombie's (2021) compilation. Several data sets from laboratory to field scale are shown on a plot of patch radius vs. seismic moment with stress-drop contours superimposed. The region of the plot most relevant to the microearthquakes during shutdown is for moments M_o between 10^6 and 10^9 Newton-meters, corresponding to moment magnitudes M_w between -2 and 0.

Different methods of obtaining stress drop give results that differ by orders of magnitude. For example, Longobardi et al. (2023) used a time domain method to find stress drops of 0.01 MPa for injection-induced earthquakes at The Geysers geothermal field, but Kwiatek et al. (2015) obtained stress drops of 1 MPa using a corner-frequency method. The earthquake magnitudes were between 1 and 1.5.

In summary, the stress drop of the triggered earthquakes at San Emidio might be anywhere from 10 kPa to several MPa, depending on how moment magnitude is interpreted for source parameters. Given the small size of slip patches, it is likely that a sufficient number of favorably oriented fractures are present to make recurrence on the same patch unlikely. If, on the other hand, stress drops were sufficiently small, patches could regain sufficient strength between shutdowns to slip again.

The Kaiser effect applies to re-activation of a slipped patch, which is unlikely to be the case. However, invoking the strengthening effect still applies in the sense that stress redistribution after a slip event requires triggering new, slightly stronger patches drawn from a statistical distribution of strength around the critical mean.

Another potential issue is that the observation of the field Kaiser effect in several enhanced geothermal projects was in the context of injection pressures on the order of megapascals (Baisch and Harjes, 2003; Kwiatek et al., 2014), whereas it is being invoked at San Emidio for small pressure increases of tens of kilopascals as drawdowns recover from shutdown near production wells. Some support for small Kaiser-effect stress memory values was noted in Section 3.1 in the case of reservoir-induced seismicity.

A final relevant case study for this discussion is that Kim and Avouac (2023) did not observe the Kaiser effect in the Otaniemei, Finland geothermal field. However, they attributed the absence of the Kaiser effect to injection locations far enough apart for different stimulation stages to mute the effect. Also, Kim and Avouac (2023) were able to model the Kaiser effect micromechanically, using rate-state friction. Previously, the Kaiser effect was primarily an empirical observation.

The San Emidio field experiment is a case study of a microearthquake cycle associated with several coupled T-H-M processes – heat extraction, fluid pumping changes, and microearthquake activity. The focus of the experiment was the 20-hour shutdown of all well injection and production on December 8, 2016. We have linked the T-H-M processes associated with the one-day perturbation caused by cessation and restarting of all pumping operations at the San Emidio geothermal field to the resumption of normal operations for a year. The T-H-M balancing mechanisms that led to a microseismic event cycle were: (1) slip on fractures and faults (M) within hours of pore pressure recovery at production wells (H), (2) strengthening due to Kaiser effect (M), and (3) sub-critical re-loading of the fractures and faults (M) due to reservoir temperature decline of a degree Celsius per year (T). The recurring nature of microseismic events implies fine-tuned coupling among T-H-M processes that produce stress changes of 10 to 100 kPa in geothermal reservoirs.

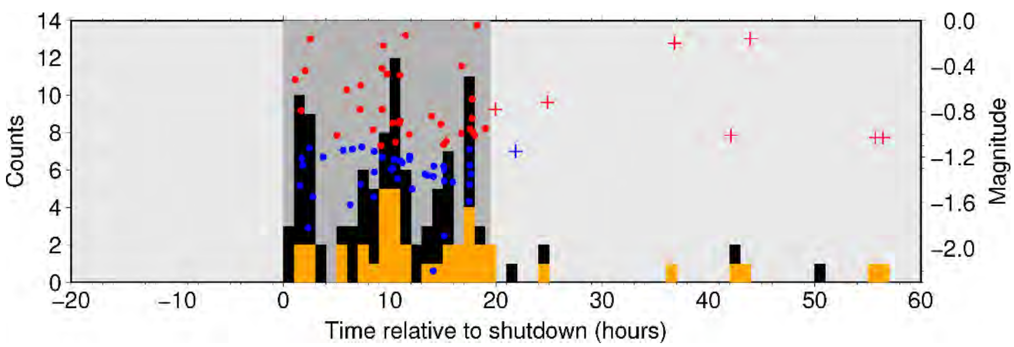

Figure 80. Microseismic event frequency with superposed coda magnitudes shown by crosses, dots, and pluses before, during, and after shutdown, respectively. Event detection might be affected by different day-night noise levels. Zero time is when shutdown began at 2016-12-08 19:33 UTC (Guo et al., 2023).

Table 20. Principal stresses, hydrostatic fluid pressure, P_{hydro}, resolved shear and normal stress on fault planes, and critical pore pressure at depths where microseismic events occur. The values are from the stress inversion by Janke et al. (2023) for the 1636-m deep Kosmos 1-9 well.

Depth, m	$S_V \cong S_{Hmax}$, MPa	S_{hmin}, MPa	P_{hydro}, MPa	Fault dip, degrees	Shear stress, MPa	Normal stress, MPa	P_{crit}, MPa
500	12.0	7.2	3.5	60	2.1	8.4	4.9
				40	2.4	10.0	6.0
600	14.4	8.6	4.2	60	2.5	10.0	5.8
				40	2.9	12.0	7.2
700	16.8	10.1	4.9	60	2.9	11.8	7.0
				40	3.3	14.0	8.5

Table 21. Reservoir fluid pressure change equivalent to 1°C temperature change. Other choices of the material coefficients scale proportionately according to Equation (9).

Poroelastic Expansion Coefficient, 1/H, GPa	Thermal Expansion, 1/°C	ΔP/ΔT, kPa/°C
20 GPa	10^{-5}/°C	100
20 GPa	10^{-6}/°C	10

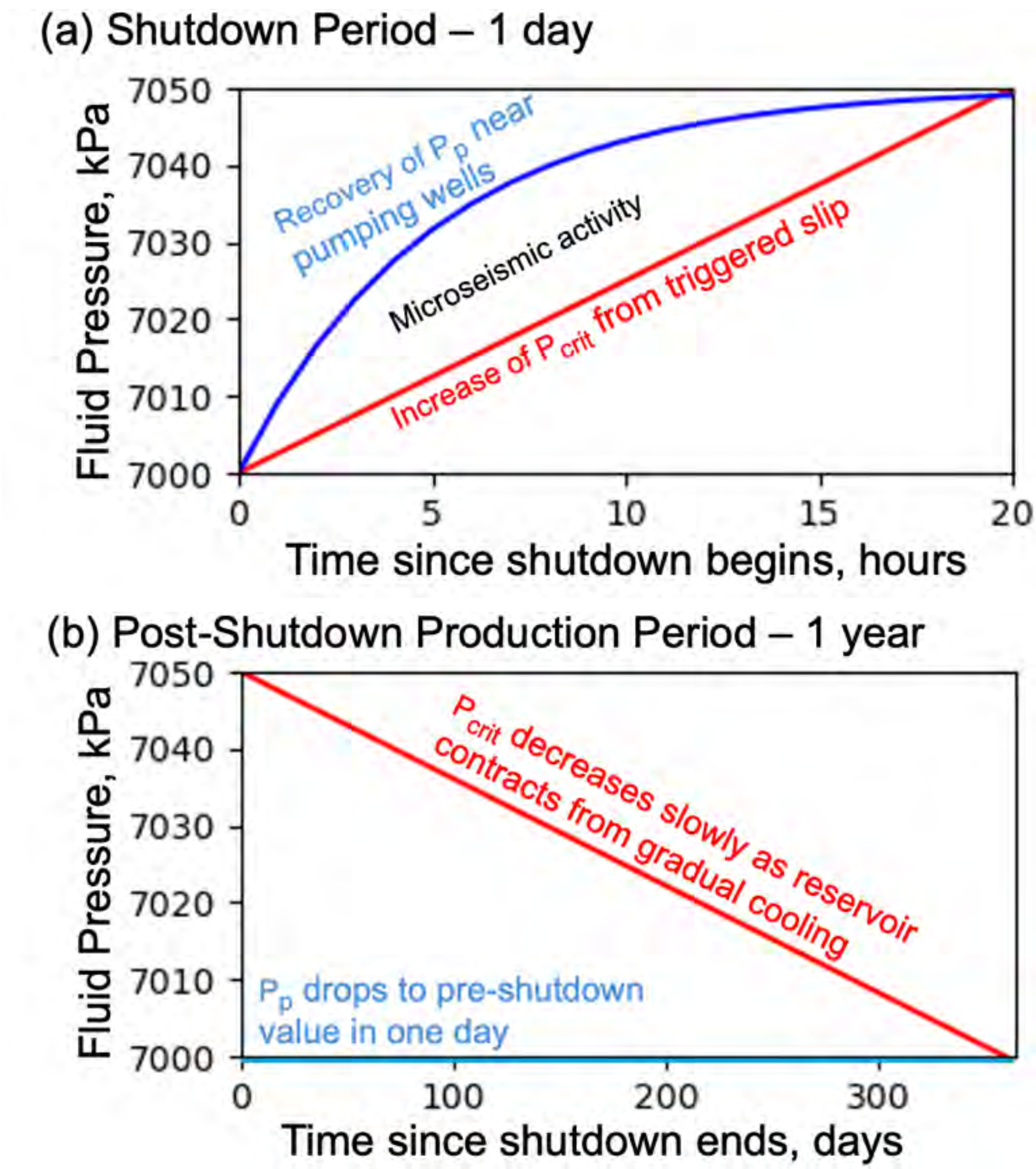

Figure 81. Conceptual modeling using estimates of critical pore pressure P_{crit} (red lines) and reservoir fluid pressure P_p (blue curves) during (a) 20-hour shutdown period and (b) one-year production period either before or after a shutdown period. The decrease of P_p between (a) and (b) is exponential for a time scale of hours in (a), but it appears as a step decrease for a time scale of several hundred days in (b).

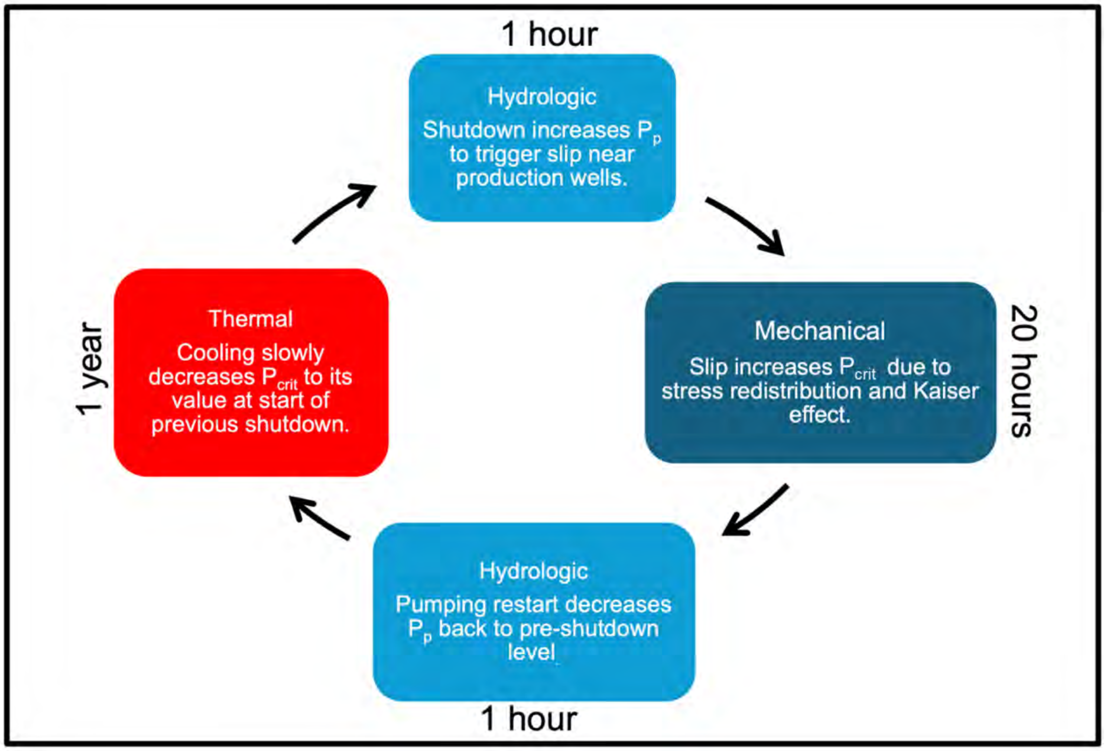

Figure 82. Hydrologic, Mechanical, and Thermal Processes that lead to microseismic earthquake cycle associated with annual shutdown of all pumping.

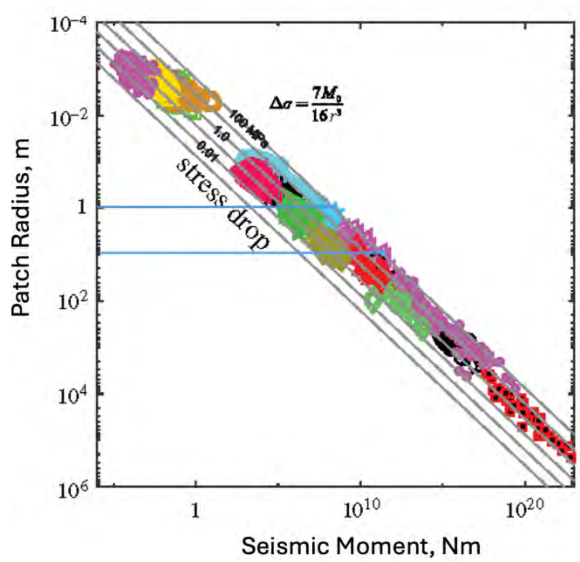

Figure 83. Slip-patch radius vs. seismic moment for different values of stress drop between 1 kPa and 100 MPa. The small rectangle between radii of 1 and 20 meters and seismic moment between 10^6 and 10^9 Nm, corresponds to moment magnitudes between –2 and 0. Colored blobs are different data sets from laboratory to field scale compiled by Abercrombie (2021).

SECTION VII. CONCLUSIONS

The rich, 4-D data sets at San Emidio constrain multiphysics T-H-M modeling. Synoptic measurements of pressure, seismicity, and deformation during three scheduled shutdowns provide information on the spatial distribution and temporal evolution of stress.

Laboratory testing shows little or no anisotropy in seismic velocity at the centimeter scale in rock samples.

We have used the GEOS multiphysics code in two sets of simulations. The *long-term* simulations account for thermal, hydrological, and mechanical (T-H-M) processes over time scales of days to decades. The *short-term* simulations account for hydro-mechanical processes over time scales on the order of hours to days. In both cases, the result is a modeled stress field $\sigma(t, x, y, z)$ as a function of time and position.

We find that the orientations of faults, fractures, and conductive fluid pathways produce pressure propagation that varies considerably, even between wells that are within few hundred meters of each other. In some cases, a single large aperture feature dominates the fluid flow, whereas a more distributed zone consisting of a network of fractures accommodates the fluid flow in other cases. Also, the orientations of the conductive fractures do not necessarily coincide with the overall orientation of the largest fault structures. The mechanical responses of these conductive features also vary on spatial scales of the order of hundreds of meters.

The azimuth of maximum compressive horizontal stress S_{Hmax} calculated from the long-term T-H-M simulation agrees to within 20 degrees of the orientation of drilling-induced tensile fractures (DITF) picked from borehole image log of Well 17A-21.

Geodetic observations from GPS and InSAR data show downward vertical displacement (subsidence) at rates of 7 ± 2 mm/year near production wells. The long-term T-H-M simulations match the shape of the deformation field near the producing wells observed by InSAR. In terms of the rate of vertical displacement, however, the T-H-M simulations are greater than the GPS and InSAR observations by a factor of ~4.

Most of the microseismic events in December 2016 and April 2022 are located within 400 m of a production well at depths between 400 and 700 m. Most of the microseismic events are observed when production is stopped.

Using the short-term H-M model, we have calculated the stress field as a function of time. We then evaluate the Coulomb failure criterion on sets of planes using the simulated stress field calculated in the GEOS solution. Assuming that the rock is critically stressed during normal operations, we derive the change in Coulomb Failure Stress ΔCFS. According to the sign convention used in rock mechanics, positive values of ΔCFS indicate conditions favorable to fault slip. The simulated change in Coulomb Failure Stress ΔCFS is positive for 28 of the 32 events (88%) during the 2016 shutdown for which focal mechanisms were determined by Guo et al. (2023).

Extending the same approach, we also calculate the modeled change ΔCFS in Coulomb failure stress on (hypothetical) optimally oriented planes at every location in the study area and at all times during the interval when seismic observations are available. The timings and locations of points when and where the simulated change in Coulomb Failure Stress ΔCFS takes a positive value are comparable to those of the microseismic events observed during the shutdown in December 2016. To perform a post-audit of the model results, we have used data from a seismic array consisting of 450 three-component seismographs deployed before, during, and after a planned shutdown in April 2022.

The observations support the working hypothesis that increasing pore-fluid pressure reduces the effective normal stress acting across fault zones. During normal operations, pumping in deep production wells decreases fluid pressures and thus increases the effective normal stresses on faults, reducing microseismicity. During planned shutdowns, the cessation of production increases pore-fluid pressure along conductive pathways that are connected to production wells, and reduces effective normal stress. As a result, micro-seismic events tend to occur on small-scale, critically stressed fault patches and fractures within the reservoir.

Thermoelastic effects over years are comparable to changes in hydraulic and mechanical stresses over time scales of hours to days. Changes in tectonic stress are not significant over the reservoir lifetimes. The stress analysis suggests that no major hazard is to be expected from normal operations or planned plant shutdowns.

Spatial variations in the local stress state are also observed, indicating stress heterogeneity in the reservoir. These results combine to indicate that the geothermal reservoir at San Emidio is a fractured, fluid filled, and permeable body that has developed along the existing normal faults.

SECTION IX. DATA MANAGEMENT PLAN

For each subtask, datasets were submitted to the DOE Geothermal Data Repository (GDR), as described in the Data Management Plan (DMP). The WHOLESCALE project used the following definitions quoted from the FOA[14] and excerpted in the DMP[15].

Data Preservation: "Data preservation means providing for the usability of data beyond the lifetime of the research activity that generated them."

Data Sharing: "Data sharing means making data available to people other than those who have generated them. Examples of data sharing range from bilateral communications with colleagues, to providing free, unrestricted access to anyone through, for example, a web-based platform."

Digital Research Data: "The term digital data encompasses a wide variety of information stored in digital form including: experimental, observational, and simulation data; codes, software and algorithms; text; numeric information; images; video; audio; and associated metadata. It also encompasses information in a variety of different forms including raw, processed, and analyzed data, published and archived data."

Research Data: "The recorded factual material commonly accepted in the scientific community as necessary to validate research findings, but not any of the following: preliminary analyses, drafts of scientific papers, plans for future research, peer reviews, or communications with colleagues. This 'recorded' material excludes physical objects (e.g., laboratory samples). Research data also do not include:

(A) Trade secrets, commercial information, materials necessary to be held confidential by a researcher until they are published, or similar information which is protected under law; and

(B) Personnel and medical information and similar information the disclosure of which would constitute a clearly unwarranted invasion of personal privacy, such as information that could be used to identify a particular person in a research study."

Validate: "In the context of DMPs, 'validate' means to support, corroborate, verify, or otherwise determine the legitimacy of the research findings. Validation of research findings could be accomplished by reproducing the original experiment or analyses; comparing and contrasting the results against those of a new experiment or analyses; or by some other means."

Protected Data: Data that "should be protected from immediate public disclosure by DOE". This category applies to "data developed outside of the proposed work at private expense that will be used in the course of the proposed work".

Limited Rights Data: Protected data that will be "kept confidential"

We implemented the DMP using two password-protected file-serving systems: (1) Shared Google Drive[16] for working versions of evolving files, such as figures and scripts; and (2) Data Foundry[17]: for sharing stable files, such as large data files. Both file-sharing systems were organized according to the Tasks and Subtasks listed in the SOPO. Table 22 summarizes all the datasets submitted to the GDR or made publicly available.

---

[14] EERE (2019), Subsurface Stress and Lost Circulation in Geothermal Drilling Funding Opportunity Announcement (FOA) Number DE-FOA-0002083, edited by Department of Energy (DOE) Office of Energy Efficiency and Renewable Energy (EERE). https://eere-Exchange.energy.gov

[15] https://foundry.openei.org/61/task1-coordination/subtask15-datamanagement?resources[]=5046865

[16] https://drive.google.com/drive/folders/0AK_zKpw3PfinUk9PVA

[17] https://foundry.openei.org/61

Table 22. WHOLESCALE dataset submissions to the GDR and other publicly available sites.

Title	Authors	URL	Citation (MLA)	Status
Passive Seismic Emission Tomography Results at San Emidio Nevada.	Warren, Ian, Folsom, Matthew, Akerley, John, and Feigl, Kurt L.	https://gdr.openei.org/submissions/1441	Warren, Ian, Folsom, Matthew, Akerley, John, and Feigl, Kurt. Passive Seismic Emission Tomography Results at San Emidio Nevada. United States: N.p., 01 Dec, 2016. Web. doi: 10.15121/1924268.	Curated
Seismic Survey 2016 Metadata at San Emidio, Nevada	Lord, Neal, Heath, Ben, Guo, Hao, Warren, Ian, Bradshaw, Sabrina, Thurber, Cliff, Akerley, John and Feigl, Kurt	https://gdr.openei.org/submissions/1386	Lord, Neal, Heath, Ben, Guo, Hao, Warren, Ian, Bradshaw, Sabrina, Thurber, Cliff, Akerley, John, and Feigl, Kurt. Seismic Survey 2016 Metadata at San Emidio, Nevada. United States: N.p., 05 Dec, 2016. Web. doi: 10.15121/1872549.	Curated
Seismic Survey 2016 data at San Emidio Nevada	Lord, Neal, Heath, Ben, Guo, Hao, Warren, Ian, Bradshaw, Sabrina, Thurber, Cliff, Akerley, John, and Feigl, Kurt	https://gdr.openei.org/submissions/1395	Lord, Neal, Heath, Ben, Guo, Hao, Warren, Ian, Bradshaw, Sabrina, Thurber, Cliff, Akerley, John, and Feigl, Kurt. Seismic Survey 2016 Data at San Emidio Nevada. United States: N.p., 05 Jan, 2016. Web. https://gdr.openei.org/submissions/1395.	Curated
WHOLESCALE Catalog of Rock Samples at San Emidio Nevada collected in January 2021 Version 2.0.	Kleich, Samantha, Bradshaw, Sabrina, Hampton, Jesse, and Feigl, Kurt	https://gdr.openei.org/submissions/1396	Kleich, Samantha, Bradshaw, Sabrina, Hampton, Jesse, and Feigl, Kurt. WHOLESCALE Catalog of Rock Samples at San Emidio Nevada collected in January 2021 Version 2.0. United States: N.p., 12 Jan, 2021. Web. doi: 10.15121/1879102.	Curated
WHOLESCALE Catalog of Rock Samples at San Emidio Nevada collected in January 2021.	Kleich, Samantha, Folsom, Matthew, Gates, Chris, Ricks, Quaid, Jahnke, Benjamin, Sone, Hiroki, Hampton, Jesse, Bradshaw, Sabrina, and Feigl, Kurt	https://gdr.openei.org/submissions/1357	Kleich, Samantha, Folsom, Matthew, Gates, Chris, Ricks, Quaid, Jahnke, Benjamin, Sone, Hiroki, Hampton, Jesse, Bradshaw, Sabrina, and Feigl, Kurt. WHOLESCALE Catalog of Rock Samples at San Emidio Nevada collected in January 2021. United States: N.p., 12 Jan, 2021. Web. doi: 10.15121/1838419.	Curated
GPS Station RINEX Files and Position Time-Series.	Feigl, Kurt	https://gdr.openei.org/submissions/1338	Feigl, Kurt. GPS Station RINEX Files and Position Time-Series. United States: N.p., 14 Oct, 2021. Web. https://gdr.openei.org/submissions/1338.	Curated
Magnetotelluric Data Collected in 2016 over the San Emidio Geothermal Field in Nevada.	Folsom, Matt, Warren, Ian, Gasperikova, Erika, Libbey, Ryan, Feucht, Daniel, and Garazini, Stefano	https://gdr.openei.org/submissions/1434	Folsom, Matt, Warren, Ian, Gasperikova, Erika, Libbey, Ryan, Feucht, Daniel, and Garazini, Stefano. Magnetotelluric Data Collected in 2016 over the San Emidio Geothermal Field in Nevada. United States: N.p., 09 Nov, 2016. Web. doi: 10.15121/1974786.	Curated
WHOLESCALE: Mass Flux Rates for Wells at San Emidio in December 2016	Cardiff, Mike, Akerley, John, and Feigl, Kurt L.	https://gdr.openei.org/submissions/1552	Cardiff, Mike, Akerley, John, and Feigl, Kurt L. WHOLESCALE: Mass Flux Rates for Wells at San Emidio in December 2016. United States: N.p., 01 Dec, 2016. Web. doi: 10.15121/2006850.	Curated
WHOLESCALE: Coordinates of wells at San Emidio, Nevada	Cardiff, Mike, Akerley, John, and Feigl, Kurt L.	https://gdr.openei.org/submissions/1551	Cardiff, Mike, Akerley, John, and Feigl, Kurt L. WHOLESCALE: Coordinates of wells at San Emidio, Nevada. United States: N.p., 25 Sep, 2023. Web. doi: 10.15121/2006837.	Curated
WHOLESCALE: Microseismic Event Catalog for San Emidio, Nevada 2022. United States	Hao Guo, Clifford H. Thurber, Peter Sobol, Neal E. Lord, Sabrina L. Bradshaw, Kurt L. Feigl	https://gdr.openei.org/submissions/1614	Guo, Hao, Thurber, Clifford H., Sobol, Peter, Lord, Neal E., Bradshaw, Sabrina L., and Feigl, Kurt L. WHOLESCALE: Microseismic Event Catalog for San Emidio, Nevada 2022. United States: N.p., 20 Apr, 2024. Web. doi: 10.15121/2373193.	Curated
WHOLESCALE: Seismic Survey Data from San Emidio Nevada 2021	Lord, Neal, Heath, Ben, Cunningham, Erin, Thurber, Cliff, Bradshaw, Sabrina, and Feigl, Kurt L.	https://gdr.openei.org/submissions/1478	Lord, Neal, Heath, Ben, Cunningham, Erin, Thurber, Cliff, Bradshaw, Sabrina, and Feigl, Kurt L.WHOLESCALE: Seismic Survey Data from San Emidio Nevada 2021. United States: N.p., 06 Apr, 2021. Web. https://gdr.openei.org/submissions/1478.	Curated
WHOLESCALE: Seismic Survey Metadata from San Emidio Nevada 2021	Lord, Neal, Heath, Ben, Cunningham, Erin, Thurber, Cliff, Bradshaw, Sabrina, and Feigl, Kurt	https://gdr.openei.org/submissions/1463	Lord, Neal, Heath, Ben, Cunningham, Erin, Thurber, Cliff, Bradshaw, Sabrina, and Feigl, Kurt. WHOLESCALE: Seismic Survey Metadata from San Emidio Nevada 2021: N.p., 06 Apr, 2021. Web. https://gdr.openei.org/submissions/1463.	Curated
WHOLESCALE Subtask 4.5 Seismic survey 2021 at San Emidio Nevada example data	Lord, Neal	https://gdr.openei.org/submissions/1356	Lord, Neal. WHOLESCALE Subtask 4.5 Seismic survey 2021 at San Emidio Nevada example data. United States: N.p., 07 May, 2021. Web. https://gdr.openei.org/submissions/1356.	In Progress (NREL to curate on DataLake)
WHOLESCALE: Seismic Waveform Data from San Emidio, Nevada 2022	Lord, Neal E., Sobol, Peter, Guo, Hao, Thurber, Clifford H., Warren, Ian, Bustos, D.J., Bradshaw, Sabrina L., and Feigl, Kurt L.	https://gdr.openei.org/submissions/1610	Lord, Neal E., Sobol, Peter, Guo, Hao, Thurber, Clifford H., Warren, Ian, Bustos, D.J., Bradshaw, Sabrina L., and Feigl, Kurt L. WHOLESCALE: Seismic Waveform Data from San Emidio, Nevada 2022. United States: N.p., 05 Apr, 2022. Web. https://gdr.openei.org/submissions/1610.	Curated
2022 seismic metadata	Kurt Feigl, Cliff Thurber, & Neal Lord.	http://ds.iris.edu/mda/4Q/?starttime=2022-03-01T00%3A00%3A00&endtime=2022-05-15T23%3A59%3A59	Kurt Feigl, Cliff Thurber, & Neal Lord. (2022). WHOLESCALE survey at San Emidio, Nevada, USA [Data set]. International Federation of Digital Seismograph Networks. https://doi.org/10.7914/m5qt-mh37	Published on publically available website
P-wave velocity tomography estimated from seismic data collected in December 2016	Guo, H., C. Thurber, I. Warren, B. A. Heath, M. Folsom, H. Sone, N. Lord, J. Akerley, and K. L. Feigl	https://agupubs.onlinelibrary.wiley.com/action/downloadSupplement?doi=10.1029%2F2023JB027008&file=2023JB027008-sup-0003-Table+SI-S02.csv	Included as supplementary information to Guo et al. JGR 2023. Guo, H., C. Thurber, I. Warren, B. A. Heath, M. Folsom, H. Sone, N. Lord, J. Akerley, and K. L. Feigl (2023), Enhanced Microseismicity During Production Pumping Cessation at the San Emidio Geothermal Field (Nevada, USA) in December 2016, Journal of Geophysical Research: Solid Earth, 128, e2023JB027008. https://doi.org/10.1029/2023JB027008	Published on publically available website
Catalog of microseismic events in December 2016, including event origin times, relocations, magnitudes, and focal mechanisms.	Guo, H., C. Thurber, I. Warren, B. A. Heath, M. Folsom, H. Sone, N. Lord, J. Akerley, and K. L. Feigl	https://agupubs.onlinelibrary.wiley.com/action/downloadSupplement?doi=10.1029%2F2023JB027008&file=2023JB027008-sup-0002-Table+SI-S01.csv	Included as supplementary information to Guo et al. JGR 2023. Guo, H., C. Thurber, I. Warren, B. A. Heath, M. Folsom, H. Sone, N. Lord, J. Akerley, and K. L. Feigl (2023), Enhanced Microseismicity During Production Pumping Cessation at the San Emidio Geothermal Field (Nevada, USA) in December 2016, Journal of Geophysical Research: Solid Earth, 128, e2023JB027008. https://doi.org/10.1029/2023JB027008	Published on publically available website

SECTION X. PROJECT OUTPUT

Publications, conference papers, and presentations

Accepted Manuscripts of (peer-reviewed) Journal Articles:

1) Jahnke, B., H. Sone, H. Guo, C. Sherman, I. Warren, C. Kreemer, C. H. Thurber, and K. L. Feigl (2023), Geomechanical analysis of the geothermal reservoir at San Emidio, Nevada, *Geothermics, 110*, 102683. https://doi.org/10.1016/j.geothermics.2023.102683
   ABSTRACT: The WHOLESCALE (Water and Hole Observations Leverage Effective Stress Calculations and Lessen Expenses) project is aiming to simulate the spatial distribution and temporal evolution of stress throughout the geothermal system at San Emidio, Nevada, United States, via a thermo-hydro-mechanical reservoir model. Focal mechanisms for microseismic events during a temporary shutdown of the geothermal power plant in 2016 were analyzed through linear stress-inversion methods to infer the in-situ reservoir stress state. This analysis was supplemented by other geophysical and geological data, including focal mechanisms from regional earthquakes, slickenlines on exposed fracture surfaces, wellbore stress indicators observed in the surrounding region, and secular strain rate measurements. From the inferences of in-situ reservoir stress, 78 different realizations of stress models were generated over reasonable ranges for the values of maximum compressive horizontal stress (S_{Hmax}) azimuth and ratios of principal stress magnitudes. Evaluation of slip tendencies on fault planes determined for the microseismic events for each realization of the initial stress model suggests the reservoir stress state as transtensional with an S_{Hmax} azimuth between N and N30°E.

2) Guo, H., C. Thurber, I. Warren, B. Heath, M. Folsom, H. Sone, N. Lord, J. Akerley, and K. L. Feigl (2023), Enhanced microseismicity during production pumping cessation at the San Emidio geothermal field (Nevada, USA) in December 2016, *J. Geophys. Res.: Solid Earth*, 128, e2023JB027008. https://doi.org/10.1029/2023JB027008
   ABSTRACT: Tectonic activity, geothermal fluids, and microseismic events (MSEs) tend to occur in similar locations as a result of spatiotemporal changes in the subsurface stress state. To quantify this association, we analyze data from a dense seismic array deployed at the San Emidio geothermal field, Nevada for 1 week in December 2016 to coincide with a 19.45-hr shutdown of all injection and production pumping operations. 123 MSEs were detected, of which 101 occurred during the shutdown. The spatial association of the MSEs with the production wells suggests a causal relationship between the production cessation and the MSEs. Here we performed a detailed analysis to investigate reservoir material properties, distribution of seismically activated faults, and local stress state. We determined the hypocenters, magnitudes, and focal mechanisms for the MSEs, P-wave tomographic velocity model, and local stress tensor. The results show that most MSEs occurred near the production wells. Magnitudes fall between −2.2 and 0.0 with larger events located closer to the production wells. Most MSEs occurred within a westward-dipping normal fault zone in the reservoir associated with anomalously low P-wave velocity values. The focal mechanism and stress inversion results show predominantly normal faulting with the maximum horizontal stress oriented north-south. We suggest that the MSEs during shutdown were triggered on pre-existing, small-scale, critically stressed fault patches in the reservoir as the pore pressure increased around the production wells when the production pumping ceased. We interpret the larger MSE magnitudes closer to the production wells as a result of higher pore pressure increase.

3) Tung, S., O. Kaven, M. Shirzaei, T. Masterlark, H. F. Wang, W.-C. Huang, and K. L. Feigl (2024), Seismicity zoning at Coso geothermal field and stress changes from fluid production and migration, Earth and Planetary Science Letters, 646, https://doi.org/10.1016/j.epsl.2024.119000
ABSTRACT: The Coso geothermal field is a major geothermal power production site in the western United States. It has been observed that low-magnitude seismic events (M < 3.71) are unevenly distributed in three distinct zones, namely, nearfield (<3 km), midfield (3–6 km), and farfield (> 6 km) from the Coso geothermal plant. These zones exhibit distinct changes in earthquake location before and during geothermal production episodes that began in 1986. After 1986, the midfield region of the main flank experiences a significantly lower seismicity rate than the surrounding areas before production episodes. During 2014–2019, the farfield earthquakes cluster in the eastern and western parts of the greater Coso area, which is discernably different from how those pre-production earthquake events were distributed along the conjugate NW-SE and SW-NW trending structures across the main flank. Here, we analyze the stage of stress with finite-element-based poroelastic simulations to illustrate how the spatiotemporal evolution of the seismicity is associated with the pattern of stress perturbations caused by fluid migration amid the operations of geothermal power plants. Generally, ~70% of co-production seismicity is found in zones of increased Coulomb stress between 2014 and 2019 at >99% confidence. Meanwhile, the midfield zone of seismic paucity overlaps with the zone of decreasing pore-fluid pressure. Overall, the results provide a physical explanation of how decadal geothermal operations at Coso have perturbed stress-field changes and contributed to the evolving characteristic seismic pattern, shedding insights into assessing the seismic hazard in other geothermal settings.

4) Guo, H., C. Thurber, E. Cunningham, M. Cardiff, N. Lord, P. Sobol, H. Wang, and K. L. Feigl (2025), Microseismicity Modulation Due to Changes in Geothermal Production at San Emidio, Nevada, USA.
This manuscript was accepted by Geophysical Research. Letters on 27 January 2025
It was provisionally assigned the following URL http://dx.doi.org/10.1029/2024GL112063
ABSTRACT: Brief cessations of geothermal production can induce seismicity, a phenomenon that has drawn increasing attention in recent years. Such observations are rare, and the underlying mechanism requires careful analysis. In April 2022, a dense seismic and hydrologic monitoring system, was deployed at the San Emidio geothermal field, Nevada, to accompany a planned power plant shutdown. Using the dense seismic array data, we detected and located ~1,800 microseismic events (MSEs) and developed a high-resolution tomographic P-wave velocity model. We observed substantially increased microseismicity during shutdown. Most MSEs occurred on pre-existing normal faults, which are contained within extremely low-velocity zones that are likely damaged, fluid-filled, and hydraulically connected to nearby production wells. Hydrologic data show rapid fluid pressure increases of <60 kPa following the shutdown. We suggest that the cessation of production rapidly increased fluid pressures along pre-existing fault zones, activating critically stressed fault patches and fractures and producing microseismicity.

Books or other non-periodical, one-time publications:

1) Kleich, S. J. (2022), Mechanical and Poroelastic Properties of Lithologic Units Within the San Emidio Geothermal System, Nevada, United States, M.S. thesis (Jesse Hampton, advisor). University of Wisconsin-Madison. https://minds.wisconsin.edu/handle/1793/83523
ABSTRACT: The primary objective of the WHOLESCALE project is to simulate the temporal evolution and spatial distribution of stress in and around the geothermal reservoir at San Emidio, Nevada, United States. To constrain stress modeling efforts, laboratory measurements of static and dynamic elastic stiffness were performed using oriented rock samples collected from outcrops located near the San Emidio geothermal field. In this work, we sought to understand (1) the static and dynamic elastic properties of the rock formations, (2) the existence or absence of anisotropy or heterogeneity-controlled behavior at the millimeter to centimeter scales, (3) whether the elastic properties are stress dependent, and (4) whether there exists any stress induced anisotropy under reasonable net mean stress variations. To evaluate the existence of anisotropy or heterogeneity, we measured ultrasonic velocities, V_p and V_s, at 45-degree increments around the circumference of oriented cylindrical specimens for each rock type. Combining the three-dimensional velocity data with geological and textural descriptions, we addressed whether the material properties are heterogeneity-controlled and/or anisotropic at the plug scale. Static and dynamic elastic moduli were also measured at the net mean stresses of interest for each of the rock types obtained. Dynamic stress dependence and whether each material analyzed contained stress induced anisotropy were evaluated via stepped hydrostatic ultrasonic velocity measurements. The work presented herein was funded in part by the Office of Energy Efficiency and Renewable Energy (EERE), U.S. Department of Energy, under Award Numbers DE-EE0007698 and DE-EE0009032.

2) Jahnke, B. (2022), Geomechanical Analysis of the Geothermal Reservoir at San Emidio, Nevada and Fracture Toughness Anisotropy of EGS Collab Testbed Rocks, M.S. thesis (Hiroki Sone, advisor). University of Wisconsin-Madison. http://digital.library.wisc.edu/1793/83225
ABSTRACT: The WHOLESCALE (Water and Hole Observations Leverage Effective Stress Calculations and Lessen Expenses) project is aiming to simulate the spatial distribution and temporal evolution of stress throughout the geothermal system at San Emidio, Nevada, United States. Towards this goal, the stress state of a thermo-hydro-mechanical reservoir model is being constrained. Focal mechanisms recovered from microseismic events during a power plant shut down in 2016 were extensively analyzed through linear stress inversion methods to infer the in situ reservoir stress state. Additionally, other geophysical data including focal mechanisms from regional earthquakes, sickenlines, wellbore stress indicators observed in the surrounding region, and secular strain rate measurements were used to check consistencies with the in-situ reservoir stress state. From the estimates of in-situ reservoir stress, 78 different realizations of stress models were generated based on a range of maximum compressive horizontal stress (S_{Hmax}) azimuths and relative principal stress magnitudes. To investigate which stress model best describes the 2016 microseismicity, slip tendency analyses were performed using each of the 78 realizations of the stress models. Stress models with azimuths of S_{Hmax} ranging from North to N20°E and relative magnitudes of S_V, S_{Hmax}, and S_{hmin} describing a normal-transtensional regime produced the highest slip tendencies at where the microseismic events occurred and are therefore the best estimates of the in-situ reservoir stress state.

Other publications, conference papers and presentations:

1) Folsom, M., R. Libbey, D. Feucht, W. I., and S. Garanzini (2020), Geophysical Observations and Integrated Conceptual Models of the San Emidio Geothermal Field, Nevada., paper presented at Workshop on Geothermal Reservoir Engineering, Stanford, California, USA. https://pangea.stanford.edu/ERE/db/GeoConf/papers/SGW/2020/Folsom.pdf
ABSTRACT: The San Emidio Desert hosts a hidden, forced-convection geothermal resource situated within a prominent right-step of the Lake Range in northwestern Nevada. The site has produced power since 1988, undergoing several phases of development since. Recent exploration drilling 1.5 to 2.5 km to the SW of the current production area has confirmed 162°C fluids 540 m below the surface with favorable permeability for development. This paper presents results from an integrated modeling study of the system that takes advantage of new geophysical data sets, including 211 broadband magnetotelluric stations, 1207 gravity stations, 176 line-km of ground magnetic data and a passive seismic experiment conducted with 1302 stations of 6 geophones each. These data are considered within the context of drilling results and other datasets to develop updated geologic and conceptual models of the geothermal system. Notable results are: (1) imaging of an extensive zone of mineralized/silicified Tertiary sediments along an outflow path and up-dip of normal faulting; (2) imaging of two distinct dome-shaped electrical conductors situated above zones of enhanced temperature and permeability; (3) coincidence of one of these zones with enhanced semblance of passive micro-seismic signals observed using a dense array; and (4) added constraints on the fault block geometry within the right step of the Lake Range, with implications for understanding the controls of deep permeability in the system.

2) Kleich, S.J., Hampton, J.C., WHOLESCALE Team (2021). Poroelasticity measurements of geothermal rocks. American Rock Mechanics Association (ARMA) Annual Symposium, Houston, Texas. https://doi.org/10.56952/ARMA-2022-0722
ABSTRACT: Although the elastic properties of rocks have been extensively studied for decades, poroelastic coefficients resulting from applied external and fluid pressures are: (1) difficult to measure precisely, and (2) often overlooked or oversimplified when modeling subsurface volumes. The physical properties of porous solids are typically affected by external stress and/or pore pressure. Physical properties such as elastic stiffness or permeability can be described as functions of external stress (σ) and pore pressure (P_p). Accordingly, the effective stress σ_e is defined as the external stress that, if applied in isolation, would produce the same effect as the combination of σ and P_p The usual assumption is that the effective stress can be described through an effective stress coefficient n such that $\sigma_e = \sigma_c - nP_p$. In the special case of volumetric strain in an isotropic poroelastic solid, this coefficient is referred to as the Biot coefficient or the Biot-Willis coefficient α. To understand the stress in a geothermal reservoir, it is important to obtain accurate estimates of effective stress coefficients. To do so, we perform laboratory measurements on various quarried granite specimens and rock samples taken from surface outcrops around the geothermal field at San Emidio, Nevada, U.S.A. The methodology uses confining pressure and pore pressure oscillations over a range of conditions. The measured values produce a data set that can be evaluated using the laws of poroelasticity to estimate the Biot coefficient. We also investigate the possibility, and magnitude, of elastic and poroelastic property anisotropy due to texture (e.g., oriented microcracks). This work will contribute to the WHOLESCALE project recently funded by the Geothermal Technologies Office of the U.S. Department of Energy. The acronym stands for "Water & Hole Observations Leverage Effective Stress Calculations and Lessen Expenses". The goal of the WHOLESCALE project is to simulate the spatial distribution and temporal evolution of stress in a geothermal system. To reach this goal, the WHOLESCALE team proposes to develop a methodology that will incorporate and interpret data from four methods of measurement into a multi-physics model that couples thermal, hydrological, and mechanical (T-H-M) processes over spatial scales ranging from the diameter of a borehole (~0.1 m) to the extent of the entire field (~10 km) and temporal scales ranging from the duration of a micro-seismic event (~1 second) to the typical lifetime of a producing field (3 decades).

3) Tung, S., C. S. Sherman, T. Masterlark, M. A. Cardiff, H. F. Wang, and K. L. Feigl (2021), Modeling Displacement, Strain, and Stress via a Library of Green's functions Calculated with the Finite Element Method: Application to Coso Geothermal Field, California, U.S.A., in *Meeting of the American Geophysical Union*, https://agu.confex.com/agu/fm21/meetingapp.cgi/Paper/963052
ABSTRACT: To calculate the displacement field at the earth's surface, we are developing a new method based on the linear superposition of multiple Green's functions for cubic voxels in the subsurface. To do so, we expand on the approach of Masterlark [2003, JGR] to allow dilation. The center of each voxel is located at a single node at the intersection of 8 cubic (finite) elements. For each voxel, we specify a unit change in volume by imposing a 3-dimensional vector displacement on each of the three orthogonal, planar, square surfaces outlined by the diagonals of the elements' shared faces. As a result, each planar square surface dilates into an octahedral shape composed of two pyramids sharing a square base, i.e. an octahedron. To describe the material properties of the medium, we are building a 3-dimensional model based on multiple geophysical data streams at the Coso geothermal field as part of Phase I of the FORGE project. We then solve the governing equations for each voxel to calculate the elastic response as a vector displacement field, i.e. the Green's function. Each such Green's function is the partial derivative of surface displacement with respect to a unit change in volume. These derivatives can be arranged as columns in the design matrix for a linear inverse problem. To find the model that best fits the displacement field observed by InSAR, we apply Bayesian inference using a prior model based on the mass fluxes of produced and injected fluids, as reported monthly to the state of California.

4) Tung, S., K. R. Blake, M. Shirzaei, M. A. Cardiff, T. Masterlark, H. F. Wang, and K. L. Feigl (2021), Temporal Evolution and Spatial Distribution of stress and strain at Coso Geothermal Field: January 2005 through June 2019, in *Fall Meeting American Geophysical Union*, edited. https://agu.confex.com/agu/fm21/meetingapp.cgi/Paper/956813
ABSTRACT: Coso geothermal field in California exhibits deformation and seismicity that vary over time scales on the order of several months. Both of these signals are intertwined with geothermal production and injection. To understand these signals, we model the time-dependent deformation fields measured by interferometric synthetic aperture radar (InSAR) and the Global Positioning System (GPS). To do so, we apply a new modeling approach based on the superposition of Green's functions [S. Tung et al., this meeting]. Then we apply Bayesian inference to evaluate the relative importance of two hypothesized mechanisms: (1) poroelastic response to production and injection of geothermal fluids; and (2) thermoelastic response to advective cooling by fluid flow. In both cases, the prior model is based on monthly flow data reported to the state of California. After selecting the most likely model for the subsurface processes driving the strain, we calculate the stress as a time-varying tensor field. This tensor can be projected onto known fault planes to evaluate the Coulomb failure criterion within each of the subsurface voxels in the model. Comparing the modeled timing and location of the failing subsurface voxels to the observed timing and location of the seismicity constitutes an additional test (i.e., post-fit audit) of the models.

5) Thurber, C., Guo, H., Heath, B., Cardiff, M., Lord, N., Warren, I., & Feigl, K. (2021). Structure and Stress Results from Nodal Seismic Array Deployments at the San Emidio Geothermal Field, Nevada, U.S.A. 2021, in Fall Meeting American Geophysical Union S41A-08. https://ui.adsabs.harvard.edu/abs/2021AGUFM.S41A..08T
ABSTRACT: We are analyzing seismic data from a 2016 deployment of more than 1,300 vertical-component nodal instruments in the San Emidio geothermal field during a planned shutdown of the power plant, as part of the WHOLESCALE project supported by the U.S. Department of Energy. Cessation of pumping was followed by a substantial increase in microseismic activity, as has been observed at some other geothermal plant sites (e.g., Brady, Blue Mountain). We model pressure changes due to pumping cessation and examine the correlation between seismic event hypocenters and changes to effective normal stress within the reservoir. We have also deployed a small array of 38 three-component (3-C) nodal instruments at San Emidio in April 2021 to coincide with another planned plant shutdown. Preliminary analysis of the two datasets reveals at least 130 microseismic events in 2016 and more than 300 in 2021 during the shutdown periods, located within approximately the same area. The large 2016 array also enabled the determination of a three-dimensional tomographic model for P-wave velocity as well as focal mechanisms for about 40 events. The tomographic model reveals large lateral variations in velocity, with structural features that are consistent with normal faults dipping roughly westward. A stress inversion of the highest-quality focal mechanisms yields a maximum compressive stress axis plunging nearly vertically toward the northeast, consistent with other information. The intermediate and minimum compressive stress axes are both close to horizontal, but their azimuths are not well constrained, with overlapping probability distributions. These results will guide the design of an array of several hundred 3-C nodal instruments to be deployed at the time of the next planned shutdown at San Emidio in 2022.

6) Jahnke, B., H. Guo, B. Heath, E. Cunningham, C. Sherman, H. Sone, I. Warren, C. Kreemer, C. H. Thurber, K. L. Feigl, and The WHOLESCALE Team (2022) Spatial-Temporal Stress Heterogeneity in the Geothermal Reservoir at San Emidio, Nevada, U.S, 47th Workshop on Geothermal Reservoir Engineering, February 7-9, Stanford, CA. https://pangea.stanford.edu/ERE/db/GeoConf/papers/SGW/2022/Jahnke.pdf
ABSTRACT: We attempt to constrain models of the reservoir stress of a geothermal reservoir in San Emidio, Nevada, which will be used in a reservoir- scale hydro-mechanical numerical model. Our reservoir stress models are based on (1) the densities of subsurface lithologies, (2) surface topography, (3) the relative magnitudes of the total vertical stress (S_V), maximum horizontal stress (S_{Hmax}), and minimum horizontal stress (S_{hmin}), and (4) the azimuth of S_{Hmax}. The models are informed from stress indicators within a ~175 km radius of San Emidio which provides constraints on (1) the relative magnitudes of S_V, S_{Hmax}, and S_{hmin}, and (2) the azimuth of S_{Hmax}. To evaluate how well the model represents the reservoir stress, focal mechanism data from microseismic events which occurred within the reservoir during a plant shutdown in 2016 are used. Stress inversions (Vavryčuk, 2014) of the focal mechanism data estimate the in situ principal stress orientations, their relative magnitudes, and preferred nodal planes. Then the principal orientations of the model stresses at the locations of microseismic events were compared to the principal stress orientations inverted from the focal mechanisms. These analyses allow us to refine the reservoir stress model that agrees with field observations and is therefore suitable to use to forward model the reservoir responses against production and injection operations. In this paper, we provide a snapshot of work in progress, including the highlights listed in the conclusions below. The work presented herein has been funded in part by the Office of Energy Efficiency and Renewable Energy (EERE), U.S. department of Energy, under Award Numbers DE-EE0007698 and DE-EE0009032.

7) Kleich, S.J., Folsom, M., Hampton, J., Feigl, K.L., & the WHOLESCALE Team. (2022). Lab-scale structural analysis and poroelastic measurements of rocks from the San Emidio Geothermal Field, Nevada, U.S., Proceedings*, 47th Workshop on Geothermal Reservoir Engineering*, , February 7-9, Stanford, CA.
https://pangea.stanford.edu/ERE/db/GeoConf/papers/SGW/2022/Kleich.pdf
ABSTRACT: In the WHOLESCALE project we aim to simulate the temporal evolution and spatial distribution of stress in and around the geothermal reservoir at San Emidio, Nevada, United States. To constrain the stress modeling efforts, we perform laboratory measurements of elastic stiffnesses and effective pressure coefficients using oriented rock samples collected from outcrops located near the San Emidio geothermal field. To help contextualize lab-scale measurements through a field-scale lens, it is important to understand whether lab-scale rock deformation is controlled by structural anisotropy and/or heterogeneity. To that end, we measure ultrasonic velocities, V_p and V_s, at 45-degree increments around the circumference of oriented cylindrical specimens for each rock type. Combining the three-dimensional velocity data with geological and textural descriptions, we address whether the velocity is controlled by heterogeneity and/or anisotropy at the plug scale. To better model stress in subsurface volumes of a geothermal field, it is also important to obtain accurate estimates of elastic stiffnesses and effective stress coefficients at the laboratory scale; particularly the Biot coefficients which are the effective stress coefficients for volumetric strain in an elastic porous solid. Using the information from the velocity structure and textural descriptions, we physically measure the associated stiffnesses and Biot coefficients to help constrain material behavior predictions within the stress model. In this paper, we provide a snapshot of the work in progress, including the highlights listed in the Conclusions below. The work presented herein has been funded in part by the Office of Energy Efficiency and Renewable Energy (EERE), U.S. Department of Energy, under Award Numbers DE-EE0007698 and DE-EE0009032.

8) Kurt L. Feigl, Sui Tung, Hao Guo, Erin Cunningham, Jesse Hampton, Samantha J. Kleich, Ben Jahnke, Ben Heath, Collin Roland, Matthew Folsom, John Akerley, Chris Sherman, Ian Warren, Corné Kreemer, Hiroki Sone, Michael A. Cardiff, Neal E. Lord, Clifford H. Thurber, Herbert F. Wang, and the WHOLESCALE Team (2022)
Overview and Preliminary Results from the WHOLESCALE project at San Emidio, Nevada, U.S., *47th Workshop on Geothermal Reservoir Engineering*, February 7-9, Stanford, CA.
https://pangea.stanford.edu/ERE/pdf/IGAstandard/SGW/2022/Feigl.pdf
ABSTRACT: The WHOLESCALE acronym stands for Water & Hole Observations Leverage Effective Stress Calculations and Lessen Expenses. The goal of the WHOLESCALE project is to simulate the spatial distribution and temporal evolution of stress in the geothermal system at San Emidio in Nevada, United States. To reach this goal, the WHOLESCALE team is developing a methodology that will incorporate and interpret data from four methods of measurement into a multi-physics model that couples thermal, hydrological, and mechanical (T-H-M) processes over spatial scales ranging from the diameter of a borehole (~0.1 m) to the extent of the entire field (~10 km) and temporal scales ranging from the duration of a microseismic event (~1 second) to the typical lifetime of a producing field (3 decades). The data sets include observations from geology, seismology, drilling, geodesy, and hydrology. The WHOLESCALE team is taking advantage of the perturbations created by changes in pumping operations to infer temporal changes in the state of stress in the geothermal system. This rheological experiment is based on the key idea that increasing pore-fluid pressure reduces the effective normal stress acting across preexisting faults. The work plan includes: (1) measuring rock-mechanical material properties in the laboratory, (2) manipulating the stress field via hydraulic and thermal methods, (3) measuring the resulting response by geophysical methods, and (4) calculating the stress, strain, pressure, and temperature in the geothermal system using an open-source, numerical simulator named GEOSX. To interpolate and interpret these rich data sets, GEOSX uses the finite-element method to solve the coupled differential equations governing the physics of a fractured, poroelastic medium under stress. The study site at San Emidio includes a volume with length of ~6 km, width ~5 km, and depth ~2 km. In this paper, we provide a snapshot of work in progress, including the highlights listed in the conclusions below. The work presented herein has been funded in part by the Office of Energy Efficiency and Renewable Energy (EERE), U.S. Department of Energy, under Award Numbers DE-EE0007698 and DE-EE0009032.

9) Kleich, S. J., M. Folsom, C. Sherman, K. L. Feigl, and J. C. Hampton (2022), Measurements of elastic moduli and stress dependence of geothermal rocks, paper presented at 56th US Rock Mechanics/Geomechanics Symposium, Santa Fe, New Mexico, USA, , 26-29 June 2022.
https://santafe2022.armarocks.org/
ABSTRACT: In the WHOLESCALE project we aim to simulate the temporal evolution and spatial distribution of stress in and around the geothermal reservoir at San Emidio, Nevada, United States. To constrain stress modeling efforts, we perform laboratory measurements of static and dynamic elastic stiffnesses using oriented rock samples collected from outcrops located near the San Emidio geothermal field. In this paper, we seek to understand (1) the static and dynamic elastic properties of the rock formations, (2) the existence or absence of anisotropy or heterogeneity-controlled behavior at the millimeter to centimeter scales, (3) whether the elastic properties are stress dependent, and (4) whether there exists any stress induced anisotropy under reasonable net mean stress variations. To evaluate the existence of anisotropy or heterogeneity, we measure ultrasonic velocities, V_p and V_s, at 45-degree increments around the circumference of oriented cylindrical specimens for each rock type. Combining the three-dimensional velocity data with geological and textural descriptions, we address whether the materials are heterogeneity-controlled and/or anisotropic at the plug scale. Static and dynamic elastic moduli were also measured at the net mean stresses of interest for each of the rock types obtained. Dynamic stress dependence and whether the material contained stress induced anisotropy was evaluated via stepped hydrostatic ultrasonic velocity measurements.

10) Guo, H., Thurber, C. H., Heath, B. A., Cardiff, M. A., Lord, N. E., Warren, I., & Feigl, K. L. (2022, April 19). *Seismic Analysis of Reservoir Conditions for Inducing Seismicity at the San Emidio Geothermal Field, Nevada, USA.* Seismological Society of America (SSA) Annual Meeting, Bellevue, Washington, USA. https://meetings.seismosoc.org/wp-content/uploads/2022/07/SSA_2022AM-Program-final.pdf
ABSTRACT: At the San Emidio geothermal field, Nevada, a substantial increase in microseismic activity during a power plant shutdown (i.e., cessation of all production and injection activities) was observed in December 2016 by a local seismic network with more than 1,300 vertical component nodal instruments. Here, we present our seismic analysis of the 2016 dataset, including locating microseismic events (MEs), P-wave velocity (V_p) tomography, focal mechanism (FM) inversion, and stress inversion, to investigate material properties, distribution of existing faults, and local stress state in the reservoir for understanding the mechanisms for inducing MEs during plant shutdown. The V_p model shows large lateral variations, with main structural features that are consistent with normal faults dipping westward. Two low-V_p zones (LVZs) to the west of the surface trace of the main fault and near some operational wells are imaged at depths of ~0.2-1.2 km below land surface. The northern LVZ is closer to two production wells and the southern one is closer to four injection wells. Most MEs occurred within or surrounding the northern LVZ. FM results show diverse faulting regimes, dominated by normal faulting. Stress inversion using high-quality FMs yields a maximum compressive stress axis plunging nearly vertically toward the northeast. The intermediate and minimum compressive stress axes are both nearly close to horizontal toward the WSW and SSE, respectively. Orientations of ME hypocenters and FMs show that a majority of MEs may occur on a large-scale fault and/or some small-scale faults/fractures within the LVZ, suggesting that the activation of faults/fractures due to pore pressure increases caused by the cessation of pumping triggered some of the MEs. Modeling pressure changes due to pumping cessation suggests fluid pressure increases of ~25-50 kPa at the hypocenters of MEs, which are predominantly near shutdown production wells. The work presented herein has been funded in part by the Office of Energy Efficiency and Renewable Energy, U.S. Department of Energy, under Award Numbers DE-EE0007698 and DE-EE0009032.

11) C. Thurber, H. Guo, E. Cunningham, B. Heath, N. E. Lord, K. L. Feigl (2022), Microseismic Activity During Three Shutdowns of the San Emidio Geothermal Plant, Nevada, 2022 American Geophysical Union Meeting.
https://ui.adsabs.harvard.edu/abs/2022AGUFM.S32B..05T/abstract
ABSTRACT: We are analyzing seismic array data from three shutdowns of the San Emidio geothermal plant in Nevada, in 2016, 2021, and 2022. In 2016, an array of ~1,300 vertical-component seismic stations operated by Microseismic Inc. recorded for about a week, and ~130 microseismic events were identified. In 2021, an array of 37 three-component stations was deployed near the center of the 2016 array and recorded for about 4 weeks as part of the WHOLESCALE project. Automated analysis of the data from only the first day of the 2021 shutdown yielded a catalog of about 900 microseismic events. In 2022, an array of 450 three-component stations was deployed as part of the WHOLESCALE project, covering most of the northern ~2/3 of the 2016 array footprint at twice the instrument spacing, and recorded for about a month. Automated analysis of the data again from just the first day of the 2022 shutdown yielded a catalog of only about 30 microseismic events. In all three cases, microseismic activity increased sharply after shutdown. In addition to the varying number of events, our preliminary location results show very different spatial distributions for the events from the three years. The 2016 events were concentrated beneath the northern part of the array where the then primary production wells were situated. The 2021 events were located along the northwest edge of the 2021 array, near a new production well. The 2022 events were located between the 2016 and 2022 events. We are proceeding with the analysis of all three data sets with a uniform workflow to produce comparable event catalogs. Next, we plan to examine potential factors that may be responsible for the very different microseismic responses to the three plant shutdowns.

12) Cardiff, M., Sherman, C., Guo, H., Cunningham, E., Folsom, M., Warren, I., Sone, H., Thurber, C., Wang, H. F., & Feigl, K. L. (2023). WHOLESCALE - Calibration and Simulation of hydro-mechanical Behavior at San Emidio, Nevada During Operational Changes. *48th Workshop on Geothermal Reservoir Engineering Stanford University*. Stanford University, Stanford, California, USA.
https://pangea.stanford.edu/ERE/db/GeoConf/papers/SGW/2023/Cardiff.pdf
ABSTRACT: Changes to geothermal pumping operations produce changes in reservoir fluid pressure that propagate according to the arrangement of fluid sources / sinks (injection / extraction wells, respectively) and reservoir permeability. These changes in fluid pressure induce changes to effective stresses acting on potential fault planes, and thus alter fault stability. For example, Cardiff et al. (2017) used a semi-analytical model, calibrated on existing pressure data, to simulate pressure changes during site shutdown and associated pumping cessation. They demonstrated that microseismic events observed post-shutdown occurred where predicted fluid pressure increases (and effective stress decreases) between 0.05 MPa - 0.15 MPa were simulated. This work investigates pressure changes associated with site shutdowns at the San Emidio Geothermal Field, Nevada. Using existing pumping and pressure change data, we have calibrated finite element numerical models based in the COMSOL and GEOSX platforms. Following calibration, we simulate expected pressure changes and stress field changes within the San Emidio reservoir during site shutdowns. A catalog of microseismic event times and locations measured post-shutdown is then compared against the spatio-temporal changes in fluid pressures and effective stress simulated by our models. In theory, once properly calibrated these models allow the prediction of future seismicity as site operational changes are implemented, such as new pumping wells or flowrate adjustments. In this paper, we provide a snapshot of work in progress. The work presented herein has been funded in part by the Office of Energy Efficiency and Renewable Energy (EERE), U.S. Department of Energy, under Award Number DE-EE0009032.

13) Feigl, K. L., Guo, H., Cunningham, E., Hampton, J., Folsom, M., Akerley, J., Cusini, M., Sherman, C., & Warren, I. (2023, February 6). The 2022 WHOLESCALE Deployment at San Emidio, Nevada, U.S. *48th Workshop on Geothermal Reservoir Engineering*. Stanford Geothermal Workshop, Stanford University, Stanford, California, USA. https://pangea.stanford.edu/ERE/db/GeoConf/papers/SGW/2023/Feigl.pdf

ABSTRACT: The WHOLESCALE acronym stands for Water & Hole Observations Leverage Effective Stress Calculations and Lessen Expenses. The goal of the WHOLESCALE project is to simulate the spatial distribution and temporal evolution of stress in the geothermal system at San Emidio in Nevada, United States. To reach this goal, the WHOLESCALE team is developing a methodology that will incorporate and interpret data from four methods of measurement into a multi-physics model that couples thermal, hydrological, and mechanical (T-H-M) processes over spatial scales ranging from the diameter of a borehole (~0.1 m) to the extent of the entire field (~10 km) and temporal scales ranging from the duration of a microseismic event (~1 second) to the typical lifetime of a producing field (3 decades). The study site at San Emidio includes a volume with length of ~6 km, width ~5 km, and depth ~2 km.

The WHOLESCALE team is taking advantage of the perturbations created by changes in pumping operations during planned shutdowns in 2016, 2021, and 2022 to infer temporal changes in the state of stress in the geothermal system. This rheological experiment is based on the key idea that increasing pore-fluid pressure reduces the effective normal stress acting across preexisting faults. The WHOLESCALE team conducted a field experiment in 2022 to collect data from seismology, drilling, geology, geodesy, and hydrology. In this paper, we provide a snapshot of work in progress. The work presented herein has been funded in part by the Office of Energy Efficiency and Renewable Energy (EERE), U.S. Department of Energy, under Award Number DE-EE0009032.

14) Sone, H., Mudatsir, O., Jin, Z., Folsom, M., Ramirez, G., & Feigl, K. L. (2023, February 6). WHOLESCALE - Characterization of Conductive Fractured Zones Based on Borehole Data at San Emidio Geothermal Field, Nevada. *48th Workshop on Geothermal Reservoir Engineering*. Stanford Geothermal Workshop, Stanford University, Stanford, California, USA. https://pangea.stanford.edu/ERE/db/GeoConf/papers/SGW/2023/Sone.pdf
ABSTRACT: Successful heat production from the San Emidio Geothermal Field, Nevada, highlights the existence of conductive pathways for subsurface fluid flow between the injection and production wells. These zones of high permeability rock mass are mainly identified from drilling records, for instance as drilling intervals where drilling breaks and lost circulation zones occur. Interpolation between the high permeability zones identified in each well allow us to estimate the approximate location and orientation of the first order planar structure (i.e., fault zone) that constitute the conductive pathway in the subsurface. However, the detailed structural nature of these permeable zone (e.g., fracture distribution, fracture orientation, gouge fill, thickness/opening) are still unknown. Such information is essential for conducting geomechanical analysis to predict the mechanical response of the permeable zone to injection and production activities. We integrate lithological, structural, petrophysical information from mud, image, and sonic logs to characterize the permeable zones at reservoir depth. Lithological boundaries identified in mud logs are used to infer fault planes necessary to match known permeable zones and offsets in lithology. Resistivity image logs reveal the abundant presence of natural fractures, potential fault zones (greater than 10 feet) hosting numerous open fractures and conductive rock mass, as well as some potential drilling-induced tensile fractures. Sonic log data also shows low-velocity zones correlated with the potential fault zones identified from the image logs. Sonic reflections also reveal the existence and clustering of reflective fracture planes in the vicinity of the borehole. Density profiles of cuttings reveal a gentle increase in density with depth, with local perturbations caused by anomalous presence of volcanic sediments. In this paper, we provide a snapshot of work in progress focused towards the geological characterizing of the permeable zones in the reservoir. The work presented herein has been funded in part by the Office of Energy Efficiency and Renewable Energy (EERE), U.S. Department of Energy, under Award Number DE-EE0009032.

15) Luo, X., Cunningham, E., Sherman, C., Kreemer, C., Batzli, S. A., Hampton, J., Sone, H., Cardiff, M. A., Lord, N. E., Thurber, C. H., Wang, H. F., & Feigl, K. L. (2023, December 15). *Measuring and Modeling Deformation in the San Emidio Geothermal Field, Nevada, U.S. 2019 – 2022* [Poster]. American Geophysical Union 2023, San Francisco, California, USA. https://agu.confex.com/agu/fm23/meetingapp.cgi/Paper/1281625

ABSTRACT: The WHOLESCALE acronym stands for Water & Hole Observations Leverage Effective Stress Calculations and Lessen Expenses. The goal of the WHOLESCALE project is to simulate the spatial distribution and temporal evolution of stress in the geothermal system at San Emidio in Nevada, United States. To reach this goal, the WHOLESCALE team is developing a methodology that will incorporate and interpret data from four methods of measurement into a multi-physics model that couples thermal, hydrological, and mechanical (T-H-M) processes. The San Emidio geothermal area is located ~100 km north of Reno Nevada in the northwestern Basin and Range province. The San Emidio geothermal system occupies a right step in a North-striking, West-dipping, normal-fault zone (e.g., Hao Guo et al., submitted to JGR, and references therein). In January 2021, two continuously operating GPS stations, SEMS and SEMN, were installed on monuments attached to idle wellheads within the geothermal field at San Emidio. A third GPS station, named GARL, is located outside the geothermal area and used as a reference. We are analyzing the GPS data to calculate daily measurements of (relative) position as time series. GPS station SEMN is subsiding relative to GARL with a mean rate of the order of several millimeters per year. We are also analyzing Interferometric Synthetic Aperture Radar (InSAR) data to measure ground deformation from two satellite missions: TerraSAR-X images acquired since 2019 and SENTINEL-1 images acquired since late 2014. To interpolate and interpret these rich data sets, we are performing numerical modeling using the Finite Element Method to solve the coupled differential equations governing the physics of a fractured, poroelastic medium under stress. The model includes a volume with length of ~10 km, width ~10 km, and depth ~3 km. We acknowledge image data acquired by the TerraSAR-X and TanDEM-X satellite missions operated by the German Space Agency (DLR). These data sets were used under the terms and conditions of Research Project RES1236. Image data sets were also acquired by the SENTINEL-1 satellite mission operated by the European Space Agency (ESA). The work presented herein has been funded in part by the Office of Energy Efficiency and Renewable Energy (EERE), U.S. Department of Energy, under Award Numbers DE-EE0007698 and DE-EE0009032.

16) Cardiff, M. A., Sherman, C., Guo, H., Luo, X., Akerley, J., Sone, H., Thurber, C. H., Wang, H. F., & Feigl, K. L. (2023, December 15). *Monitoring and Modeling of Pumping-induced Pressure Changes at a Natural Geothermal Reservoir Complex: The WHOLESCALE Project at San Emidio, NV*. American Geophysical Union 2023, San Francisco, California, USA. https://agu.confex.com/agu/fm23/meetingapp.cgi/Paper/1359142 ABSTRACT: Injection and extraction of fluids from geothermal reservoirs alters the natural flow of fluids and heat, and similarly produces pore pressure changes that propagate within the reservoir's current permeability structure. In some scenarios, fluid pore pressure changes may be substantial enough to induce seismicity with concomitant alteration to the permeability structure. The San Emidio geothermal field, located ~100 km north of Reno, NV consists of a network of pumping and re-injection wells located within a right-stepping extensional zone associated with a broader regional westward-dipping Basin and Range structural setting. As part of the WHOLESCALE project, pumping and pressure change data from this site was provided by ORMAT Technologies, Inc. encompassing a set of targeted tests carried out in 2016 and 2017. Additionally, ORMAT has shared long-term operational data from the site at daily temporal resolution with the project team, which provides an opportunity to perform long-term modeling of stress changes at San Emidio. To characterize the San Emidio site hydrologically, we use an existing conceptual model of the San Emidio site – consisting of mapped reservoir units and fault structures – and employ inverse modeling to assess permeability within each of these features, using the targeted test data as inputs and a finite-element based model for simulating pressure changes. Employing the method of multiple working hypotheses, we assess the ability of different permeability models to fit existing monitoring data. The models employed range from relatively homogeneous reservoirs to fault-block-dominated and fault-dominated flow. Following inverse modeling, we evaluate the changes to reservoir pore pressures (and thus, effective stress) over longer time periods, including changes to reservoir operations such as site shutdowns. This work was funded in part by the Office of Energy Efficiency and Renewable Energy (EERE), U.S. Department of Energy, under Award Numbers DE-EE0007698 and DE-EE0009032.

17) Luo, X., C. Sherman, K. L. Feigl, J. Murphy, J. Akerley, H. Sone, M. A. Cardiff, J. Hampton, H. Guo, N. E. Lord, P. E. Sobol, C. H. Thurber, and H. F. Wang (2024), WHOLESCALE Modeling of Hydro-Mechanical Processes at San Emidio, Nevada, U.S. on Time Scales of Days, paper presented at PROCEEDINGS, 49th Workshop on Geothermal Reservoir Engineering, Stanford, California Feb. 6-8,2024.https://pangea.stanford.edu/ERE/pdf/IGAstandard/SGW/2024/Luo.pdf
ABSTRACT: The WHOLESCALE acronym stands for Water & Hole Observations Leverage Effective Stress Calculations and Lessen Expenses. The goal of the WHOLESCALE project is to simulate the spatial distribution and temporal evolution of stress in the geothermal system at San Emidio in Nevada, United States. The WHOLESCALE team is taking advantage of the perturbations created by changes in pumping operations during planned shutdowns in 2016, 2021, and 2022 to infer temporal changes in the state of stress in the geothermal system. This rheological experiment is based on the key idea that increasing pore-fluid pressure reduces the effective normal stress acting across preexisting faults. We are developing a fully coupled, hydro-mechanical ("H-M") numerical model to describe seismic observations during the shutdowns using the open-source GEOS code developed at Lawrence Livermore National Laboratory. To construct the model configuration and set values for the material properties, we build on a 3-dimensional geologic and structural model of the reservoir that was updated in 2022 from earlier studies. To constrain the modeled values of permeability, we build on a sensitivity analysis of 3-dimensional hydrologic models of the San Emidio reservoir during transient events such as plant flow tests and temporary, planned shutdowns. To specify the initial conditions and boundary conditions for the mechanical simulation, we use several indicators of stress. The fluid-flow boundary conditions for the models are driven by flow rates recorded at production and injection wells. In refining the models, we consider two different time scales. In this paper, we focus on short time scales on the order of minutes to days. In a companion paper (Feigl et al., this meeting), we consider long time scales of the order of years. To validate the modeling, we consider microseismic events recorded over ten days in December 2016 by a seismic array deployed before, during, and after a planned shutdown in December 2016. In this paper, we provide a snapshot of work in progress.

18) Feigl, K. L., X. Luo, C. Sherman, C. Kreemer, S. A. Batzli, M. A. Cardiff, and H. F. Wang (2024), WHOLESCALE modeling of thermo-hydro-mechanical processes at San Emidio, Nevada, U.S. on time scales of years, paper presented at PROCEEDINGS, 49th Workshop on Geothermal Reservoir Engineering, Stanford University, California, February 12-14, 2024. https://pangea.stanford.edu/ERE/pdf/IGAstandard/SGW/2024/Feigl.pdf
ABSTRACT: The WHOLESCALE acronym stands for Water & Hole Observations Leverage Effective Stress Calculations and Lessen Expenses. The goal of the WHOLESCALE project is to simulate the spatial distribution and temporal evolution of stress in the geothermal system at San Emidio in Nevada, United States. To reach this goal, the WHOLESCALE team is developing a fully coupled, thermo-hydro-mechanical ("T-H-M") numerical model to describe geodetic observations during the shutdowns using the open-source GEOS code developed at Lawrence Livermore National Laboratory (Settgast et al., 2018). In refining the models, we consider two different time scales. In this paper, we focus on long time scales of the order of years. In a companion paper (Luo et al., 2024), we consider short time scales on the order of minutes to days. To calibrate the model, we consider two types of geodetic data: GPS (Global Positioning System) and InSAR (Interferometric Synthetic Aperture Radar). The GPS data set consists of daily time series of displacement in three dimensions. These have been estimated from data collected from two continuously operating stations, SEMS and SEMN, installed on monuments attached to idle wellheads within the geothermal field at San Emidio as well as from a third GPS station, named GARL, located outside the geothermal area in the mountain range to the northeast of the power plant. The shape of the modeled displacement field agrees approximately with that observed by InSAR near the producing wells at the center of the geothermal field. The modeled rate of vertical displacement, however, agrees with that estimated from GPS and InSAR data only to within a factor of four.

19) Thurber, C. H., Cunningham, E., Guo, H., Roecker, S. W., Lord, N. E., & Feigl, K. L. (2024, April 29). *Detailed Analysis of Microseismic Activity Associated with Shutdowns of the San Emidio Geothermal Plant, Nevada*. Seismological Society of America (SSA) Annual Meeting 2024, Anchorage Alaska. https://meetings.seismosoc.org/wp-content/uploads/2024/02/SSA-Program-2024-Rev-I.pdf
ABSTRACT: We are analyzing dense seismic array data encompassing shutdowns of the San Emidio geothermal plant in Nevada in 2016 and 2022. In 2016, an array of ~1,300 vertical-component seismographs operated by Microseismic Inc. recorded for about a week. In 2022, an array of 450 three-component seismographs was deployed as part of the WHOLESCALE project, covering most of the northern ~2/3 of the 2016 array footprint at twice the instrument spacing, and recorded for about a month. The data are being analyzed with two workflows to detect and locate the microseismic events. The first generates a microseismic event catalog directly from the raw continuous seismic data. The second produces high-precision event locations via a sequence of repicking arrivals, waveform cross-correlation, and double-difference relocation. Analysis of the 2022 data set reveals intense seismic activity commencing soon after shutdown and returning to the previous background rate shortly after restart. The events fall into several main clusters that include some linear features. Preliminary results for the 2016 data set show a similar pattern of heightened activity during the shutdown, revealing an order of magnitude more events than a previous catalog estimated using a back-projection approach. The work presented herein has been funded in part by the Office of Energy Efficiency and Renewable Energy (EERE), U.S. Department of Energy, under Award Numbers DE-EE0007698 and DE-EE0009032. The seismic instruments deployed in 2022 were provided by the Incorporated Research Institutions for Seismology (now the EarthScope Consortium) through the PASSCAL Instrument Center at New Mexico Tech. Data collected will be available through the EarthScope Data Management Center. The facilities of the EarthScope Consortium are supported by the National Science Foundation's Seismological Facility for the Advancement of Geoscience (SAGE) Award under Cooperative Support Agreement EAR-1724509.

20) Wang, H. F., Sone, H., Cardiff, M., Guo, H., Thurber, C., Luo, X., & Feigl, K. L. (2024, June 23). *Poroelastic Stress Cycling and Microseismic Activity at the San Emidio Geothermal Field, NV (USA).* 58th US Rock Mechanics/Geomechanics Symposium, Golden, Colorado, USA. https://doi.org/10.56952/ARMA-2024-0813
ABSTRACT: Guo et al. (2023) presented a hypothetical scenario of Thermal-Hydrologic-Mechanical (T-H-M) processes that included a microearthquake cycle associated with annual plant shutdowns at the San Emidio Geothermal Field in northwestern Nevada (USA). Their scenario focused on the relative magnitudes of fluid pressure, Pp, and critical pore fluid pressure, P_{crit}, which is the magnitude of pore pressure above which Coulomb failure triggers seismicity. The scenario was based on three sets of observations and inferences associated with the 20-hour shutdown in December 2016 during which all pumping operations stopped: 1) Simulation of fluid-pressure changes, 2) Observation of microseismic events before, during, and after the shutdown, and 3) Stress inversion of focal mechanisms. We examine the T-H-M coupling between stress, pore fluid pressure, and temperature in terms of the critical value P_{crit} using first-order estimates for failure on small slip patches in a normal-fault zone.

b. Website(s)

Nothing to report.

c. Technologies or techniques

Nothing to report.

d. Inventions, patent applications, and/or licenses

Nothing to report.

e. Other products

Nothing to report.

f. What was the impact on the development of human resources?

During project performance period, the individuals listed in Table 1 benefited from collaborating with other members of the team. In particular, five postdoctoral research associates gained training and experience, thus enhancing their professional development:

Ben Heath, Ph.D. - https://orcid.org/0000-0002-9460-3042
Now Duty Scientist at National Tsunami Warning Center
Erin Cunningham, Ph.D. - https://orcid.org/0000-0002-9680-6812
Now Geophysicist at Oak Ridge National Laboratory
Hao Guo, Ph.D. - https://orcid.org/0000-0001-8287-3689
Now Assistant Scientist, Dept. of Geoscience, U. Wisconsin-Madison
Sui "Jay" Tung, Ph.D. - https://orcid.org/0000-0002-4708-2133
Now Assistant Professor at Texas Tech
Xi Luo, Ph.D. - https://orcid.org/0009-0004-6401-9971
Pursuing second M.S. in Data Science

SECTION XIII. FIELD PHOTOS

Figure 84. Experimental geothermal injection at San Emidio well 58B-33 flowing at 250 gallons/minute during rig development (Matt Folsom 2020/12/22).

Figure 85. Cliff Reed driving a lifter used to install a GPS station on an idle well head in the southern part of the geothermal field at San Emidio in January 2021 (photo Kurt Feigl).

Figure 86. Erin Cunningham staking the location of a seismic station with real-time kinematic GPS in March 2022 (photo Neal Lord).

Figure 87. Ben Jahnke mending a fence between seismic stations during the "planting" stage of the WHOLESCALE deployment in March 2022.

Figure 88. Planting a seismograph, just before filling in the hole to improve coupling between the sensor and the earth, removing the stake to reduce wind noise, and dusting off the top of the instrument to improve the reception of GPS signals. From left to right, Anya Wolterman, DJ Bustos, Ben Jahnke, and Samantha Kleich.

3428 *Figure 89. Joe Pavone with his 4WD toolbox.*

SECTION XIV. ACKNOWLEDGEMENTS

The WHOLESCALE team thanks the following individuals at Ormat Technologies, Inc: Curtis Peach, Cliff Reed, Joe Pavone, Manolo Di Donato, Leeta Miller, Alan Pinuelas-Molina, David Schwab, Lupé Gonsalez Ortiz, Zack Young, and Robin Zuza.

We thank the individuals who contributed to the field work: DJ Bustos (PASSCAL), Alan Horton (PASSCAL), Zirou Jin (UW-Madison), Nina Miller (UNR), and Bret Pecoraro (UNR).

We thank Steven Roecker for helping us with running the REST software workflow.

For the 2022 seismic survey, seismic instruments were provided by the EarthScope Primary Instrument Center (EPIC, formerly the IRIS PASSCAL Instrument Center) at New Mexico Tech. Data collected during this experiment are available through the IRIS Data Management Center. "The facilities of the EarthScope Consortium are supported by the National Science Foundation under Cooperative Agreement EAR-0552316 and by the Department of Energy National Nuclear Security Administration.[18]

The work presented herein has been funded by the Office of Energy Efficiency and Renewable Energy (EERE), U.S. Department of Energy, under Award Number DE-EE0009032.

"Some of the results for this study were generated using Seequent software. Seequent is the Bentley Systems subsurface company."

This study includes SAR images acquired by TerraSAR-X and TanDEM-X satellite missions operated by the German Space Agency (DLR). These data were used under the terms and conditions of Research Project RES1236.

Access to data from the SENTINEL-1 satellite mission operated by the European Space Agency was provided free of charge as described by the Updated ESA Earth Observation Data Policy (Simplified version)[19].

"NASA's provision of the complete ESA Sentinel-1 synthetic aperture radar (SAR) data archive through the ASF DAAC is by agreement between the U.S. State Department and the European Commission (EC). As part of the Earth-observation Copernicus program, the Sentinel mission will provide scientists with accurate, timely, and easily accessible information to help shape the future of our planet. Content on ASF's Sentinel web pages is adapted from the ESA Sentinel-1 website"[20]

Passive seismic data collections were completed at San Emidio in late 2016 by Microseismic Inc. as part of DOE project number DE-EE0007698 as described on the metadata available in the GDR[21].

Parts of this work were performed under the auspices of the U.S. Department of Energy by Lawrence Livermore National Laboratory under Contract DE-AC52-07NA27344.

[18] https://www.passcal.nmt.edu/content/general-information/policy/instrument-use-agreement
[19] https://earth.esa.int/eogateway/documents/d/earth-online/esa-eo-data-policy
[20] https://asf.alaska.edu/datasets/daac/sentinel-1/
[21] https://gdr.openei.org/submissions/1386

SECTION XV. BIBLIOGRAPHY

Agram, P. S., and M. Simons (2015), A noise model for InSAR time-series, Journal of Geophysical Research: Solid Earth, 2014JB011271. http://dx.doi.org/10.1002/2014JB011271

Akerley, J., I. Warren, E. Gasperikova, and S. Pullammanappallil (2023), A Novel Approach to Map Permeability Using Passive Seismic Emission Tomography, United States. https://www.osti.gov/biblio/1986084

Ansari, H., F. D. Zan, and R. Bamler (2017), Sequential Estimator: Toward Efficient InSAR Time Series Analysis, IEEE Transactions on Geoscience and Remote Sensing, 55, 5637-5652.

Aster, R. C., B. Borchers, and C. H. Thurber (2005), Parameter estimation and inverse problems, xii, 301 p. pp., Elsevier Academic Press, Amsterdam ; Boston.

Bekaert, D. P., M. Karim, J. P. Linick, H. Hua, S. Sangha, M. Lucas, . . . S. E. Owen (2019), Development of open-access Standardized InSAR Displacement Products by the Advanced Rapid Imaging and Analysis (ARIA) Project for Natural Hazards, paper presented at AGU Fall Meeting Abstracts.

Berrada Baby, H., P. Golé, and J. Lavergnat (1988), A model for the tropospheric excess path length of radio waves from surface meteorological measurements, Radio Science, 23, 1023-1038. https://doi.org/10.1029/RS023i006p01023

Bhandari, A. R., P. B. Flemings, P. J. Polito, M. B. Cronin, and S. L. Bryant (2015), Anisotropy and Stress Dependence of Permeability in the Barnett Shale, Transport in Porous Media, 108, 393-411. https://doi.org/10.1007/s11242-015-0482-0

Blacker, T. D., S. J. Owen, M. L. Staten, W. R. Quadros, B. Hanks, B. W. Clark, . . . S. Showman (2016), CUBIT geometry and mesh generation toolkit 15.1 user documentation, United States. https://www.osti.gov/biblio/1430472

Blewitt, G., C. Kreemer, W. C. Hammond, and J. Gazeaux (2016), MIDAS robust trend estimator for accurate GPS station velocities without step detection, Journal of Geophysical Research: Solid Earth, 121, 2054-2068. https://doi.org/10.1002/2015JB012552

Blewitt, G., W. C. Hammond, and C. Kreemer (2018), Harnessing the GPS Data Explosion for Interdisciplinary Science, Eos, 99. https://doi.org/10.1029/2018EO104623

Byerlee, J. (1978), Friction of rocks, Pure Appl. Geophys., 116, 615-626.

Cardiff, M. A., C. Sherman, H. Guo, X. Luo, J. Akerley, H. Sone, . . . K. L. Feigl (2023b of Conference), Monitoring and Modeling of Pumping-induced Pressure Changes at a Natural Geothermal Reservoir Complex: The WHOLESCALE Project at San Emidio, NV, abstract presented at AGU.

Cardiff, M., Akerley, J., & Feigl, K. L. (2016). WHOLESCALE: Mass Flux Rates for Wells at San Emidio in December 2016 (p. 2 files) [dataset]. DOE Geothermal Data Repository; University of Wisconsin-Madison. https://doi.org/10.15121/2006850

Cardiff, M., Akerley, J., & Feigl, K. L. (2023). WHOLESCALE: Coordinates of wells at San Emidio, Nevada (p. 1 files) [dataset]. DOE Geothermal Data Repository; University of Wisconsin - Madison. https://doi.org/10.15121/2006837

Cardiff, M., C. Sherman, H. Guo, E. Cunningham, M. Folsom, I. Warren, . . . K. L. Feigl (2023a), WHOLESCALE - Calibration and Simulation of hydro-mechanical Behavior at San Emidio, Nevada During Operational Changes, paper presented at Stanford Geothermal Workshop, Stanford, California. https://pangea.stanford.edu/ERE/db/GeoConf/papers/SGW/2023/Cardiff.pdf

Cardiff, M., C. Sherman, H. Guo, E. Cunningham, M. Folsom, I. Warren, H. Sone, C. Thurber, H. F. Wang, and K. L. Feigl (2023), WHOLESCALE - Calibration and Simulation of hydro-mechanical Behavior at San Emidio, Nevada During Operational Changes, paper presented at Stanford Geothermal Workshop, Stanford, California. https://pangea.stanford.edu/ERE/db/GeoConf/papers/SGW/2023/Cardiff.pdf

Chamberlin, T. C. (1890), The Method of Multiple Working Hypotheses, Science, 15, 92-96. http://www.jstor.org.ezproxy.library.wisc.edu/stable/1764336

Chen, C., and A. A. Holland (2016), PhasePApy: A Robust Pure Python Package for Automatic Identification of Seismic Phases, Seismological Research Letters, 87, 1384-1396. https://doi.org/10.1785/0220160019

Comte, D., M. Farías, D. Calle-Gardella, A. Navarro-Aranguiz, S. Roecker, and A. Rietbrock (2023), Anomalous intraslab structure revealed by the analysis of aftershocks of the Mw 6.7 Coquimbo-La Serena earthquake of 20 January 2019, Tectonophysics, 846, 229660. https://www.sciencedirect.com/science/article/pii/S0040195122004541

Davatzes, N., and S. Hickman (2009), Fractures, stress and fluid flow prior to stimulation of well 27-15, Desert Peak, Nevada, EGS Project, paper presented at Proceedings.

Duncan, P. M., and L. Eisner (2010), Reservoir characterization using surface microseismic monitoring, GEOPHYSICS, 75, 75A139-175A146. https://doi.org/10.1190/1.3467760

Efron, B., and G. Gong (1983), A Leisurely Look at the Bootstrap, the Jackknife, and Cross-Validation, The American Statistician, 37, 36-48. https://www.tandfonline.com/doi/abs/10.1080/00031305.1983.10483087

Efron, B., and R. Tibshirani (1986), Bootstrap methods for standard errors, confidence intervals, and other measures of statistical accuracy, Statistical Science, 1, 54-77.

Eneva, M., G. Falorni, W. Teplow, J. Morgan, G. Rhodes, and D. Adams (2011), Surface Deformation at the San Emidio Geothermal Field, Nevada, from Satellite Radar Interferometry, GRC Transactions, 35.

Faulds, J. E. (2014), 3D Model of the San Emidio Geothermal Area [data set], Geothermal Data Repository. https://gdr.openei.org/submissions/365.

Faulkner, D. R., A. C. Lewis, and E. H. Rutter (2003), On the internal structure and mechanics of large strike-slip fault zones: field observations of the Carboneras fault in southeastern Spain, Tectonophysics, 367, 235-251. https://www.sciencedirect.com/science/article/pii/S0040195103001343

Feigl, K. L., E. C. Reinisch, S. A. Batzli, H. Sone, M. A. Cardiff, J. C. Hampton, N. E. Lord, C. H. Thurber, H. F. Wang, and C. Sherman (2020), Spatio–Temporal Analysis of Deformation at San Emidio Geothermal Field, Nevada, USA between 1992 and 2010, paper presented at Proceedings 45th Workshop on Geothermal Reservoir Engineering Stanford University, Stanford, California, February 10-12, 2020. https://pangea.stanford.edu/ERE/db/GeoConf/papers/SGW/2020/Feigl.pdf

Feigl, K. L., E. C. Reinisch, S. Batzli, and N. Bearson (2018), UW Madison HTCondor InSAR Workflow (software repository). https://github.com/ecreinisch/bin_htcondor

Feigl, K. L., H. Guo, E. Cunningham, J. Hampton, M. Folsom, J. Akerley, M. Cusini, C. Sherman, I. Warren, C. Kreemer, H. Sone, M. A. Cardiff, N. E. Lord, P. E. Sobol, S. A. Batzli, C. H. Thurber, and H. F. Wang (2023), The 2022 WHOLESCALE deployment at San Emidio, Nevada, U.S., paper presented at 48th Workshop on Geothermal Reservoir Engineering, Stanford University, Stanford, California, February 6-8, 2023 SGP-TR-224. https://pangea.stanford.edu/ERE/db/GeoConf/papers/SGW/2023/Feigl.pdf

Feigl, K. L., S. Tung, H. Guo, E. Cunningham, J. Hampton, S. J. Kleich, B. Jahnke, B. Heath, C. Roland, M. Folsom, J. Akerley, M. Cusini, C. Sherman, I. Warren, C. Kreemer, H. Sone, M. A. Cardiff, N. E. Lord, C. H. Thurber, and H. F. Wang (2022b), Overview and Preliminary Results from the WHOLESCALE project at San Emidio, Nevada, U.S., paper presented at 47th Workshop on Geothermal Reservoir Engineering, Stanford, California. https://pangea.stanford.edu/ERE/pdf/IGAstandard/SGW/2022/Feigl.pdf

Feigl, K. L., X. Luo, C. Sherman, C. Kreemer, S. A. Batzli, M. A. Cardiff, and H. F. Wang (2024), WHOLESCALE modeling of thermo-hydro-mechanical processes at San Emidio, Nevada, U.S. on time scales of years, paper presented at PROCEEDINGS, 49th Workshop on Geothermal Reservoir Engineering, Stanford University, California, February 12-14, 2024. https://pangea.stanford.edu/ERE/pdf/IGAstandard/SGW/2024/Feigl.pdf

Feigl, K., C. Thurber, and N. Lord (2022a), WHOLESCALE survey at San Emidio, Nevada, USA [Data set]. https://doi.org/10.7914/m5qt-mh37

Folsom, M., Libbey, R., Feucht, D., I., Warren., & Garanzini, S. (2020). Geophysical Observations and Integrated Conceptual Models of the San Emidio Geothermal Field, Nevada. Workshop on Geothermal Reservoir Engineering, Stanford, California, USA. https://pangea.stanford.edu/ERE/db/GeoConf/papers/SGW/2020/Folsom.pdf

Folsom, M., R. Libbey, D. Feucht, I. Warren, and S. Garanzini (2021), Geophysical observations and integrated conceptual models of the San Emidio Geothermal Field, Nevada, paper presented at Nevada Petroleum & Geothermal Society, February 4th, 2021.

Folsom, M., R. Libbey, D. Feucht, W. I., and S. Garanzini (2020), Geophysical Observations and Integrated Conceptual Models of the San Emidio Geothermal Field, Nevada., paper presented at Workshop on Geothermal Reservoir Engineering, Stanford, California, USA. https://pangea.stanford.edu/ERE/db/GeoConf/papers/SGW/2020/Folsom.pdf

Gabriel, A. K., R. M. Goldstein, and H. A. Zebker (1989), Mapping small elevation changes over large areas: differential radar interferometry, J. Geophys. Res., 94, 9183-9191.

Gonzalez, L. F., A. C. Aguiar, and M. Karplus (2022), Data mining microseismicity associated to the Blue Mountain geothermal site, Lawrence Livermore National Lab.(LLNL), Livermore, CA (United States). https://www.osti.gov/servlets/purl/1844493

Guo, H., & Thurber, C. (2021). Double-difference seismic attenuation tomography method and its application to the Geysers geothermal field, California. Geophysical Journal International, 225(2), 926–949. https://doi.org/10.1093/gji/ggab017

Guo, H., and H. Zhang (2017), Development of double-pair double difference earthquake location algorithm for improving earthquake locations, Geophysical Journal International, 208, 333-348. https://doi.org/10.1093/gji/ggw397

Guo, H., C. H. Thurber, B. A. Heath, M. Cardiff, N. Lord, I. Warren, and K. L. Feigl (2022), Seismic analysis of reservoir conditions for inducing seismicity at the San Emidio geothermal field, Nevada, U.S.A., abstract presented at Annual Meeting Seismological Society of America, Bellevue, WA, USA, 19-23 April 2022.

Guo, H., C. Thurber, I. Warren, B. A. Heath, M. Folsom, H. Sone, N. Lord, J. Akerley, and K. L. Feigl (2023), Enhanced Microseismicity During Production Pumping Cessation at the San Emidio Geothermal Field (Nevada, USA) in December 2016, Journal of Geophysical Research: Solid Earth, 128, e2023JB027008. https://doi.org/10.1029/2023JB027008

Guo, H., H. Zhang, R. M. Nadeau, and Z. Peng (2017), High-resolution deep tectonic tremor locations beneath the San Andreas Fault near Cholame, California, using the double-pair double-difference location method, Journal of Geophysical Research: Solid Earth, 122, 3062-3075. https://doi.org/10.1002/2016JB013919

Guo, H., McGuire, J. J., & Zhang, H. (2021). Correlation of porosity variations and rheological transitions on the southern Cascadia megathrust. Nature Geoscience, 14(5), 341–348. https://doi.org/10.1038/s41561-021-00740-1

Guo, H., Zhang, H., & Froment, B. (2018). Structural control on earthquake behaviors revealed by high-resolution *Vp*/Vs imaging along the Gofar transform fault, East Pacific Rise. Earth and Planetary Science Letters, 499, 243–255. https://doi.org/10.1016/j.epsl.2018.07.037

Guo, H., C. Thurber, E. Cunningham, M. Cardiff, N. Lord, P. Sobol, H. Wang, and K. L. Feigl (submitted 2024/08/22 to Geophys. Res. Lett.), Microseismicity Modulation Due to Changes in Geothermal Productionat San Emidio, Nevada, USA.

Hampton, J., S. J. Kleich, M. Folsom, C. Sherman, K. L. Feigl, and WHOLESCALE_Team (2022 of Conference), Laboratory poroelastic measurements of geothermal rocks, abstract presented at 56th US Rock Mechanics/Geomechanic Symposium.

Hardebeck, J. L., and A. J. Michael (2006), Damped regional-scale stress inversions: Methodology and examples for southern California and the Coalinga aftershock sequence, Journal of Geophysical Research: Solid Earth, 111. https://doi.org/10.1029/2005JB004144

Hardebeck, J. L., and P. M. Shearer (2002), A New Method for Determining First-Motion Focal Mechanisms, Bulletin of the Seismological Society of America, 92, 2264-2276. http://www.bssaonline.org/content/92/6/2264.abstract

Heidbach, O., M. Rajabi, K. Reiter, M. Ziegler, and W. team (2016), World stress map database release 2016, in GFZ Data Services. http://www.world-stress-map.org

Hettema, M. H. H., Schutjens, P. M. T. M., Verboom, B. J. M., & Gussinklo, H. J. (2000). Production-Induced Compaction of a Sandstone Reservoir: The Strong Influence of Stress Path. SPE Reservoir Evaluation & Engineering, 3(04), 342–347. https://doi.org/10.2118/65410-PA

Hickman, S. H., and N. C. Davatzes (2010), In-Situ Stress and Fracture Characterization for Planning of an EGS Stimulation in the Desert Peak Geothermal Field, Nevada, paper presented at Thirty-Fifth Workshop on Geothermal Reservoir Engineering SGP-TR-188, Stanford University, February 1-3, 2010. https://digitalcommons.unl.edu/usgsstaffpub/418/

Hickman, S., and M. Zoback (1998), Tectonic controls on fracture permeability in a geothermal reservoir at Dixie Valley, Nevada, Medium: ED; Size: 12 p. http://www.osti.gov/energycitations/servlets/purl/656552-pqPyck/webviewable/

Jaeger, J. C., and N. G. W. Cook (1979), Fundamentals of Rock Mechanics, 3rd edition ed., 593 pp., Chapman and Hall, London.

Jahnke, B. (2022), Geomechanical Analysis of the Geothermal Reservoir at San Emidio, Nevada and Fracture Toughness Anisotropy of EGS Collab Testbed Rocks, M.S. thesis, University of Wisconsin-Madison (H. Sone, advisor).

Jahnke, B., H. Guo, B. Heath, E. Cunningham, C. Sherman, H. Sone, I. Warren, C. Kreemer, C. H. Thurber, K. F. Feigl, and WHOLESCALE_Team (2022), Spatial-Temporal Stress Heterogeneity in the Geothermal Reservoir at San Emidio, Nevada, U.S., paper presented at 45th Workshop on Geothermal Reservoir Engineering, February 7-9, 2022, Stanford University, Stanford, California,. https://pangea.stanford.edu/ERE/pdf/IGAstandard/SGW/2022/Jahnke.pdf

Jahnke, B., H. Sone, H. Guo, C. Sherman, I. Warren, C. Kreemer, C. H. Thurber, and K. L. Feigl (2023), Geomechanical analysis of the geothermal reservoir at San Emidio, Nevada, Geothermics, 110, 102683. https://doi.org/10.1016/j.geothermics.2023.102683

Jeremic, A., M. Thornton, and P. Duncan (2016 of Conference), Ambient passive seismic imaging with noise analysis, abstract presented at 2016 SEG International Exposition and Annual Meeting.

Jolivet, R., M. Simons, P. S. Agram, Z. Duputel, and Z. K. Shen (2015), Aseismic slip and seismogenic coupling along the central San Andreas Fault, Geophysical Research Letters, 42, 297-306. http://dx.doi.org/10.1002/2014GL062222

Kilb, D., and J. L. Hardebeck (2006), Fault Parameter Constraints Using Relocated Earthquakes: A Validation of First-Motion Focal-Mechanism Data, Bulletin of the Seismological Society of America, 96, 1140-1158. https://doi.org/10.1785/0120040239

Kleich, S. J. (2022a), Mechanical and Poroelastic Properties of Lithologic Units Within the San Emidio Geothermal System, Nevada, United States, M.S. thesis, University of Wisconsin-Madison (J. Hampton, advisor).

Kleich, S. J. F., Hampton, Jesse, Feigl, Kurt L. WHOLESCALE_Team (2022b), Lab-scale structural analysis and poroelastic measurements of rocks from the San Emidio Geothermal Field, Nevada, U.S, paper presented at 47th Workshop on Geothermal Reservoir Engineering, Stanford, California. https://pangea.stanford.edu/ERE/pdf/IGAstandard/SGW/2022/Kleich.pdf

Kleich, S. J., M. Folsom, C. Sherman, K. L. Feigl, and J. C. Hampton (2022c), Measurements of elastic moduli and stress dependence of geothermal rocks, paper presented at 56th US Rock Mechanics/Geomechanics Symposium, Santa Fe, New Mexico, USA,, 26-29 June 2022. https://santafe2022.armarocks.org/

Kleich, S., S. Bradshaw, J. Hampton, and K. Feigl (2022a), WHOLESCALE Catalog of Rock Samples at San Emidio Nevada collected in January 2021 Version 2.0 [data set]. https://gdr.openei.org/submissions/1396.

Kreemer, C., G. Blewitt, and E. C. Klein (2014), A geodetic plate motion and Global Strain Rate Model, Geochemistry, Geophysics, Geosystems, 15, 3849-3889. http://dx.doi.org/10.1002/2014GC005407

Kreemer, C., G. Blewitt, and P. Davis (2020), Geodetic evidence for a buoyant mantle plume beneath the Eifel volcanic area, NW Europe, Geophysical Journal International, 222., 1316-1332. https://doi.org/10.1093/gji/ggaa227

Krieger, G., A. Moreira, H. Fiedler, I. Hajnsek, M. Werner, M. Younis, and M. Zink (2007), TanDEM-X: A Satellite Formation for High-Resolution SAR Interferometry, IEEE Trans. Geoscience Remote Sensing, 45, 3317-3341. http://dx.doi.org/10.1109/tgrs.2007.900693

Kumar, R., N. Bennett, A. Donald, G. Martinez, and E. Velez (2019), 3D Borehole Sonic Imaging for Input to Structural Modeling-A Quantitative Approach, paper presented at Society of Petroleum Engineers SPE Middle East Oil and Gas Show and Conference, Manama, Bahrain, 18-21 March 2019. http://onepetro.org/SPEMEOS/proceedings-pdf/19MEOS/4-19MEOS/D041S042R001/1144769/spe-194810-ms.pdf/1

Kusumawati, D., D. P. Sahara, S. Widiyantoro, A. D. Nugraha, M. Muzli, I. Imran, N. T. Puspito, and Z. Zulfakriza (2021), Fault Instability and Its Relation to Static Coulomb Failure Stress Change in the 2016 Mw 6.5 Pidie Jaya Earthquake, Aceh, Indonesia, Frontiers in Earth Science, 8.

Kuttruff, H. (1991), Basic Concepts of Acoustics, in Ultrasonics: Fundamentals and Applications, edited by H. Kuttruff, pp. 11-47, Springer Netherlands, Dordrecht. https://doi.org/10.1007/978-94-011-3846-8_2

Liu, F., P. Fu, R. J. Mellors, M. A. Plummer, S. T. Ali, E. C. Reinisch, Q. Liu, and K. L. Feigl (2018), Inferring Geothermal Reservoir Processes at the Raft River Geothermal Field, Idaho, USA, Through Modeling InSAR-Measured Surface Deformation, Journal of Geophysical Research: Solid Earth, 123, 3645-3666. http://dx.doi.org/10.1029/2017JB015223

Lord, N. E., P. Sobol, H. Guo, C. H. Thurber, I. Warren, D. J. Bustos, S. L. Bradshaw, and K. L. Feigl (2022), WHOLESCALE: Seismic Waveform Data from San Emidio, Nevada 2022, University of Wisconsin - Madison. https://gdr.openei.org/submissions/1610

Lord, N., B. Heath, E. Cunningham, C. Thurber, S. Bradshaw, and K. Feigl (2021a), WHOLESCALE: Seismic Survey Metadata from San Emidio Nevada 2021, Department of Geoscience - University of Wisconsin-Madison. https://doi.org/10.15121/2349481

Lord, N., B. Heath, E. Cunningham, C. Thurber, S. Bradshaw, and K. L. Feigl (2021b), WHOLESCALE: Seismic Survey Data from San Emidio Nevada 2021, University of Wisconsin - Madison. https://doi.org/10.15121/2349480

Lord, N., B. Heath, H. Guo, I. Warren, S. Bradshaw, C. Thurber, J. Akerley, and K. Feigl (2016a), Seismic Survey 2016 Data at San Emidio Nevada, University of Wisconsin - Madison. https://doi.org/10.15121/2008357

Lord, N., B. Heath, H. Guo, I. Warren, S. Bradshaw, C. Thurber, J. Akerley, and K. Feigl (2016b), Seismic Survey 2016 Metadata at San Emidio, Nevada, University of Wisconsin. https://doi.org/10.15121/1872549

Lord, N., Heath, B., Cunningham, E., Thurber, C., Bradshaw, S., & Feigl, K. (2021). WHOLESCALE Seismic Survey 2021 Metadata at San Emidio, Nevada [dataset]. Department of Geoscience - University of Wisconsin-Madison; Geothermal Data Repository. https://gdr.openei.org/submissions/

Lord, N., Heath, B., Guo, H., Warren, I., Bradshaw, S., Thurber, C., Akerley, J., & Feigl, K. (2016). Seismic Survey 2016 Data at San Emidio Nevada (p. 3 files) [dataset]. DOE Geothermal Data Repository; University of Wisconsin-Madison. https://doi.org/10.15121/2008357

Luo, X., C. Sherman, K. L. Feigl, J. Murphy, J. Akerley, H. Sone, M. A. Cardiff, J. Hampton, H. Guo, N. E. Lord, P. E. Sobol, C. H. Thurber, and H. F. Wang (2024), WHOLESCALE Modeling of Hydro-Mechanical Processes at San Emidio, Nevada, U.S. on Time Scales of Days, paper presented at PROCEEDINGS, 49th Workshop on Geothermal Reservoir Engineering, Stanford, California February 6-8, 2024. https://pangea.stanford.edu/ERE/pdf/IGAstandard/SGW/2024/Luo.pdf

Martinez-Garzon, P., Kwiatek, G., Ickrath, M., & Bohnhoff, M. (2014). MSATSI: A MATLAB Package for Stress Inversion Combining Solid Classic Methodology, a New Simplified User-Handling, and a Visualization Tool. Seismological Research Letters, 85(4), 896–904. https://doi.org/10.1785/0220130189

Martínez-Garzón, P., G. Kwiatek, H. Sone, M. Bohnhoff, G. Dresen, and C. Hartline (2014b), Spatiotemporal changes, faulting regimes, and source parameters of induced seismicity: A case study from The Geysers geothermal field, Journal of Geophysical Research: Solid Earth, 119, 8378-8396.

Martínez-Garzón, P., G. Kwiatek, M. Ickrath, and M. Bohnhoff (2014a), MSATSI: A MATLAB Package for Stress Inversion Combining Solid Classic Methodology, a New Simplified User-Handling, and a Visualization Tool, Seismological Research Letters, 85, 896-904. https://doi.org/10.1785/0220130189

Massonnet, D., and K. L. Feigl (1998), Radar interferometry and its application to changes in the Earth's surface, Reviews of Geophysics, 36, 441-500. https://doi.org/10.1029/97RG03139

Matlick, J. S. (1995), San Emidio Geothermal System, Empire, Nevada: GRC Field Trip ~ October 1995, Mesquite Group, Inc., Fullerton, California. https://data.nbmg.unr.edu/public/Geothermal/GreyLiterature/Matlick_SanEmidioGeoSystem_1995.pdf

Moeck, I. (2011), Stress Inversion and 2D fault stress modeling San Emidio: Project Report to PI Teplow, 19 page pp.

Oppenheimer, D. H., P. A. Reasenberg, and R. W. Simpson (1988), Fault plane solutions for the 1984 Morgan Hill, California, Earthquake Sequence: Evidence for the state of stress on the Calaveras Fault, Journal of Geophysical Research: Solid Earth, 93, 9007-9026. https://doi.org/10.1029/JB093iB08p09007

Pan, Z., Y. Ma, L. D. Connell, D. I. Down, and M. Camilleri (2015), Measuring anisotropic permeability using a cubic shale sample in a triaxial cell, Journal of Natural Gas Science and Engineering, 26, 336-344. https://www.sciencedirect.com/science/article/pii/S1875510015002723

Pitz, W., and D. Miller (2010), The TerraSAR-X Satellite, Geoscience and Remote Sensing, IEEE Transactions on, 48, 615-622. http://dx.doi.org/10.1109/TGRS.2009.2037432

Pulliam, R. J., F. Sepulveda, J. S. Thangraj, D. Quiros, J. Queen, M. Queen, and J. Iovenitti (2019), Development of a Novel, Near Real Time Approach To Geothermal Seismic Exploration And Monitoring Via Ambient Seismic Noise Interferometry, Medium: ED pp, Baylor Univ., Waco, TX (United States). https://www.osti.gov/servlets/purl/1648329

Reinisch, E. C. (2018b), UW Madison HTCondor InSAR Workflow (Source Code). https://github.com/ecreinisch/bin_htcondor.git

Reinisch, E. C., M. Cardiff, and K. L. Feigl (2016), Graph theory for analyzing pair-wise data: application to geophysical model parameters estimated from interferometric synthetic aperture radar data at Okmok volcano, Alaska, Journal of Geodesy, 1-16. http://dx.doi.org/10.1007/s00190-016-0934-5

Reinisch, E. C., M. Cardiff, J. Akerley, I. Warren, and K. L. Feigl (2019), Spatio–Temporal Analysis of Deformation at San Emidio Geothermal Field, Nevada, USA Between 1992 and 2010, Remote Sensing, 11, 1935. http://dx.doi.org/10.3390/rs11161935

Rhodes, G. T. (2011), Structural controls of the San Emidio Geothermal System, M.S. thesis, vi, 73 leaves pp, University of Nevada Reno advisor).

Rhodes, G. T., J. E. Faulds, and A. R. Ramelli (2011), Preliminary Geologic Map of the Northern Lake Range, San Emidio Geothermal Area, Washoe County, Nevada, Nevada Bureau of Mines and Geology. http://data.nbmg.unr.edu/public/freedownloads/of/of2011-11.zip

Rhodes, G. T., J. E. Faulds, and W. Teplow (2010), Structural Controls of the San Emidio Desert Geothermal Field, Northwestern Nevada, paper presented at Geothermal Resource Council Transactions.

Salvi, S., S. Stramondo, G. J. Funning, A. Ferretti, F. Sarti, and A. Mouratidis (2012), The Sentinel-1 mission for the improvement of the scientific understanding and the operational monitoring of the seismic cycle, Remote Sensing of Environment, 120, 164-174. http://dx.doi.org/10.1016/j.rse.2011.09.029

Sandwell, D., R. Mellors, X. Tong, M. Wei, and P. Wessel (2011), Open radar interferometry software for mapping surface deformation, Eos, Transactions American Geophysical Union, 92, 234-234. http://topex.ucsd.edu/gmtsar

Sandwell, D., R. Mellors, X. Tong, X. Xu, M. Wei, and P. Wessel (2016), GMTSAR: An InSAR Processing System Based on Generic Mapping Tools. , UC San Diego: Scripps Institution of Oceanography. http://topex.ucsd.edu/gmtsar/tar/GMTSAR_2ND_TEX.pdf

Settgast, R. R., J. A. White, B. C. Corbett, A. Vargas, C. Sherman, P. Fu, and C. Annavarapu (2018), GEOSX Simulation Framework: General multi-physics simulation framework targeting exascale computing platforms, Medium: X; OS: Any pp., Lawrence Livermore National Lab. (LLNL), Livermore, CA (United States). https://www.osti.gov/biblio/1422506

Sherman, C. S., Morris, J. P., Fu, P., & Settgast, R. R. (2019). Recovering the Microseismic Response from a Geomechanical Simulation. Geophysics, 84(4), Article 4.

Sherman, C. S., Templeton, D. C., Morris, J. P., & Matzel, E. (2016). Modeling Induced Microseismicity in an Enhanced Geothermal System. In Proceedings of the 50th US Rock Mechanics/Geomechanics Symposium. American Rock Mechanics Association.

Siler, D. L., J. E. Faulds, B. Mayhew, and D. D. McNamara (2016), Analysis of the favorability for geothermal fluid flow in 3D: astor Pass geothermal prospect, Great Basin, northwestern Nevada, USA, Geothermics, 60. http://dx.doi.org/10.1016/j.geothermics.2015.11.002

Sone, H., Z. Jin, O. Mudatsir, I. Warren, M. Folsom, and K. L. Feigl (2023), WHOLESCALE - Characterization of Conductive Fractured Zones Based on Borehole Data at San Emidio Geothermal Field, Nevada, paper presented at Stanford Geothermal Workshop. https://pangea.stanford.edu/ERE/db/GeoConf/papers/SGW/2023/Sone.pdf

Templeton, D. C., E. Matzel, and T. Cladouhos (2017), Evolution of microseismicity at the Blue Mountain geothermal site, Lawrence Livermore National Lab.(LLNL), Livermore, CA (United States). https://www.osti.gov/servlets/purl/1399704

Teplow, W. J., and I. Warren (2015), Finding Large Aperture Fractures in Geothermal Resource Areas Using a Three-Component Long-Offset Surface Seismic Survey, PSInSAR and Kinematic Structural Analysis, Medium: ED; Size: 52 p. pp, US Geothermal, Inc., Boise, ID (United States). https://doi.org/10.2172/1213113

Thurber, C. H., H. Guo, E. Cunningham, S. W. Roecker, J. Hampton, N. E. Lord, and K. L. Feigl (2024 of Conference), Detailed Analysis of Microseismic Activity Associated with Shutdowns of the San Emidio Geothermal Plant, Nevada, abstract presented at Seismological Society of America, Anchorage, Alaska April 29 to May 3, 2024. https://meetings.seismosoc.org/wp-content/uploads/2024/02/SSA-Program-2024-Rev-I_Technical-Program.pdf

Tosha, T., M. Sugihara, and Y. Nishi (1998), Revised hypocenter solutions for microearthquakes in the Kakkonda geothermal field, Japan, Geothermics, 27, 553-571. https://www.sciencedirect.com/science/article/pii/S0375650598000339

UNR (2014), Slip and Dilation Tendency Analysis of the San Emidio Geothermal Area [data set]. https://gdr.openei.org/submissions/371

Vavryčuk, V. (2014), Iterative joint inversion for stress and fault orientations from focal mechanisms, Geophysical Journal International, 199, 69-77.

Waldhauser, F., W. L. Ellsworth, and D. Oppenheimer (2004), Persistence of the Parkfield seismicity patterns through the 2004 mainshock, paper presented at AGU Fall Meeting Abstracts, December 1, 2004.

Wang, H. F., H. Sone, M. Cardiff, H. Guo, C. Thurber, X. Luo, and K. L. Feigl (2024), Poroelastic Stress Cycling and Microseismic Activity at the San Emidio Geothermal Field, NV (USA), paper presented at 58th US Rock Mechanics/Geomechanics Symposium, Golden, Colorado, USA., June 23, 2024. https://golden2024.armarocks.org/

Warren, I. (2010), Three-Component Long Offset Surface Seismic Survey Data Used to Find Large Aperture Fractures in Geothermal Resources - San Emidio Geothermal Resource Area, U.S. Geothermal Inc. https://doi.org/10.15121/1422726

Warren, I., E. Gasperikova, and S. Pullammanappallil (2019a), Final Phase 1 Report DE-EE0007698: A Novel Approach to Map Permeability Using Passive Seismic Emission Tomography. https://subterraseis.com/wp-content/uploads/2019/10/Doc1.pdf

Warren, I., E. Gasperikova, S. Pullammanappallil, S. Sennert, and M. Grealy (2018), Mapping Geothermal Permeability Using Passive Seismic Emission Tomography Constrained by Cooperative Inversion of Active Seismic and Electromagnetic Data, paper presented at Proceedings, 43rd Workshop on Geothermal Reservoir Engineering Stanford University, Stanford, California, 2018 SGP-TR-213, February 12-14, 2018. https://pangea.stanford.edu/ERE/pdf/IGAstandard/SGW/2018/Warren.pdf

Warren, I., E. Gasperikova, S. Pullammanappallil, S. Sennert, and M. Grealy (2019b), A Novel Approach to Map Permeability Using Passive Seismic Emission Tomography, paper presented at World Geothermal Conference.

Warren, I., M. Folsom, J. Akerley, and K. Feigl (2016a), Passive Seismic Emission Tomography Results at San Emidio Nevada, Ormat Technologies, Inc. https://doi.org/10.15121/1924268

Winn, C. L., P. Dobson, C. Ulrich, T. Kneafsey, T. S. Lowry, Z. Cesa, R. Zuza, J. Akerley, B. Delwiche, and A. Samuel (2021), When Where and Why: The Geologic Context of Lost Circulation While Drilling in a Crystalline Geothermal Reservoir, paper presented at PROCEEDINGS, 46th Workshop on Geothermal Reservoir Engineering, Stanford University, Stanford, California, February 15-17, 2021. https://www.osti.gov/servlets/purl/1847220

Xu, X., and D. T. Sandwell (2020), Toward Absolute Phase Change Recovery With InSAR: Correcting for Earth Tides and Phase Unwrapping Ambiguities, IEEE Transactions on Geoscience and Remote Sensing, 58, 726-733. https://ieeexplore.ieee.org/document/8850313/

Yarce, J., A. F. Sheehan, and S. Roecker (2023), Temporal Relationship of Slow Slip Events and Microearthquake Seismicity: Insights From Earthquake Automatic Detections in the Northern Hikurangi Margin, Aotearoa New Zealand, Geochemistry, Geophysics, Geosystems, 24, e2022GC010537. https://doi.org/10.1029/2022GC010537

Yunjun, Z., H. Fattahi, and F. Amelung (2019), Small baseline InSAR time series analysis: Unwrapping error correction and noise reduction, Computers & Geosciences, 133.

Zan, F. D., M. Zonno, and P. López-Dekker (2015), Phase Inconsistencies and Multiple Scattering in SAR Interferometry, IEEE Transactions on Geoscience and Remote Sensing, 53, 6608-6616.

Zheng, Y., H. Fattahi, P. Agram, M. Simons, and P. Rosen (2022), On Closure Phase and Systematic Bias in Multilooked SAR Interferometry, IEEE Transactions on Geoscience and Remote Sensing, 60, 1-11. http://doi.org/10.1109/tgrs.2022.3167648.

LAST PAGE

This page is intentionally blank. Thanks for reading this far!